

# The design of DNA-containing biomaterials for forensic science

A Thesis Submitted to the Committee of Graduate Studies in Partial  
Fulfillment of the Requirements for Degree of Doctor of Philosophy in the  
Faculty of Arts and Science

TRENT UNIVERSITY

Peterborough Ontario, Canada

© Copyright by Amanda M. Orr 2023

Environmental and Life Science Ph.D. Graduate Program

September 2023

## Abstract

The design of DNA-containing biomaterials for forensic science.

Amanda M. Orr

Access to human blood for forensic research and training in bloodstain pattern analysis (BPA) can be difficult due to many ethical, safety and cost concerns. Mammalian blood alternatives can be sourced, especially from local and willing abattoirs, but some concerns remain, and the added difficulties of high variation and species-specific differences in cellular components pose other issues. Therefore, synthetic alternatives to human blood provide practical options for the BPA community. This thesis explores the use of alginate hydrogels as a base material for forensic blood substitute (FBS) development. Hydrogels are first explored as a suitable environment for DNA stability and functionality and compared to other polymer systems. The ability of DNA to remain intact while undergoing electrospray ionization (ESI) is also investigated. The FBS design focuses on mimicking the fluid properties and genetic capabilities of whole human blood - a material not developed in FBSs previously. ESI was used to develop microparticles (MPs) that serve as cellular components of human blood (the red blood cells - RBCs, and white blood cells - WBCs). The microparticles were ionically crosslinked using calcium to provide small MPs (RBCs) or covalently crosslinked with functional DNA to provide larger WBC-like functional

particles. The integration of these novel MPs into alginate-based materials is optimized and their use in BPA scenarios is explored. The FBS is tested in BPA scenarios of dripping experiments, impact patterns, and the ability to extract and amplify the contained DNA. In addition, the stability (or shelf-life) of the FBS was also assessed. The FBS exhibited similar spreading ratios to blood and demonstrated feasibility in use for impact angle ( $\alpha$ ) determination and impact pattern creation. Importantly, the DNA contained within the FBS could be processed with analogous protocols used in DNA evidence processing, enhancing its applicability to BPA research and training.

## Keywords

Bloodstain pattern analysis, forensic materials, forensic blood substitutes, synthetic DNA design, Combined DNA Index System (CODIS) loci, alginate hydrogels, electrospray ionization

## Abbreviations and Symbols

### *Abbreviations*

(3-Glycidyloxypropyl)trimethoxysilane	GPTMS
1-ethyl-3-(3-dimethylaminopropyl) carbodiimide•HCl	EDC
2-(N-morpholino)ethanesulfonic acid	MES
5' amine-terminated DNA	N-DNA
$\alpha$ -L-gulonate	G block
Acetonitrile	ACN
Alginate covalently crosslinked with DNA	AXD0N
Alginate covalently crosslinked with N-DNA	AXD1N
Alginate covalently crosslinked with N-DNA-N	AXD2N
Arginine-Glycine-Aspartic Acid amino acid	RGD
Attenuated total reflectance	ATR
$\beta$ -D-mannuronate	M block
Bloodstain pattern analysis	BPA
Calcium alginate ionic crosslinked hydrogel	CA
Calcium alginate tissue gels	CATGs
Calcium chloride	CaCl <sub>2</sub>
Calcium ion	Ca <sup>2+</sup>
Carbonyl group	C=O
Carboxyl group	COOH
Carboxylate ion	COO <sup>-</sup>
Combined DNA index system	CODIS
Deoxyribonucleic acid	DNA
Dual-amine-terminated DNA	N-DNA-N
Electrospray ionization	ESI
Epoxide ring	R-COC
Extracellular matrix	ECM
Forensic blood substitute	FBS
Fourier transform infrared spectroscopy	FTIR
Fourier transform ion cyclotron resonance mass spectrometry	FT-ICR MS
Free ion decay	FID
High-resolution mass spectrometry	HRMS
Horseradish peroxidase	HRP
Hydrogen peroxide	H <sub>2</sub> O <sub>2</sub>
Hydroxyl groups	R-OH
Isopropanol	IPA
Linear viscoelastic region	LVR

Matrix-assisted laser desorption ionization	MALDI
Methanol	MeOH
Methoxy group	R-O-CH <sub>3</sub>
Microparticle	MP
N-Hydroxysulfosuccinimide	Sulfo-NHS
National Academy of Sciences	NAS
National Institute of Standards and Technology	NIST
Nitrogen gas	N <sub>2</sub>
Packed cell volume %	PCV%
Partial Least Squares-Discriminant Analysis	PLS-DA
Poly(ethylene glycol)	PEG
Polydimethylsiloxane	PDMS
Polymerase chain reaction	PCR
Polyvinylpyrrolidone	PVP
Post-mortem interval	PMI
Potassium ion	K <sup>+</sup>
President's Council of Advisors on Science and Technology	PCAST
Primary amine	NH <sub>2</sub>
Proton	H <sup>+</sup>
Red blood cell	RBC
Relative fluorescent unit	RFU
Scanning electron microscopy	SEM
Short tandem repeat	STR
Single amine-terminated DNA	N-DNA
Single stranded DNA	ssDNA
Sodium carbonate	NaCO <sub>3</sub>
Sodium ion	Na <sup>+</sup>
Sodium trifluoroacetate	NaTFA
Solution-gelation	Sol-gel
Tetraethylorthosilicate	TEOS
Thermogravimetric analysis	TGA
Three-dimensional	3D
Time of flight	TOF
Time since deposition	TSD
Variable importance in projection	VIP
White blood cell	WBC
Xanthan gum	XG

## *Symbols*

Angular frequency	$\omega$
Carbon 13 isotope	$^{13}\text{C}$
Charge	$z$
Complex viscosity	$\eta^*$
Density	$\rho$
Effective viscosity	$\mu_{\text{eff}}$
Experimental $m/z$ value	$M_{\text{experimental}}$
Flow rate	$Q$
Hydrogen 2 isotope	$^2\text{H}$
Impact angle	$\alpha$
Impact velocity	$v$
Inertia	$I$
Initial droplet diameter	$D_0$
Loss modulus	$G''$
Mass to charge ratio	$m/z$
Maximum stain diameter	$D_s$
Minimum strain	$\gamma_0$
Minimum torque	$T_{\text{min}}$
Monoisotopic mass	$M$
Nitrogen 15 isotope	$^{15}\text{N}$
Ohnesorge Number	$Oh$
Oxygen 17 isotope	$^{17}\text{O}$
Peak width at FWHM	$\Delta m/z$
Resolution using the full width at half maximum	$R_{\text{FWHM}}$ or $R$
Reynolds number	$Re$
Spray distance	$d$
Spreading Ratio	$D_s/D_0$
Storage modulus	$G'$
Strain constant	$F_\gamma$
Stress constant	$F_\tau$
Surface tension	$\sigma$
Tan delta	$\tan\delta$
Theoretical $m/z$	$M_{\text{theoretical}}$
Viscosity	$\eta$
Voltage	$V$
Weber number	$We$

## Acknowledgements

To my supervisors:

I would first like to thank my incredible supervisors, Dr. Paul Wilson and Dr. Theresa Stotesbury. Your encouragement, support, and expertise throughout my degree have been treasured. A particular thank you to Dr. Stotesbury: in the past 6 years, you have been an amazing role model and have guided me outside of my comfort zone where I might even be able to finally admit that I am now a chemist...

To NSERC:

Thank you for believing in me and my research and honouring me as a recipient of the Doctoral Alexander Graham Bell Canada Graduate Scholarship. In addition, the support from my supervisors (NSERC Discovery Grants to Dr. Paul Wilson - RGPIN-2015-05637 & Dr. Theresa Stotesbury - RGPIN-2020-05816) has made this research possible.

To (the now Dr.) Mike Illes:

You are the reason I got into research and the world of bloodstain pattern analysis and have been there each step of the way. I cannot say thank you enough.

To Dr. Naomi Stock:

Thank you for your insight throughout this project and for teaching me the ways of High-Resolution Mass Spectrometry - your kind words and support have been valued.

To Dr. Brad Easton (Ontario Tech University) & Ed Wilson (Trent University):

I would like to thank Dr. Easton for the help and insight in building our electrospray device. In addition, Ed Wilson of the Trent Machine Shop for his help in constructing components of the electrospray device.

To my lab mates past and present:

Thank you to each member of the Stotesbury and Wilson labs over the years - I am grateful for our memories both inside and outside of the lab. To Sumiko Polacco - your encouragement and positive energy made the transition into my graduate path wonderful. To Bridget and Austin - you both have always been willing to help me in my quest to make the DNA functional and I could not have done it without you. To Mitchell Tiessen & Colin Elliott - you both have continually offered guidance, collaboration, and support in my research and life and for that, I am eternally grateful. To the current members of the lab (Erin, Lelo, Shaijieni, Daisee, Jerika and Meaghan) - you have all made the trips to Oshawa worthwhile and I truly have enjoyed getting to know you all.

To my family and friends:

You have been a constant source of encouragement and support and I am thankful for you all.



# Table of Contents

Abstract.....	ii
Keywords .....	iv
Abbreviations and Symbols .....	v
Acknowledgements .....	viii
List of Figures .....	xiii
List of Tables.....	xix
Chapter 1 .....	1
1.1 <i>Blood and its Versatility in Forensic Science</i> .....	1
1.2 <i>Blood Properties</i> .....	2
1.3 <i>Modelling the Fluid Mechanics of Blood</i> .....	4
1.4 <i>Forensic Blood Substitutes</i> .....	6
1.5 <i>Alginate Hydrogels</i> .....	9
1.6 <i>Objectives</i> .....	13
1.7 <i>Thesis Outline</i> .....	14
Chapter 2 .....	16
<i>Preface</i> .....	16
<i>Abstract</i> .....	17
<i>Keywords</i> .....	18
2.1 <i>Introduction</i> .....	19
2.2. <i>Materials and Methods</i> .....	22
2.2.1 <i>Materials and hydrogel preparation</i> .....	22
2.2.2 <i>DNA Extraction, Amplification and Analysis</i> .....	24
2.2.3 <i>Drying Experiment</i> .....	26
2.2.4 <i>Rheology</i> .....	28
2.2.5 <i>Locus Amplification</i> .....	28
2.2.6 <i>Data Analysis</i> .....	29
2.3. <i>Results</i> .....	29
2.3.1 <i>DNA Extraction and Amplification</i> .....	29
2.3.2 <i>Drying Experiment</i> .....	31
2.3.3 <i>Rheological Characterization</i> .....	33

2.3.4 Locus Amplification.....	35
2.4. <i>Discussion</i> .....	36
2.4.1 DNA Strands .....	36
2.4.2 DNA Extraction and Amplification .....	38
2.4.3 Drying Experiment .....	40
2.4.4 Rheological Characterization.....	42
2.4.5 Locus Amplification.....	44
2.5. <i>Conclusions</i> .....	45
Chapter 3 .....	47
<i>Preface</i> .....	47
<i>Graphical Abstract</i> .....	48
<i>Keywords</i> .....	48
<i>Abstract</i> .....	49
3.1 <i>Introduction</i> .....	51
3.2 <i>Methods and Materials</i> .....	55
3.2.1 Chemicals.....	55
3.2.2 FT-ICR MS Instrumentation .....	56
3.2.3 Solvent Selection .....	57
3.3 <i>Results and Discussion</i> .....	58
3.3.1 Instrumental Conditions.....	59
3.3.2 Solvent Choice.....	60
3.3.3 Charge State Calculations.....	66
3.3.4 Mass Spectral Interpretation.....	70
3.3.5 Mass Accuracy .....	72
3.3.6 Resolution.....	75
3.3.7 Applications of HRMS to Forensic Science .....	82
3.4. <i>Conclusions</i> .....	83
3.5 <i>Using HRMS to Characterize ssDNA Binding</i> .....	85
3.5.1 <i>Methods</i> .....	85
3.5.1.1 <i>Chemicals</i> .....	85
3.5.1.2 <i>Time Studies</i> .....	86
3.5.1.3 <i>Statistical Assessments</i> .....	89
3.5.2 <i>Results &amp; Discussion</i> .....	90
3.5.3 <i>Conclusions</i> .....	100
Chapter 4 .....	102
<i>Preface</i> .....	102
<i>Graphical Abstract</i> .....	103
<i>Keywords</i> .....	103

<i>Abstract</i> .....	104
<i>4.1 Introduction</i> .....	106
<i>4.2. Experimental Section</i> .....	110
4.2.1 Materials .....	110
4.2.2 Crosslinking Scheme .....	111
4.2.3 Materials Characterization .....	113
4.2.3.1 Rheology.....	113
4.2.3.2 Fourier Transform Infrared Spectroscopy.....	114
4.2.3.3 Scanning Electron Microscopy.....	114
4.2.3.4 Thermogravimetric Analysis.....	115
4.2.4 Electrospray Ionization Optimization & Microparticle Generation.....	115
4.2.5 DNA Extraction and Amplification of the MPs.....	116
<i>4.3. Results and Discussion</i> .....	117
4.3.1 Rheology .....	117
4.3.2 FTIR Spectroscopy.....	123
4.3.3 SEM .....	126
4.3.4 Influence of ssDNA Structure.....	129
4.3.5 Microparticle Generation & Applications.....	134
<i>4.4. Conclusions</i> .....	138
Chapter 5 .....	140
<i>Preface</i> .....	140
<i>Graphical Abstract</i> .....	141
<i>Keywords</i> .....	141
<i>Abstract</i> .....	142
<i>5.1 Introduction</i> .....	144
<i>5.2. Experimental</i> .....	148
5.2.1 Materials .....	148
5.2.2 Microparticles .....	148
5.2.3 Material Optimization .....	150
5.2.4 FBS Material .....	151
5.2.5 Material Characterization .....	152
5.2.6 Data Analysis.....	155
5.2.7 DNA Functionality in FBS .....	156
5.2.8 FBS Stability.....	157
<i>5.3. Results &amp; Discussion</i> .....	158
5.3.1 Material Optimization .....	158
5.3.2 Forensic Blood Simulant (FBS) .....	169
5.3.3 BPA Scenarios.....	174
5.3.4 FBS Stability.....	176
5.3.5 Genetic capabilities.....	180
<i>5.4 Conclusions</i> .....	183

Chapter 6 .....	185
6.1 <i>General Conclusion of Thesis</i> .....	185
6.2 <i>General Commentary on FBS Performance</i> .....	187
6.3 <i>Future Work in FBS Design</i> .....	189
6.4 <i>Final Remarks</i> .....	192
References .....	193
Appendix I .....	242
Appendix II .....	252

## List of Figures

<b>Figure 1.1.</b> Composition of human blood.....	3
<b>Figure 1.2.</b> Structure of A: alginate M and G blocks, B: linear arrangement and C: egg-box model from ionic crosslinking with CaCl <sub>2</sub> . Adapted from Davis et al. <sup>65</sup> and Christensen et al. <sup>66</sup> . ....	10
<b>Figure 2.1.</b> Experimental setup for CATG sampling during drying experiment. Grid pattern represents a 1 cm x 1 cm grid, where single samples were taken for swabbed (S) and cut (C) samples. Image (a) represents the dried CATG before sampling, and (b) after sampling. ....	27
<b>Figure 2.2.</b> STR genotyping results of ssDNA (Allele 1) extracted from liquid CATGs with various concentrations of DNA between 1000-0.0001 ng/μL. ....	31
<b>Figure 2.3.</b> Detected allele peak height (RFUs) from samples containing various DNA concentrations between 1000-0.0001 ng/μL. Ranges shown are from fresh (n=44) and dried samples (n=32). Dried samples were aged for 21 days at room temperature and include both cut and swabbed samples.....	32
<b>Figure 2.4.</b> Differences in DNA extracted between swabbing (n=16) and cutting (n=16) a sample from the dried CATGs. Both methods sampled a 1 cm x 1 cm area of the same dried CATG. Significant differences between swabbed and cut sampling is noted with a (*); where (*) is p values ≤0.05, (**) is p values ≤0.01; and (***) is p values ≤ 0.001). Differences were found at concentrations of 0.001 ng/μL (p=0.006), 0.01 ng/μL (p=0.0004), 1 ng/μL (p=0.01) and 100 ng/μL (p=0.04). ....	33
<b>Figure 2.5.</b> Rheological characterization of CATG and CA materials based on frequency sweeps. Data shown are: (A) storage modulus (G'), (B) loss modulus (G''), (C) complex viscosity (η*), and (D) loss factor (tanδ) as a function of angular frequency (ω). Frequency sweeps were measured at angular frequencies from 0.05-150 rad/s at 22°C. ....	35
<b>Figure 2.6.</b> Co-amplification results for the integration of Allele 1 and 2 into the CATGs. The genotyping results show the amplification of two alleles added in 1:1 ratio: (A) 25 μL of each strand and (B) 50 μL of each strand.....	36
<b>Figure 3.1.</b> FT-ICR mass spectrum of 26-mer oligo (5 μM) in two optimal solvents. Using water + 20 mM imidazole (blue), charge states from -5 to -11 were observed, with the highest ion signal intensity for -6 to -8. Using 50:50 water:acetonitrile + 20 mM imidazole (orange) the -5 charge state is the base peak; -4 and -15 were also observed. ....	63
<b>Figure 3.2.</b> Comparison of the same 5 μM 28-base oligonucleotide using four different solvents: 50:50 v/v water and acetonitrile (A), 50:50 v/v water, acetonitrile and 20 mM imidazole (B), 50:50 v/v water, acetonitrile and 10 mM ammonium acetate (C), and 50:50 v/v water, acetonitrile, 20 mM imidazole, and 10 mM ammonium acetate (D). * Denotes the theoretical monoisotopic peak at 1720.687367 m/z.....	65
<b>Figure 3.3.</b> Structure of the first 6 base pairs found at the 5' end of the characterized 28-mer DNA strand (monoisotopic mass = 8608.473216 Da). The sequence of the strand is 5'-TTCATCTCAGACTGGGATTCAGAAAGGC-3'. The entire strand's structure was	

created using MarvinSketch program and was used to determine the monoisotopic mass..... 68

**Figure 3.4.** Mass spectrum of a 5  $\mu$ M 28-base oligonucleotide using water and 20 mM imidazole as a solvent (A). The theoretical mass spectrum based on the monoisotopic mass of 8608.473216 Da is shown in (B). The -6 charge states are shown for both spectra. Observed mass accuracy was -0.167336 ppm using the base peak. .... 72

**Figure 3.5.** Analysis of 28-base DNA strand (monoisotopic mass = 8608.473216 Da) at four different resolutions,  $R_{FWHM(-5)}$  = 490,074 (A); 119,427 (B); 7800 (C); and 701 (D). The number of data points per scan were: (A) 16M, (B) 4M, (C) 128K, and (D) 32K. Labelled peaks show their FWHM values. Resolutions are at nominal m/z 1721. .... 76

**Figure 3.6.** ESI mass spectrum of 28-mer oligo in four different resolutions, using 16M (A), 4M (B), 128K (C), and 32K (D) data points per scan. The average resolutions for these scan sizes at the -4 charge are:  $R_{FWHM(-4)}$  = 383,103 (A); 116960 (B); 1142 (C); and 873 (D). The spectra shown represents the -4 and -5 charge states of the 28-mer DNA strand. The solvent shown in these spectra is 50:50 water:acetonitrile + 20 mM imidazole + 10 mM ammonium acetate. .... 77

**Figure 3.7.** ESI mass spectrum of 28-mer oligo at four different data points per scan sizes: 16M (A), 4M (B), 128K (C), and 32K (D). Each spectrum represents four different resolutions:  $R_{FWHM(-5)}$  = 490,074 (A); 119,427 (B); 7800 (C); and 701 (D). Spectra show the -5 charge state of the 28-mer DNA strand in 50:50 water: acetonitrile + 20 mM imidazole + 10 mM ammonium acetate. Black dashed line represents the theoretical m/z of the average mass for the 28-base strand which is 8612.674 Da. .... 80

**Figure 3.8.** Set up for analysis of DNA and sol-gel/GPTMS binding with FT-ICR MS. The samples were fed through a T-connector pushing DNA sample (1) sol-gel or GPTMS (2) which was merged into the ESI source (3). .... 89

**Figure 3.9.** Spectra from time study after 1 hr of reaction of DNA and DNA + 0.1% v/v sol-gel analyzed in water + 20 mM imidazole. The inlet shows a smaller range of 850-1400 m/z. .... 92

**Figure 3.10.** Spectra from TS5 after 1 hr of reaction of DNA, DNA + GPTMS and GPTMS (left). Arrows indicate a "second set" of DNA-like signals. The spectra shown on the right are a close-up of the DNA and DNA + GPTMS of -13 charge ions compared to the theoretical mass of the DNA + GPTMS molecule. .... 93

**Figure 3.11.** PLS-DA from TS2 of reaction between DNA and DNA + sol-gel. Image on the left shows the plots without sample names, and image on the right has sample name/time. .... 95

**Figure 3.12.** PLS-DA from TS5. Filtered for  $\geq 15,000$  Da. Thirteen GPTMS samples were not included due to no masses present over the cut-off (8 hour - replicates 1, 4, 6; 24 hour - replicates 1, 2, 3, 5, 6; 48 hour - replicates 1, 2, 3, 4, 6). .... 96

**Figure 4.1.** Amplitude sweeps (A), frequency sweeps (B) and  $\tan\delta$  (C) for 6 different ionic and dual crosslinked materials. The filled in symbols represent the Storage Modulus ( $G'$ ) and the corresponding non-filled symbols are the Loss Modulus ( $G''$ ) for a given sample. Overlaid lines represent potential inertial limits based on low torque and instrument inertial effects as outlined by Ewoldt<sup>203</sup>. Limits are based on geometry-

specific stress constant ( $F\tau$ ), minimum torque of instrument ( $T_{min}$ ), minimum strain ( $\gamma_0$ ), instrument inertia ( $I$ ), geometry-specific strain constant ( $F\gamma$ ) and frequency ( $\omega$ )..... 120

**Figure 4.2.** FTIR spectra for six different alginate materials. Materials AX<sub>0</sub>, AXD10, AXD25, and AXD50 were covalently crosslinked using EDC/Sulfo-NHS only (no Ca<sup>2+</sup>); and samples A<sub>0</sub> and APD50 were mixed without the addition of EDC/NHS or Ca<sup>2+</sup>. 124

**Figure 4.3.** SEM images of six different materials with/without crosslinkers and with/without N-DNA-N. Samples from left to right are: A<sub>0</sub> (A, B), AX<sub>0</sub> (C, D), AXD10 (E, F), AXD25 (G, H), AXD50 (I, J), and APD50 (K, L). The first row shows magnification at approximately 1000 x, and the second row is 2000 x. High resolution images of these scans can be found in Appendix II Figures A2.3-A2.8. .... 128

**Figure 4.4.** Amplitude sweeps (A) and frequency sweeps (B) and  $\tan\delta$  (C) for 4 ssDNA with varying amine reactivities: no DNA (Ca-AX<sub>0</sub>), ssDNA with no terminal amines (Ca-AXD0N), one terminal amine (Ca-AXD1N), and two terminal amines (Ca-AXD2N) covalently crosslinked with alginate. The samples were made to be dual crosslinked with Ca<sup>2+</sup>. The filled in symbols represent the Storage Modulus ( $G'$ ) and the corresponding non-filled symbols are the Loss Modulus ( $G''$ ) for a given sample. .... 131

**Figure 4.5.** FTIR spectra (left) 4 different alginate materials crosslinked with no DNA (AX<sub>0</sub>), ssDNA with no terminal amines (AXD0N), ssDNA with one terminal amine (AXD1N), and ssDNA with two terminal amines (AXD2N). Images on the right show the corresponding SEM images of each material. Two SEM images are included to show the variation in surface morphologies: AXD2N (A, B), AXD1N (C, D), AXD0N (E, F), AX<sub>0</sub> (G, H). .... 132

**Figure 4.6.** TGA curves of four different dual crosslinked alginate materials covalently crosslinked with no DNA (Ca-AX<sub>0</sub>), ssDNA with no terminal amines (Ca-AXD0N), ssDNA with one terminal amine (Ca-AXD1N), and ssDNA with two terminal amines (Ca-AXD2N). Samples were made to be dual crosslinked with Ca<sup>2+</sup>. The dashed curves represent Weight/°C, while the solid curves are the Weight % at each temperature. .... 133

**Figure 4.7.** Microparticle (MP) size distribution of four different materials: 2.5% w/v alginate in MES buffer (A), AX<sub>0</sub> (B), AXD10 (C) and AXD50 (D) electrosprayed with 0.5% v/v Tween 20 into a CaCl<sub>2</sub> bath. Inlet images show microscopic images of MPs visualized in brightfield mode at 40x magnification. Corresponding genotype of ssDNA extracted and amplified from AXD10 (E) and AXD50 (F) microparticles. .... 136

**Figure 5.1.** Viscosity profiles of (A) materials with various alginate concentrations (1, 2, 2.5% w/v) and CaCl<sub>2</sub> concentrations (0.5, 1, 2.5, 5 mM) used to ionically crosslink alginate. (B) Viscosity profile of various 1% w/v alginate materials with two xanthan gum concentrations:  $1.0 \times 10^{-3}$  w/v % (purple) and  $5.0 \times 10^{-3}$  w/v % (orange). Square symbols represent the base material (alginate with XG), triangles represent the base material with 2.5 mM CaCl<sub>2</sub>, and the circles represent the addition of microparticles to the ionic crosslinked materials at different v/v % concentrations (5, 10, 20%). All materials have 2% w/v Allura red. The dashed lines represent the range of reported human blood viscosity profile<sup>49</sup> fitted with a polynomial trend line. .... 160

**Figure 5.2.** Viscosity profiles of materials made using 1% w/v alginate, 0.0005% w/v XG (AX5), 2% w/v Allura red with various CaCl<sub>2</sub> concentrations ("C", 1, 1.5, 2 mM) and MP concentration (v/v %, 0, 10%). The dashed lines represent the range of reported human blood viscosity profile<sup>49</sup> fitted with a polynomial trend line. .... 163

**Figure 5.3.** Viscosity profiles of materials made using 1% w/v alginate, 0.0005% w/v XG and 2 mM CaCl<sub>2</sub> (AX5C2) with various filler concentrations: talc ("Ta", 0, 0.25% w/v), ferric citrate ("Fe", 0, 0.5% w/v), Tween 20 ("Tw", 0, 0.0025, 0.025, 0.0375 % v/v), and MP concentration (0, 5, 7.5, 10% v/v) (A). Profiles in (B) shows a narrow range of MPs (8-9.5%) with various filler combinations. All materials contain 2% w/v Allura red dye. The dashed lines represent the range of reported human blood viscosity profile<sup>49</sup> fitted with a polynomial trend line. .... 166

**Figure 5.4.** Influence of ferric citrate on material viscosity (A). The dashed lines represent the range of reported human blood viscosity profile<sup>49</sup> fitted with a polynomial trend line. The effect of ferric citrate on drip stain features of average stain diameter (B) and the average number of spines (C) compared to bovine blood (n=2) is also shown. .... 168

**Figure 5.5.** SEM image of concentrated MPs (A), the FBS components (B) and the average viscosity profiles (C) of FBS (n=7) and FBS with 0.4% v/v blue dye (FBS+B, n=4). The error bars represent the standard deviation of the replicates. The dashed lines represent the range of reported human blood viscosity profile<sup>49</sup> fitted with a polynomial trend line. Image in B was created with BioRender.com..... 170

**Figure 5.6.** Overall comparison between FBS candidate (AX5C2 + Ferric citrate + Talc + Tween 20 + 9.5% particles), FBS + B (FBS material + 0.4% v/v blue dye) and bovine blood for 90° drip stains made on 67 lb coverstock. The comparison shows (a) the average spreading ratio (D<sub>s</sub>/D<sub>o</sub>) and (b) the average number of spines..... 173

**Figure 5.7.** Comparison of FBS vs FBS + B drip stains with bovine blood (rep 1) from 10-90° impact angles. Comparisons show the stain features at A: 20°, 60 cm and B: 50°, 60 cm and C: the measured impact angle between the three materials. .... 175

**Figure 5.8.** Impact pattern (A) made using FBS+B candidate and a close-up of upward moving stain morphology (B)..... 176

**Figure 5.9.** Viscosity profile of FBS base (AX5C2, includes red dye, talc and ferric citrate), and the FBS+B material over 10 weeks (left). The FBS + B material contains 0.5% v/v DNA-crosslinked MPs. The dashed lines represent the range of reported human blood viscosity profile<sup>49</sup> fitted with a polynomial trend line. The image on right is a microscopic image of MPs within the FBS after 12 weeks of storage..... 179

**Figure 5.10.** Process of DNA extraction from FBS material swabbed from various substrates. Each material was able to produce the included allele crosslinked in the MPs within the FBS. Image was created with BioRender.com. .... 182

**Figure A1.1.** Copyright permission obtained from BioRender for Figure 1.1 on page 3. .... 242

**Figure A1.2.** Copyright permission obtained for Figure 1.2 on page 10. Copyrights are obtained from the American Chemical Society (top) and Carbohydrate Polymers (bottom) for the manuscripts where Figure 1.2 was adapted from. .... 243



<b>Figure A1.3.</b> Copyright permission obtained from Elsevier (Forensic Science International) for Chapter 2 publication. ....	244
<b>Figure A1.4.</b> Copyright permission obtained from Elsevier (Forensic Chemistry) for Chapter 3 publication. ....	244
<b>Figure A1.5.</b> Copyright permission obtained from BioRender for Figure 3.8 on page 88. ....	245
<b>Figure A1.6.</b> Copyright permission obtained from the American Chemical Society (ACS Applied Polymer Materials) for Chapter 4 publication. ....	246
<b>Figure A1.7.</b> Copyright permission obtained from BioRender for Chapter 4 Graphical Abstract on page 100. ....	247
<b>Figure A1.8.</b> Copyright permission obtained from BioRender for Scheme 1 on page 109. ....	248
<b>Figure A1.9.</b> Copyright permission obtained from BioRender for Chapter 5 Graphical Abstract on page 135. ....	249
<b>Figure A1.10.</b> Copyright permission obtained from BioRender for graphic in Figure 5.5 on page 161. ....	250
<b>Figure A1.11.</b> Copyright permission obtained from BioRender for graphic in Figure 5.10 on page 170. ....	251
<b>Figure A2.1.</b> FTIR spectra for six different ionic and dual crosslinked alginate materials. Materials AX <sub>0</sub> , AXD10, AXD25, and AXD50 were covalently crosslinked using EDC/Sulfo-NHS and calcium (+Ca <sup>2+</sup> , dual crosslinked); and samples A <sub>0</sub> and APD50 were mixed with calcium, but without the addition of EDC/NHS (+Ca <sup>2+</sup> , ionic crosslinked). ....	252
<b>Figure A2.2.</b> SEM images of ionically crosslinked and dual crosslinked materials with Ca <sup>2+</sup> . Samples from left to right are: Ca-A <sub>0</sub> (A-C), Ca-AX <sub>0</sub> (D-F), Ca-AXD10 (G-I), Ca-AXD25 (J-L), Ca-AXD50 (M-O), and Ca-APD50 (P-R). The first two rows represent magnification at approximately 1000 x except for D, which shows larger particles at 500 x, and the bottom row is 4000 x. ....	253
<b>Figure A2.3.</b> High resolution SEM images of sample A <sub>0</sub> (1% w/v alginate) taken at 1000 x (A) and 2000 x (B) magnification. ....	254
<b>Figure A2.4.</b> High resolution SEM images of sample AX <sub>0</sub> (1% w/v alginate crosslinking control) taken at 1000 x (A) and 2000 x (B) magnification. ....	255
<b>Figure A2.5.</b> High resolution SEM images of sample AXD10 (1% w/v alginate covalently crosslinked with 10 nmol of N-DNA-N) taken at 1000 x (A) and 2000 x (B) magnification. ....	256
<b>Figure A2.6.</b> High resolution SEM images of sample AXD25 (1% w/v alginate covalently crosslinked with 25 nmol of N-DNA-N) taken at 1000 x (A) and 2000 x (B) magnification. ....	257
<b>Figure A2.7.</b> High resolution SEM images of sample AXD50 (1% w/v alginate covalently crosslinked with 50 nmol of N-DNA-N) taken at 1000 x (A) and 2000 x (B) magnification. ....	258
<b>Figure A2.8.</b> High resolution SEM images of sample APD50 (1% w/v alginate mixed with 50 nmol of N-DNA-N) taken at 1000 x (A) and 2000 x (B) magnification. ....	259

**Figure A2.9.** Time-lapse of FBS droplet drying. Images A-E represent ~30 s time intervals between images. \* Denotes the same cluster of MPs and the arrow indicates drying front. ....261

**Figure A2.10.** Appearance of FBS base material (1% w/v alginate,  $5.0 \times 10^{-2}$  w/v % XG, 2 mM CaCl<sub>2</sub>, "AX5C2") with ferric citrate (left) or talc (right). ....262

**Figure A2.11.** Microscope images of MPs within the FBS material before (A) and after (B) applied shear rates of 1-1200 s<sup>-1</sup>. ....262

**Figure A2.12.** Amplitude sweep (A) and frequency sweep (B) of a concentrated MP solution (blue) and FBS + B (black). Filled-in symbols represent the storage modulus (G') and non-filled symbols represent the loss modulus (G''). ....263

**Figure A2.13.** Drip stains dropped from 20 and 100 cm on six substrates: acetate paper, cardboard, paper, linoleum tile, tile, and wood (left). And the corresponding average stain diameter (D<sub>s</sub>, n=4) (right). ....263

**Figure A2.14.** Image of filtration tube during extraction procedure where the red dye precipitates inside the filter (A) and the resulting PCR plate with various dilutions of extracted material from FBS (B). From left to right, the extracted DNA was added as 1:40 dilution, 1:20 dilution, 1:10 dilution, and stock. ....264

## List of Tables

<b>Table 2.1.</b> Primer Sequences and DNA repeats for Alleles 1 and 2 in CATG biomaterials. ....	23
<b>Table 3.1.</b> Assessment of various solvent matrices for optimal DNA analysis using ESI FT-ICR MS. Solvents assessed were various combinations of ultrapure water, isopropanol (IPA), acetonitrile (ACN), and methanol (MeOH). Solvents containing imidazole and ammonium acetate contained concentrations of 20 mM imidazole and 10 mM ammonium acetate for all solvents. ....	58
<b>Table 3.2.</b> Considerations for oligonucleotide analysis using HRMS. Considerations are: pH, solvent, other molecules, concentration of DNA, and temperature. * Variation depends on the molecular weight .....	66
<b>Table 3.3.</b> Theoretical m/z values of 28-mer DNA strand based on theoretical calculations of m/z up to a charge of -15. Monoisotopic mass of 28-mer strand is 8608.473216 Da. Calculated m/z values represent the loss of z number of protons (H <sup>+</sup> ) in the first column. Respective columns show the m/z values accommodating one to five <sup>13</sup> C isotopes. ....	69
<b>Table 3.4.</b> Average mass accuracy values (ppm) for the HRMS analysis of 26- and 28-base single stranded DNA in two solvents (50:50 water:acetonitrile + 20 mM imidazole and water + 20 mM imidazole) that were used to analyze 26- and 28-base single stranded DNA. The "-" symbol denotes no observed peaks for designated charge states. Note: smaller ppm values correspond to higher mass accuracy .....	74
<b>Table 3.5.</b> Comparison of theoretical m/z of average mass of 28-base oligonucleotide (average mass = 8612.674 Da) to observed m/z values of base peak for different data points per scan, or resolutions. ....	82
<b>Table 3.6.</b> Outline of six time studies conducted with N-DNA and sol-gel or GPTMS. T0-T4 represents a "time zero" where the solutions were just made, and each number represents a replicate. *No imidazole was present in the solvent. ....	87
<b>Table 3.7.</b> GPTMS molecule identification during a 7-day time study. The tentative structure and m/z of monoisotopic mass are shown (left side) and the corresponding m/z values for each sample (right). Only three decimal places are shown for the m/z values. Designations are low signal (L), high signal (Y), and non-confirmed (NC) - which are designations that have differences beyond 0.01 m/z. ....	98
<b>Table 4.1.</b> Outline of crosslinking reactions. The presence of "X" indicates that the covalent crosslinkers EDC and Sulfo-NHS were added to reaction, whereas "P" indicates the DNA was mixed with alginate without EDC/Sulfo-NHS. Identification in square brackets represents the classification with the addition of Ca <sup>2+</sup> . ....	113
<b>Table 5.1.</b> Overview of components tested in FBS candidates. Combinations include some or all components listed. A full detailed table can be found in Appendix II Table A2.1. ....	151

**Table 5.2.** Summarized property measurements of FBS material, FBS + blue dye (FBS + B), the bovine blood used (n=2) and the reported human ranges for each property summarized previously<sup>25</sup>. †The density was measured relative to MilliQ water. .... 169

**Table 5.3.** Summarized property measurements of DNA-FBS + blue dye (FBS + B) over 12 weeks. .... 180

**Table A2.1.** The composition of each FBS candidate material assessed in this work. Components include alginate, CaCl<sub>2</sub> (Ca), xanthan gum (XG), electrospayed microparticles (MPs), ferric citrate (FeCit), magnesium silicate (talc) and Tween 20 (Tween 20). .... 260

# Chapter 1

An introduction to blood, DNA, and hydrogels

---

## 1.1 Blood and its Versatility in Forensic Science

The analysis of blood in criminal investigations has been well documented<sup>1,2</sup>, and its probative value can be used to answer important questions such as the 'who', 'what' and 'where' of forensic scenarios. Bloodstain pattern analysis (BPA) analyzes the size, shape, and distribution of bloodstains and bloodstain patterns observed at a crime scene in order to provide information on the events that occurred during bloodshed. Despite their value, forensic science and BPA have deservedly faced scrutiny for lack of scientific rigour. This has been emphasized in the 2009 National Academy of Sciences (NAS) report addressing the needs of the forensic community<sup>3</sup> and the President's Council of Advisors on Science and Technology (PCAST) report which suggested the need for objectivity and error rates studies<sup>4</sup>. While much research has been completed since 2009 to strive to achieve accuracy, reliability, and objectivity in BPA methodologies<sup>5-10</sup>, the field has been recognized as still needing to reduce subjectivity in BPA<sup>11-13</sup>. Understanding the behaviour of blood at the crime scene requires continued efforts into fundamental research to model blood formation and interpretation. These research endeavours will ultimately require more access to research and

training for the BPA field, where the need for reliable blood sources to conduct this research is paramount.

## **1.2 Blood Properties**

Blood is a complex fluid that is primarily made of red blood cells (RBCs), white blood cells (WBCs) and platelets all suspended in a liquid plasma<sup>1,14</sup> (Figure 1.1). The RBCs account for the majority of the solid components and are small, (~8  $\mu\text{m}$ ) flexible disc-shaped cells that have high deformability<sup>15-17</sup>. The ratio of the RBCs to the total volume of blood, which is referred to as the packed cell volume, or PCV%, ranges between 40-50%<sup>18-25</sup>. The PCV% varies with many factors such as sex, age, and activity levels<sup>23</sup>. The WBCs, which make up <1% of the total blood volume are larger than RBCs (~15-25  $\mu\text{m}$ ) and contain deoxyribonucleic acid (DNA) within their nucleus that encodes for the genetic information useful for developing DNA profiles<sup>1,26</sup>. Blood plasma is composed of mostly water (92%) but also contains proteins (albumins, globulins, fibrinogen), salts, lipids and dissolved gases<sup>1,27,28</sup>. Given the high water content of plasma, it has traditionally been considered a Newtonian fluid (a material whose viscosity remains constant under various applied shear stresses), but it

has been shown that plasma in fact has viscoelastic properties influenced by the interaction of plasma proteins<sup>15,27,29</sup>.

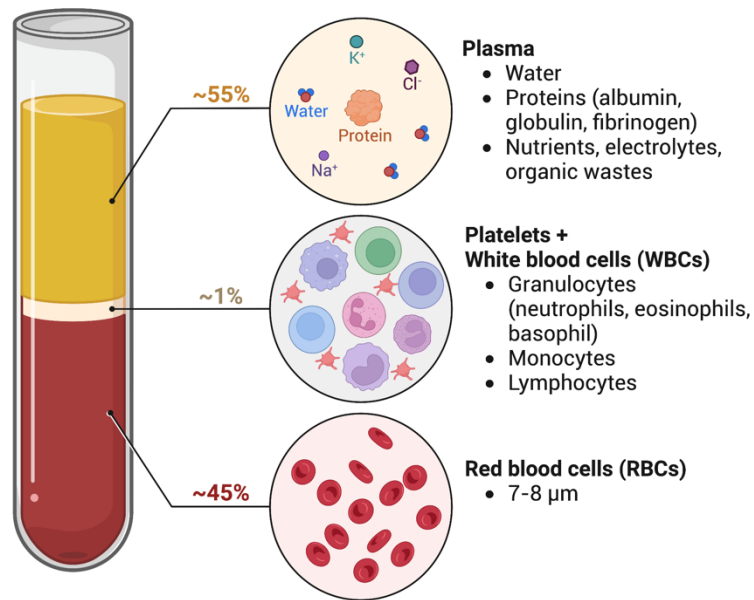


Figure 1.1. Composition of human blood<sup>a</sup>.

Related to BPA, blood has four main fluid properties that are relevant to its behaviour at the crime scene. Viscosity is described as a material's resistance to flow and is influenced by factors such as temperature and PCV%, where it ranges anywhere between 3.2-6.93 mPa·s<sup>18,20,21,23-25,30</sup>. Surface tension is the force (or energy) per unit area and related to the ability of a droplet to remain intact, is also influenced by temperature, and typically ranges from 51-61 mN·m<sup>-1</sup>

---

<sup>a</sup> Created with BioRender.com. Copyright is in Appendix I.

<sup>18,20,21,23,25,31,32</sup>. The density of a material corresponds to its mass per volume (between 1052–1063 kg/m<sup>3</sup> <sup>18,20,21,23,25</sup>), and as described previously, the PCV% also plays an important role in the properties of blood, which is ~45% in humans<sup>21</sup>. Each of these properties is inherently linked and primarily relies on the RBCs, since more RBCs lead to a higher PCV%, an increased viscosity and density, and influences the overall surface tension.

### **1.3 Modelling the Fluid Mechanics of Blood**

When studying how blood impacts a surface, we consider the spreading and splashing dynamics relating to blood's properties in addition to the properties of the target surface. Blood is a non-Newtonian fluid, meaning its viscosity changes with applied shear rates, and more specifically it is shear-thinning or pseudoplastic (its viscosity decreases with increased shear rates)<sup>17,21</sup>. The spreading dynamics of blood are influenced by its shear thinning behaviour and fluid properties, namely the viscosity, density, surface tension and PCV%<sup>21,28</sup>. The shear-thinning behaviour of blood is also driven by the RBCs. At low shear rates, the RBCs aggregate into stacks (called "rouleaux") and have an increased resistance to flow (more viscous); at higher shear rates, the rouleaux break down, and the flexible RBCs elongate and orient in a more horizontal fashion,



which can flow more easily and decreases the overall viscosity<sup>33,34</sup>. RBCs, therefore, play a large role in the spreading dynamics of blood and have been shown to also be influential in the drying mechanisms as well <sup>35</sup>, emphasizing the importance of these cellular components in BPA scenarios.

Modelling blood in forensic scenarios can be done through the use of the dimensionless Reynolds (Re), Weber (We), and Ohnesorge (Oh) numbers <sup>21,28,36,37</sup>. To understand the ratio between inertial and viscous forces, the Re number is calculated using Equation 1; the We number represents the ratio between inertial to surface tension forces and is calculated using Equation 2; and the Oh number is the ratio between these two, described in Equation 3.

$$Re = \frac{\rho v D_0}{\eta} \quad (1)$$

$$We = \frac{\rho v^2 D_0}{\sigma} \quad (2)$$

$$Oh = \frac{\sqrt{We}}{Re} \quad (3)$$

The variables are the density ( $\rho$ ), impact velocity ( $v$ ), the initial droplet diameter ( $D_0$ ), the viscosity ( $\eta$ ) - typically the effective viscosity, and the surface tension ( $\sigma$ ). These numbers allow for the relative assessment of various properties relating to bloodstain formation and can provide an intuitive interpretation of raw data<sup>21</sup>.

For example, using these models, predictions can be made for the maximum spread factor ( $D_s/D_0$ ) where  $D_s$  is the final stain diameter, the number of spines and scallops for dripping bloodstains<sup>21,38</sup>, and used in blood simulant (synthetic or mammalian) validation to assess a material's spreading and splashing behaviour<sup>37</sup>.

#### **1.4 Forensic Blood Substitutes**

Access to human blood in forensic science can be problematic, relating to ethical, biohazardous, and cost concerns<sup>39</sup>. Other mammalian alternatives have been explored in forensic research, but only blood sourced from ovine (sheep)<sup>18,19</sup>, equine (horse)<sup>20</sup>, porcine (pig)<sup>40,41</sup>, and bovine (cow)<sup>25</sup> sources have actually been validated for bloodstain and bloodstain pattern simulation in BPA scenarios. These materials can be sourced locally from abattoirs, limiting the costs associated with human blood use, but their use still poses ethical issues (e.g., *should we use animal blood?*), translational issues (e.g., *how applicable is this behaviour to human blood at the crime scene?*), and training limitations relating to the inability to generate human DNA profiles. Additionally, species-specific differences exist in the relative size and concentration of the cellular components of blood<sup>25,30,42-45</sup>. Despite this, the high number of studies using

animal blood stresses the need for access to blood in research, where synthetic alternatives can provide many benefits.

Forensic blood substitutes (FBSs) are materials that are designed for forensic purposes as alternatives to human blood. If designed appropriately, FBSs can provide chemically safe, practical, and relevant (physical, biological, and chemical) alternatives that can be used in forensic research and training<sup>46</sup>. FBS materials have been explored in the past two decades using a variety of chemistries. In 2002, Millington<sup>47</sup> reported on the development of a FBS material that could be formulated using easily accessed materials such as flour, dessert mix, strawberry sugar syrup, sodium chloride, glycerol, and various food colourings. In 2016, Li *et al.*<sup>48</sup> used a FBS made of Acrysol 110 mixed with water and Direct Red 81 dye to obtain a material with relevant viscosity to human blood. When comparing the wicking of porcine blood and the FBS, they found that the wicking into fabric surfaces produced similar stain features, but was overall larger due to the lack of solid components in the artificial material<sup>48</sup>. Stotesbury *et al.*<sup>49,50</sup> used hybrid inorganic-organic silicon solution-gelation (sol-gel) chemistry to design materials that had similar fluid properties to human blood, and validated its spreading dynamics and use in impact patterns<sup>51</sup> in BPA

scenarios. Importantly, these works in combination with earlier work by Stotesbury *et al.*<sup>37</sup> enhanced the validation criteria for the performance of FBS materials. Later, Polacco *et al.*<sup>52</sup> demonstrated the sol-gel base is a suitable system for the integration of horseradish peroxidase (HRP), an enzyme with structural similarity to hemoglobin, that is capable of simulated reaction with luminol. In 2018, Li<sup>53</sup> described a FBS made using an emulsion technique using styrene and polyvinylpyrrolidone (PVP) as a stabilizer to develop small particles (1-3  $\mu\text{m}$ ). In this work, it was demonstrated that their FBS had similar fluid properties to human blood (surface tension, viscosity, PCV%), and showed similar stain diameter ( $D_s$ ) and number of spines and scallops on hard non-porous surfaces and some porous surfaces<sup>53</sup>. Two years later, work done by Lee *et al.*<sup>54</sup> presented the development of a FBS that combined an amino acid solution, hyaluronate acid, hemoglobin from bovine blood, potassium ferricyanide, and bovine serum albumin. They reported that their materials showed similar properties to human blood (viscosity, viscoelasticity, surface tension, density), and showed similar stain features when dripped on steel and glass which outperformed commercial substitutes on paper surfaces<sup>54</sup>. The most recent discussion of a FBS material for forensic science applications was described by Rubio *et al.*<sup>55</sup> using an emulsification technique to generate small

polydimethylsiloxane (PDMS) microparticles ( $9.76 \pm 3.26 \mu\text{m}$ ) that possessed the flexible and deformable mechanical properties of RBCs. Their work focused on mimicking the mechanical properties of the RBCs and obtaining a relevant PCV%; they also found that the material's viscosity was like human blood<sup>55</sup>. To date, the design of FBS materials has used various methodologies to produce varying degrees of success in mimicking human blood; however, the rise in particle-based materials highlights the consensus of the field to develop FBSs that incorporate RBC-like particles into their design. An area that has not been explored for FBS development is the use of hydrogels, which is discussed next.

## **1.5 Alginate Hydrogels**

Alginate is a negatively charged linear polysaccharide that is derived from seaweed and is composed of repeating blocks of  $\beta$ -D-mannuronate (M block) and  $\alpha$ -L-guluronate (G block) that occur in an intermixed homogenous (MM, GG) or heterogenous (MG) fashion<sup>56-59</sup> (Figure 1.2). Alginate can ionically crosslink with divalent cations such as calcium ( $\text{Ca}^{2+}$ ) under mild gelation conditions (e.g., relatively fast timescales, performed at room temperature, in aqueous solutions, and in neutral pH conditions) to form what is called an "egg-box" model<sup>59</sup> (Figure 1.2). Typically, it is assumed that the ionic crosslinking occurs only

between the negatively charged G blocks and  $\text{Ca}^{2+}$ , where strains of alginate that have more G blocks would lead to a stiffer gel<sup>56,60</sup>. The hydrophilic components of alginate hydrogels (the  $\text{COO}^-$  groups) lead to high water-absorbing capabilities and similar mechanical properties to the extracellular matrix (ECM) in the human body<sup>56,59,60</sup>. This feature, in addition to the non-toxic, bioinert, and biodegradability properties of alginate has driven its use in many applications relating to biomedical fields, drug delivery, tissue scaffolding and food packaging, among others<sup>56,57,61-64</sup>.

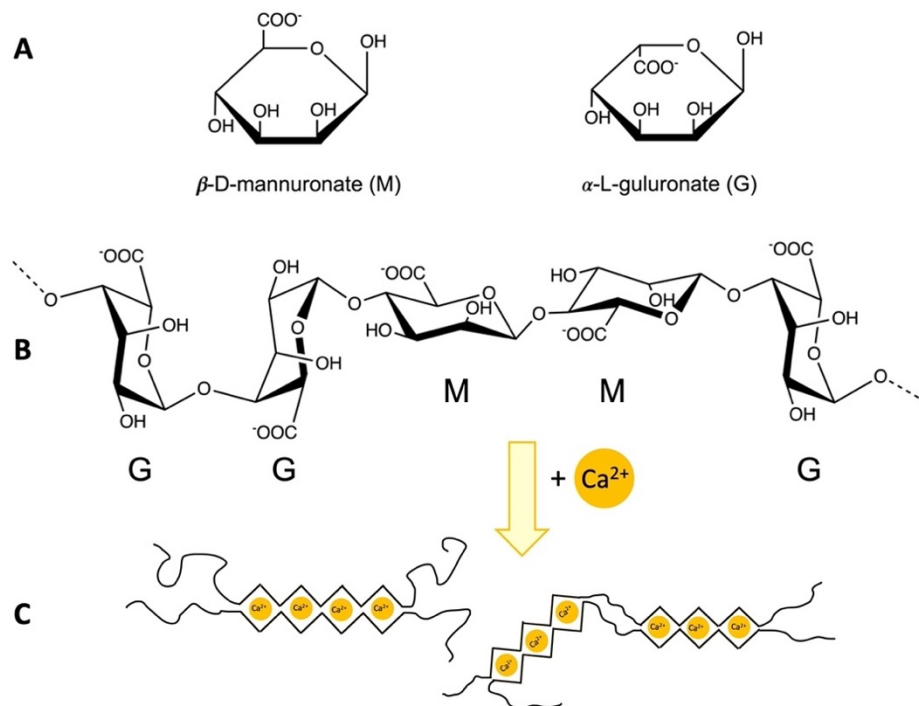


**Figure 1.2.** Structure of A: alginate M and G blocks, B: linear arrangement and C: egg-box model from ionic crosslinking with  $\text{CaCl}_2$ . Adapted from Davis et al.<sup>65</sup> and Christensen et al.<sup>66</sup>.<sup>b</sup>

<sup>b</sup> Copyright permission is in Appendix I.

Further, by using covalent crosslinking strategies (covalently binding crosslinkers to the alginate backbone), hydrogels can be designed with precise control over properties to tailor materials with biological, chemical and physical processes exhibited by the human body<sup>61</sup>. For example, hydrogels developed with biological functionalities (biofunctional) can mimic processes within the human body, such as interaction with cell signalling and/or biological pathways to obtain desired effects<sup>62,67-69</sup>. The type of crosslinker used in the hydrogel growth typically reflects the end application of the material, whether it be modifications to improve mechanical stability<sup>70-74</sup>, bioprintability<sup>75-77</sup>, or the inclusion of functional crosslinkers<sup>78,79</sup>. By including various lengths of amine-modified poly(ethylene glycol) (PEG) linkers, hydrogels of different mechanical strengths can be developed<sup>80,81</sup>. The bioprintability of hydrogel materials can also be improved through the use of many different crosslinking chemistries<sup>82,83</sup>, such as those that lead to both biocompatible and self-healing gels when crosslinked with semicarbazone imine linkages<sup>84</sup>. An example of functional materials includes scaffolding alginate hydrogels which can be made by covalently attaching the cell-specific ligand, RGD (Arginine-Glycine-Aspartic Acid), to alginate. Desired cell types can be introduced into the functional RGD-modified alginate to create cell-crosslinked hydrogels which can be used for

regenerative applications<sup>85,86</sup>. The inclusion of the RGD linker on the alginate backbone is also a critical component for cellular signalling pathways in a functional ECM mimetic<sup>61</sup>. Other functional hydrogels typically are developed for the purpose of biosensing, either through electrochemical or stimuli-responsive materials (light, temperature, pH, etc.)<sup>59,69</sup>.

Relating to blood, hydrogel-based materials have been used in the design of particle-based blood analogues for biomedical purposes<sup>15</sup>, and have used a variety of techniques such as electrospray ionization (ESI) to develop particles of RBC size and shape<sup>87</sup>. ESI offers a beneficial technique for particle generation since its soft ionization technique allows for the transfer of large molecules (such as alginate polymers - functionalized or non, and/or bioactive components) into the gaseous phase, and can achieve nanometer to micron-sized particles<sup>88</sup>, relevant to mimicking the various sizes of blood cells. Importantly, ESI apparatuses for microparticle generation can be set up relatively easily with a variety of customizable configurations.



## 1.6 Objectives

The objectives of this work explore the design, characterization, and implementation of deoxyribonucleic acid (DNA), and more specifically single-stranded DNA (ssDNA) in forensic scenarios with a specific focus on the design of functional blood simulants. This work has four main objectives.

**Objective 1:** *To introduce hydrogels as a viable material for soft tissue simulation, providing stable environments for ssDNA designed to mimic human DNA.*

- a) Design ssDNA to amplify with known human primer sets for CODIS loci; and,
- b) Encapsulate DNA in hydrogel-based materials and assess their functionality and stability.

**Objective 2:** *To optimize a method to accurately analyze short ssDNA using high-resolution mass spectrometry (HRMS).*

- a) Use Fourier-transform ion cyclotron resonance mass spectrometry (FT-ICR MS) as a technique to characterize ssDNA;
- b) Design and optimize a method that can allow for accurate mass determination of real-time binding of DNA within sol-gel matrices; and
- c) Assess the ability of DNA to remain intact during ESI.

**Objective 3:** *To covalently crosslink alginate and DNA and design an ESI device that can be used for microparticle (MP) generation resemblant of blood cells.*

- a) Covalently crosslink the DNA with alginate and understand the effect this has on material properties;
- b) Design and optimize an ESI device that can obtain small and relevant MP sizes;
- c) Explore the use of this apparatus for the development of DNA-crosslinked alginate MPs; and,

- d) Understand the ability to produce MPs on a large scale.

**Objective 4:** *To design a FBS using hydrogel-based materials that incorporate multiple components of human blood functionality and assess its use in forensic research and training.*

- a) Design and optimize the FBS materials to obtain desired fluid properties of human blood;
- b) Measure the FBS stability to understand storage conditions and shelf life;
- c) Evaluate the performance of FBS in basic BPA scenarios such as drip stain simulation and impact patterns; and
- d) Assess the functionality of the DNA within the FBS for training applications.

## **1.7 Thesis Outline**

This thesis focuses on the main theme of ssDNA and is divided into two sub-themes. The first sub-theme deals with 1) the design and characterization of DNA relevant to forensic genotyping. The second sub-theme assesses 2) the use of alginate-based hydrogels as a suitable material for the incorporation of ssDNA for soft tissue simulant with a focus on whole human blood imitation.

The thesis is organized as follows. The functionality of ssDNA in alginate hydrogels is assessed and the hydrogel components are optimized (Chapter 2). The use of HRMS and ESI for the analysis of ssDNA is explored, and DNA binding

within a sol-gel matrix is investigated using this optimized technique (Chapter 3). Dual amine-terminated ssDNA is covalently crosslinked to alginate, and its binding is characterized using a variety of techniques (Chapter 4). In addition, the DNA-alginate crosslinked materials are used to create MPs using an optimized ESI apparatus (Chapter 4). The design of an alginate-xanthan gum based FBS is presented, and its performance in BPA scenarios is evaluated (Chapter 5). Finally, future directions and conclusions of this research are discussed (Chapter 6).

# Chapter 2

---

Calcium-alginate tissue gels (CATG): Proof-of-concept biomaterial development<sup>c</sup>.

## Preface

Type: Original Research Article  
Submitted to: Forensic Science International  
Status: Published

Title: Calcium-alginate tissue gels (CATG): Proof-of-concept biomaterial development.

Authors: Amanda Orr<sup>a</sup>, Paul Wilson<sup>b</sup>, Theresa Stotesbury<sup>c</sup>

<sup>a</sup> Environmental and Life Sciences PhD Program, Trent University, Peterborough, Ontario, Canada, 1600 West Bank Drive, K9L 0G2

<sup>b</sup> Biology Department, Trent University, Peterborough, Ontario, Canada, 1600 West Bank Drive, K9L 0G2

<sup>c</sup> Faculty of Science, Forensic Science, Ontario Tech University, 2000 Simcoe Street North, Oshawa, ON, L1G 0C5

---

<sup>c</sup> A. Orr, P. Wilson, T. Stotesbury. Forensic Science International. 2021. 329:1-9. DOI: 10.1016/j.forsciint.2021.111055

## **Abstract**

Hydrogels are desirable materials to the field of forensic science and offer many advantages for use as tissue simulants in research and training scenarios. In this work, we demonstrate a proof-of-concept study for our biomaterial described as the Calcium-Alginate Tissue Gel (CATG). CATG biomaterials integrate functional DNA strands designed to amplify with known human primer sets for genetic profiling. Our range of CATG materials demonstrate successful DNA extraction, PCR amplification and genotyping when both fresh and aged for 21 days. The rheological properties of the CATGs were measured and the incorporation of DNA into the CATGs was assessed. Overall, the CATGs demonstrated increased viscoelastic behaviour with the addition of DNA. In addition, two methods of sampling were considered, where it was found that cutting a sample of the dried CATG produced higher allele peak heights in the genotype compared to swabbing. Overall, our CATG biomaterials can be designed for multiple applications in forensic science with tunable functions for various training and research needs.

## **Keywords**

Tissue simulant; ionic crosslinking; hydrogel; human DNA; forensic standard; biomaterial design; DNA extraction.

## 2.1 Introduction

Hydrogels are versatile polymeric materials that have been used in the development of many functional biomaterials for a variety of biomedical applications. By definition, hydrogels have a high water content and typically are comprised of a crosslinked network of polymers<sup>89,90</sup>. Common polymers used to form hydrogels include hyaluronic acid, collagen, chitosan, and alginate<sup>56,72,90-92</sup>. These naturally occurring polymers are desirable due to their relevant mechanical properties, as well as their biocompatibility and non-toxic nature<sup>61,62</sup>. In addition, the polymers can be chemically modified to contain various adaptations and crosslinkers for targeted applications in tissue regeneration<sup>68,78,92-97</sup>, drug delivery systems<sup>98-100</sup>, stimuli-responsive materials<sup>68,101-103</sup>, and biosensors<sup>67,69,104-106</sup>, to name a few.

Traditionally, hydrogels that are used for biomedical purposes focus on *in vitro* or *in vivo* capabilities and applications given the tunable similarities between hydrogels and living tissues<sup>73,78</sup>. Of note, studies have used crosslinkers that contain cell-specific adhesion receptors which undergo targeted degradation in the body<sup>107,108</sup>. Typically, hydrogels are used for tissue generation as scaffolds that house relevant cell types and/or biomolecules which promote the

regeneration of multiple tissue types<sup>78,92</sup>. While hydrogels have been researched extensively as therapeutic and regenerative biomaterials and their applications are continually advanced, there has been limited use of hydrogels for applications in forensic science<sup>109,110</sup>, particularly as it relates to biological evidence in *ex vivo* conditions.

Hydrogels are attractive materials for the forensic sciences given their tunable structures which can obtain a variety of relevant properties. Their applicability in research settings is especially suitable since hydrogels can mimic physiological behaviours of human tissues both mechanically and chemically<sup>78,111</sup>. For example, hydrogels are desirable for the development of biological tissue simulants including blood or other soft tissues due to the ability to tailor the mechanical properties, such as the viscoelastic capabilities, stress relaxation, self-healing and degradation<sup>78</sup>. Because of their demonstrated similarities to human tissues, hydrogel simulants can be beneficial to the forensic community as standard reference materials with known and controlled properties and behaviours.



A prevalent area of forensic science research focuses on biological tissue degradation in both post-mortem and *ex vivo* conditions, especially considering DNA degradation<sup>112</sup>. Other areas look at biological markers to estimate the post-mortem interval (PMI) or time since deposition (TSD) from various biological tissue types<sup>113-115</sup>. Also of importance is the use of standardized materials in fundamental studies in forensic science, especially where access to human samples is not possible<sup>47,50,54,110,116-120</sup>. Therefore, hydrogel-based materials that contain desirable functionalities can be of value to understanding relevant questions regarding tissue and biomarker degradation in a forensic context.

In this work, we provide a proof-of-concept study for the development of calcium-alginate tissue gels (CATGs) for forensic research and training applications. Alginate is a well-suited polymer for CATG development as it is non-toxic, bioinert, and easily tailored for many applications<sup>56,61-63</sup>. Alginate is a naturally occurring linear polysaccharide that contains repeating blocks of (1-4)-linked  $\beta$ -D-mannuronic acid (M) and  $\alpha$ -L-guluronic acid (G) residues<sup>94</sup>. Alginate can form a hydrogel through ionic crosslinking between the reactive carboxyl ( $\text{COO}^-$ ) groups on the G residues and divalent cations, such as calcium

(Ca<sup>2+</sup>)<sup>57,61,64</sup>. The CATGs developed in this research are designed with integrated functional DNA strands that have forensic relevance. Specifically, we designed short single stranded DNA (ssDNA) that is incorporated within the CATGs to mimic human short tandem repeat (STR) profiles. By integrating DNA that is smaller than a typical locus, CATGs can be used as training materials where they can be processed similar to biological evidence, while the contained genetic profile is unlike a human profile from analogous loci. The CATGs can be designed to contain relevant human or non-human DNA for specific training scenarios, as well as tailored for various biological tissue simulants. This study focuses on the proof-of-concept development for the CATGs as both liquid and semi-solid materials and assessed the feasibility for DNA extraction and analysis.

## **2.2. Materials and Methods**

### 2.2.1 Materials and hydrogel preparation

Alginic acid sodium salt was purchased from Sigma Aldrich (Oakville, ON) and used as received. Calcium chloride dihydrate (CaCl<sub>2</sub>•2H<sub>2</sub>O) (Westlab Adlergrove, BC) was dissolved in Milli-Q® water to make a stock aqueous solution of 100 mM. Synthetic single stranded DNA (ssDNA) was purchased

from Integrated DNA Technologies (Coralville, IA), and a 100  $\mu$ M stock solution was prepared for further dilutions. Three phosphorothioate bond modifications were included at both the 5' and 3' ends to resist against exonuclease activity. The synthetic strand(s) was designed to amplify using published primer sets for the CSF1PO locus (Table 2.1) which contained five AGAT repeats and is designated as "Allele 1". A second strand, "Allele 2", was designed to be 2 repeats longer than the original strand and was used in the locus amplification assessment later.

**Table 2.1.** *Primer Sequences and DNA repeats for Alleles 1 and 2 in CATG biomaterials.*

	Sequence	Allele	Product Length	Reference
Reverse Primer	5'- AAC CTG AGT CTG CCA AGG ACT AGC - 3'			CSF1PO <sup>121</sup>
Forward Primer	5'- TTC CAC ACA CCA CTG GCC ATC TTC -3'			
Template	AGAT x5	1	98	
Strand	AGAT x7	2	106	

To generate ionically crosslinked calcium-alginate hydrogels, alginate acid was allowed to mix in Milli-Q<sup>®</sup> water overnight to fully dissolve to create a 1% w/v alginate solution. Next, DNA and alginate were mixed using a benchtop vortex. A 50 mM solution of calcium chloride was added, where the ratio between alginate to calcium was maintained at 4:1. The samples were vortexed again in

two 10-second intervals to achieve homogenous liquid hydrogel solutions. DNA-containing calcium-alginate hydrogels are designated as Calcium-Alginate Tissue Gels (CATGs). For hydrogels without DNA, CaCl<sub>2</sub> was added directly to the 1% w/v alginate solution without the addition of DNA and vortexed similar to the DNA-containing materials. These are referred to as CA, as there are no genetic component(s).

We assessed a range of DNA concentrations integrated into the CATGs from 1000-0.0001 ng/μL to understand the detection limits of DNA within the hydrogels. A total of 8 CATG samples were prepared which contained DNA (1000, 100, 10, 1, 0.1, 0.01, 0.001, and 0.0001 ng/μL), as well as two negative samples which did not contain DNA (CA).

### 2.2.2 DNA Extraction, Amplification and Analysis

To extract the DNA from the CATGs, we used the Monarch<sup>®</sup> DNA Gel Extraction Kit (New England Biolabs), and DNA was eluted with 20 μL of Invitrogen<sup>™</sup> UltraPure water (ThermoFisher Scientific). Two replicates of each of the fresh liquid CATGs were prepared for the extraction, as well as two replicates of the negative CA controls. The extraction procedure was optimized by assessing two

ratios of sample to gel dissolving buffer. One method explored the addition of 100  $\mu\text{L}$  of the liquid CATG/CA to approximately 450  $\mu\text{L}$  of the gel dissolving buffer, which was extracted immediately following mixing. In the second method, 250  $\mu\text{L}$  of CATG/CA was added to 550  $\mu\text{L}$  of buffer, which was the volume limit in the column. For this method, the CATG/CA-buffer mixture was left overnight to allow for complete dissolving. The samples were incubated in an Eppendorf ThermoMixer F1.5 at 52°C and 500 rpm for 20 minutes. After incubation, the manufacturer's protocol<sup>d</sup> was followed as suggested.

The extracted DNA was directly added to a PCR reaction without further dilution where 2  $\mu\text{L}$  was used as a DNA template. The extracted DNA was not quantified prior to PCR amplification due to its single stranded nature. The PCR conditions were as follows: 95°C for 10 minutes; 94°C for 30 seconds; 53°C for 1 minute; 72°C for 1 min; this process was repeated for a total of 30 times with a final step of 65°C for 15 minutes.

---

<sup>d</sup> Protocol NEB #T1020

Once amplified, a 1:20 dilution was prepared on a separate plate, and the diluted samples were genotyped using an ABI 3730 DNA Analyzer with a GeneScan 500 ROX size standard. To assess variability in each ABI run, a second dilution plate was prepared for each sample, and resubmitted to obtain a second replicate for the genotyping results.

### 2.2.3 Drying Experiment

To assess the effect of drying on the ability to extract DNA from the CATGs, 2.5 mL of each sample was allowed to dry in a Petri dish for 21 days at room temperature (Temperature:  $23.1^{\circ}\text{C} \pm 0.6^{\circ}\text{C}$ ; Relative Humidity:  $56.2\% \pm 3.2\%$ ). The CA hydrogels were also prepared as a negative control in the drying experiments similar to the fresh samples.

To assess whether DNA could be extracted from dried CATGs, two methods of sample processing were explored. The Petri dishes were placed over a 1 cm x 1 cm grid paper so that the hydrogels could be sampled over consistent areas between samples and methods (Figure 2.1). First, sterile swabs were inserted into individual aliquots of distilled water, similar to common evidence processing methods. A 1 cm x 1 cm area was swabbed using the wetted swab

to bind DNA from the dried CATG. An attempt was made to obtain as much of the rehydrated hydrogel on the swab as possible. The swab was then inserted into a 1.5 mL centrifuge tube containing 500  $\mu$ L of gel dissolving buffer (Monarch<sup>®</sup> DNA Gel Extraction Kit) and left to dissolve overnight.

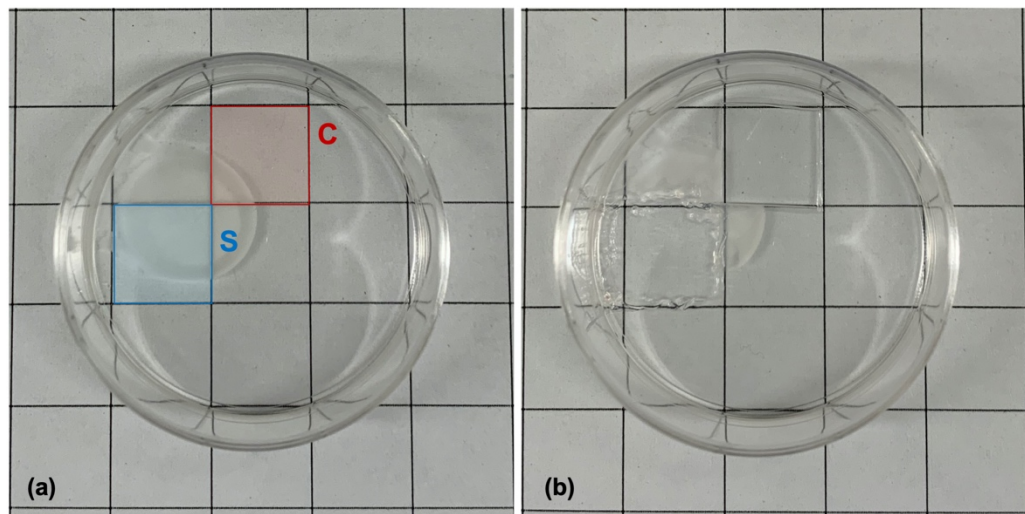


**Figure 2.1.** Experimental setup for CATG sampling during drying experiment. Grid pattern represents a 1 cm x 1 cm grid, where single samples were taken for swabbed (S) and cut (C) samples. Image (a) represents the dried CATG before sampling, and (b) after sampling.

The second method explored the efficacy of cutting a sample from the dried CATGs. Cuts were made using individual sterile scalpels along the outline of a 1 cm x 1 cm area. The piece was removed using individual sterile forceps and inserted into a 1.5 mL centrifuge tube containing 500  $\mu$ L of gel dissolving buffer and left overnight. Samples were then extracted using the modified protocol similar to the fresh samples.

#### 2.2.4 Rheology

Rheological characterization of the materials was performed using a Discovery HR20 stress-controlled rheometer with an advanced Peltier plate and solvent trap system (TA Instruments). All tests were performed using a 40 mm parallel plate geometry at 22°C. Oscillation amplitude tests were performed at 1 Hz and between 0.01-100% strain to determine the linear viscoelastic region (LVR) of the sample(s). Oscillation frequency tests were performed between angular frequencies ( $\omega$ ) of 0.05-150 rad/s at 1% strain determined from the LVR, and 15 points per decade were collected. The gap was set to 500  $\mu\text{m}$ , and a solvent trap filled with water was used to reduce evaporation of the sample during runs.

#### 2.2.5 Locus Amplification

Allele 1 was used in the CATGs to optimize DNA extraction and understand its viscoelastic properties. To assess the possibility of multiplexing in the future within these materials, we added a second strand, Allele 2, into the CATG. Allele 2 contained seven AGAT repeats total, which corresponded to a difference of 8 bases between Allele 1 and 2. For the co-amplification, 1:1 volume ratio of the



two alleles were added into the CATGs using 25  $\mu\text{L}$  or 50  $\mu\text{L}$  (1  $\text{ng}/\mu\text{L}$  each). Extraction, amplification, and analysis were all performed like section 2.2.2.

### 2.2.6 Data Analysis

Comparisons between materials was done using a two-way ANOVA where the independent variables were DNA concentration (1000-0.0001  $\text{ng}/\mu\text{L}$ ) and sample type (fresh or dried), and the dependant variable was allele peak height. A Tukey's Honest Significant Difference test was used post-hoc to determine where the significant differences in the data occurred, if present. Linear regressions were performed on allele peak height data as a function of DNA concentration for both the fresh and dried samples. Comparisons between swabbed and cut samples was done using a Student's T-test where comparisons were made at each DNA concentration.

## 2.3. Results

### 2.3.1 DNA Extraction and Amplification

DNA extractions were performed with each of the eight liquid CATGs (1000-0.0001  $\text{ng}/\mu\text{L}$ ) and the two CA negative controls. Two extraction methods were

explored with two replicates of each sample and two replicates submitted for genotyping. The overall extraction efficiency of the first extraction method (100  $\mu\text{L}$  CATG/CA in 450  $\mu\text{L}$  buffer) for the fresh samples was 100.0%, and 43.8% for the second method (250  $\mu\text{L}$  CATG/CA in 550  $\mu\text{L}$  buffer).

The amplified product was visualized on an ABI DNA Analyzer, which showed successful extraction and amplification of the DNA from the CATG materials (Figure 2.2). No alleles were observed in the negative controls, demonstrating that no contamination occurred during CATG preparation or extraction. The lowest concentration of 0.0001 ng/ $\mu\text{L}$  in the CATG showed relatively smaller allele peak heights of the visualized product compared to the other concentrations (Figure 2.2), which was also confirmed through the statistical assessments. Replicate extractions had unconfirmable alleles for this concentration where the peak heights were below a minimum threshold of 500 Relative Fluorescence Units (RFUs). Therefore, 0.0001 ng/ $\mu\text{L}$  was reasoned to be the lower detection limit for the DNA concentration in CATG.

Allele peak height weakly correlated with DNA concentration (Figure 2.2), which was also shown with the linear regressions for the fresh ( $R^2= 0.33$ ) and dry ( $R^2=$

0.47) samples. However, there was a significant difference between peak heights ( $p < 0.01$ ), with most of the differences occurring from the relative peak height of the 0.0001 ng/ $\mu$ L concentration.

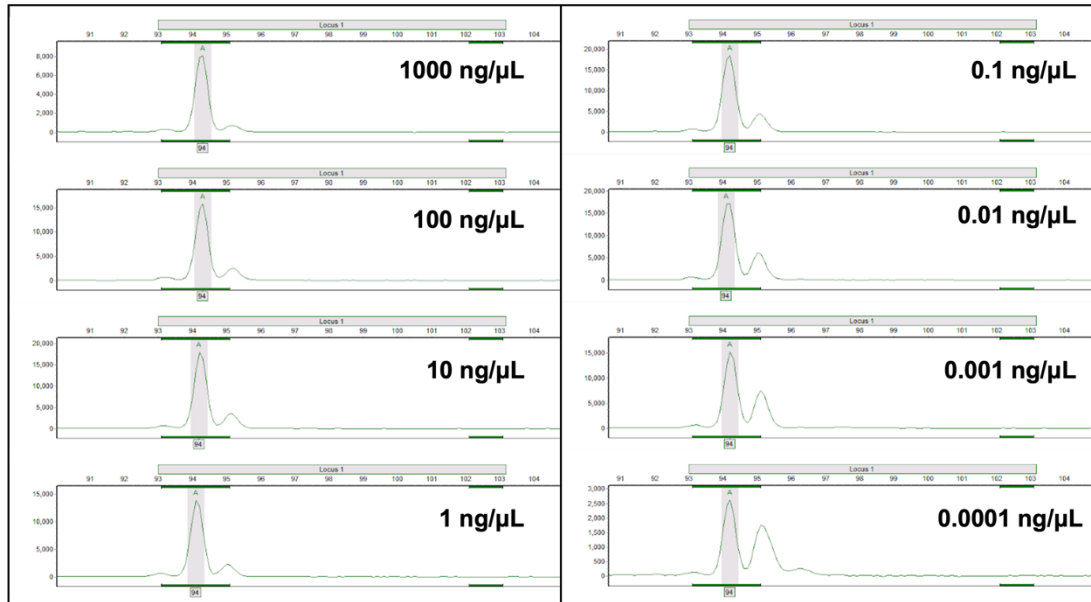


**Figure 2.2.** STR genotyping results of ssDNA (Allele 1) extracted from liquid CATGs with various concentrations of DNA between 1000-0.0001 ng/ $\mu$ L.

### 2.3.2 Drying Experiment

DNA STR genotyping was also successful for the dried CATGs. There were no significant differences found in the allele peak heights between fresh and dried samples ( $p = 0.61$ ). Drying at ambient conditions for 21 days did not influence the ability to extract DNA, and in some cases, the overall heights of the detected peaks were higher compared to the fresh samples (Figure 2.3). The fresh

samples in Figure 2.3 include all confirmable allele peak heights for each extraction type and replicate (1000 and 10 ng/ $\mu$ L n=8; 100 and 1 ng/ $\mu$ L n=6; 0.1-0.0001 ng/ $\mu$ L n=4). Similar to the fresh samples, no allele attributed to Allele 1 was observed in the CA hydrogel negative controls. Both swabbing and cutting the CATGs were successful methods of extracting DNA, although typically cutting the sample outperformed swabbing the hydrogels (Figure 2.4). There was a significant difference in the peak heights between swabbed and cut samples when accounting for DNA concentration ( $p=0.007$ ).

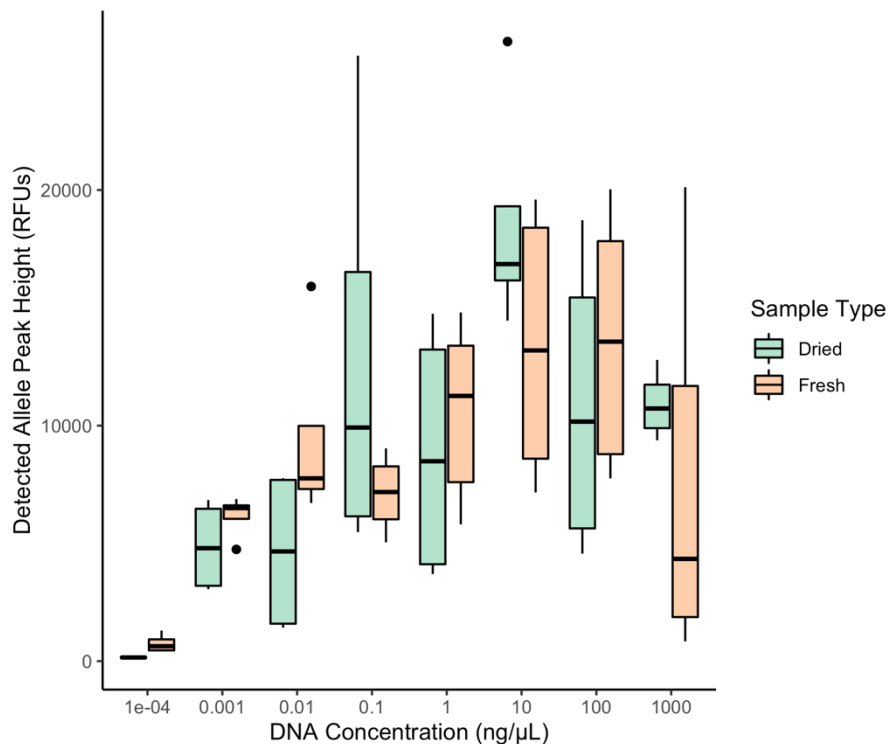


**Figure 2.3.** Detected allele peak height (RFUs) from samples containing various DNA concentrations between 1000-0.0001 ng/ $\mu$ L. Ranges shown are from fresh (n=44) and dried samples (n=32). Dried samples were aged for 21 days at room temperature and include both cut and swabbed samples.

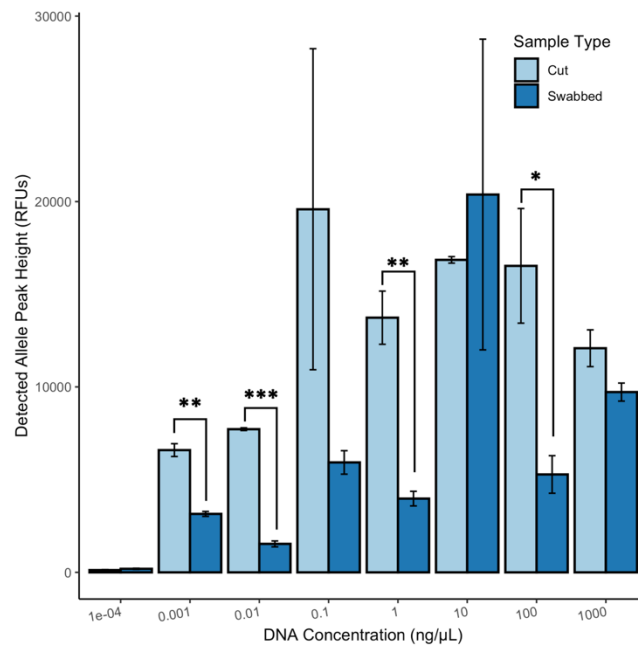


**Figure 2.4.** Differences in DNA extracted between swabbing ( $n=16$ ) and cutting ( $n=16$ ) a sample from the dried CATGs. Both methods sampled a 1 cm x 1 cm area of the same dried CATG. Significant differences between swabbed and cut sampling is noted with a (\*); where (\*) is  $p$  values  $\leq 0.05$ , (\*\*) is  $p$  values  $\leq 0.01$ ; and (\*\*\*) is  $p$  values  $\leq 0.001$ . Differences were found at concentrations of 0.001 ng/μL ( $p=0.006$ ), 0.01 ng/μL ( $p=0.0004$ ), 1 ng/μL ( $p=0.01$ ) and 100 ng/μL ( $p=0.04$ ).

### 2.3.3 Rheological Characterization

The rheological characterization was performed by conducting frequency sweeps with 1% strain, which was within the LVR. In general, in each material the storage modulus ( $G'$ ) was always higher than the loss modulus ( $G''$ ), indicating dominant elastic properties. No crossover between  $G'$  and  $G''$  was observed for any of the CATG or CA materials, except for CATG with 0.01 ng/μL which exhibited an uncharacteristic  $G'$  curve compared to the others (Figure 2.5, A).

The hydrogel that did not contain DNA (CA) had a lower storage modulus compared to each CATG material, indicating increased microstructure in the CATGs versus CA materials (Figure 2.5, A). There was no clear relationship in the moduli values based on the concentration of DNA added to the CATGs, although general trends were observed where higher DNA concentrations tended to have higher  $G'$  values, and lower DNA concentrations in the CATGs exhibited lower relative  $G'$  values.

The higher DNA concentrations in the CATGs showed less dependence on the angular frequency compared to other CATG/CA materials. In addition, some  $G'$  curves indicate a weaker structure versus the others, such as the 0.01 ng/ $\mu$ L CATG (Figure 2.5, A). Generally, the CA material had lower  $G'$ ,  $G''$  and complex viscosities ( $\eta^*$ ) but had generally higher loss factor ( $\tan\delta$ ) values compared to the CATG materials (Figure 2.5, A-D).

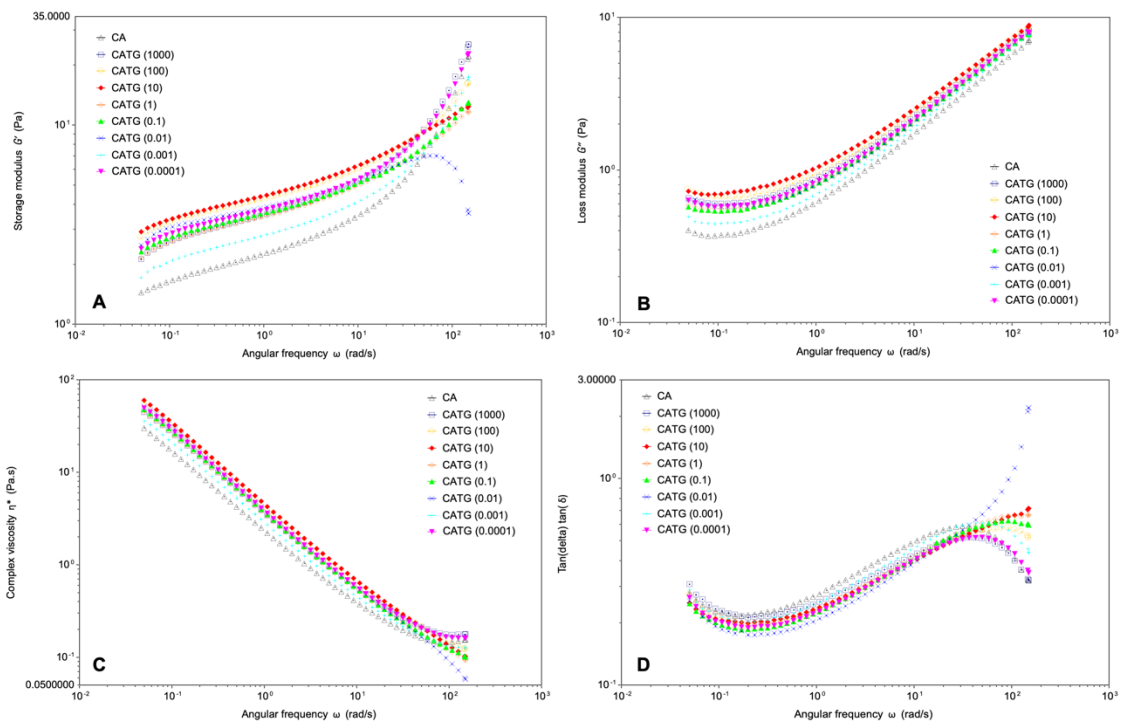


**Figure 2.5.** Rheological characterization of CATG and CA materials based on frequency sweeps. Data shown are: (A) storage modulus ( $G'$ ), (B) loss modulus ( $G''$ ), (C) complex viscosity ( $\eta^*$ ), and (D) loss factor ( $\tan\delta$ ) as a function of angular frequency ( $\omega$ ). Frequency sweeps were measured at angular frequencies from 0.05-150 rad/s at 22°C.

### 2.3.4 Locus Amplification

The addition of the second allele showed successful co-amplification within CATGs (Figure 2.6). Allele 2 was preferentially amplified compared to Allele 1, which had a consistently higher allele peak height. Both volumes added of each allele, 25  $\mu$ L and 50  $\mu$ L of each, generated accurate STR profiles.

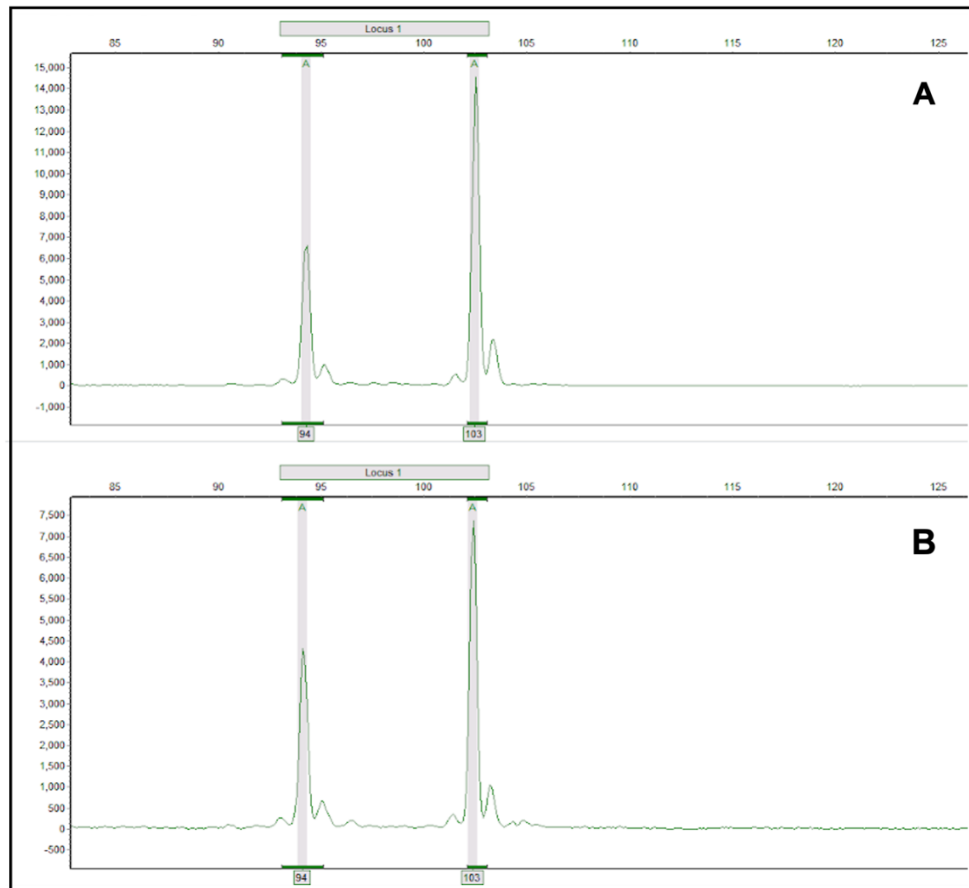


**Figure 2.6.** Co-amplification results for the integration of Allele 1 and 2 into the CATGs. The genotyping results show the amplification of two alleles added in 1:1 ratio: (A) 25 µL of each strand and (B) 50 µL of each strand.

## 2.4. Discussion

### 2.4.1 DNA Strands

The DNA used in the CATGs were designed to amplify using published CODIS primer sets outlined on the National Institute of Standards and Technology (NIST) Database<sup>121,122</sup>. The CSF1PO locus was chosen as an initial locus as it is a



simple tetranucleotide repeat, AGAT, and was designed to be smaller than reported allele sizes in the human population. The typical size range for alleles at the CSF1PO locus for the chosen primer set is 287-331 base pairs, corresponding to 5-16 repeats, respectively<sup>122</sup>. The size of the alleles at our synthetic CSF1PO locus is 98 bases for Allele 1 and 106 bases for Allele 2. The purpose of the smaller size was to ensure that a full or partial profile extracted from CATGs is unlike a human profile from analogous loci, but still can be used with typical kits for training. In this study, we did not use the primer sets from common kits such as Identifiler or PowerPlex, but this could be easily adjusted for specific training needs.

One noted variation observed in the analyzed DNA strands was the determined size of the alleles in the genotype. The determined sizes were slightly smaller than the actual size, where Allele 1 aligned at 94 bases, and Allele 2 was 102.9 bases (Figure 2.6). This attributes to a size difference of 4 and 3 bases smaller for Alleles 1 and 2, respectively. This observation is likely caused by the size of the ladder used on the ABI instrument, where the optimal fragment sizes for alignment with GS500 is much larger than the allele sizes used<sup>123</sup>, and would likely be resolved if a smaller ladder was used.

#### 2.4.2 DNA Extraction and Amplification

The small size of the DNA strands was thought to be an issue for the functionality of the CATGs, as leaching of the DNA from the calcium-alginate network is possible for smaller strand sizes<sup>124</sup>. However, the DNA integrated into the CATGs was able to be easily extracted and amplified using standard protocols. The extraction process used a DNA gel extraction kit as the method of DNA extraction from the CATGs. Because the DNA encapsulated within the CATGs is single stranded, other extraction techniques such as gel electrophoresis was not practical<sup>124</sup>. More pertinently, the use of an extraction kit was a necessary step to provide demonstrative training scenarios for typical biological evidence processing.

Gel extraction kits are typically used for the isolation of double stranded DNA after visualization with agarose gel electrophoresis. Agarose is also a naturally occurring polysaccharide similar to alginate, which initiates crosslinking via hydroxyl (OH) groups unlike alginate which initiates via its carboxyl (COO<sup>-</sup>) moieties<sup>125</sup>. Because of the similarities between alginate and agarose, it was reasoned that the gel extraction kits would be as effective in isolating the DNA on the columns from alginate-based materials as compared to removal from

agarose. The gel dissolving buffer in the gel extraction kit contains guanidine thiocyanate and sodium iodide<sup>126</sup>. Both sodium iodide and guanidine thiocyanate play a critical role in DNA binding to extraction columns<sup>127-129</sup>. In addition, given that guanidine thiocyanate is a chaotropic agent, it can cause the disruption of the ionic bonds between calcium and alginate, simultaneously breaking down the hydrogel structure. This breakdown is supported by the observation of small alginate particles in the eluent discard solution after the subsequent wash steps.

Two variations of the extraction protocol were explored. The first added 100  $\mu\text{L}$  of the liquid CATG to approximately 450  $\mu\text{L}$  of the gel dissolving buffer. In the second method, 250  $\mu\text{L}$  of CATG was added to 550  $\mu\text{L}$  of buffer, bringing the total volume to 800  $\mu\text{L}$ , the maximum volume capacity of the extraction columns. The first method typically performed better than the second based on the alleles detected (100.0% extraction efficiency with method 1 versus 43.8% in method 2). These efficiency variations could be attributed to the differences in CATG volume added to the column in each method. The manufacturer suggested ratio for buffer to agarose is 4:1 for optimal DNA extraction using the gel extraction kits. By adding a larger volume of CATG in method 2, the suggested ratio could

not be achieved in a single column, which lead to increased clogging on the column in method 2 as more CATG was left undissolved. Therefore, the suggested method to extract DNA from CATGs is to dissolve 100  $\mu\text{L}$  of the liquid material in 450  $\mu\text{L}$  of gel dissolving buffer.

#### 2.4.3 Drying Experiment

The CATGs were dried for 21 days in room temperature to assess whether DNA could be extracted from both fresh liquid and dried semi-solid materials. The purpose of this specific study was to address the potential of using CATGs as a dried coating in training scenarios. Additionally, time of drying was also a consideration for DNA extraction ability. The dried CATGs were able to produce STR genotypes similar to the fresh samples (Figure 2.3), demonstrating the ability of DNA to remain encapsulated over time similar to another study<sup>130</sup>. The ends of the DNA strands were modified with phosphorothioate bonds to protect against DNA degradation in solution from exonucleases and prolong stability<sup>131,132</sup>. The inclusion of these modifications was intended to improve the stability and functionality of the ssDNA over long periods of time since fragmentation from exonucleases is inhibited. The influence of these bonds on the prolonged stability of the DNA in the hydrogels was not directly explored in

this research but could be a reason that DNA extraction was so efficient after a 21-day drying time.

We explored two methods of sampling the materials, which was designed to compare swabbing versus excising the CATGs. Swabbing with a cotton swab is a standard procedure for sampling biological evidence<sup>133,134</sup>. This method works by moistening the swab with sterile water and concentrating the sample on the tip of the swab to obtain DNA from a piece of evidence. We performed a similar method and found that regardless of the solid-like state of the dried CATGs after 3 weeks, DNA could still be collected from the object, which in this case was a Petri dish. Cutting the CATG was done to simulate collecting a tissue sample, although this is typically collected by a pathologist instead of processing at the scene<sup>133</sup>. Here, the cut samples were visually different from a typical tissue sample but demonstrates a similar process which could be applied using other tissue variations of the CATG.

The cut samples were shown to have higher RFU values compared to the swabbed samples (Figure 2.3). This observation is likely caused by the more complete removal of the CATG in the cut samples compared to the swabbed.

An attempt was made to sample an equal area between cut and swabbed methods, but swabbing was challenging as rehydration of the CATG caused the formation of tacky particles which were difficult to fully collect on the swab. Regardless, swabbing, a more standard practise, was still able to obtain accurate DNA STR profiles for our designed locus. In addition, placing the swab/cut directly into the gel dissolving buffer overnight and extracting as normal yielded similar DNA profiles to the fresh materials (Figure 2.3).

Both methods demonstrate the promising potential for the CATGs as training standards in forensic scenarios. The CATG materials explored in this study can be used to coat forensically relevant pieces of evidence, which can be swabbed by trainees to obtain relevant genetic profiles. Future work will build on the ability to simulate tissue collection by tailoring the CATGs to resemble various tissues such as blood, skin, or muscles.

#### 2.4.4 Rheological Characterization

For the rheological assessments, we wanted to evaluate if there were differences in the viscoelastic properties of the two different material types (with and without DNA). The CATGs differed from CA in their loss factor ( $\tan\delta$ ) profiles. CA

exhibited higher  $\tan\delta$ , characteristic in materials with more liquid-like properties, or in this case less relative microstructure. The CATGs had higher storage moduli ( $G'$ ) values and complex viscosities ( $\eta^*$ ) overall compared to the CA material. A higher  $G'$  is attributed to more elastic properties, likely caused by the presence of DNA in the CATGs leading to a more structured or entangled arrangement of crosslinks. When a DNA-alginate solution is mixed with calcium, DNA becomes encapsulated within the ionic crosslinks of calcium-alginate, leading to higher storage modulus values. In addition, DNA and alginate are both negatively charged molecules and would therefore exhibit repulsion in solution, also increasing stiffness. These arguments were also supported by the increased viscosity observed for the CATGs versus CA materials (Figure 2.5, C).

Interestingly, the concentration of DNA in the CATGs did not exhibit any clear linear trends for the four variables evaluated, although there were differences in the respective curves for  $G'$ , implying structural differences (Figure 2.5). Intuitively, it would be expected that more molecular components, achieved with higher DNA concentrations, would lead to more structured materials. While we did not observe a distinct linear relationship between DNA concentration and  $G'$ , there were general trends exhibited. For example, CATGs with low DNA

concentrations (0.001 ng/ $\mu$ L) had the lowest  $G'$  of all the CATGs and exhibited a curve shape similar to the CA materials (Figure 2.5A). In addition, the CATG with a 0.01 ng/ $\mu$ L DNA concentration was the only material to exhibit a crossover point, where  $G'=G''$ , followed by a subsequent decrease in  $G'$ . Clearly, there is a relationship between the structural arrangement and the concentration of DNA added to the CATGs. Future work will explore the rheological profiles in more detail to fully understand this relationship and characterization will assist in the development of other tissue types with variable applications and functions. This will also explore the development of CATGs with more similar storage moduli to human tissues (>100 Pa) as the soft liquid materials studied herein currently possess low moduli when fresh<sup>135</sup>. The rheological properties of the dried materials were not assessed in this research, but would exhibit increased storage modulus, likely to more realistic tissue moduli ranges.

#### 2.4.5 Locus Amplification

The CATGs, as expected, are capable of functioning in reactions similar to biological tissues under a heterozygote profile. While we only explored co-amplification for two alleles at a single locus, it justifies the potential for the CATGs to integrate more loci or other DNA types based on the needs of the



forensic community. The calcium-alginate hydrogel is a suitable material to encapsulate and stabilize the contained DNA, as demonstrated through our drying study. Because of this, it is reasoned that optimizing the ratios of other DNA strands for a multiplexing reaction would be the limiting factor in the generation of a fully functional genetic profile CATG. This would open the door for opportunities for training materials that exhibit complex mixtures, multiple species, and other training standards of value.

## **2.5. Conclusions**

This study shows the potential for CATG materials to be used as tissue simulants in forensic science research and training. Short, single stranded DNA was successfully integrated into calcium-alginate hydrogels, which could be easily extracted and amplified using standard forensic procedures. In addition, the potential of these materials to be easily tailored for co-amplification was demonstrated. The effect of drying on the functionality of the CATGs was also explored where drying in ambient conditions for 21 days did not inhibit the ability to extract and amplify DNA. This is promising for intended coating applications of the CATGs and suggests a stable environment for DNA

functionality. The CATGs exhibited higher  $G'$  and viscosities compared to non-DNA containing materials. Rheological assessments also suggested an effect on the viscoelasticity based on the concentration of DNA added to the CATGs, although no clear relationship was observed in this current study. The non-toxic, bioinert, and tunable nature of CATGs can provide safe alternatives to traditional training materials in forensic science. Future work with the CATGs will continue to develop relevant tissue simulants such as blood and other soft tissues with relevant biomechanical and biochemical properties.

## Chapter 3

---

The use of high-resolution mass spectrometry (HRMS) for the analysis of DNA and other macromolecules: A how-to guide for forensic chemistry<sup>e</sup>.

### Preface

Type: Original Research Article

Submitted to: Forensic Chemistry

Status: Published

Title: The use of high-resolution mass spectrometry (HRMS) for the analysis of DNA and other macromolecules: A how-to guide for forensic chemistry.

Authors: Amanda Orr<sup>a</sup>, Theresa Stotesbury<sup>b</sup>, Paul Wilson<sup>c</sup>, Naomi L. Stock<sup>d</sup>

<sup>a</sup> Environmental and Life Sciences Program, Trent University, 1600 West bank Drive, Peterborough Ontario Canada K9L 0G2

<sup>b</sup> Forensic Science Department and Chemistry Department, Trent University, 1600 West bank Drive, Peterborough Ontario Canada K9L 0G2

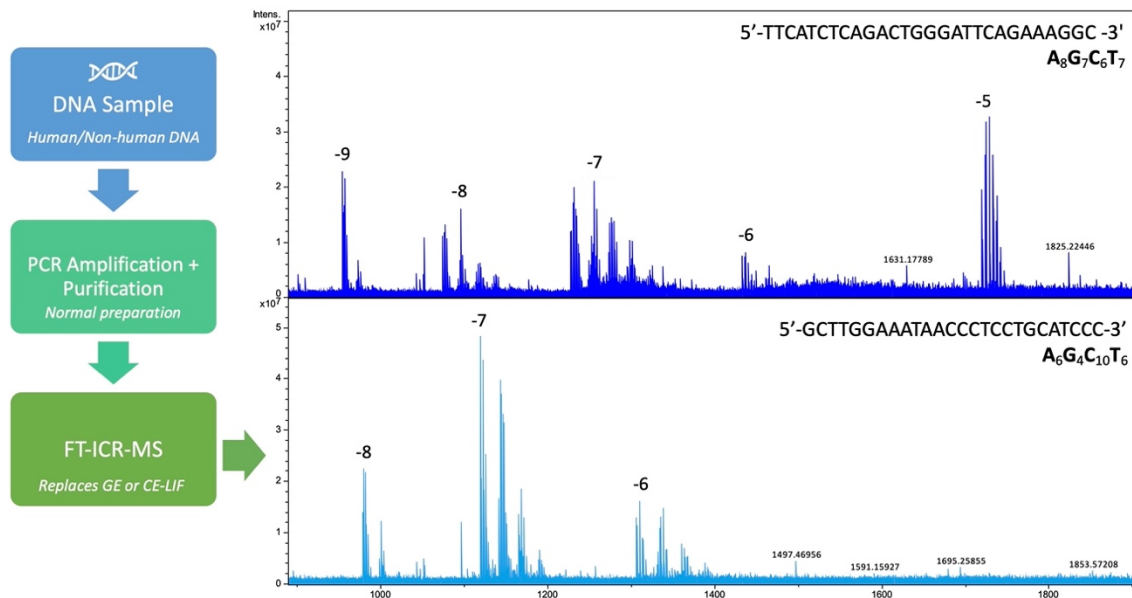
<sup>c</sup> Biology Department, Trent University, 1600 West bank Drive, Peterborough Ontario Canada K9L 0G2

<sup>d</sup> Water Quality Centre, Trent University, 1600 West bank Drive, Peterborough Ontario Canada K9L 0G2

---

<sup>e</sup> A. Orr, T. Stotesbury, P. Wilson, N.L. Stock. Forensic Chemistry. 2019. 14:1-12. DOI: 10.1016/j.forc.2019.100169

## Graphical Abstract



## Keywords

Matrix assessment; Fourier transform-ion cyclotron resonance mass spectrometry (FT-ICR MS); alternative PCR workflow; solvent choice; short oligonucleotides.

## Abstract

High-resolution mass spectrometry (HRMS) is a highly effective technique for the analysis of DNA and other biological macromolecules, and has potential to be a valuable tool for forensic chemists. In this work, we introduce the concepts of HRMS, discuss benefits of the technique, and outline the steps involved in developing an application utilizing this platform. We examine the importance of optimizing instrumental conditions, selecting an appropriate solvent, and interpreting mass spectra with considerations to determining charge state, mass accuracy and resolution. Specifically, we present a method for the analysis of short single stranded oligonucleotides (26-base and 28-base) using Fourier-transform ion cyclotron mass spectrometry (FT-ICR MS), while exploring the importance of sample matrix. Results of this work indicate that analysis of small oligonucleotides with 50:50 water:acetonitrile + 20 mM imidazole ( $C_3H_4N_2$ ) produced a mass spectrum with the -5 charge state as the base peak. Charge states of -4 and -15 were also observed, although at much lower ion intensity. Analysis of the oligonucleotides using water + 20 mM imidazole produced a charge state distribution from -5 to -11 over the mass range  $m/z$  200 to 2500. These two solvents, paired with the optimized HRMS method, produced multiple charge states, high resolution mass spectra, and high ion signal

intensity that allowed for unambiguous peak identification. This work serves as a “how-to guide” for forensics scientists who require efficient and accurate HRMS protocols. Our research supports using nucleic acids for diagnostics to analyze oligonucleotides, short DNA fragments and other biological macromolecules using HRMS.

### 3.1 Introduction

High-resolution mass spectrometry (HRMS) is a technique that offers both high resolution and high mass accuracy<sup>136,137</sup>. Resolution is the ability of the instrument to separate adjacent peaks in a mass spectrum, while mass accuracy is a measure of how closely a mass can be measured in comparison to the calculated theoretical value. These terms are closely related because generally mass accuracy improves as resolution increases<sup>136</sup>. Generating accurate mass values are extremely powerful for the identification of unknowns, as they can be used to predict chemical (molecular) formulas of analytes. Likewise, HRMS instruments are capable of separating isotopic peaks of an analyte. Isotopes of elements found in biomolecules such as carbon, oxygen, hydrogen and nitrogen contribute to the average mass of a molecule<sup>138</sup>, and are observed as separate, isotopic peaks on a mass spectrum. For example, the first peak in a given isotopic distribution corresponds to the monoisotopic mass of the molecule, which is the mass of a molecule based on the mass of the most abundant isotopes of each of the contained atoms<sup>139</sup>. A common isotopic distribution that is easily identified is the <sup>13</sup>C isotopic distribution. This distribution is characterized by the first peak representing the monoisotopic peak (only <sup>12</sup>C), and each adjacent peak after corresponds to the addition of one

or more  $^{13}\text{C}$  atoms. The ability to identify isotopic distributions is important as it can help identify the most common isotopes found in a molecule.

HRMS instruments include Fourier transform ion cyclotron resonance mass spectrometers (FT-ICR MS) in addition to Orbitrap and Time of Flight (TOF) analyzers. FT-ICR MS has demonstrated utility in identifying and interpreting biological macromolecules such as oligonucleotides<sup>140-145</sup>. This mass spectrometer determines the mass-to-charge ratio ( $m/z$ ) of ions based on the cyclotron frequency of the ions in a magnetic field and a Fourier-transform of the data is necessary to produce a mass spectrum. These instruments are beneficial as they use small sample volumes, provide high resolution and mass accuracy, and can be coupled to soft-ionization techniques. Electrospray ionization (ESI) is a soft ionization process because the ions are generally formed in solution without fragmentation of the molecule itself<sup>139</sup>. Pairing HRMS instruments, like the FT-ICR MS, with soft-ionization techniques such as ESI allows for the analysis of large biomolecules such as proteins and oligonucleotides. ESI permits the analysis of intact molecules and produces multiply charged species, which allows for observation of ions at lower  $m/z$



values. ESI is also a beneficial technique for these large molecules as it is able to preserve non-covalent interactions in the gas phase<sup>146</sup>.

Analysis of oligonucleotides can also be done using matrix-assisted laser desorption ionization (MALDI), another soft ionization technique, but it has been reported that when analyzing oligonucleotides that are longer than approximately 20 bases, there is a loss of purine base(s)<sup>140</sup>, which inherently affects the mass of the ions. However, because MALDI produces singly charged ions, the complexity of the spectra can be diminished using this technique. The choice of ionization source should reflect the length of oligonucleotides being analyzed, and the ability of the user to appropriately analyze the resulting spectra.

The benefits of high-resolution and high-mass accuracy achieved with HRMS allow for identification and interpretation of biomolecules of forensic relevance. For example, HRMS is useful in determining the elemental composition of an unknown using the accurate mass<sup>140,147,148</sup>. By assessing elemental compositions, e.g. the chemical formula, for molecules such as oligonucleotides, the DNA or RNA base composition can be determined using

this information<sup>140</sup>. High mass accuracy allows for unambiguous determination of the bases in a sample as each particular combination will result in a unique mass value, and therefore a unique  $m/z$  value as well. With HRMS, it is also possible to determine the sequence of DNA and RNA strands based on accurate assessment of masses, as well as assessment of microsatellite repeats for comparison<sup>149</sup>. While this type of information is outside of the scope of this paper, sequence determination approaches have been outlined elsewhere<sup>140,141,150</sup>.

In this guide, we identify the typical steps and considerations involved in the analysis of biological molecules, such as oligonucleotides, using HRMS. This includes calculating  $m/z$  values and charge distributions, solvent choice and optimizing instrument conditions, calculating mass accuracy and resolution, and interpretation of spectral results. We discuss each of these steps as we present our research on the development of an HRMS method for the analysis of short single stranded oligonucleotides with a focus on matrix (solvents and additives) assessment. We identify two matrices that are appropriate for analysis of oligonucleotides based on our work. Our work is meant to act as a useful

resource for anyone implementing HRMS in both operational and research contexts.

## **3.2 Methods and Materials**

### 3.2.1 Chemicals

The two DNA strands used in this research were a single stranded 28-base (8608.47 Da) and a single-stranded 26-base (7847.34 Da) strand that were designed and purchased from Integrated DNA Technologies (Coralville, IA, USA). The sequence of the 28-base oligo was 5'-TTCATCTCAGACT-GGGATTCAGAAAGGC-3', and the sequence of the 26-base strand was 5'-GCTTGGAATAACCCTCCTGCATCCC-3'. The DNA samples were reconstituted in Ultrapure water. Ultrapure water was obtained from Invitrogen™, ThermoFisher Scientific (Waltham, MA, USA). Acetonitrile, methanol and isopropanol, all HPLC-grade, were obtained from ThermoFisher Scientific (Whitby, ON, Canada). Ammonium acetate and imidazole were purchased from Sigma-Aldrich (Oakville, ON, Canada) and used as received.

### 3.2.2 FT-ICR MS Instrumentation

For this research, a 7T Bruker Solarix FT-ICR MS, equipped with an ESI source operating in negative ion mode, was used. All samples were analyzed using the following conditions: 50°C dry gas temperature, 180  $\mu\text{L/h}$  flow rate, a capillary voltage of 5 kV, and a nebulizer gas ( $\text{N}_2$ ) pressure of 4.0 bar with a dry gas flow of 4.0 L/min. For all analyses, the accumulation time was optimized for  $\sim 1 \times 10^9$  ions in the ICR cell. For the majority of the samples, 4 M data points were collected per scan (free ion decay (FID) time was 3.9147 s). The number of data points in the transient controls the resolving power of the instrument. When investigating resolution, samples were also analyzed using 32K (FID time = 0.0306 s), 128K (FID time = 0.1223 s), and 16M data points (FID time = 15.6587 s). External calibration of the instrument was conducted using sodium trifluoroacetate (NaTFA) (0.1 mg/mL). For all analyses, the mass range was  $m/z$  200-5000 and 200 scans were acquired. All spectra were acquired using Bruker *ftms* Control software (version 2.1.0) and analyzed using Bruker Compass DataAnalysis software (version 5.0) for charge identification and deconvolution.

### 3.2.3 Solvent Selection

For the matrix assessment, we analyzed four solvents of various imidazole and ammonium acetate concentrations to determine optimal conditions for DNA analyses using FT-ICR MS. The four solvents that were assessed were: UltraPure water, water and acetonitrile, water and isopropanol, and water and methanol, all in 50:50 (v/v) preparations. The DNA was assessed at a concentration of 5  $\mu$ M for all samples. After analysis of the mass spectra using the above solvents, the three solvents that produced resolved spectra with considerable signal were chosen and analyzed with the addition of: 20 mM imidazole; 10 mM ammonium acetate; and a combination of 20 mM imidazole/10 mM ammonium acetate. The conditions for the matrix assessment are shown below in Table 3.1.

**Table 3.1.** Assessment of various solvent matrices for optimal DNA analysis using ESI FT-ICR MS. Solvents assessed were various combinations of ultrapure water, isopropanol (IPA), acetonitrile (ACN), and methanol (MeOH). Solvents containing imidazole and ammonium acetate contained concentrations of 20 mM imidazole and 10 mM ammonium acetate for all solvents.

DNA Concentration	Solvent	Temperature
5 $\mu$ M	Ultrapure Water	50°C
	50:50 H <sub>2</sub> O:IPA	
	50:50 H <sub>2</sub> O:ACN	
	50:50 H <sub>2</sub> O:MeOH	
	Ultrapure Water + Imidazole	
	Ultrapure Water + Ammonium Acetate	
	50:50 Ultrapure Water + Imidazole + Ammonium Acetate	
	50:50 H <sub>2</sub> O:ACN + Imidazole	
	50:50 H <sub>2</sub> O:ACN + Ammonium Acetate	
	50:50 H <sub>2</sub> O:ACN + Imidazole + Ammonium Acetate	
	50:50 H <sub>2</sub> O:MeOH + Imidazole	
	50:50 H <sub>2</sub> O:MeOH + Ammonium Acetate	
	50:50 H <sub>2</sub> O:MeOH + Imidazole + Ammonium Acetate	

### 3.3 Results and Discussion

There are many factors that affect the quality of a resulting spectrum and therefore must be considered in optimization protocols. It is important to note that with the analysis of oligonucleotides using HRMS instruments, there will be variation of results between instruments, and even within instruments of the

same make and model<sup>151</sup>. Thus, these are general guidelines that may differ for spectral optimization.

### 3.3.1 Instrumental Conditions

Instrumental conditions, especially ESI parameters including nebulizer gas pressure and temperature, spray voltage and flow rates influence the resulting mass spectrum and require optimization. The literature reports varying flow rates, between ~ 10  $\mu\text{L/hr}$  to 300  $\mu\text{L/hr}$ , for oligonucleotide analysis<sup>143,152,153</sup>, but will depend on the instrument being used. The flow rate must ensure there is a constant spray of ions that can be detected<sup>136</sup>. Based on our work using an FT-ICR MS instrument, we found that a flow rate of 180  $\mu\text{L/hr}$  was appropriate. This flow rate was sufficient to produce a constant signal and resulted in low sample consumption, which is ideal for the analysis of oligonucleotides, as they are generally prepared in small volume quantities.

The nebulizer gas temperature is influential because it is the temperature applied to the electrosprayed sample to assist in evaporation of the solvent<sup>136</sup>. When analyzing oligonucleotides, the conformations of the oligonucleotides can change with temperature. For example, Hofstadler *et al.*<sup>140</sup>, used a

countercurrent dry gas temperature equivalent to room temperature to maintain the double stranded conformation of the DNA, while assisting in desolvation of the sample. There is variation in the reported dry gas temperatures in the literature, where temperatures vary anywhere from room temperature to 200°C<sup>140,143,145,152,154</sup>. In our research, we found that a dry gas temperature of 50°C was optimal to produce ions of intact DNA molecules. We found that increasing the temperature resulted in a loss of ions, possibly due to the degradation of the DNA molecules with higher temperatures. The ability of the non-volatile oligonucleotides to enter into the gas phase at this low temperature was assisted by the volatility of the solvents used, which is discussed in the next section.

### 3.3.2 Solvent Choice

The choice of the solvent for analysis of any analyte is important to the resultant spectra, which is especially true for larger, more complex molecules. Larger biomolecules tend to have multiple sites for protonation/deprotonation. The pH of the solvent significantly dictates the charge state(s) of the molecule<sup>142</sup>. If electrolytes are present in the solvent, adducts can form with the biomolecule in solution<sup>155</sup>, which can lead to larger than anticipated  $m/z$  values and more



complicated mass spectra. Appropriate solvents must also consider instrumental compatibility. When using ESI, solvents must be protic (contain a labile H<sup>+</sup>) or, in the case of aprotic solvents, mixed with a protic solvent. For example, acetonitrile itself is aprotic, but, when mixed with methanol and/or water can be an appropriate solvent mixture for ESI protocols. Solvents should also be (semi)volatile to assist in allowing the generally non-volatile analytes, such as biological macromolecules, to become ionized and enter into the gas phase during ESI<sup>141,142</sup>. In addition, organic solvents have been identified to produce a larger ion abundance<sup>141</sup>.

There are many options for solvents, but the choice of solvent should accommodate minimal interaction with the analyte and allow for ionization of the analyte without the formation of adducts. Commonly used solvents for the analysis of oligonucleotides are methanol, acetonitrile, and isopropanol, although these are not exhaustive. We have assessed the ability to use these solvents for analysis of short oligonucleotide strands (26- and 28- bases) in our matrix assessment study. In our analysis, we found that two solvents were appropriate for oligonucleotide HRMS analysis: (i) water and 20 mM imidazole, and (ii) 50:50 (v/v) water: acetonitrile and 20 mM imidazole (Figure 3.1). Using

water and 20 mM imidazole as a solvent produced a mass spectrum with charge states between -5 to -11; the -6 to -8 charge states had the largest ion signal intensity. Dissolving the DNA in 50:50 (v/v) water:acetonitrile and 20 mM imidazole produced a mass spectrum with the -5 charge state as the base peak. Charge states between -4 and -15 were also observed. It is important to note that ion signal intensity was more than 5 times greater when the DNA strands were analyzed in water, acetonitrile and 20 mM imidazole. The difference in ion signal intensity and charge state distribution observed for the two different solvents exhibit the effect that solvent has on the resulting spectra. Different solvents can promote larger charge states, as is the case with the water, acetonitrile and 20 mM imidazole solvent, and can also affect the intensity of the ions. Calculation of charge states will be explored below.

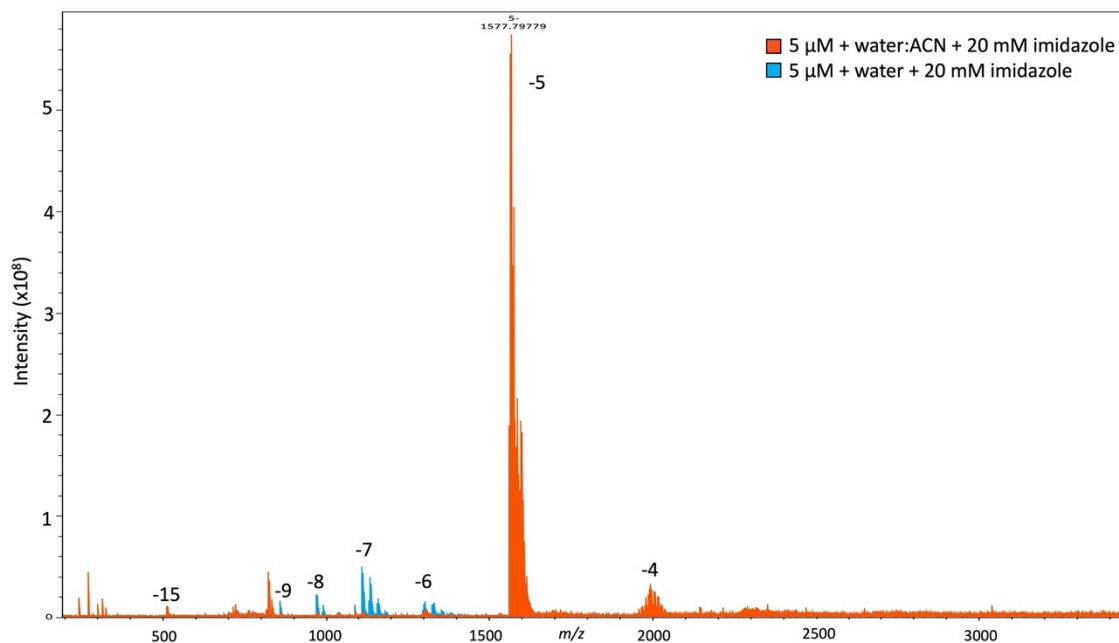


**Figure 3.1.** FT-ICR mass spectrum of 26-mer oligo (5  $\mu\text{M}$ ) in two optimal solvents. Using water + 20 mM imidazole (blue), charge states from -5 to -11 were observed, with the highest ion signal intensity for -6 to -8. Using 50:50 water:acetonitrile + 20 mM imidazole (orange) the -5 charge state is the base peak; -4 and -15 were also observed.

The addition of volatile compounds such as imidazole, ammonium acetate or piperidine to the solvent solution can help to decrease the cation adducts attracted to the negatively charged phosphate backbone of DNA, and improve the ion intensity of peaks and decrease charge state <sup>141,145</sup> (Figure 3.2). From Figure 3.2 we can see that the addition of imidazole, ammonium acetate or a combination of the two leads to improved mass spectra in terms of increased ion signals and increased resolution compared to analysis of the oligonucleotides without these molecules. In addition, Figure 3.2 showcases the

benefits of these cation-reducing molecules on the resulting mass spectrum of oligonucleotides. In Figure 3.2 (A), the DNA is analyzed with only water and acetonitrile as a solvent. The -5 charge state occurs at higher  $m/z$  values compared to the analysis with imidazole and/or ammonium acetate. If we were to infer mass from the analysis in (A), it would result in higher mass determinations of the molecule, and therefore a larger error in the assignment of base compositions or sequencing. In addition, because there is such a low signal to noise for the water and acetonitrile solvent, we would likely not be able to conduct meaningful determinations as the signals are not well resolved. The addition of cation-reducing agents, such as imidazole or ammonium acetate, significantly improve the quality of the spectra and can then be used to conduct useful analyses of the oligonucleotides.

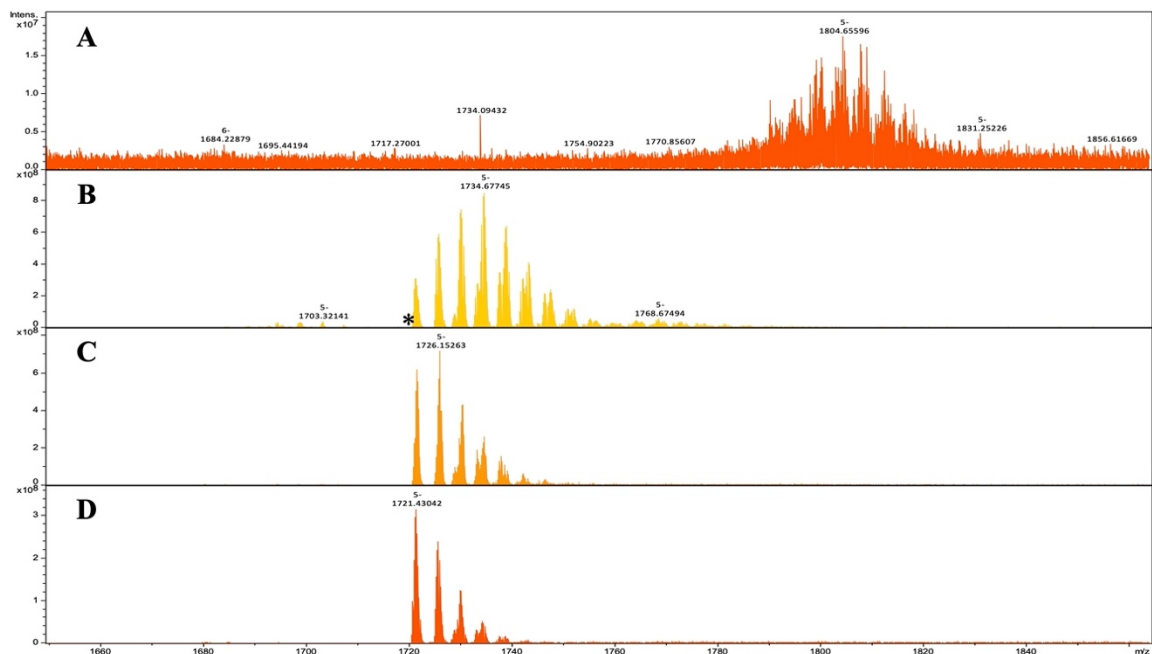


**Figure 3.2.** Comparison of the same 5  $\mu\text{M}$  28-base oligonucleotide using four different solvents: 50:50 v/v water and acetonitrile (A), 50:50 v/v water, acetonitrile and 20 mM imidazole (B), 50:50 v/v water, acetonitrile and 10 mM ammonium acetate (C), and 50:50 v/v water, acetonitrile, 20 mM imidazole, and 10 mM ammonium acetate (D). \* Denotes the theoretical monoisotopic peak at 1720.687367 m/z.

Along with solvent choice, there is also the consideration of the concentration of analyte being analyzed. The amount of analyte is important as having too low of a concentration can cause low signal to noise ratios or generation of too little ions to be detected<sup>151</sup>. The analyzed concentration will depend on the instrument being used, and also the information sought from the molecule being analyzed<sup>142</sup>. For example, the concentration should reflect whether molecular weight information or non-covalent interactions are being investigated<sup>142</sup>. For oligonucleotide investigations using HRMS, reported

concentrations vary between 0.05  $\mu\text{M}$  to 15  $\mu\text{M}$ <sup>143,150</sup>, but more commonly are analyzed with concentrations 1-10  $\mu\text{M}$ <sup>142</sup>. In our research, we found that a concentration of 5  $\mu\text{M}$  provided high signal-to-noise ratios with high mass accuracy. A concentration of 5  $\mu\text{M}$  was chosen as preliminary assessments found that a concentration of DNA that was 0.5  $\mu\text{M}$  was too low (data not shown). Table 3.2 below summarizes the components of oligonucleotide analysis discussed thus far.

**Table 3.2.** Considerations for oligonucleotide analysis using HRMS. Considerations are: pH, solvent, other molecules, concentration of DNA, and temperature. \* Variation depends on the molecular weight

Considerations for Oligonucleotide Analysis with HRMS	
pH	Higher - increase in negative ions - increase in charge state
Solvent	Volatile - acetonitrile, methanol, isopropanol, (water, as co-solvent)
Additives	Imidazole, ammonium acetate, piperidine
[DNA]	1 - 10 $\mu\text{M}$ (~7.5 - 80 ng/ $\mu\text{L}$ )*
Temperature	Analysis dependent (room temperature - 200 °C)

### 3.3.3 Charge State Calculations

To acquire structural and composition information about oligonucleotides from mass spectra and confirm the charge assignment of an identified peak(s) from software, it is important to not only know how to calculate charge states but also

understand why the charges are assigned. To calculate the theoretical  $m/z$  of the sample, the exact monoisotopic mass of the oligonucleotide must be determined. The monoisotopic mass refers to the mass of a molecule based on the mass of the most abundant isotope of the contained atoms<sup>139</sup>. In this work, exact masses are calculated using six decimal places. When working with shorter strands, it may be acceptable to use a chemical sketching program, such as MarvinSketch, to draw the molecule and calculate its exact mass (Figure 3.3). This is particularly useful if the DNA strand is chemically modified in any way. For longer strands (>30 bp), there are various programs available that are able to calculate the monoisotopic mass, such as the Mongo Oligo Mass Calculator developed by the RNA Institute<sup>156</sup>, based on entry of the sequence of the DNA strand.

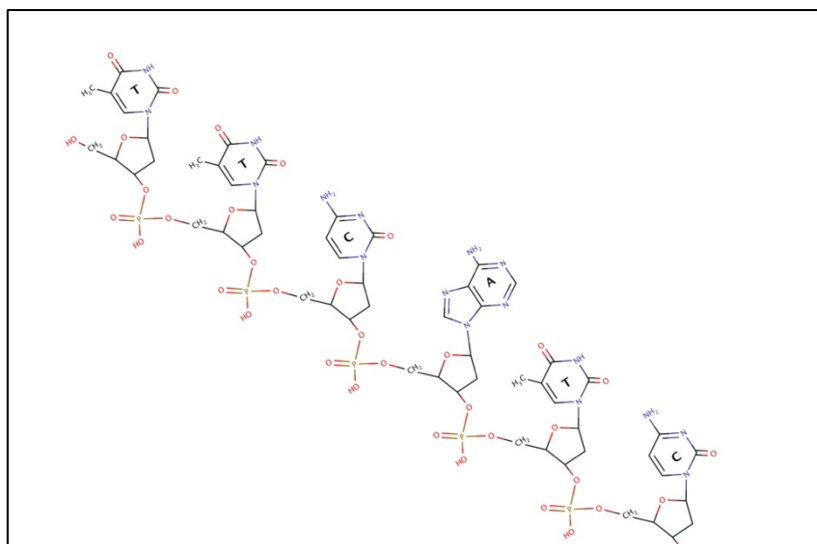


**Figure 3.3.** Structure of the first 6 base pairs found at the 5' end of the characterized 28-mer DNA strand (monoisotopic mass = 8608.473216 Da). The sequence of the strand is 5'-TTCATCTCAGACTGGGATTGAGAAAGGC-3'. The entire strand's structure was created using MarvinSketch program and was used to determine the monoisotopic mass.

Once the monoisotopic mass has been determined, simple calculations can be applied to compute the theoretical mass to charge,  $m/z$ , distribution for the specific oligo, as shown in Equation 4:

$$m/z = \frac{M - z [H^+]}{z} \quad (4)$$

where  $M$  is the monoisotopic mass,  $[H^+]$  is the exact mass of a proton (1.007276), and  $z$  is the charge of the ion. It is important to note that when using HRMS and calculating  $m/z$  values, the exact mass of a proton should be used and not the exact mass of a hydrogen atom (1.007825); the difference between the two being the mass of an electron (0.00055). To illustrate the concept of  $m/z$



calculations, if we wanted to calculate the theoretical  $m/z$  for the -3 charge state of a DNA molecule with an exact mass of 8608.473216 Da, it would be:

$$m/z = \frac{(8608.473216) - (3)(1.007276)}{3}$$

$$m/z = 2868.483796$$

The theoretical  $m/z$  for any charge state can be calculated using the formula shown above. The theoretical  $m/z$  for charge states -1 to -15 for a DNA molecule with an exact mass of 8608.473216 Da are shown in Table 3.3.

**Table 3.3.** Theoretical  $m/z$  values of 28-mer DNA strand based on theoretical calculations of  $m/z$  up to a charge of -15. Monoisotopic mass of 28-mer strand is 8608.473216 Da. Calculated  $m/z$  values represent the loss of  $z$  number of protons ( $H^+$ ) in the first column. Respective columns show the  $m/z$  values accommodating one to five  $^{13}C$  isotopes.

Charge	$m/z$ [ $-H^+$ ]	$m/z$ 1 $^{13}C$	$m/z$ 2 $^{13}C$	$m/z$ 3 $^{13}C$	$m/z$ 4 $^{13}C$	$m/z$ 5 $^{13}C$
1	8607.465940	8608.469295	8609.472650	8610.476005	8611.479360	8612.482715
2	4303.229332	4303.731010	4304.232687	4304.734365	4305.236042	4305.737720
3	2868.483796	2868.818248	2869.152699	2869.487151	2869.821603	2870.156054
4	2151.111028	2151.361867	2151.612706	2151.863544	2152.114383	2152.365222
5	1720.687367	1720.888038	1721.088709	1721.289380	1721.490051	1721.690722
6	1433.738260	1433.905486	1434.072712	1434.239938	1434.407163	1434.574389
7	1228.774612	1228.917948	1229.061285	1229.204621	1229.347958	1229.491294
8	1075.051876	1075.177295	1075.302715	1075.428134	1075.553554	1075.678973
9	955.489748	955.601232	955.712716	955.824200	955.935684	956.047167
10	859.840046	859.940381	860.040717	860.141052	860.241388	860.341723
11	781.581198	781.672412	781.763626	781.854840	781.946055	782.037269
12	716.365492	716.449105	716.532718	716.616331	716.699944	716.783557
13	661.182971	661.260153	661.337334	661.414515	661.491696	661.568877
14	613.883668	613.955336	614.027004	614.098673	614.170341	614.242009
15	572.890938	572.957829	573.024719	573.091609	573.158500	573.225390

### 3.3.4 Mass Spectral Interpretation

The monoisotopic peak corresponds to the monoisotopic mass, and is the first peak in an isotopic distribution, which represents the loss of  $z$  number of  $H^+$  ions for a given molecule. When analyzing large biomolecules, the monoisotopic peak often has the smallest peak intensity, where the largest peak in the isotopic distribution, the base peak, is close to the average mass of the molecule. Generally, when the isotopic distributions are resolved, as is the case in Figure 3.5 B below, each peak after the monoisotopic peak represents the addition of one proton to the molecule. Generally, this is  $^{13}C$ , but can also include  $^2H$ ,  $^{15}N$ , or  $^{17}O$ . As the resolution is increased, more isotopic contributions can be identified, as we can see in Figure 3.5 A, where the peaks start to have fronting or tailing on the peak shapes, indicating the identification of isotopes that were not visible in spectra collected at lower resolutions.

The monoisotopic peak(s) for each identified charge state (generally identified by software) should be compared to the theoretical  $m/z$  values calculated previously. This determines if the charge states have been assigned correctly, as well as assesses the appropriateness of the solvent for generating spectra with high mass accuracy. An example of this was shown in Figure 3.2 where the

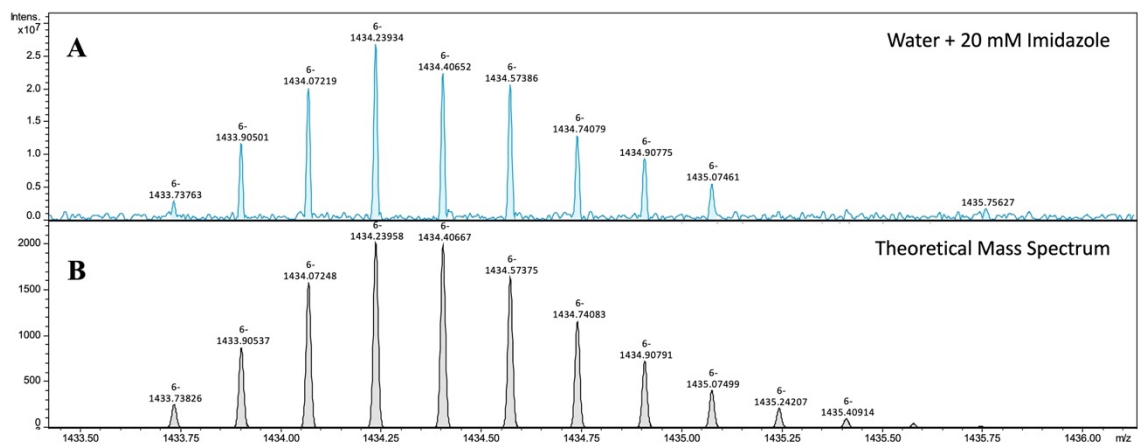
spectra in (A) has a -5 charge identified but occurs at a higher  $m/z$  than the spectra in (B). The matrix in Figure 3.2 (A) leads to increased mass of the DNA strand, where it is identified as a charge state of -5. Contrarily, with the addition of the cation-reducing molecule imidazole to the same solvent, we can see that the peaks become more resolved and closer to the theoretical monoisotopic mass, as denoted by \*. The difficulty in determining the  $m/z$  value of the monoisotopic peak in Figure 3.2 (A) is due to the low signal to noise ratios observed for this solvent. Because of this, we can use the difference between the base peaks to attempt to identify adducts that are being added to the DNA strands. The base peaks are labelled in Figure 3.2, and the identified difference between the two base peaks is  $m/z$  69.97851.

Table 3.3 represents the charge state calculations of an 8608.473216 Da DNA strand, where the charge states for the monoisotopic mass are shown, as well as calculated  $m/z$  peaks for  $^2\text{H}$ ,  $^{13}\text{C}$ ,  $^{15}\text{N}$ , and  $^{17}\text{O}$  isotopes as these isotopes are an important consideration for actual spectral interpretation. An important note is that these calculations explained represent the theoretical form of a molecule with the loss of  $z$  number of  $\text{H}^+$  ions. Complex solvents and heterogeneous samples can lead to mass spectra that do not precisely correspond to the

theoretical mass calculations. For example, common cation additions to DNA can occur with sodium ( $\text{Na}^+$ ) and potassium ( $\text{K}^+$ ) ions. It may therefore be necessary to consider these adducts for spectral interpretation, as they are helpful with identifying peaks that do not correlate to the theoretical  $m/z$  values.

### 3.3.5 Mass Accuracy

Comparison between the experimental peaks with theoretical peaks will also allow for intuitive interpretation of spectra. An example of the theoretical mass spectrum, generated using Bruker Compass DataAnalysis software, compared to the experimental mass spectrum is shown in Figure 3.4.



**Figure 3.4.** Mass spectrum of a 5  $\mu\text{M}$  28-base oligonucleotide using water and 20 mM imidazole as a solvent (A). The theoretical mass spectrum based on the monoisotopic mass of 8608.473216 Da is shown in (B). The  $-6$  charge states are shown for both spectra. Observed mass accuracy was  $-0.167336$  ppm using the base peak.

Comparison between the experimental and theoretical isotopic distributions can also be quantified by determining the mass accuracy using the following equation:

$$\text{Mass accuracy (ppm)} = \frac{M_{\text{experimental}} - M_{\text{theoretical}}}{M_{\text{theoretical}}} \times 10^6 \quad (5)$$

where  $M_{\text{experimental}}$  is the experimental  $m/z$  value and the  $M_{\text{theoretical}}$  is the theoretical  $m/z$  value. To determine the mass accuracy of the base peak for the spectra in Figure 3.4, we use Equation 5 as follows:

$$\begin{aligned} \text{Mass accuracy (ppm)} &= \frac{1434.23934 - 1434.23958}{1434.23958} \times 10^6 \\ &= -0.17 \text{ ppm} \end{aligned}$$

Therefore, the mass accuracy for the observed base peak in Figure 3.4 was -0.17 ppm, indicating high mass accuracy compared to the theoretical distribution. The negative sign indicates that the observed value was lower than the theoretical values, but these low values give confidence in the corresponding mass calculations of the oligonucleotides which can allow for accurate determinations of base compositions or sequence determination. Determining the base composition can be done by comparing the determined experimental mass to the mass for various combinations of bases. Given the high accuracy, we can unambiguously assign the base makeup of the analyzed DNA strand by

comparing theoretical combinations of bases to the determined mass. Sequencing of analyzed oligonucleotides using HRMS has been outlined in other articles<sup>140,141,150,155</sup>, and is beyond the scope of this paper.

In our research, the highest mass accuracy (smallest ppm value) was observed when analyzing the DNA strands with a solvent of water and 20 mM imidazole. The average mass accuracy values for the two solvents are presented in Table 3.4 below.

**Table 3.4.** Average mass accuracy values (ppm) for the HRMS analysis of 26- and 28-base single stranded DNA in two solvents (50:50 water:acetonitrile + 20 mM imidazole and water + 20 mM imidazole) that were used to analyze 26- and 28-base single stranded DNA. The “-” symbol denotes no observed peaks for designated charge states. Note: smaller ppm values correspond to higher mass accuracy

Charge State	28-base		26-base	
	50:50 Water:Acetonitrile + Imidazole	Water + Imidazole	50:50 Water:Acetonitrile + Imidazole	Water + Imidazole
-4	153.239309	-	3331.651543	-
-5	-8.369947	45.691043	-23.135809	0.274049
-6	12.017535	-13.442545	-17.807049	-16.910374
-7	2.887711	-11.735319	13.244430	-0.160647
-8	310.570407	28.392339	-3.745251	-12.980799
-9	11.759488	-9.182156	1.451040	-11.109091
-10	8.940396	-0.477085	638.855134	53.658831
-11	10.244317	-0.556756	-	-
-15	6426.048087	-	2730.491142	-

As we can see from Table 3.4, the observed mass accuracy was on average much higher with the water + 20 mM imidazole solvent compared to the 50:50 water:acetonitrile + 20 mM imidazole solvent. While the 50:50 water:acetonitrile + 20 mM imidazole was shown to produce high signals for the -5 and -4 charge states, the overall mass accuracy of the spectra is lower compared to the other solvent. Based on these results, we identify water + 20 mM imidazole as an ideal solvent for high mass accuracy for charge states between -5 to -11. If it is required that high charge states, such as -15, be observed to analyze large oligonucleotides so that they can be viewed in a smaller  $m/z$  range, the 50:50 water:acetonitrile + 20 mM imidazole solvent is favourable, although there is considerably low mass accuracy for that charge state.

### 3.3.6 Resolution

The resolution of mass spectra can be calculated by measuring the width of a peak at a designated percentage of height of the peak<sup>136</sup>. The most commonly used method in HRMS is calculating resolution using the full width half maximum (FWHM), which measures the peak width at 50% of the height. Resolution,  $R$  is calculated using Equation 6:

$$R_{\text{FWHM}} = \frac{m/z}{\Delta m/z} \quad (6)$$

where  $m/z$  is the  $m/z$  value for the peak being used to calculate  $R$ , and  $\Delta m/z$  is the peak width at FWHM, and is usually provided by the instrument software. We analyzed the 28-base DNA strand at four different resolutions. An example calculation for the resolution for spectra C in Figure 3.5 is:

$$R = \frac{1720.63362}{0.276}$$

$$R = 6231$$

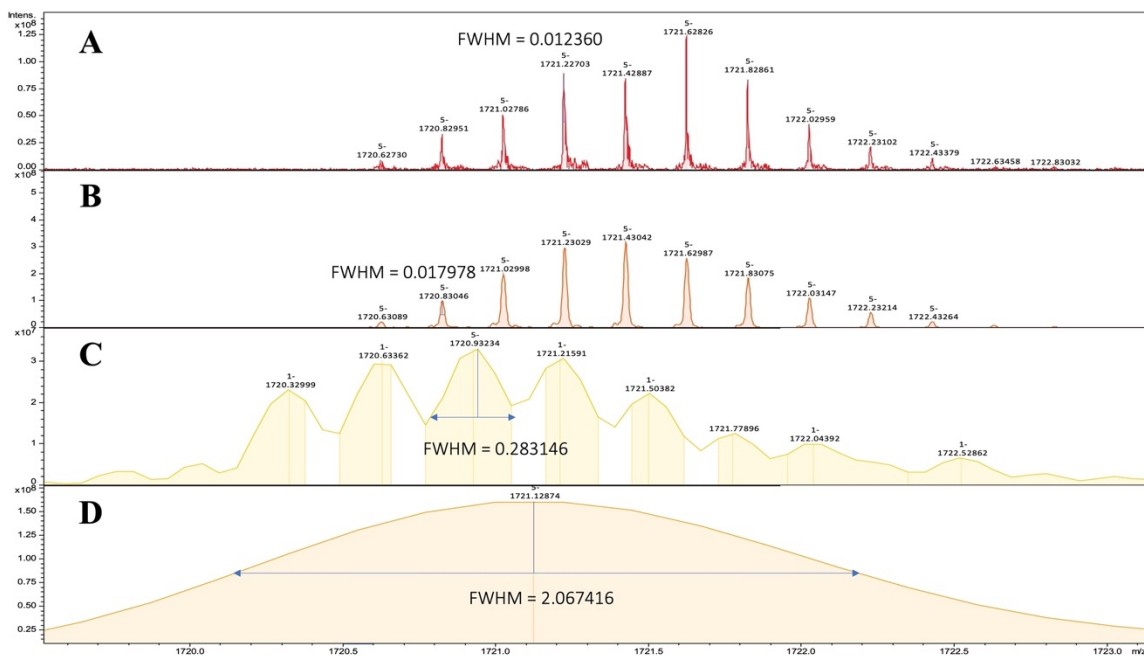


**Figure 3.5.** Analysis of 28-base DNA strand (monoisotopic mass = 8608.473216 Da) at four different resolutions,  $R_{FWHM(-5)} = 490,074$  (A); 119,427 (B); 7800 (C); and 701 (D). The number of data points per scan were: (A) 16M, (B) 4M, (C) 128K, and (D) 32K. Labelled peaks show their FWHM values. Resolutions are at nominal  $m/z$  1721.

Figure 3.5 directly showcases the influence that resolution has on resulting spectra. At too low of resolutions the isotopic distributions are not separated,



and the entire isotopic distribution can be contained by one peak, as is the case in spectra D where  $R = 811$  for the monoisotopic peak. In Figure 3.6, we can see the effect that resolution has on multiple peaks of the same charge.

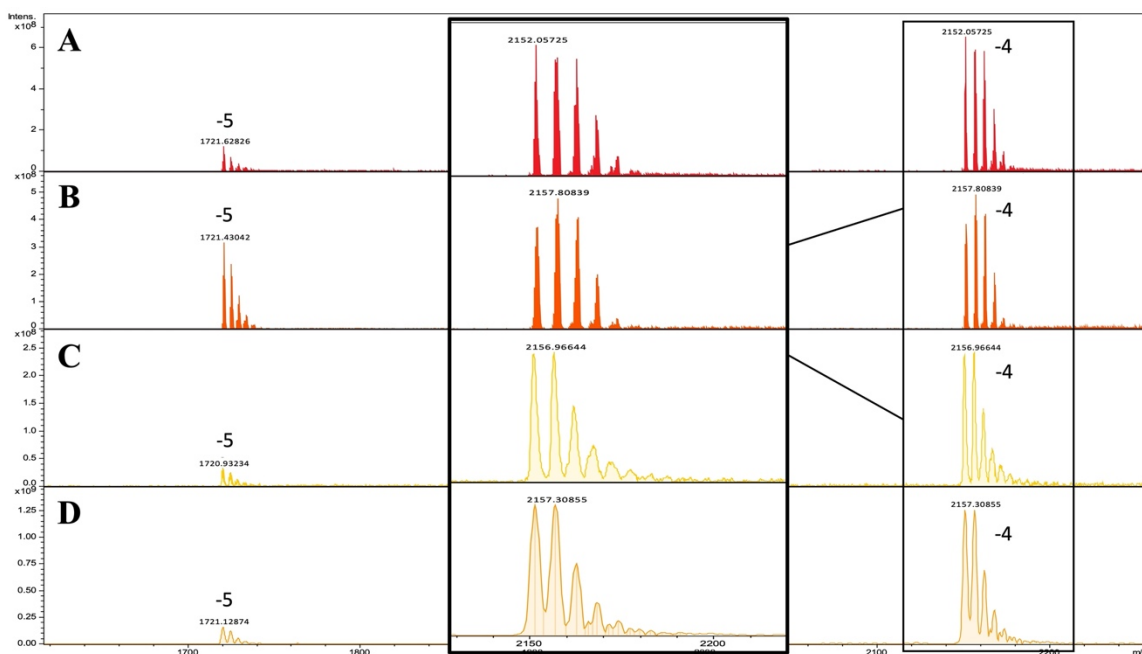


**Figure 3.6.** ESI mass spectrum of 28-mer oligo in four different resolutions, using 16M (A), 4M (B), 128K (C), and 32K (D) data points per scan. The average resolutions for these scan sizes at the -4 charge are:  $R_{FWHM(-4)} = 383, 103$  (A); 116960 (B); 1142 (C); and 873 (D). The spectra shown represents the -4 and -5 charge states of the 28-mer DNA strand. The solvent shown in these spectra is 50:50 water:acetonitrile + 20 mM imidazole + 10 mM ammonium acetate.

It is important to address resolution and its effect on the ability to perform meaningful analysis of oligonucleotides as different instruments are capable of various resolving powers. The purpose of resolution comparison was to assess the samples from the lowest to highest resolutions capable with the Bruker

Solarix FT-ICR MS and provide a general idea of spectral data that would be attained using another instrument with lower resolution capabilities, such as an Orbitrap instrument. Figure 3.6 depicts the range of resolving power capabilities of the FT-ICR MS instrument used in this research, where the lowest resolving power is attributed to 32K data points (resolution of approximately 800), with the highest being 16M (resolution of approximately 313,000). Even though there are clear differences in the resolution between the different resolving power values, the peaks are still conserved between the different values. In Figure 3.6, for the -4 charge there are five main peaks clusters identified. With analysis at the 32K resolving power, approximately six peaks are observed, although this lower resolution has only six peaks total. In the higher resolving power scans, we can see that the six peaks are each cluster that contain multiple peaks within. However, due to the lower resolution in 32K compared to 16M, those clusters are only detected as one broad peak.

As a general rule of thumb, the minimum resolution required to fully resolve the isotopic distribution of a molecule is equal to the mass of the ion<sup>136</sup>. For example, the nominal monoisotopic mass of the 28-base strand is 8608 Da and therefore the minimum resolution needed is 8600. The nominal resolutions for

the 32K, 128K, 4M and 16M scan sizes were found to be on average 701, 7800, 119428, and 490075, for the -5 charge states respectively. The resolutions were calculated automatically using software via the FWHM as explained above. These resolution values correspond to the minimum resolution needed to fully resolve the isotopic distribution of the 28-base oligo based on the observed data. In Figures 3.6 and 3.7, it can be seen that the isotopic pattern is not separated sufficiently until analysis in 4M, which corresponds to a resolution of 97,245. In spectra C of Figures 3.6 and 3.7, the sample was analyzed with a scan size of 128K, or a resolution of approximately 6145. As this value is below that of the mass of the molecule, there was not sufficient resolving power to effectively separate the ions. There is also evidence that there was insufficient resolving power at the scan size of 128K and lower because the resulting peaks are wider than the distribution observed at the more resolved spectra<sup>136</sup>.

Even though lower resolution was determined to be insufficient to fully resolve the isotopic patterns, it can be observed that these lower scan sizes do still detect the base peaks that are observed with higher scan sizes. The wider peak envelopes observed in the lower scan sizes would lead to a larger mass error, but if only lower scan sizes are available to a user, these still can provide intuitive

mass spectrometry analyses of oligonucleotides. The average mass for the 28-base oligonucleotide is 8612.674 Da, which corresponds to a  $m/z$  value at 1721.527524, as is shown in Figure 3.7.

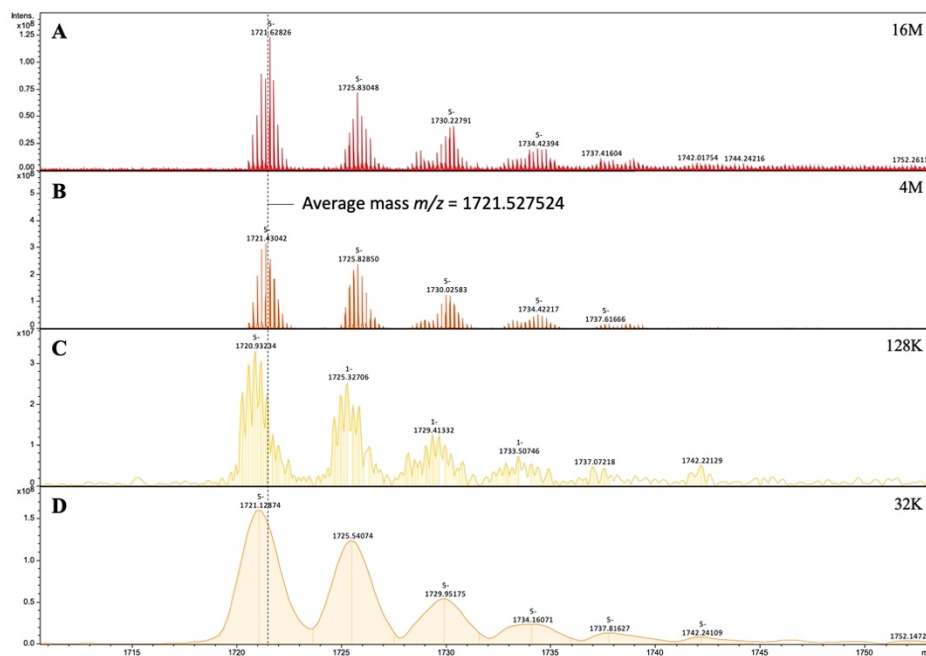


**Figure 3.7.** ESI mass spectrum of 28-mer oligo at four different data points per scan sizes: 16M (A), 4M (B), 128K (C), and 32K (D). Each spectrum represents four different resolutions:  $RFWHM(-5) = 490,074$  (A);  $119,427$  (B);  $7800$  (C); and  $701$  (D). Spectra show the -5 charge state of the 28-mer DNA strand in 50:50 water: acetonitrile + 20 mM imidazole + 10 mM ammonium acetate. Black dashed line represents the theoretical  $m/z$  of the average mass for the 28-base strand which is 8612.674 Da.

Clearly, lower resolution does have an effect on the mass accuracy of the analyte and peak distribution. At the lowest resolution analyzed, the peak envelope shifted to the left, or lower than, the average mass of the 28-base oligonucleotide. This is true for both the average mass (identified by the middle of the peak distribution) and the monoisotopic mass. However, as we increase

the resolution, the distribution shifts such that the base peaks come closer to the average mass of the sample, demonstrating that increased resolution also increases mass accuracy. Generally, the average mass can be in between two peaks, or close to the base peak but does not necessarily need to be represented by a detected peak<sup>136</sup>.

If information regarding the mass of the analyte is required, lower resolutions will only be able to give average mass values, as the monoisotopic peaks are not shown in the lower resolution scans, such as 32K data points. Because of these shifted distributions, it can lead to erroneous monoisotopic and average mass determinations, specifically mass determinations that are smaller than the actual mass. Having said this, even at the lower resolutions, the general distributions of the analyte are conserved, regardless of the isotopic distributions being lost. This indicates that lower resolving instruments can be used to infer general information about oligonucleotides but should be avoided for high mass accuracy analyses. The mass accuracies of the average masses are shown below in Table 3.5. It should be noted that the differences in Table 3.5 represent the difference between the theoretical  $m/z$  for the average mass at -5 charge state and the base peak.

**Table 3.5.** Comparison of theoretical  $m/z$  of average mass of 28-base oligonucleotide (average mass = 8612.674 Da) to observed  $m/z$  values of base peak for different data points per scan, or resolutions.

Theoretical Average mass $m/z$	Data Points per scan	Observed $m/z$ of base peak	$\Delta$ in $m/z$	Average mass accuracy (ppm)
1721.527524	16M	1721.628260	0.503680	58.515475
	4M	1721.430420	-0.485520	-56.405720
	128K	1720.932340	-2.975920	-345.730168
	32K	1721.128740	-1.993920	-231.645440

### 3.3.7 Applications of HRMS to Forensic Science

The benefits of HRMS outlined in this paper have direct application to forensic science. The ability of these instruments to sequence DNA strands shows promise for their use in the field yielding high mass accuracies that lead to confident sequence determinations. The low sample consumption is ideal for any DNA analyses, as it allows for multiple analyses on the samples due to a minimal quantity required for analysis with HRMS. The protocol discussed within this paper consumes only 180  $\mu\text{L}$  of sample per hour, where the scan time takes roughly twenty minutes to complete. Not only does HRMS allow for low sample consumption, but also relatively quick analyses. In addition to DNA analyses, HRMS can also be used for drug identification<sup>138,157-159</sup>, identification of explosives<sup>160</sup>, and any other application that exploits knowledge of a molecule's

mass. We believe that these techniques can benefit the field of forensic science in many subfields such as toxicology, chemistry, and biology.

### **3.4. Conclusions**

The purpose of this paper was to provide a resource for method development to fully utilize the potential of HRMS for the analysis of biological macromolecules. Specifically, we outline the method development process for oligonucleotide analysis and discuss calculating  $m/z$  values and charge distributions, choosing appropriate solvents, and optimizing instrument conditions, calculating mass accuracy and resolution, and interpretation of spectral results. The benefit of HRMS lies in its ability to accurately determine the mass of a molecule which can be helpful to identify base composition in oligonucleotides, as well as the structure of proteins. Based on our characterization, those conducting HRMS analyses of biomolecules such as oligonucleotides will be able to optimize and develop protocols that can provide both high resolution and high mass accuracy of oligonucleotides. Our characterization demonstrates that interconnecting of HRMS into informative markers such as DNA can be applied to forensic applications such as DNA

quality characterization, methylation, accurate mass determinations, low sample consumption and confirmation of DNA-binding for training purposes or protocol optimization. These assays are also cost-effective and have shorter analysis times, the latter being particularly important in reducing forensic backlogs. Further to this, the potential exists for HRMS to be applied to RNA, proteins assays and other macromolecules.

Ultimately, the potential uses for these instruments includes sequencing of and structure reconstruction of DNA and RNA strands, determination of protein structures and many other applications that rely on high mass accuracy. The optimization and introduction of such applications to forensic science will ultimately require collaboration between forensic scientists, chemists and biologists. This collaboration will be beneficial not only to the multidisciplinary nature of forensic science but will also help strengthen the field of forensic science by developing quantitative methods for analysis of biomolecules relevant to forensic science.

End of publication. The next sections are unpublished experimental results.



### 3.5 Using HRMS to Characterize ssDNA Binding

HRMS is a formidable technique for the high-accuracy analysis of ssDNA mass, as shown above. Using this concept, we wondered if it were possible to use FT-ICR MS to show the real-time binding of amine-terminated ssDNA within a hybrid inorganic-organic silicon solution-gelation (sol-gel) material. The aging process of the sol-gel material generates spherical colloidal particles, with an inorganic silica core and an outer surface decorated with organic epoxide rings (R-COC)<sup>49</sup>. The epoxides can undergo 'ring opening' in the presence of a variety of conditions but are mainly opened in the presence of primary amines (R'-NH<sub>2</sub>). This mechanism has been explored in the development of microarrays, where an epoxide-functionalized surface can immobilize ssDNA probes with a terminal NH<sub>2</sub> group<sup>161</sup>. We aimed to use a similar mechanism to immobilize amine-terminated ssDNA within the sol-gel to develop a DNA-containing material capable of performing as a sol-gel FBS with bound DNA<sup>49,50</sup>.

#### 3.5.1 Methods

##### 3.5.1.1 Chemicals

(3-Glycidyloxypropyl)trimethoxysilane (GPTMS) was purchased from Gelest Chemicals and tetraethylorthosilicate (TEOS) was purchased from Sigma

Aldrich. The sol-gel was made using both GPTMS and TEOS using a previously described protocol<sup>49</sup>. A 5' amine-terminated ssDNA (N-DNA) of 58 bases in length with a 3-carbon spacer on the 3' end was purchased from Integrated DNA Technologies (Toronto, ON). The DNA sequence was: 5'-GGCCTCCATTTCACAGAATTTCAAGATAGATAGATTAAAGGACACAGTCTGGGACAA-3'; three phosphorothioate bonds were also included on the 5' end (M = 18279.039772 Da). Estrone (Sigma Aldrich, Oakville, ON) was used as an internal standard for certain time studies.

#### *3.5.1.2 Time Studies*

To assess the interaction of the two matrices (sol-gel or GPTMS) with N-DNA, six sets of time studies were conducted, which explored N-DNA mixed with sol-gel (TS1, TS2) or GPTMS (TS3-TS6). The time studies are outlined below in Table 3.6.

**Table 3.6.** Outline of six time studies conducted with N-DNA and sol-gel or GPTMS. T0-T4 represents a "time zero" where the solutions were just made, and each number represents a replicate. \*No imidazole was present in the solvent.

Study	Solvent	Samples	Time points
TS1	Water + 20 mM imidazole	6 $\mu$ M DNA 6 $\mu$ M DNA + 0.05% sol-gel	T0 - T4; 1 hr; 2 hr; 4 hr; 8 hr; 24 hr
TS2	Water + 20 mM imidazole	6 $\mu$ M DNA 6 $\mu$ M DNA + 0.05% sol-gel	T0 - T1; 1 hr; 2 hr; 4 hr; 8 hr; 24 hr
TS3	Water + 20 mM imidazole	6 $\mu$ M DNA 6 $\mu$ M DNA + 50 ppm GPTMS* 6 $\mu$ M DNA + 50 ppm GPTMS 50 ppm GPTMS* 50 ppm GPTMS	0 hr; 1 hr; 2 hr; 4 hr; 8 hr; 24 hr
TS4	Water + 20 mM imidazole	6 $\mu$ M DNA 6 $\mu$ M DNA + 50 ppm GPTMS* 6 $\mu$ M DNA + 50 ppm GPTMS 50 ppm GPTMS* 50 ppm GPTMS	0 hr; 2 hr; 24 hr
TS5	50:50 ACN:Water + 20mM imidazole + 1 ppm estrone	6 $\mu$ M DNA 6 $\mu$ M DNA + 50 ppm GPTMS 50 ppm GPTMS	x3 replicates of each 1 hr; 8 hr; 24 hr; 48hr; TS6: + 72 hr, 7 days
TS6	50:50 ACN:acetic acid + 20mM imidazole + 1 ppm estrone	6 $\mu$ M DNA 6 $\mu$ M DNA + 50 ppm GPTMS 50 ppm GPTMS	x2 replicates of each 1 hr; 8 hr; 24 hr; 48hr; 72 hr, 7 days

The mixtures were analyzed with a solvent of either water and 20 mM imidazole (TS1-TS4), 50:50 volume ratio of water and ACN with 20 mM imidazole (TS5) or 50:50 volume ratio of ACN and acetic acid (0.05 M) (TS6) and acquired at 4M for a total of 75-100 scans, depending on the time study. The use of 50:50

water:ACN was chosen from our initial matrix optimization outlined above to promote ionization by using a more volatile solvent. For the sample preparation, a T-connector was used to merge a DNA-solution and either a sol-gel or GPTMS solution into the ESI source (Figure 3.8). First, the DNA solution was pumped into the ESI source (200  $\mu$ L/hr) with one end of the T-connector blocked until a DNA signal was observed on the FT-ICR MS. Next, the sol-gel/GPTMS solution was connected to the previously blocked end of the T-connector to merge with the flowing DNA solution at the same flow rate. This solution was pumped into the ESI source until sol-gel/GPTMS signal was observed. After sufficient time had elapsed, both pumps were stopped, and the capillary tubing, containing the merged solution, was removed and capped with parafilm, then stored in the fridge (4°C) for a designated time. Control samples of just DNA or GPTMS/sol-gel were prepared in a similar way. This was repeated for the total number of time points being analyzed. Once a certain time had elapsed, e.g., 4 hours, the capillary was removed from the fridge, connected to the ESI source and analyzed with the FT-ICR MS.

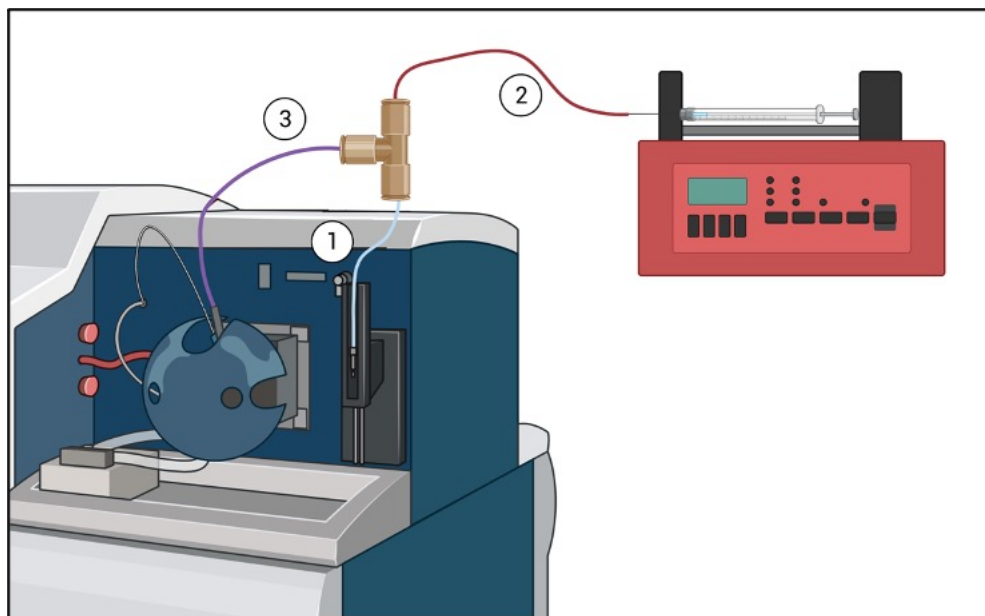


**Figure 3.8.** Set up for analysis of DNA and sol-gel/GPTMS binding with FT-ICR MS. The samples were fed through a T-connector pushing DNA sample (1) sol-gel or GPTMS (2) which was merged into the ESI source (3).<sup>f</sup>

### 3.5.1.3 Statistical Assessments

To compare the spectra, individual spectral files were made for each sample, time, and replicate. These files were composed of the monoisotopic mass and the corresponding intensities to account for both the  $m/z$  and the charge of the ions to compare detected masses in each spectrum. The spectral files were filtered by masses greater than 15,000 Da. The spectral files were formatted for

---

<sup>f</sup> Created with BioRender.com. Copyright permission is in Appendix I.

analysis with the MetaboAnalyst 5.0 software<sup>162,163</sup> and Partial Least Squares-Discriminant Analysis (PLS-DA) were performed.

### 3.5.2 Results & Discussion

The analysis of DNA and sol-gel using FT-ICR MS led to overall complex spectra, with an observed loss of some of the DNA-specific ions (Figure 3.9). The loss of DNA signal could suggest either suppression of the DNA signal from the sol-gel matrix or a change in mass from DNA binding to large colloidal particles. The complexity of the spectra further makes the identification of DNA-sol-gel binding difficult. This was because without an idea of the mass or charges of the colloids, predicting a DNA-colloid complex was problematic.

TS5 assessed 6  $\mu\text{M}$  amine-DNA, 6  $\mu\text{M}$  amine-DNA + 50 ppm GPTMS, and 50 ppm GPTMS. A key observation from this time study was the appearance of a “second set” of DNA-like peaks when the DNA was mixed with GPTMS. This can be seen in Figure 3.10 below in the purple spectra, and more closely on the right. The “second set” of peaks occurs close to the theoretical mass of a potential DNA-GPTMS coupling, but does not have the same  $m/z$  values as the theoretical monoisotopic mass (Figure 3.10). This second set of DNA features

was observed up to 48 hrs (TS5), but peaks attributed to single DNA molecules were also observed, indicating that there are still unbound DNA molecules even after 48 hours of reaction in the capillary tube.

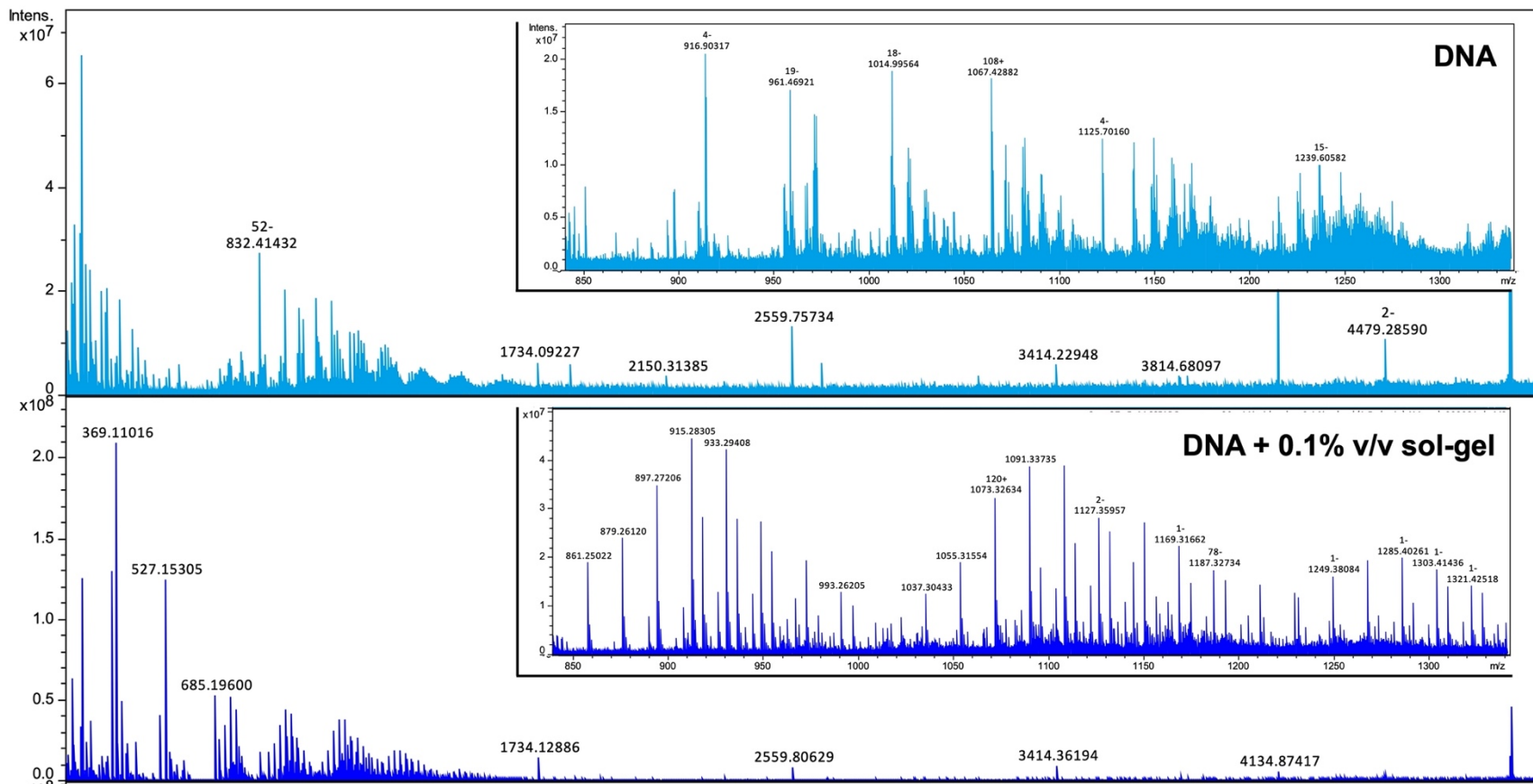
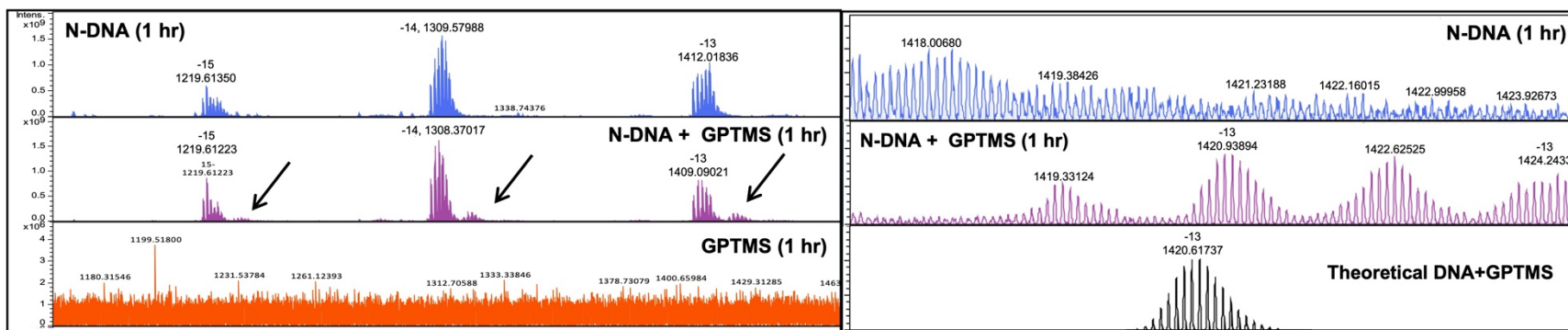


Figure 3.9. Spectra from time study after 1 hr of reaction of DNA and DNA + 0.1% v/v sol-gel analyzed in water + 20 mM imidazole. The inlet shows a smaller range of 850-1400 m/z.





**Figure 3.10.** Spectra from TS5 after 1 hr of reaction of DNA, DNA + GPTMS and GPTMS (left). Arrows indicate a "second set" of DNA-like signals. The spectra shown on the right are a close-up of the DNA and DNA + GPTMS of -13 charge ions compared to the theoretical mass of the DNA + GPTMS molecule.

The main issue with the time studies was that there was no direct  $m/z$  value that directly corresponded to the theoretical  $m/z$  value(s) of a GPTMS-bound DNA molecule, despite ions corresponding to the monoisotopic mass of DNA being identified. We attribute this to the multi-charge potential of the ionization process and a complex system of even ssDNA and GPTMS. The use of statistical assessments of the spectra over time could prove useful, although it is difficult to say whether any statistical differences observed between spectra would conclusively indicate binding. This is especially true given that there are clear differences in the spectra between DNA, DNA+GPTMS and GPTMS, which could be due to binding or changes in solvent properties and therefore the ionization process. To avoid this potential influence, we filtered for monoisotopic masses that were similar or larger than the mass of an unbound DNA molecule. For example, we conducted a PLS-DA which showed differentiation in both the DNA and DNA + sol-gel spectra (TS1, Figure 3.11) and the DNA, DNA + GPTMS and GPTMS spectra (TS5, Figure 3.12). TS6, which used the 50:50 ACN:acetic acid solvent could not be analyzed with PLS-DA since the ions where multiply-charged DNA species exist in the spectrum did not have identified charge states, which led to no observed masses over the cut-off of 15 000 Da.

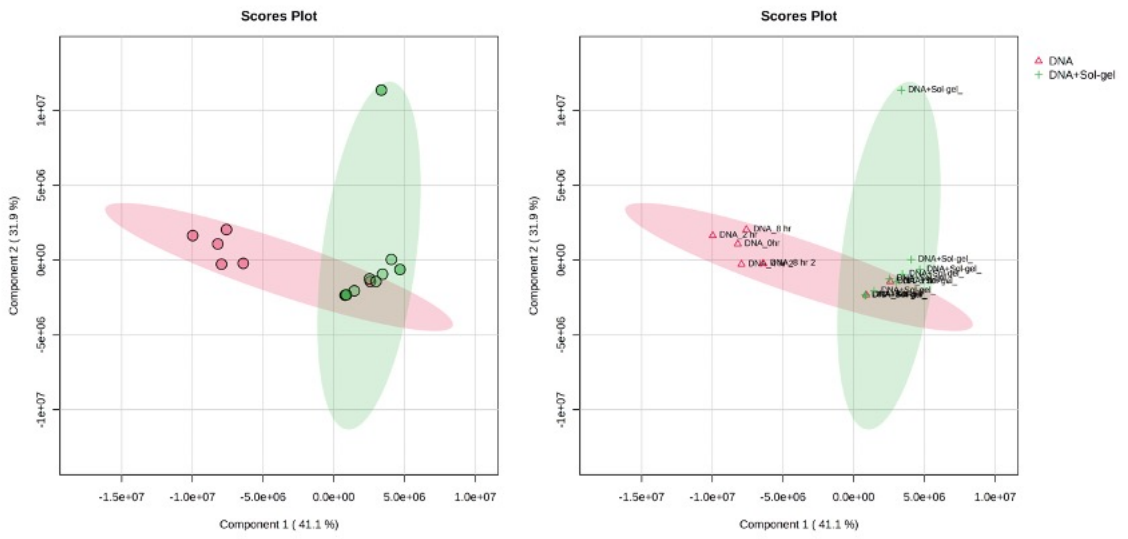


**Figure 3.11.** PLS-DA from TS2 of reaction between DNA and DNA + sol-gel. Image on the left shows the plots without sample names, and image on the right has sample name/time.

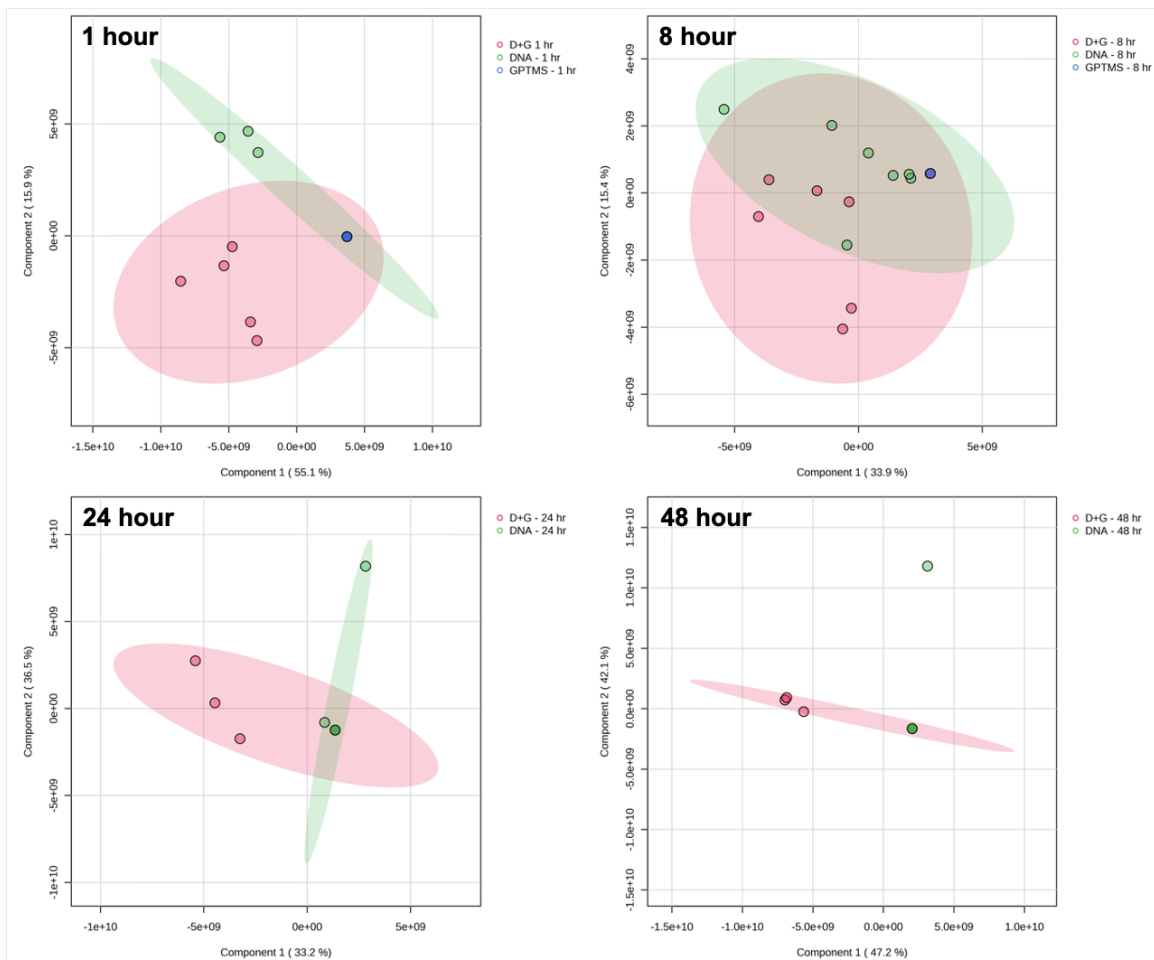


**Figure 3.12.** PLS-DA from TS5. Filtered for  $\geq 15,000$  Da. Thirteen GPTMS samples were not included due to no masses present over the cut-off (8 hour - replicates 1, 4, 6; 24 hour - replicates 1, 2, 3, 5, 6; 48 hour - replicates 1, 2, 3, 4, 6).

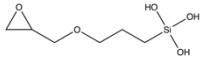
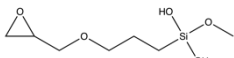
In both the time studies that investigated DNA and sol-gel reaction and DNA and GPTMS, the highest variable importance in projection (VIP) scores within the respective PLS-DAs were attributed to masses larger than the single DNA molecule - suggesting the differences are being caused by complexed molecules. For example, in the DNA + sol-gel experiment, the five highest VIPs were monoisotopic masses of 19168.96214, 19145.89498, 19138.94467,

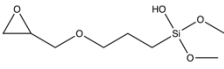
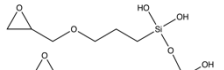
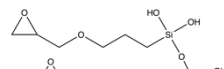
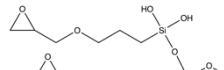
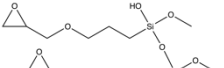


19277.01418, and 19235.05746 – although their relative concentrations were higher in the DNA only spectra. In the DNA + GPTMS study, however, the highest VIPs were masses of 18332.27754, 18331.26738, 18334.2689, 18351.20732, and 18330.26954, which were highest in the DNA+GPTMS spectra. The monoisotopic mass of the DNA molecule in this reaction is 18279.03977, where there is an approximate mass change of ~53 Da higher between the monoisotopic mass and the highly contributing peaks in the DNA+GPTMS spectra. The monoisotopic mass of a GPTMS monomer ranges depending on the hydrolysis, but for simplicity can range between 236.10800 to 194.06105 Da, representing a GPTMS molecule with 3 methoxy (R–O–CH<sub>3</sub>) groups to GPTMS with hydroxyl groups (R–OH), respectively. In fact, for a DNA and GPTMS complex, we would expect this mass to range between 18473.1008 to 18545.1947 Da, assuming only this range of hydrolysis of GPTMS. Theoretically, the DNA is in a charged state anywhere between -10 to -21 for our system; we assume the GPTMS molecule exists in a -1 state and does not exceed above a tetramer (see below). In the VIP scores, there are contributing masses which fit within the expected mass range of a DNA-GPTMS complex; these most often correspond to *m/z* values of the extra set of peaks being observed (Figure 3.10). Again, while this suggests that GPTMS-related mass

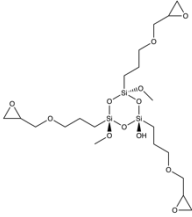
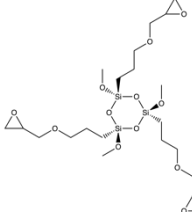
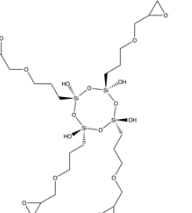
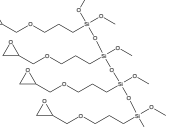
adducts are occurring with the DNA, we cannot be certain that we are observing binding exclusively.

Beyond DNA binding, a valuable finding from the time studies was the identification of various ions attributed to GPTMS hydrolysis and polymerization (Table 3.7). We observed similar structures to other works<sup>164,165</sup> in the GPTMS aging. Interestingly, there were monomers of GPTMS still observed after 7 days. This could be due to the surface area restrictions within the capillary tubing. The large number of GPTMS conformations further explains the difficulty in identifying a single DNA-GPTMS complex, where this complex could be a combination of any DNA or GPTMS confirmation at various charge states.

**Table 3.7.** GPTMS molecule identification during a 7-day time study. The tentative structure and *m/z* of monoisotopic mass are shown (left side) and the corresponding *m/z* values for each sample (right). Only three decimal places are shown for the *m/z* values. Designations are low signal (L), high signal (Y), and non-confirmed (NC) - which are designations that have differences beyond 0.01 *m/z*.

GPTMS Structure ( <i>m/z</i> of monoisotopic mass)	Time Elapsed in Reaction					
	0 hr	8 hr	24 hr	48 hr	72 hr	7 days
 193.054	<b>GPTMS</b>					
	L	L	L	Y	Y	Y
	193.05375	193.054	193.054	193.054	193.054	193.054
	<b>DNA + GPTMS</b>					
		L	Y	Y	Y	Y
		193.054	193.054	193.054	193.054	193.054
 207.069	<b>GPTMS</b>					
	L	L	L	L	L	L
	207.06945	207.069	207.06937	207.069	207.069	207.069
	<b>DNA + GPTMS</b>					
	NC-L	L	L	L	L	
	207.070	207.069	207.069	207.069	207.069	

<b>GPTMS</b>						
 221.085	Y	L				
	221.085	221.085				
<b>DNA + GPTMS</b>						
	Y	Y	Y	L	Y	
	221.085	221.085	221.085	221.085	221.085	
<b>GPTMS</b>						
 369.104	Y	Y	Y	Y	Y	Y
	369.104	369.104	369.104	369.104	369.104	369.104
<b>DNA + GPTMS</b>						
	L	Y	Y	Y	Y	Y
	369.104	369.105	369.104	369.104	369.104	369.104
<b>GPTMS</b>						
 383.120	L	L	NC-L	NC-L	NC-L	NC-L
	383.120	383.120	383.11214	383.11212	383.119	383.119
<b>DNA + GPTMS</b>						
		L	Y	Y	NC-L	NC-L
		383.120	383.120	383.120	383.11244	383.11993
<b>GPTMS</b>						
 397.13583	L	L				
	397.13583	397.135				
<b>DNA + GPTMS</b>						
		Y	Y	Y	L	
		397.136	397.136	397.136	397.136	
<b>GPTMS</b>						
 411.151						
<b>DNA + GPTMS</b>						
		L	L			
		411.151	411.151			
<b>GPTMS</b>						
 527.144	Y	Y	Y	Y	Y	Y
	527.144	527.144	527.144	527.144	527.144	527.144
<b>DNA + GPTMS</b>						
	Y	Y	Y	Y	Y	Y
	527.144	527.145	527.144	527.144	527.145	527.145
<b>GPTMS</b>						
 541.160				L		
				541.160		
<b>DNA + GPTMS</b>						
		L	L			
		541.160	541.160			
<b>GPTMS</b>						

 555.175		NC-L 555.137	NC-L 555.137		NC-L 555.137	
	<b>DNA + GPTMS</b>					
			NC-L 555.092	NC-L 555.092	NC-L 555.092	NC-L 555.092
 569.191	<b>GPTMS</b>					
			NC 569.155	NC 569.155	NC 569.155	
	<b>DNA + GPTMS</b>					
		NC-L 569.155	NC-L 569.156	NC-L 569.155		
 703.195	<b>GPTMS</b>					
	Y 703.19492	Y 703.195	Y 703.194	Y 703.194	Y 703.195	Y 703.195
	<b>DNA + GPTMS</b>					
Y 703.195	L 703.195	Y 703.195	Y 703.195	Y 703.195	Y 703.195	
 805.303	<b>GPTMS</b>					
			NC 805.366	NC 805.366		
	<b>DNA + GPTMS</b>					
		NC-L 805.367	NC-L 805.367	NC-L 805.367	NC-L 805.367	

### 3.5.3 Conclusions

The time studies were conducted to follow up on the high potential of HRMS for the analysis of DNA molecules. It was reasoned that using FT-ICR MS we could observe DNA binding in the sol-gel matrix. The sol-gel was complex, and the attribution of designated peaks was difficult due to the uncertainty in potential masses. The analysis with DNA and GPTMS reactions observed a “second set” of DNA morphology peaks that indicate larger DNA structures than a single



DNA molecule of the same charge state. However, we were unable to observe a monoisotopic mass value corresponding to a DNA-GPTMS complex exclusively. We also observed the self-polymerization of GPTMS over time, complexes of up to four GPTMS-containing molecules were observed in our solvent system.

The overall complex nature of the sol-gel, in addition to its other caveats justifies the exploration of a more favourable environment for DNA binding that could be better characterized and controlled. Our work with alginate and CATGs supports the use of hydrogel-based polymers as a favourable environment for DNA functionality and its modification potential provides promising avenues for forensic blood simulant development and soft tissue design.

# Chapter 4

DNA crosslinked alginate hydrogels: Characterization, microparticle development and applications in forensic science<sup>9</sup>.

## Preface

Type: Original Research Article  
Submitted to: ACS Applied Polymer Materials  
Status: Published

Title: DNA crosslinked alginate hydrogels: Characterization, microparticle development and applications in forensic science.

Authors: Amanda Orr<sup>a</sup>, Paul Wilson<sup>b</sup>, Theresa Stotesbury<sup>c</sup>

<sup>a</sup> Environmental and Life Sciences PhD Program, Trent University, Peterborough, Ontario, Canada, 1600 West Bank Drive, K9L 0G2

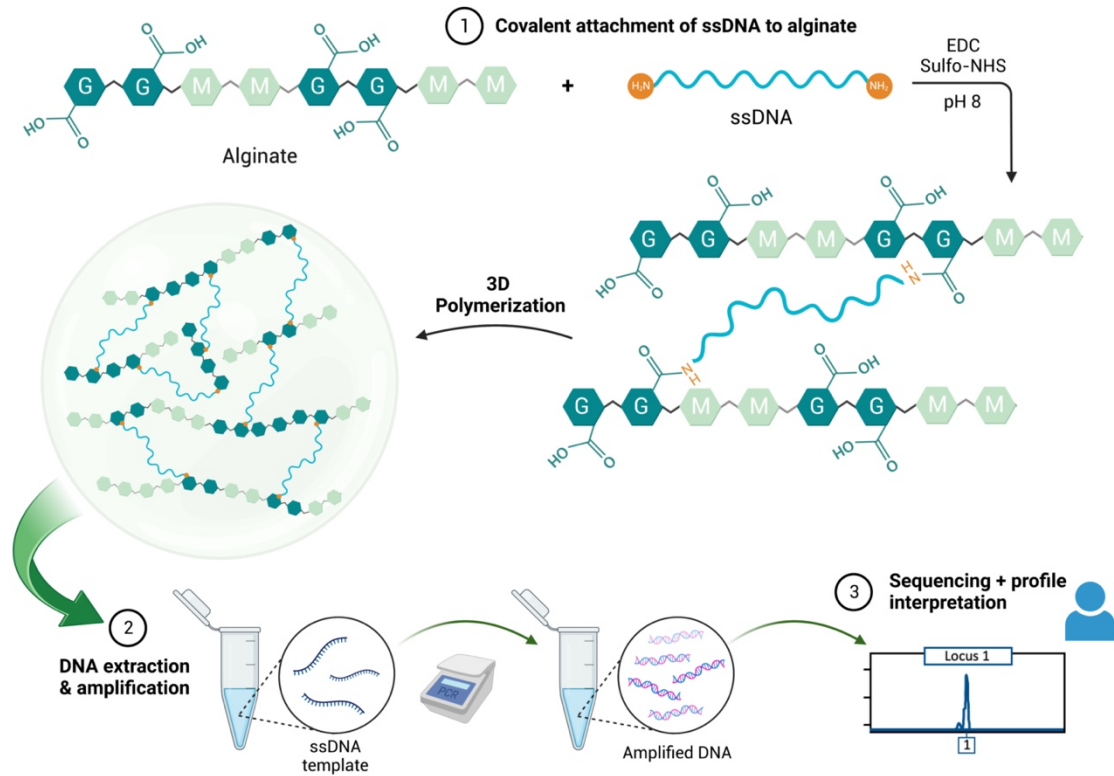
<sup>b</sup> Biology Department, Trent University, Peterborough, Ontario, Canada, 1600 West Bank Drive, K9L 0G2

<sup>c</sup> Faculty of Science, Forensic Science, Ontario Tech University, 2000 Simcoe Street North, Oshawa, ON, L1G 0C5

---

<sup>9</sup> Reprinted (adapted) with permission from A. Orr, P. Wilson, T. Stotesbury. ACS Applied Polymer Materials. 2023. 5(1):583-592. DOI: 10.1021/acsapm.2c01673 Copyright 2023 American Chemical Society.

## Graphical Abstract<sup>h</sup>



## Keywords

Forensic biomaterials; covalent crosslinking; tissue simulant; carbodiimide chemistry; chemical hydrogel; standard reference material; functional DNA.

<sup>h</sup> Created with BioRender.com. Copyright permission is in Appendix I.

## **Abstract**

Alginate-based hydrogels provide many advantages in the design of functional tissue mimetics given their low toxicity and mechanical similarities to native tissue types. However, deoxyribonucleic acid (DNA)-crosslinked alginate hydrogels are often not explored despite the added functional capabilities of DNA inclusion into the hydrogel. We have previously demonstrated the potential of DNA-encapsulated ionic alginate hydrogels to serve as human genetic training standards for forensic biology research and training. In this work, we present further development of these materials through covalent attachment of the DNA to alginate for targeted forensic applications. These crosslinked materials not only promote a more stable 3D polymeric network, but also achieve localization of the functional ssDNA - which is particularly desirable for the development of human white blood cell (WBC) mimetics for forensic science. Herein, we investigated the covalent attachment of dual amine terminated ssDNA (N-DNA-N) to alginate of three different concentrations and various amine functionalities (none, one terminal amine and two terminal amines). Fourier transform infrared spectroscopy analysis confirmed the formation of amide bonds, indicative of successful crosslinking between the N-DNA-N and alginate. Rheological characterization showed that each DNA-

crosslinked material forms similar structures, but the higher DNA concentration behaved like a dynamic viscoelastic material. Scanning electron microscopy visualization indicated that each material had distinct topographies, where the covalent crosslinked alginate-DNA materials had more ordered particles and networked structures. It was revealed that the covalent crosslinking occurs primarily from the terminal amines on the DNA strands, further suggesting the formation of a 3D network. From here, microparticles (MPs) using the dual amine DNA-crosslinked materials were developed, and the particle morphology, sizes, and DNA functionality were assessed. It was determined that MPs made using DNA-crosslinked materials had larger particle diameters compared to the non-DNA controls and these MPs could be successfully processed in a relevant forensic scenario through extraction, amplification, and genotyping. The functionality of the DNA-crosslinked MPs demonstrates their feasibility for use as WBC mimetics that can be used as a standalone material and/or integrated into a forensic blood simulant containing genetic components.

## 4.1 Introduction

Alginate-based hydrogels have continually been developed in the areas of bioengineering, biomedicine, and the food industry owing to the many benefits of alginate such as biodegradability, printability, and low toxicity<sup>56,64,77,166,167</sup>. Alginate is a desirable polymer for these applications not only due to its biocompatibility and mechanical similarities to the extracellular matrix (ECM)<sup>61</sup>, but also due to its versatile crosslinking potential. Covalent crosslinking of alginate can be used to design chemically modified hydrogels (chemical gels) with targeted functions, mechanical, and/or chemical capabilities. Alginate is composed of repeating blocks of  $\beta$ -D-mannuronate (M) and  $\alpha$ -L-guluronate (G), each containing carboxyl (COOH) functional groups. The COOH moieties are one of the main sources of covalent crosslinking of alginate<sup>168</sup>, where typical crosslinking can be achieved through incorporation of photoionizable groups<sup>169-171</sup>, click chemistry<sup>172</sup>, carbodiimide chemistry<sup>62,173</sup>, or through esterification reactions with alcohol- or alkyl halide-functionalized groups<sup>59</sup>. Other types of crosslinking include ionic and pH-induced crosslinking, but are often not used in biomaterial development due to properties such as gel instability and lack of stiffness when compared to covalently crosslinked materials<sup>73,94</sup>. Recent work has even demonstrated the potential of hydrogels to

be developed without the use of traditional crosslinkers, where hydrogel polymerization is controlled via physical forces such as hydrogen bonding and electrostatic interactions while retaining similar properties to crosslinked hydrogels<sup>174</sup>.

Hydrogels can incorporate a variety of crosslinkers including deoxyribonucleic acid (DNA). DNA-based hydrogels are an emerging and attractive option for polymer materials primarily due to the predictable and base-specific binding of DNA<sup>175</sup>. Furthermore, DNA integration into hydrogels procures additional benefits such as controlled biodegradation, spatial control, and stimuli-responsive behaviour<sup>175,176</sup>. DNA-containing hydrogels are extremely versatile and programmable materials that make these hydrogels useful in host recognition or controlled transfection of DNA<sup>94</sup>, biosensing<sup>177</sup>, and drug delivery applications<sup>176,178</sup>. Commonly, these materials incorporate aptamers in the hydrogel matrix; which are short single stranded ligands with high specificity for a given target molecule(s)<sup>179</sup>. The aptamers can be used as either single stranded crosslinkers, or can be hybridized with its complementary strand to form crosslinked hydrogels<sup>175,179</sup>. Most often, the aptamers are constructed through functionalization or decoration of polymers<sup>180</sup> that primarily provide

functional properties within a hydrogel<sup>176</sup>. However, the DNA can be included for both mechanical and functional purposes, where the three-dimensional (3D) crosslinked networks are formed through hybridization of two complementary immobilized single stranded DNA (ssDNA). Beyond aptamer-based DNA hydrogels, various forms of DNA can be integrated into the polymer network, including X- or Y-DNA/nanostars, i-Motifs, DNAzymes, and Guanine (G)-quadruplexes using a variety of modification strategies<sup>105,176,181</sup>. For example, using X- and Y-shaped DNA, hydrogels can be easily tuned to possess properties such as self-healing<sup>182</sup>, controlled stiffness and degradation<sup>183</sup>, all while produced under physiological and non-toxic conditions. G-quadruplexes and i-motifs can be used to achieve hydrogels with photo-responsiveness and shape-memory functionalities<sup>184,185</sup>, and DNAzymes can be effective in the colorimetric detection of hydrogen peroxide (H<sub>2</sub>O<sub>2</sub>) down to 1.0 μm<sup>186</sup>.

While DNA-crosslinked hydrogels have been investigated previously, the included sequence was usually some form of an aptamer, and materials typically use other polymer bases such as polyacrylamide<sup>175,177,187,188</sup>, polyethylene glycol<sup>175,189</sup>, or even DNA itself<sup>190,191</sup>, but infrequently alginate. Of the few examples of alginate-DNA crosslinked hydrogels in the literature, these



materials typically bind the DNA from one end of a short aptamer sequence to alginate<sup>192-194</sup>, or crosslink the hydrogel through imine linkages formed between DNA and oxidized alginate<sup>178</sup>. The work described herein presents a DNA-alginate hydrogel structure not previously investigated, where a single long ssDNA of approximately 100 bases is crosslinked in an alginate system by both ends. In addition, we discuss novel applications of DNA-based hydrogels in the niche field of forensic science. Relating to forensic science, few DNA-based hydrogels have been discussed for the detection of analytes such as drugs and metabolites, identification of biological evidence<sup>195</sup>, and imaging of latent fingerprints<sup>196</sup>, although none use alginate. Beyond these applications, and the focus of this research, is the development of functional tissue mimetics or standard reference materials with controlled hydrogel properties. These materials can assist in training and understanding the complex degradation mechanisms experienced by biological tissues in crime scene scenarios.

The present work focused on the 3D crosslinking of alginate and functional dual amine terminated ssDNA, which has not been reported previously. Alginate is not only desirable for many of the reasons explained above, but its soft material characteristics makes it favourable in the design of functional tissue mimetics

with genetic components. The purpose of this research was to characterize the covalent crosslinking between alginate and dual amine ssDNA to expand on our previous research with ionically crosslinked DNA-encapsulated alginate hydrogels (CATGs)<sup>197</sup>. Here, we explore covalent crosslinking with DNA strands of similar size (98 bases); where the dual amine-terminated 98-base ssDNA was covalently crosslinked to alginate using carbodiimide chemistry. These covalently crosslinked alginate-DNA hydrogels are desirable to localize DNA binding in the alginate and develop more stable hydrogels, which have significant forensic applications. In particular, we investigated the ability of the DNA-crosslinked materials to be used in microparticle (MP) formation and assess their use as white blood cell (WBC) mimetics.

## **4.2. Experimental Section**

### 4.2.1 Materials

1% w/v alginate (low viscosity, Sigma, Oakville, ON) was dissolved in 2-(N-morpholino)ethanesulfonic acid (MES) buffer (0.05 M, pH 6.0) and allowed to mix overnight at room temperature ( $22^{\circ}\text{C} \pm 2^{\circ}\text{C}$ ). 1-ethyl-3-(3-dimethylaminopropyl) carbodiimide•HCl (EDC, BioShop, Burlington, ON) and

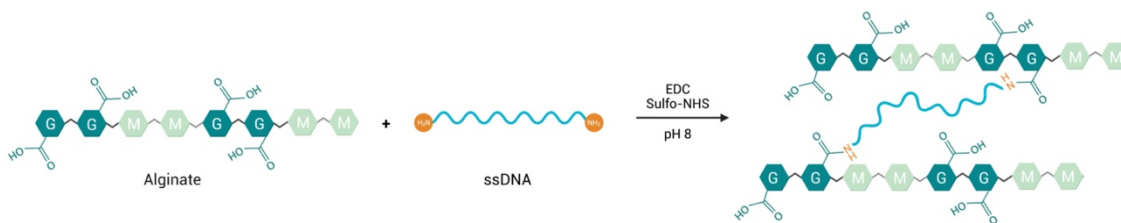
*N*-Hydroxysulfosuccinimide (Sulfo-NHS, ThermoFisher, Mississauga, ON) were used as received. The ssDNA crosslinker was purchased from Integrated DNA Technologies (Toronto, ON) and reconstituted in UltraPure™ water to create a 100 µM stock solution. The crosslinker was a 98-base ssDNA<sup>197</sup> with primary amine groups (NH<sub>2</sub> - R) on both the 5' and 3' ends (N-DNA-N). Various amine modified ssDNA were also investigated, including: i) primary amines on both the 5' and 3' ends - "N-DNA-N" (AXD2N), ii) primary amine on the 5' end - "N-DNA" (AXD1N) and iii) no terminal amines - "DNA" (AXD0N) (Table 4.1).

#### 4.2.2 Crosslinking Scheme

Each crosslinking reaction had a total volume of 5 mL. First, 1% w/v alginate (MES) was added to individual vials on a stir plate, and EDC (261 µmol) and Sulfo-NHS (65 µmol) were added and allowed to react for 20 minutes at room temperature (22°C ± 2°C). 100 µL of NaOH (1 M) was added to raise the pH to 8 before the addition of the ssDNA (N-DNA-N, N-DNA or DNA). Various concentrations of the DNA crosslinker were added (0.01, 0.025 and 0.05 µmol = 0.02, 0.05 and 0.1 µmol amines, respectively) to assess the effects of crosslinking on the materials. The general reaction scheme is shown below (Scheme 1). The samples were allowed to react for 24 hours and EDC/Sulfo-NHS

removal was completed using Amicon Ultra 30K MWCO filtration units. Three filtration/wash steps were performed: i) filtration step (1000 x g, 30 minutes), ii) wash step 1 (1000 x g, 15 minutes), and iii) wash step 2 (1000 x g, 15 minutes). 1 mL of MilliQ® water was added to each sample before each of the wash steps. In total, nine materials were formed: seven different materials with the carbodiimide crosslinkers present, as well as two controls without crosslinkers (Table 4.1).

**Scheme 4.1.** Covalent attachment of dual amine-terminated ssDNA to alginate polymer.<sup>i</sup>



<sup>i</sup> Created with BioRender.com. Copyright permission is in Appendix I.

**Table 4.1.** Outline of crosslinking reactions. The presence of "X" indicates that the covalent crosslinkers EDC and Sulfo-NHS were added to reaction, whereas "P" indicates the DNA was mixed with alginate without EDC/Sulfo-NHS. Identification in square brackets represents the classification with the addition of Ca<sup>2+</sup>.

Main Crosslinking [+ Ca <sup>2+</sup> ]	Material	EDC ( $\mu\text{mol}$ )	Sulfo-NHS ( $\mu\text{mol}$ )	ssDNA Structure	ssDNA	
					Concentration (nmol)	pH
<b>Covalent [Dual]</b>	AX <sub>0</sub>	261	65	--	--	
	AXD10	261	65	N-DNA-N	10	8
	AXD25	261	65	N-DNA-N	25	
	AXD50	261	65	N-DNA-N	50	
	AXD0N	261	65	DNA	50	
	AXD1N	261	65	N-DNA	50	8
	AXD2N	261	65	N-DNA-N	50	
<b>Non-Covalent [Ionic]</b>	A <sub>0</sub>	--	--		--	8
	APD50	--	--		50	

## 4.2.3 Materials Characterization

### 4.2.3.1 Rheology

For the rheological characterization, samples were made to be dual crosslinked (4:1 volume ratio alginate:calcium (50 mM CaCl<sub>2</sub>); where "alginate" in this case refers to the final material - or "material" - from Table 4.1). Rheological assessments were conducted using a Discovery HR20 stress-controlled rheometer with an advanced Peltier plate and a solvent trap system (TA Instruments). All rheological tests were conducted at 22°C using a 40 mm parallel plate geometry with Millipore water in the solvent trap and a 500  $\mu\text{m}$

gap. Oscillation amplitude sweeps and frequency sweeps were performed between strains of 0.01-150% and frequencies of 0.05-200 rad/s, respectively. The frequency sweeps were conducted at a strain of 2%.

#### *4.2.3.2 Fourier Transform Infrared Spectroscopy*

Fourier transform infrared (FTIR) spectroscopy and scanning electron microscopy (SEM) analyses were performed using both the DNA crosslinked materials and controls, both with and without the addition of  $\text{Ca}^{2+}$ . For the FTIR characterization, 1 mL disposable transfer pipettes were used to place three drops of each material into individual Petri dishes where they were allowed to dry. The dried films were placed directly on the FTIR crystal for analysis. FTIR measurements were conducted using a Thermo Fisher Nicolet 380 FTIR spectrometer in absorbance mode (ATR) between wavenumbers of 4000-500  $\text{cm}^{-1}$  with a total of 32 scans.

#### *4.2.3.3 Scanning Electron Microscopy*

SEM analyses were used for morphological characterization of the materials, using a Hitachi's FlexSEM 1000 Scanning Electron Microscope. The materials were allowed to air dry on stainless steel stubs, and analyzed at 5 kV. Images

were magnified at 500 (100  $\mu\text{m}$  scale), 1K (50  $\mu\text{m}$  scale), and 2K (20  $\mu\text{m}$  scale) SE, and certain images were analyzed at 4K SE (10  $\mu\text{m}$  scale).

#### 4.2.3.4 Thermogravimetric Analysis

Thermogravimetric analysis (TGA) was used for materials characterization of the different amine variation ssDNA materials, where only dual crosslinked materials were investigated. For this, a TA Instrument SDT Q600 thermal analyzer was used. The dual crosslinked materials were freeze-dried for 24 hours prior to TGA, and the freeze-dried materials (8 - 12 mg) were analyzed between 25°C to 800°C, with a heating rate of 10°C/min, and under Argon gas (50 mL/min).

#### 4.2.4 Electrospray Ionization Optimization & Microparticle Generation

Before microparticle (MP) development with the crosslinked materials, an optimization experiment was first conducted using alginate dissolved in water, Alg(H<sub>2</sub>O), to understand the effects of concentration, voltage (V), spraying distance ( $d$ ), and flow rate ( $Q$ ) on MP formation. For the purposes of this research, the optimized conditions were found to be: 2.5% w/v alginate + 0.5% v/v Tween 20 at a flow rate of 2  $\mu\text{L}/\text{min}$ , with 10 kV applied to the needle tip that was 4 cm from the CaCl<sub>2</sub> collection bath (7.35 wt/v%). Following the

optimization, MPs were created using the 2.5% w/v alginate dissolved in MES buffer, Alg(MES), a crosslinking control (AX<sub>0</sub>) and two DNA crosslinked materials - a low concentration of DNA (AXD10) and a high concentration (AXD50). Each crosslinked material was made using the same conditions as described in Section 4.2.2, with the exception that 2.5% w/v alginate was used instead of 1% w/v. The DNA used in the crosslinking reactions was the dual amine terminated 98-base strand (N-DNA-N).

The electrosprayed MPs were washed three times with MilliQ<sup>®</sup> water before visualizing on an EVOS FL Auto microscope (Life Technologies) under 20x and 40x magnification in the brightfield mode. Once imaged, the images were imported into Fiji (Image J, 2.3.0/1.53q), scaled, and the particle diameters were manually measured using the "Measure" tool. RStudio (2022.07.1) was used to statistically compare the respective particle diameters using a student's t-test, and generate the particle size distributions.

#### 4.2.5 DNA Extraction and Amplification of the MPs

Finally, the washed MPs underwent an extraction and amplification process, similar to a method used in our previous work with CATGs<sup>197</sup>. Specifically, the



MP solutions were first inverted to ensure homogenous distribution of MPs, and 100  $\mu\text{L}$  was added to 450  $\mu\text{L}$  of gel dissolving buffer (Monarch<sup>®</sup> DNA Gel Extraction Kit, New England Biolabs). The MPs were incubated at 52°C and 500 rpm for 20 minutes (Eppendorf ThermoMixer F1.5), and the manufacturer's protocol was followed as suggested hereafter. The DNA was eluted with 20  $\mu\text{L}$  of Invitrogen<sup>™</sup> UltraPure water (ThermoFisher Scientific). 2  $\mu\text{L}$  of the extracted DNA was added to a 10  $\mu\text{L}$  PCR reaction (95°C for 10 minutes; 94°C for 30 seconds; 53°C for 1 minute; 72°C for 1 min; repeated for a total of 30 times with a final step of 65°C for 15 minutes). A 1:50 dilution of the amplified product was genotyped using an ABI 3730 DNA Analyzer with a GeneScan 500 ROX size standard.

### **4.3. Results and Discussion**

#### 4.3.1 Rheology

The rheological analyses show that overall, the ionically crosslinked samples have much higher storage ( $G'$ ) and loss ( $G''$ ) moduli compared to the dual crosslinked counterparts (Figure 4.1). This is unlike other studies with dual crosslinking<sup>169,171,198</sup>; however, there are two likely explanations for the lower

moduli values in the dual crosslinked samples. First, the egg box model of  $\text{Ca}^{2+}$ -Alg hydrogels leads to tighter junctions, and therefore stiffer gels compared to the hydrogels crosslinked with elastic and larger ssDNA. Furthermore, if alginate is bound to either N-DNA-N, or in the case of the Ca-AX<sub>0</sub>, likely bound to Sulfo-NHS (see Section 4.3.2), there are fewer available  $\text{COO}^-$  groups to participate in  $\text{Ca}^{2+}$  coordination, leading to softer materials. Additionally, the DNA used in this research is typically larger than the length of DNA incorporated into other hydrogels through 3D crosslinking or functionalization. For example, aptamers can typically range between 20 and 60 nucleotides<sup>199</sup>, but in a majority of work that includes functionalized ssDNA, the DNA sizes are less than 40 nucleotides. Furthermore, the attachment of ssDNA is usually bound by a single end, where the 3D hydrogel formation is achieved through either hybridization of complementary sequences of bound strands<sup>192</sup> or through hybridization of another unbound complementary strand<sup>200</sup>. Using similar attachment strategies to the one used in our research (ssDNA immobilized by both the 5' and 3' ends), Murakami *et al.*<sup>177</sup> used 29-base amine-terminated ssDNA to investigate the ability of the DNA-crosslinked hydrogel to shrink or swell when bound to complementary strands, but did not investigate the rheological profile of these materials. Pan *et al.*<sup>201</sup> investigated the effect of rigid and flexible DNA strands

on the hydrogel rheology and found that flexible chains can lead to better stability and stretchability, although Jiang and coauthors have shown that longer DNA strands can lead to softer gels<sup>202</sup>. In our hydrogels, we observed the latter, where the long ssDNA incorporated into our hydrogels leads to very flexible, and soft gel characteristics. Because of this, we do not see linear trends in our moduli values, where the  $G'$  should be much larger than  $G''$  as the DNA concentration (and theoretically number of crosslinks) is increased.

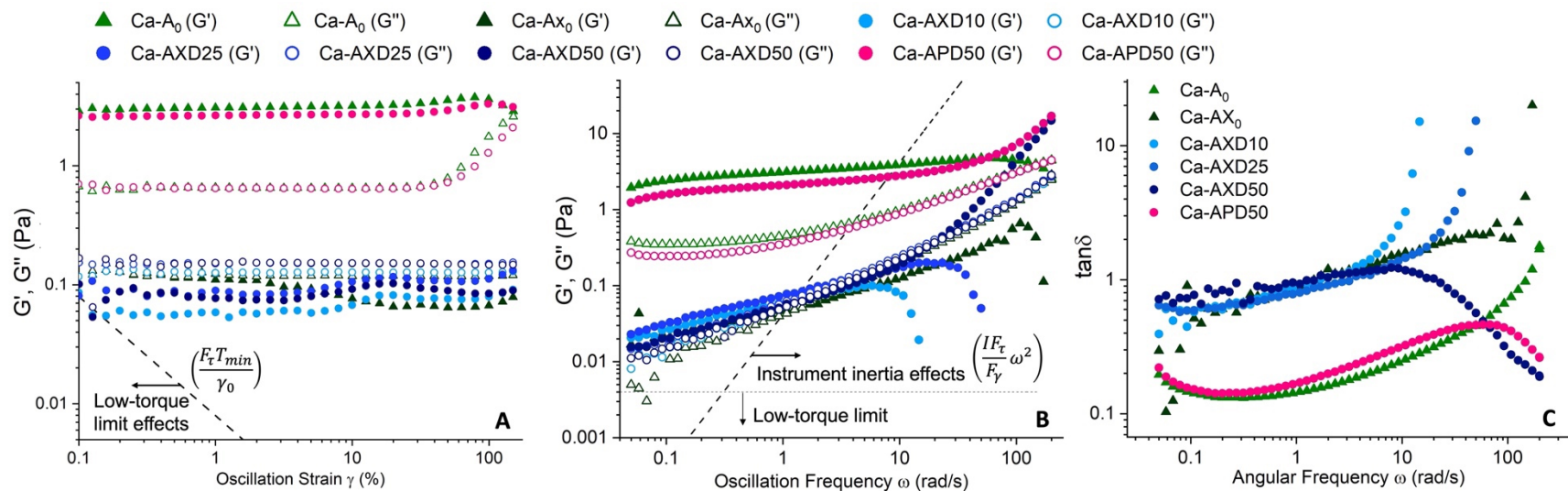


**Figure 4.1.** Amplitude sweeps (A), frequency sweeps (B) and  $\tan \delta$  (C) for 6 different ionic and dual crosslinked materials. The filled in symbols represent the Storage Modulus ( $G'$ ) and the corresponding non-filled symbols are the Loss Modulus ( $G''$ ) for a given sample. Overlaid lines represent potential inertial limits based on low torque and instrument inertial effects as outlined by Ewoldt<sup>203</sup>. Limits are based on geometry-specific stress constant ( $F_\tau$ ), minimum torque of instrument ( $T_{min}$ ), minimum strain ( $\gamma_0$ ), instrument inertia ( $I$ ), geometry-specific strain constant ( $F_\gamma$ ) and frequency ( $\omega$ ).

In the amplitude sweeps, the dual crosslinked materials each had  $G'' > G'$  indicating the formation of viscous materials instead of elastic (Figure 4.1, A). Each DNA crosslinked material showed similar curve characteristics, demonstrating similar structural formations, and had distinct behaviour in the amplitude sweeps as demonstrated in another study<sup>204</sup>. The DNA exhibits strain stiffening at the higher oscillation strains due to its elastic nature. This behaviour is different from the Ca-AX<sub>0</sub> sample as the material has a smaller linear viscoelastic region and exhibits more of a structural breakdown in the same strain range (Figure 4.1, A).

In the frequency sweeps, the Ca-AXD50 was the only material of the dual crosslinked materials that did not exhibit structural breakdown at higher frequencies (Figure 4.1, B). This breakdown was concentration-dependant, where Ca-AXD10 deforms first (7.9 rad/s), followed by Ca-AXD25 (23.2 rad/s), and then Ca-AX<sub>0</sub> (107.7 rad/s), whereas the Ca-AXD50 does not show structural breakdown (Figure 4.1, B). In the high frequency region (>100 rad/s), Ca-AXD50 behaves like a viscoelastic material<sup>205</sup>, where  $G' > G''$ , and the material shows high frequency dependence. Frequency dependence can indicate dynamic

gels<sup>206</sup>, which is likely the case. Besiri *et al.*<sup>207</sup> have shown that higher frequencies can lead to increased distribution of  $\text{Ca}^{2+}$  during *in situ* assessments of Ca-alginate crosslinking. These higher frequencies can theoretically disrupt the coordinated  $\text{Ca}^{2+}$  ions in the dual crosslinked materials, causing structural deformation. Consequently, the Ca-AXD50, which has more covalent crosslinks, can then withstand the higher frequencies despite the reorganization of the  $\text{Ca}^{2+}$  ions. The Ca-AXD50 also showed less frequency dependence at lower frequencies in the  $\tan\delta$  (Figure 4.1, C), indicating a more relatively stiff material compared to its other dual-crosslinked counterparts. It should be noted that other work has suggested the influence of inertial effects in the high frequency range of low viscosity materials which can be misinterpreted as structural response<sup>203</sup>. When the inertial limits are overlayed over the rheological data (Figure 4.1) the high frequency region could be influenced by inertial effects, although replicate analyses suggest this is a true material behaviour (see Section 4.3.4).

Interestingly, even though we see a distinct structural difference in the Ca-AXD50 in the frequency sweep, there was not a large difference between the Ca-AXD50 and Ca-AXD25 in the amplitude sweep. In fact, the Ca-AXD25 shows

a higher  $G'$  compared to the Ca-AXD50. This observation could be due to the  $\text{Ca}^{2+}$  interactions offsetting the extra DNA crosslinking occurring in the Ca-AXD50; where less DNA crosslinks in the Ca-AXD25 means that more  $\text{Ca}^{2+}$  can interact with the  $\text{COO}^-$  groups, leading to higher  $G'$  overall.

#### 4.3.2 FTIR Spectroscopy

The FTIR spectra showed similar trends to the rheology analyses, especially regarding the AXD50 sample. The main comparison is shown between the DNA-crosslinked samples (AXD10, AXD25, and AXD50) and controls (AX<sub>0</sub>, A<sub>0</sub>, and APD50) (Figure 4.2). The control materials were included to directly assess the effects of the covalent crosslinkers (AX<sub>0</sub>) as well as the presence of ssDNA on the hydrogel structure (APD50).

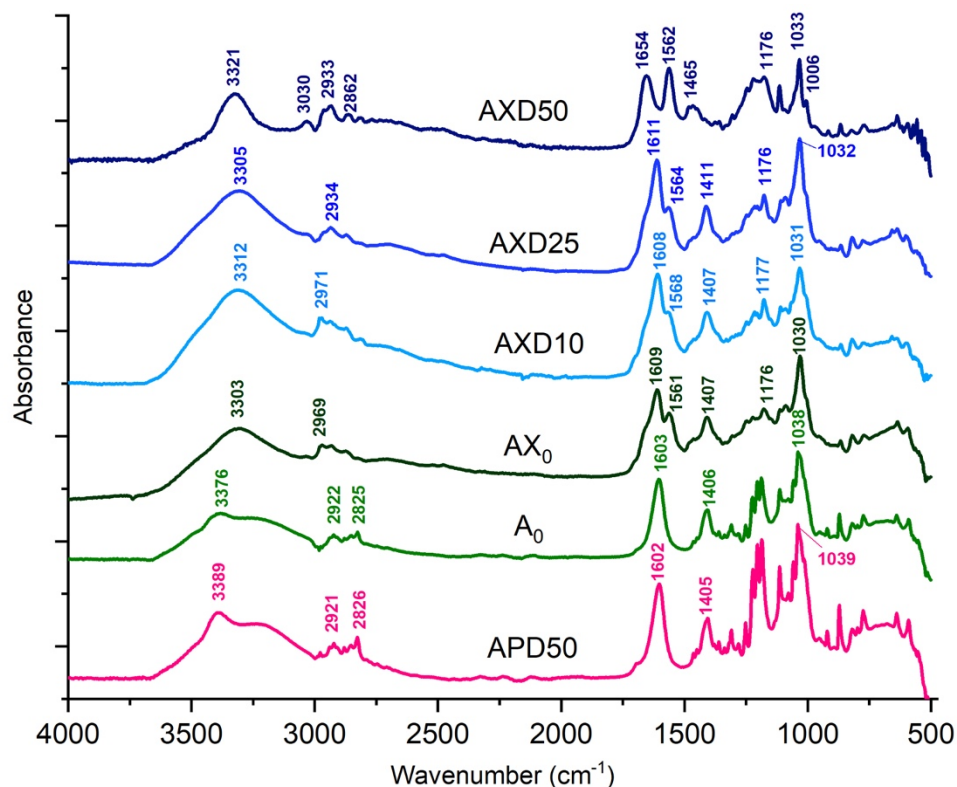


**Figure 4.2.** FTIR spectra for six different alginate materials. Materials AX<sub>0</sub>, AXD10, AXD25, and AXD50 were covalently crosslinked using EDC/Sulfo-NHS only (no Ca<sup>2+</sup>); and samples A<sub>0</sub> and APD50 were mixed without the addition of EDC/NHS or Ca<sup>2+</sup>.

Alginate was observed to have characteristic peaks at 1603 and 1406 cm<sup>-1</sup>, which corresponds to the COO<sup>-</sup> moieties of the M and G blocks, specifically the symmetrical stretching of the carbonyl groups (C=O) at 1603 cm<sup>-1</sup> and asymmetrical stretching (C-OH) at 1406 cm<sup>-1</sup><sup>208</sup>. In the presence of EDC/Sulfo-NHS, the 1603 cm<sup>-1</sup> peak is split into two peaks at 1609 and 1561 cm<sup>-1</sup>, which is likely due to residual C=O in solution from Sulfo-NHS. This is also supported



given that S=O stretching can be seen only in the covalent materials at 1176 cm<sup>-1</sup>.

In the AXD50 material, there is an even further red shift in the split peaks to 1654 cm<sup>-1</sup>, attributed to the amide I bond formation. There is also an additional simultaneous loss of the 1407 cm<sup>-1</sup> peak. Both changes indicate the loss of COO<sup>-</sup> groups, which occurs during amide bond formation from N-DNA-N binding to the alginate (Scheme 4.1). Other indicators of amide bond formation are observed in the increased absorbance of the peak at 1562 cm<sup>-1</sup>, likely due to the N-H deformation of amide II<sup>209</sup>. There is also a more distinct peak at 3321 cm<sup>-1</sup>, which is reasoned to be caused by N-H stretching of the amide A bond<sup>209</sup>. The addition of N-DNA-N in the alginate material without crosslinkers (APD50) shows relatively no change to the COO<sup>-</sup> groups. This indicates that the presence of DNA alone is not leading to the amide bond detection observed in the DNA-crosslinked materials, which naturally exist in three of the four DNA bases. An interesting note is the slight shift of the asymmetrical stretch of the COO<sup>-</sup> to a higher wavenumber in the Ca-APD50 sample from 1415 cm<sup>-1</sup> to 1417 cm<sup>-1</sup> (Appendix A2.1). A shift to lower wavenumbers can indicate ionic binding between alginate and Ca<sup>2+</sup><sup>210</sup>. The higher shift in Ca-APD50 could be due to the

interaction of the N-DNA-N ions with the negatively charged alginate leading to less  $\text{Ca}^{2+}$  interaction overall. <sup>210</sup>

In both the FTIR and SEM assessments, the calcium-crosslinked samples (ionic, dual) showed less distinct differences overall (Appendix II Figures A2.1, A2.2), especially between covalently crosslinked samples. This is likely the result of the calcium ionic crosslinks masking any underlying covalent linkages between DNA and alginate, as mentioned previously. It should be noted that even though materials made with the addition of calcium showed less distinct differences in the SEM and IR assessments, the rheological assessments did observe distinct differences, largely as the technique can directly probe the viscoelastic properties of materials on a more sensitive molecular level.

#### 4.3.3 SEM

Analyses with SEM showed that the DNA-crosslinked materials had more order and structured surfaces compared to encapsulated N-DNA-N (APD50) and the non-DNA containing materials ( $\text{AX}_0$ ,  $\text{A}_0$ ) (Figure 4.3). Both the  $\text{A}_0$  (Figure 4.3, A and B) and  $\text{AX}_0$  (Figure 4.3, C and D) materials had relatively smooth and pitted surface morphologies compared to any of the DNA-containing materials. The

DNA-crosslinked materials exhibited varying surface morphologies, signifying more structured and complex materials (Figure 4.3, E-J). Compared to the DNA-crosslinked materials, the APD50 sample displayed a more porous structure, with a less structured fibrous surface (Figure 4.3, K and L). This contrasts its covalently crosslinked counterpart, where more circular aggregations were observed with more apparent order (Figure 4.3, J) and intricate networks (Figure 4.3, I).

As mentioned previously, the calcium crosslinked samples (dual or ionic) demonstrated less distinct surface morphologies between samples, but still showed general material differences including more bulbous surfaces in the non-crosslinked controls and particle shape differences between the DNA-crosslinked materials compared to the alginate controls (see Appendix II).

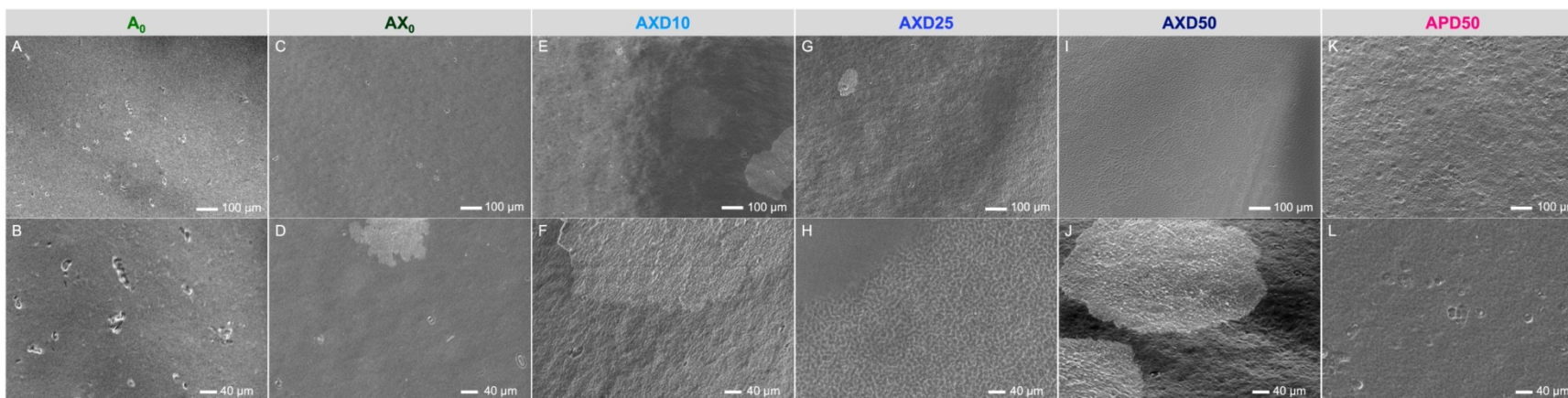


**Figure 4.3.** SEM images of six different materials with/without crosslinkers and with/without N-DNA-N. Samples from left to right are:  $A_0$  (A, B),  $AX_0$  (C, D), AXD10 (E, F), AXD25 (G, H), AXD50 (I, J), and APD50 (K, L). The first row shows magnification at approximately 1000 x, and the second row is 2000 x. High resolution images of these scans can be found in Appendix II Figures A2.3-A2.8.

#### 4.3.4 Influence of ssDNA Structure

The different ssDNA structures used in the crosslinking reaction (N-DNA-N, N-DNA, and DNA) appear to influence the overall material properties. When assessed with rheology, materials crosslinked with either dual ended amine ssDNA (Ca-AXD2N) or single amine ssDNA (Ca-AXD1N) did not exhibit any structural breakdown at high frequencies, similar to Ca-AXD50, and were unlike the alginate material covalently crosslinked with DNA without any terminal amines (Ca-AXD0N) (Figure 4.4). The replicate dual amine DNA crosslinked material (Ca-AXD2N) demonstrated more of a linear viscoelastic region (LVR) in the amplitude sweep (Figure 4.4, A) compared to the first reaction (Ca-AXD50, Figure 4.1, A). When ssDNA without any terminal amines was reacted in a covalent crosslinking reaction (Ca-AXD0N), the material had a lower  $G'$  compared to the materials crosslinked with DNA that contain terminal amines (Figure 4.4, A). Interestingly, the Ca-AXD0N material behaved differently than both encapsulated ssDNA (Ca-APD50, Figure 4.1, A) and the alginate covalent controls (Ca-AX<sub>0</sub>, Figures 4.1, A and Figure 4.4, A), indicating a unique material influenced by the lack of terminal amines. Furthermore, the FTIR analyses detected no amide bonds the AXD0N material (Figure 4.5), suggesting that the DNA without terminal amines did not attach covalently to the alginate as the

AXD2N and AXD1N did. Without chemically attaching to the alginate backbone directly, the EDC can still react with the phosphate backbone of the DNA<sup>211</sup>, which could be causing nonspecific reactions between DNA molecules and thereby result in a structurally weak material. This is also supported by the SEM observations, where the AXD0N material appears more porous similar to the AX<sub>0</sub> material, but is unlike the AXD1N and AXD2N which have more smooth and structured surfaces (Figure 4.5, A-H).

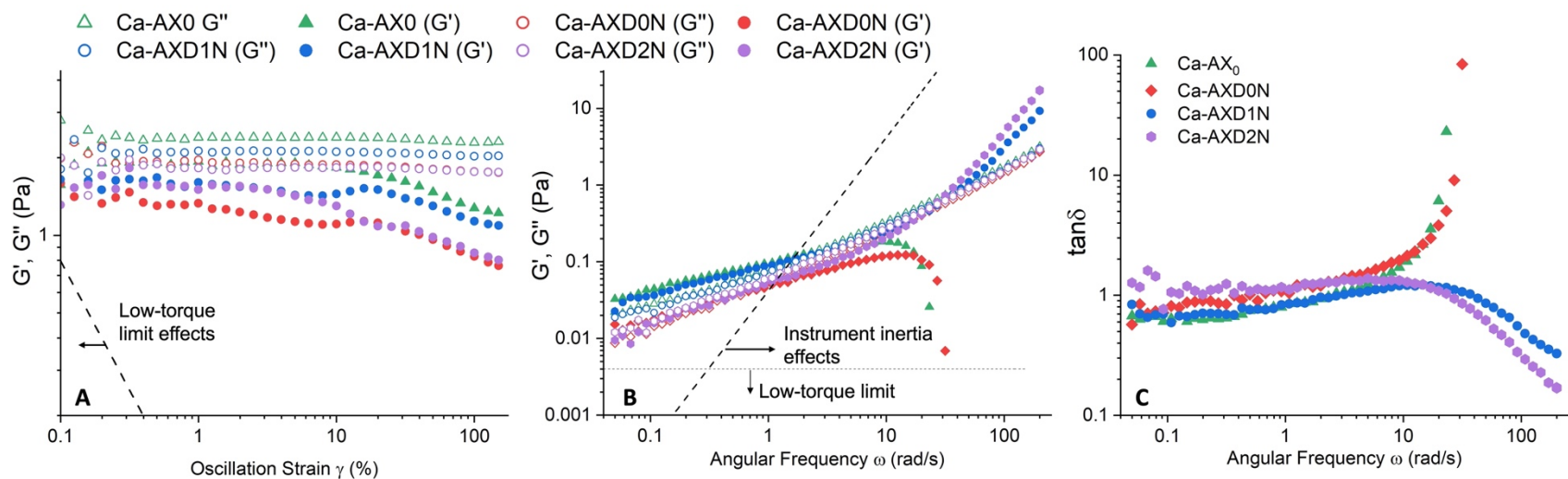


**Figure 4.4.** Amplitude sweeps (A) and frequency sweeps (B) and  $\tan\delta$ (C) for 4 ssDNA with varying amine reactivities: no DNA (Ca-AX<sub>0</sub>), ssDNA with no terminal amines (Ca-AXD0N), one terminal amine (Ca-AXD1N), and two terminal amines (Ca-AXD2N) covalently crosslinked with alginate. The samples were made to be dual crosslinked with Ca<sup>2+</sup>. The filled in symbols represent the Storage Modulus (G') and the corresponding non-filled symbols are the Loss Modulus (G'') for a given sample.

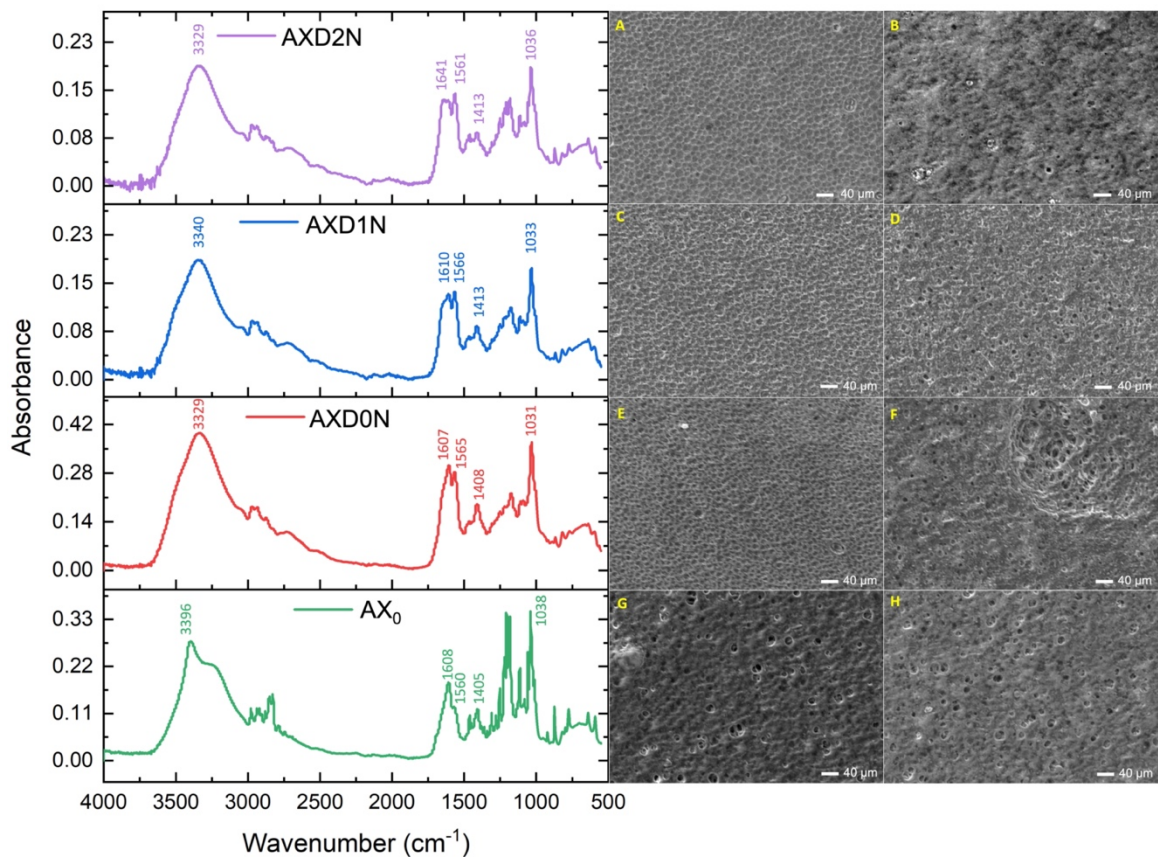


**Figure 4.5.** FTIR spectra (left) 4 different alginate materials crosslinked with no DNA (AX<sub>0</sub>), ssDNA with no terminal amines (AXD0N), ssDNA with one terminal amine (AXD1N), and ssDNA with two terminal amines (AXD2N). Images on the right show the corresponding SEM images of each material. Two SEM images are included to show the variation in surface morphologies: AXD2N (A, B), AXD1N (C, D), AXD0N (E, F), AX<sub>0</sub> (G, H).

Finally, TGA denoted overall similar degradation profiles (Figure 4.6), with slight variation during each degradation event. Ayouch *et al.*<sup>212</sup> indicate that alginate-based materials can undergo three degradation events; between 30-150°C (water desorption), 200-300°C (decomposition of carbon in alginate backbone and formation of sodium carbonate - Na<sub>2</sub>CO<sub>3</sub>), and 600-700°C (two-stage breakdown of Na<sub>2</sub>CO<sub>3</sub>). Our TGA analyses showed similar degradation



characteristics in the materials, with more distinct material differences shown at higher temperatures. The Ca-AXD2N material had the least relative amount of weight loss (74.37%) compared to Ca-AXD1N (78.16%), Ca-AXD0N (77.38%) and Ca-AX<sub>0</sub> (82.49%). At higher temperatures (over 600°C), the alginate control (Ca-AX<sub>0</sub>) was more easily degraded compared to the other materials, which is likely due to the strong molecular networks of the DNA-crosslinked materials<sup>213</sup>, and explains why the Ca-AXD2N has more residual material.

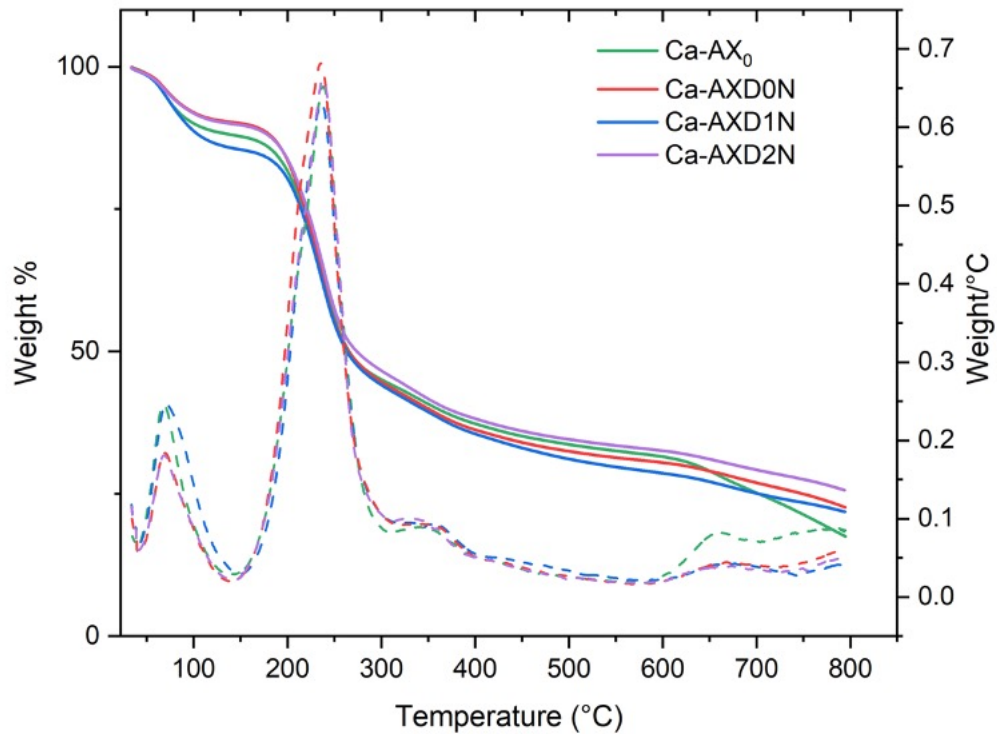


**Figure 4.6.** TGA curves of four different dual crosslinked alginate materials covalently crosslinked with no DNA (Ca-AX<sub>0</sub>), ssDNA with no terminal amines (Ca-AXD0N), ssDNA with one terminal amine (Ca-AXD1N), and ssDNA with two terminal amines (Ca-AXD2N). Samples were made to be dual crosslinked with Ca<sup>2+</sup>. The dashed curves represent Weight/°C, while the solid curves are the Weight % at each temperature.

Together, the analyses signify that the amine modification of ssDNA at either one or both terminal ends leads to the immobilization of DNA to alginate. The ability to covalently attach the DNA by either one end or both ends is particularly beneficial as it allows for many applications of the hydrogel materials. Specifically, the development of microparticles (MPs) using DNA-crosslinked alginate is of particular interest and is discussed in the next section.

#### 4.3.5 Microparticle Generation & Applications

Human reference standards with the hydrogels can be developed in many forms, but one valuable application is the development of forensic blood simulants that have both relevant fluid properties and genetic capabilities similar to human blood<sup>39,46</sup>. To accomplish this, the covalently crosslinked alginate and ssDNA hydrogels were used to develop MPs of relevant WBC size(s). MPs can be effectively generated through electrospray ionization (ESI), where the covalent crosslinked alginate-DNA is extruded through an electrified needle into a calcium bath with a counter electrode. The overall MP size and morphology are influenced by many factors<sup>88</sup>, but the covalent materials must be able to coordinate effectively with  $\text{Ca}^{2+}$  to achieve relevant MPs, especially for our applications.

The MPs assessed in this work included those derived from Alg(MES), AX<sub>0</sub>, AXD10 and AXD50, all with 2.5% w/v alginate. The 2.5% Alg(MES) was used as a control to compare with materials that had undergone the conditions of a crosslinking reaction (AX<sub>0</sub>) and a crosslinking reaction with both low (AXD10) and high (AXD50) ssDNA concentrations. Tween 20 was added to the materials as a non-ionic co-solvent to lower the surface tension of the materials<sup>214,215</sup>, which allowed for a more stable Taylor cone and more homogenous particle distributions. The two non-DNA materials (2.5% Alg(MES) and AX<sub>0</sub>) had similar average particle diameters ( $p = 0.78$ ), and were smaller than the DNA-crosslinked MPs (Figure 4.7). The AXD10 material had MPs that were statistically different from both 2.5% Alg(MES) ( $p = 0.0003$ ) and AX<sub>0</sub> ( $p = 0.0004$ ). Similarly, the AXD50 was also statistically different from both 2.5% Alg(MES) ( $p = 6.81 \times 10^{-5}$ ) and AX<sub>0</sub> ( $p = 9.91 \times 10^{-5}$ ). Interestingly, it appears that by crosslinking alginate with DNA, the MPs are larger than MPs electrosprayed without DNA. This is true irrespective of the concentration of DNA attached to alginate, as both AXD10 and AXD50 had similar average particle sizes ( $p = 0.68$ ). This finding is appropriate for the development of human blood simulants, as WBCs are typically larger than red blood cells (RBCs) naturally.

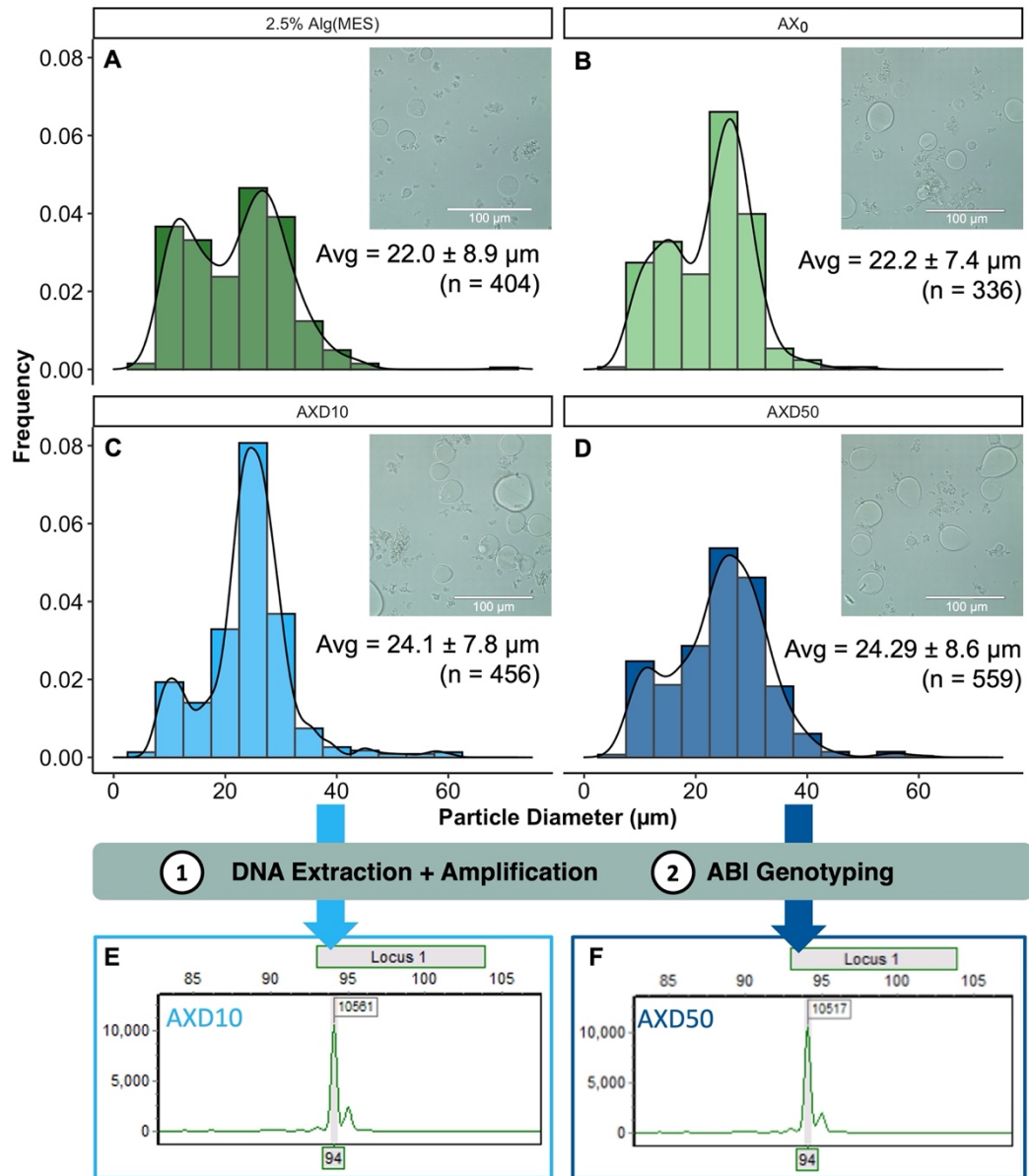


**Figure 4.7.** Microparticle (MP) size distribution of four different materials: 2.5% w/v alginate in MES buffer (A), AX<sub>0</sub> (B), AXD10 (C) and AXD50 (D) electrosprayed with 0.5% v/v Tween 20 into a CaCl<sub>2</sub> bath. Inlet images show microscopic images of MPs visualized in brightfield mode at 40x magnification. Corresponding genotype of ssDNA extracted and amplified from AXD10 (E) and AXD50 (F) microparticles.

Therefore, by simply crosslinking alginate with ssDNA, the particles formed (our “WBCs”) would be larger than those electrosprayed without DNA (our “RBCs”) under the same conditions. Having two different cell mimetic types is not only important for the overall functionality of the blood material, but also the incorporation of viscoelastic RBCs is a critical feature to accurately simulate blood drop dynamics of spreading and splashing<sup>16</sup> in crime scene scenarios. Another important consideration in forensic blood simulants is the ability for materials to be processed in a similar manner to blood evidence - specifically, the ability to extract, amplify and genotype the contained DNA. We investigated the overall functionality of the candidate WBCs and determined that following a typical blood processing procedure with an additional modification to break down the alginate material<sup>197</sup>, the crosslinked DNA was extracted, amplified and produced an interpretable genotype similar to non-crosslinked controls. This is promising because it indicates that the crosslinked DNA still remains both functional and intact through the electrospraying process, a critical finding for developing forensic materials. This work shows that our alginate-DNA crosslinked MPs are viable materials as WBC mimetics with forensic applications given their ability to retain functional DNA that is mimetic of human Combined DNA Index System (CODIS) loci. Future work will incorporate these WBCs into

an alginate-based whole blood simulant that has both fluid properties and biological components similar to human blood for forensic research and training. Regardless, the material can be used as is for applications in forensic science.

#### **4.4. Conclusions**

This work explored the effect of covalent crosslinking between amine-terminated ssDNA and alginate and its role in generating MPs for forensic blood simulants. The covalent attachment of ssDNA to alginate provides more stable linkages and immobilization of the DNA within the hydrogels. The characterization of the alginate-DNA hydrogels demonstrated covalent crosslinking between alginate and ssDNA based on the detection of amide bonds in the highest DNA concentration material. The rheological assessments also showed that the AXD50 material had less frequency dependence in the  $\tan\delta$ , as well as dynamic gel characteristics in the high frequency range, unlike the other covalent crosslinked materials. This unique behaviour can be attributed to the higher number of crosslinks formed in the high DNA concentration material, where the flexible ssDNA allows for soft gel characteristics. Similarly, SEM revealed that the DNA crosslinked alginate

hydrogels were more structured, with interconnected networks distinct from the alginate and DNA control materials. Finally, investigation into the molecular dynamics of the alginate and DNA crosslinking suggests that the binding of ssDNA primarily occurs from the primary amines at the 5' and 3' ends, further supporting the development of 3D crosslinked networks in the reaction.

The attachment of DNA to the alginate backbone while maintaining functionality in the MP form lends the material to such roles as mimetic WBCs in forensic blood simulants. The low  $G'$  characteristics of the covalent crosslinked Alg-DNA hydrogel is favourable for the development of MPs containing immobilized DNA, much like traditional WBCs in human blood. This work provides the baseline for the development of our alginate-based forensic blood simulant. Future works include characterizing these materials in complex biological and physical processes that occur during evidence formation and degradation at the crime scene.

# Chapter 5

Alginate/Xanthan gum hydrogels as forensic blood substitutes for bloodstain formation and analysis<sup>10</sup>.

## Preface

Type: Original Research Article

Submitted to: Soft Matter

Status: Published

Title: Alginate/Xanthan gum hydrogels as forensic blood substitutes for bloodstain formation and analysis.

Authors: Amanda Orr<sup>a</sup>, Paul Wilson<sup>b</sup>, Theresa Stotesbury<sup>c</sup>

<sup>a</sup> Environmental and Life Sciences PhD Program, Trent University, Peterborough, Ontario, Canada, 1600 West Bank Drive, K9L 0G2

<sup>b</sup> Biology Department, Trent University, Peterborough, Ontario, Canada, 1600 West Bank Drive, K9L 0G2

<sup>c</sup> Faculty of Science, Forensic Science, Ontario Tech University, 2000 Simcoe Street North, Oshawa, ON, L1G 0C5

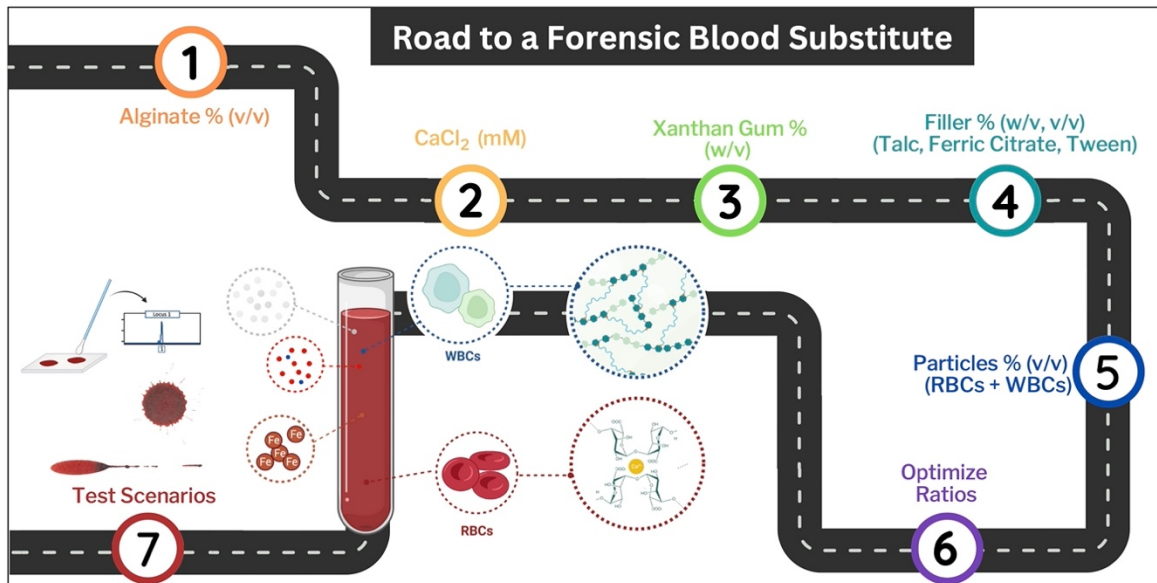
---

<sup>10</sup> Reproduced from Reference <sup>243</sup> with permission from the Royal Society of Chemistry (A. Orr,

P. Wilson, T. Stotesbury. Soft Matter. 2023. 19:3711-3722. DOI: 10.1039/D3SM00341H).



## Graphical Abstract<sup>11</sup>



## Keywords

Human blood simulant; forensic science; synthetic DNA; bloodstain pattern analysis; crime scene training; shelf life.

---

<sup>11</sup> Created with BioRender.com. Copyright permission is located in Appendix I.

## Abstract

Understanding the behaviour of human blood outside of the body has important implications in forensic research, especially related to bloodstain pattern analysis (BPA). The design of forensic blood substitutes (FBSs) can provide many advantages, including the incorporation of multiple physiological components for use as safe and reliable materials for forensic applications. In this work, we present the design of synthetic alginate and xanthan gum-based hydrogels that contain electrosprayed microparticles (MPs) with and without crosslinked DNA. In addition to the MPs, the alginate/xanthan gum FBS materials include fillers to alter the physical appearance and fluid properties of the material. The optimized FBS consisted of alginate (1% w/v) and xanthan gum ( $5.0 \times 10^{-3}$  % w/v), 2 mM  $\text{CaCl}_2$ , ferric citrate (0.5% w/v), magnesium silicate (0.25% w/v), Allura Red dye (2% w/v), 0.025% v/v Tween 20 and 9.5% v/v MPs. The FBS was tested in passive dripping experiments relevant to BPA scenarios at various impact angles. The spreading ratio ( $D_s/D_0$ ) was determined for  $90^\circ$  stains made on a paper surface and compared to bovine blood where the FBS was shown to simulate accurate and predictable spreading behaviour. In addition, we simulated other common BPA scenarios (e.g., impact patterns) and evidence processing potential. The FBS could be swabbed, and the DNA could

be extracted, amplified, and genotyped analogous to human blood evidence. A stability test was also conducted which revealed a shelf-life of over 4 weeks where the material remains relevant to human blood at physiological temperature.

## 5.1 Introduction

Blood evidence is commonly encountered in crime scene scenarios and can provide detail into the 'who', 'what' and 'where' as it relates to criminal investigations. The 'who' can be revealed through DNA genotyping to establish a genetic profile, and bloodstain pattern analysis (BPA) experts can analyse the bloodstain size, shape, and distribution to ascertain the events of bloodshed that took place<sup>1,2</sup>. Access to human blood for training and research in forensic science can be an issue due to high costs, biohazards relating to blood-borne pathogens, and ethical concerns<sup>39,46,47</sup>. These obstacles have driven the need for whole-blood alternatives in forensic science research and training, particularly alternatives that can simulate *ex-vivo* formation and degradation conditions for blood. While an influx of research has been conducted to understand and validate appropriate mammalian sources<sup>18-20,25,41,216</sup>, the use of whole animal blood can still pose procurement issues and has limited capabilities in training (e.g., cannot generate human genetic profiles). The use of synthetic materials that can simulate blood behaviour in forensic scenarios (forensic blood substitutes, or FBSs) on multiple levels (physical, biological, and chemical) can provide valuable materials for forensic science research and training.

FBS materials can provide advantages such as standardized fluid properties, increased shelf life as well as chemical and biological safety<sup>39,46</sup>. These materials have explored everything from the use of household product mixtures containing flour, glycerol, syrup etc.<sup>37,47</sup>; aqueous Acrysol and dye material<sup>48</sup>; silicon solution-gelation (sol-gel) materials<sup>49,50</sup>; hyaluronate- and amino acid-containing materials<sup>54</sup>; to emulsion-based materials using styrene and polyvinylpyrrolidone (PVP)<sup>53</sup> or polydimethylsiloxane (PDMS) microparticles<sup>55</sup>. The available commercial blood materials have limited rheological properties and bloodstain features in comparison to human blood<sup>50,54</sup>, limiting their use in BPA research and training. Recent FBS research describes materials that contain multi-functional and/or multi-component structures. For example, materials have been developed using hybrid inorganic-organic silicon sol-gel chemistries that can mimic the rheology and spreading dynamics of blood<sup>49-51</sup>, in addition to materials that possess the chemiluminescent properties of blood with reaction to luminol<sup>52</sup>. Other work has developed a material that contains amino acids, bovine serum albumin, bovine hemoglobin and potassium ferricyanide to create materials that can simulate drip stains, and suggest functional materials that can react with luminol<sup>54</sup>. Most recently, a particle-based blood simulant was

designed that contains a similar particle amount to that of human packed cell volume (PCV%)<sup>55</sup> and addresses the identified value of red blood cell (RBC) deformability in blood spreading and splashing<sup>16</sup>.

In BPA, it is important to understand the spreading and splashing of blood when in contact with a variety of target surfaces in different environments. This is especially important to increase the reproducibility of pattern classification and the development of more objective and quantitative methods within the field<sup>5,6,9,38,217</sup>. The use of FBSs in this area can be used to investigate the complex impact mechanisms of relevant fluids in forensic contexts. In addition, FBS use in training scenarios provides standardized materials that can accurately depict bloodshed events and can be safely implemented into training programs at the practitioner and academic levels. As mentioned, the incorporation of multiple functions of human blood into FBS materials can provide enhanced training and research opportunities.

The work described herein presents a multi-component FBS that integrates electrosprayed microparticles (with and without DNA) that resemble the cellular components of blood into an alginate-based hydrogel. In this way, we

wondered if it were possible to design a material that has similar fluid properties to whole human blood but also contains genetic components to provide the 'who' through the integration of synthetic DNA designed to mimic human DNA loci<sup>197,218</sup>. We explore the use of alginate and xanthan gum co-polymers as the basis of the FBS, which is appropriate since their hydrogel properties have a high water content, characteristic of blood plasma which is mostly water<sup>27</sup>. We further explore the addition of other fillers (Allura red, magnesium silicate, ferric citrate, and surfactant) into our FBS material to modify the visual features of the FBS to better resemble blood. Allura red and magnesium silicate (talc powder) were added to achieve appropriate colouring and opacity of whole blood. Ferric citrate was included to obtain the deep colouring of blood, increase opacity, and provide oxidative capabilities to the material, and the use of a surfactant (Tween 20) allowed for modification of the surface tension of the FBS. The optimization of these fillers is investigated and their influence on the overall properties is discussed. The performance of the optimized FBS material is assessed and compared to both the human blood range and bovine blood to understand the feasibility of the FBS in training and research capacities.

## 5.2. Experimental

### 5.2.1 Materials

Low-viscosity alginic acid sodium salt, ferric citrate ( $C_6H_5FeO_7$ ), magnesium silicate (talc,  $MgO_3Si$ ), and Allura red ( $C_{18}H_{14}N_2Na_2O_8S_2$ ) were all purchased from Sigma Aldrich (Oakville, ON) and used as received. Calcium chloride dihydrate ( $CaCl_2 \cdot 2 H_2O$ ) (Westlab, Adlergrove, BC) was dissolved in MilliQ water to make various stock aqueous solutions (500 - 100 mM). Tween 20 was obtained from MP Biomedicals (Solon, OH) and xanthan gum (Bob's Red Mill) was used. For the microparticles (MPs) that contain DNA, the dual-amine ssDNA was purchased from Integrated DNA Technologies (Toronto, ON) and were crosslinked as described previously<sup>218</sup>.

### 5.2.2 Microparticles

Microparticles (MPs) were made using a custom-built electrospray ionization device that has been optimized and described previously<sup>218</sup>. In brief, the optimized parameters were found to be a working distance (needle to 7.35% w/v  $CaCl_2$  bath) of 4 cm, a flow rate of 2  $\mu$ L/min, with 10 kV applied to the tip of a 30-gauge hypodermic needle. The optimized particles were made using either an alginate solution (2.5% w/v in MilliQ water + 0.5% v/v Tween 20) or a



dual amine DNA-crosslinked alginate material (2.5% w/v alginate crosslinked with 10 nmol ssDNA in MES buffer + 0.5% v/v Tween 20).<sup>218</sup>The electrospray setup was optimized to achieve the smallest possible MP size for large-scale production ( $22.0 \pm 8.9 \mu\text{m}$  for the alginate solution;  $24.1 \pm 7.8 \mu\text{m}$  for the DNA-alginate crosslinked materials<sup>218</sup>).

Once formed, the collected MPs were centrifuged and washed with MilliQ water for a total of four times ( $3000 \times g$ , 8 minutes). After each spin, the supernatant was removed and replaced with MilliQ water, mixed, and spun down again. The washed MPs were compiled and stored until needed for incorporation into the blood material. Visualization on an EVOS FL Auto microscope (Life Technologies) was done to ensure no lysis of the particles occurred during the washing and centrifugation.

The MPs were visualized with scanning electron microscopy (SEM) using a Hitachi FlexSEM 1000. A concentrated solution of washed MPs was placed on 3M™ Copper Foil EMI Shielding Tape 1182 attached to stainless steel stubs and dried overnight at room temperature. SEM images were taken at 5 kV and magnifications of 1000x and 4000x.

### 5.2.3 Material Optimization

For the base material, various concentrations of weight per volume (w/v %) alginate were assessed (1, 2, 2.5%), which were dissolved overnight in MilliQ water. Upon the use of xanthan gum (XG), a serial dilution was made, reaching a final concentration of  $1.0 \times 10^{-3}$  or  $5.0 \times 10^{-3}$  % w/v XG. Once these aqueous XG solutions were made, they were used as the solvent for alginate preparation (e.g., 1% w/v alginate dissolved and mixed in a  $1.0 \times 10^{-3}$  % XG solution). The initial choice of dye (Allura red) was based on visual similarities to human blood colour and was kept constant at 2% w/v throughout all experiments.

The additional fillers that were explored were talc, ferric citrate, and Tween 20 to modify the properties of the bulk material. Finally, the MPs were assessed for optimal concentrations in a volume by volume (v/v %) ratio. A summarization of the component concentrations explored during optimization is shown in Table 5.1. To integrate MPs, the combined and washed MPs were spun down (if not already) and the supernatant was removed, attempting to remove as much of the supernatant as possible without removing any particles. The supernatant was transferred to a clean tube and was combined with other supernatants, spun

down, and any MPs remaining were reused. The concentrated MPs were briefly vortexed to mix any remaining liquid, creating a homogenous, pipettable mixture. An appropriate v/v % was transferred using a micropipette. The full list of optimized material components can be found in Appendix II.

**Table 5.1.** Overview of components tested in FBS candidates. Combinations include some or all components listed. A full detailed table can be found in Appendix II Table A2.1.

<b>Xanthan Gum</b> (w/v %) ×10 <sup>-3</sup>	<b>Alginate</b> (w/v %)	<b>Filler(s)</b>	<b>Filler Amount</b> (v/v or w/v %)	<b>Particles</b> (v/v %)
		Allura Red (w/v %)	2%	
		Talc (w/v %)	0 0.25%	0 5
			0	7.5
1.0 %	1%	Ferric citrate	0.5%	8
	2%	(w/v %)	0.75%	9.5
5.0 %	2.5%		1%	10
			0	15
		Tween 20 (v/v %)	0.0025 0.025 0.0375	20

#### 5.2.4 FBS Material

To make the candidate FBS, a 5.0 ×10<sup>-3</sup> % w/v solution of XG was created. To this, 1% w/v alginate was added, and mixed overnight at room temperature (22°C ± 2°C). For visual simulation of the appearance of blood, fillers, such as

talc powder (magnesium silicate), ferric citrate and Allura red dye were also added. To ensure a homogenous mixture, Allura red (2% w/v), ferric citrate (0.5% w/v) and talc (0.25% w/v) were all added to the 1% w/v alginate in  $5.0 \times 10^{-3}$  % XG and mixed overnight. Typically, an equilibration period of 30 minutes was allowed for mixing between each filler addition. The following day, 2 mM  $\text{CaCl}_2$  was added in a 4:1 volume ratio of alginate/XG/talc/ferric citrate/Allura red to  $\text{CaCl}_2$ . This material constitutes what we describe as the “FBS base”.

The optimized FBSs contained 9.5% v/v of the washed/concentrated MPs; the MPs were added to an empty tube, followed by an appropriate amount of the FBS base. Finally, Tween 20 was added using a 5% v/v stock solution to achieve a final concentration of 0.025% v/v. The components were vortexed together and at least an hour was allowed before use.

### 5.2.5 Material Characterization

All FBS measurements were conducted at room temperature ( $22^\circ\text{C} \pm 2^\circ\text{C}$ ). Viscosity, density, and surface tension were measured as follows. A rheometer was used as a preliminary screening technique to assess the bulk viscosity of the materials during optimization. Flow sweeps were performed using a Discovery

HR20 stress-controlled rheometer with an advanced Peltier plate and a solvent trap system (TA Instruments) between shear rates of 1 to 1200 s<sup>-1</sup> using a 40 mm 2° cone with a 60 μm truncation gap. For all FBS candidate materials, rheological assessments were performed at 22°C. Flow sweeps were plotted for all materials; the low torque limit<sup>203</sup> was calculated using a minimum torque value of 0.01 μN·m. Oscillation amplitude and frequency sweeps were also performed with a solution of concentrated MPs and the FBS to understand the viscoelasticity. Amplitude sweeps were performed between strains of 0.01–150% and frequency sweeps between frequencies of 0.05–200 rad s<sup>-1</sup> at a strain of 3.5% for the FBS and 0.05–350 rad s<sup>-1</sup> at 0.1% strain for the MP solution. The relative density of select materials was measured relative to MilliQ water by weighing a known volume of material in a 1000 μL Hamilton gas-tight syringe. Surface tension was measured using the pendant drop method. A Canon EOS Rebel T6i DSLR camera equipped with a Canon EF-5 60 mm macro lens was used to capture the falling droplets and the surface tension was measured using the “Pendant Drop” plugin in FIJI (version 2.9.0/1.53t).

Drip stains were also created to visually assess the performance of the materials in passive dripping scenarios, which measured the average stain diameter ( $D_s$ )

and the average number of spines. Preliminary screening assessed 90° passive drip stains made at 20, 60 and 100 cm from a hard paper surface (67 lb coverstock). Bovine blood (Windcrest Meat Packers, Port Perry, ON, n=2) was included as a comparison control for the drip stains since comparison to human blood was difficult to source the specific target surfaces used in the literature. The bovine blood contained 12.5% v/v acid citrate dextrose (ACD-A) anticoagulant, which has previously demonstrated similar properties to human blood<sup>25</sup>. The fluid properties of the bovine blood were measured, including the viscosity, density, surface tension and packed cell volume (PCV%). All bovine blood properties except the PCV% were analyzed at both room temperature ( $21.8^{\circ}\text{C} \pm 0.4^{\circ}\text{C}$ ,  $38\% \pm 8\% \text{RH}$ ) and physiological temperature ( $37^{\circ}\text{C} \pm 2^{\circ}\text{C}$ ) in a similar manner to the synthetic materials. A bovine drip stain library was made from impact angles ( $\alpha$ ) between 10°-80° (drop heights of 20, 60 and 120 cm) and 90° (20, 40, 60, 80, 100, and 120 cm).

Once an optimized FBS material was determined, a full suite of drip stains was also made at similar angles/heights as the bovine blood (10-80°, 20, 60 and 120 cm; 90°, 20-120 cm) for comprehensive comparative analysis<sup>37</sup>. The drip stains were made by manually dropping the material (FBS or bovine blood) from a

glass pipette perpendicular to the target surface (in the case of 90° stains) or perpendicular to the floor where the target surface was angled to 10, 20, 30, 40, 50, 60, 70, and 80° and fixed for the generation of drip stains. In all cases, the average mass of the droplets was measured to determine the droplet volume for modelling the spreading ratio (final stain diameter divided by the initial droplet diameter -  $D_s/D_0$ ). For this drip stain experiment, the FBS with 0.4% v/v blue food colouring dye (Club House) was used (FBS+B). Other relevant bloodstain patterns were made such as impact patterns (FBS, FBS + B) and 90° drip stains on various surfaces (FBS - acetate, tile, linoleum, 110 lb cardstock, wood, and cardboard) similar to those above. The impact patterns were made by manually striking a secured hockey puck that contained approximately 1 mL of FBS material with a hammer. The hockey puck was placed 24 cm out from the target surface.

#### 5.2.6 Data Analysis

Drip stains (both 90° and angled) were scanned as a JPEG image at 400 dpi. The images were imported into FIJI, scaled, and the stain characteristics (stain area,  $D_s$ , and impact angle) were measured; the number of spines were manually counted by one researcher. The measurements were conducted as follows:

angled drip stains (10-80°) were fitted at the maximum width with the ellipse tool and the major and minor axes values were measured; for 90° stains, the ellipse tool was used to measure the  $D_s$  while held as a perfect circle. The impact angle was found by taking the inverse sine of the width to length ratio of the ellipse of the stain. The stain area was determined by converting the image to a binary image and the "Analyze Particles" function was used with a lower threshold of 50 mm<sup>2</sup>.

#### 5.2.7 DNA Functionality in FBS

To provide a functional training aid for forensic scenarios, we assessed the functionality of our alginate-DNA crosslinked MPs in the FBS material. For the purposes of a DNA-containing FBS (DNA-FBS) 9% v/v MPs were mixed with 0.5% v/v alginate-DNA crosslinked MPs for a total of 9.5% v/v MP concentration, similar to the FBS. The DNA-FBS was prepared the same way as the FBS, where the only difference was the use of different particle compositions (9% MPs + 0.5% DNA-crosslinked MPs).

To mimic scenarios related to crime scene DNA processing, 90° drip stains were made on 6 target surfaces (tile, linoleum, acetate paper, 110 lb cardstock, wood,



and cardboard). The stains were allowed to dry, and individual wetted sterile swabs were used to swab a single stain on each surface. The swabs were placed in 500  $\mu$ L of gel dissolving buffer overnight (Gel Extraction Kit, New England Biolabs) and followed a validated procedure demonstrated in our previous work with DNA-encapsulated hydrogels<sup>197</sup>. The following day, the swab-containing tubes were incubated at 52 °C and 500 rpm for 20 min (Eppendorf ThermoMixer F 1.5), and hereafter the manufacturer's protocol was followed as suggested. 20  $\mu$ L of ultrapure water was used to elute the DNA. The extracted DNA was added to a PCR reaction as either stock solution or a 1:10, 1:20 or 1:40 dilution (PCR: 95 °C for 10 min; 94 °C for 30 s; 53 °C for 1 min; 72 °C for 1 min; repeat for a total of 30 times with a final step of 65 °C for 15 min). Once amplified, a 1:50 dilution was prepared and genotyped using an ABI 3730 DNA Analyzer with a GeneScan 500 ROX size standard.

#### 5.2.8 FBS Stability

To evaluate the shelf-life of the FBS material, a stability test was conducted to understand the aging of the material. A 15 mL batch was made and used for the duration of the stability experiment and the FBS material was left at room temperature (21.6°C  $\pm$  0.3°C, RH= 30%  $\pm$  1%). The material assessed for stability

included the blue food colouring dye, 9% v/v MPs, and 0.5% v/v MPs crosslinked with DNA (DNA-FBS). A complete assessment of both fluid property measurements (viscosity, surface tension, and relative density) and drip stain features (number of spines and  $D_s/D_0$ ) were measured at 1 day, 4 days, 1 week, 2 weeks, 3 weeks and 4 weeks after making the FBS. A DNA extraction was performed at 4 weeks using approximately 100 mL of the liquid FBS ( $n = 4$ ). Continued measurements of select FBS properties were conducted at 6, 10, and 12 weeks which were chosen based on the availability of the remaining FBS sample. At 12 weeks, an evaluation of the MPs in the FBS material was also conducted using an EVOS FL Auto microscope (Life Technologies) under 20 $\times$  and 40 $\times$  magnification in brightfield mode.

### **5.3. Results & Discussion**

#### 5.3.1 Material Optimization

In total, seven variables were optimized in the FBS materials to obtain an ideal human blood simulant; these consisted of concentrations of alginate, XG,  $\text{CaCl}_2$ , talc, Tween 20, ferric citrate and MPs. Blood is an inherently complex fluid composed of soft-solid components (RBCs, white blood cells - WBCs, and

platelets) suspended in liquid plasma<sup>14</sup>. Blood is a non-Newtonian fluid that is shear-thinning due to the RBC aggregation and elongation at increased shear rates<sup>15,16,21</sup>. When designing FBS materials, this complex behaviour should be considered, and the role that blood components have in the fluid behaviour related to forensic scenarios is also important. For example, the spreading and splashing of blood are primarily governed by the fluid properties of blood, namely the viscosity, PCV% (the ratio of solid to liquid components), surface tension, and density<sup>21,28,219</sup>. RBCs influence many of these parameters and reasonably should be incorporated into FBSs, especially given their role in complex non-Newtonian behaviour of blood<sup>14,16,21,220</sup>. Therefore, the fluid properties and inclusion of particle-based components that resemble blood cells are important in FBS performance. In the FBS optimization, materials that had similar properties to the human blood range directed their concentration choice in the optimization process.

The amount of alginate used (w/v %) influenced the viscosity of the materials, and their shear-thinning behaviour (Figure 5.1, A). The low torque limit was calculated and fell below the viscosity values in our tested range; therefore, it is not visible in Figure 5.1's flow sweep plots and all subsequent flow sweeps. In

general, the higher amount of alginate used, the higher the viscosity; in addition, the higher concentration of  $\text{CaCl}_2$  used to ionically crosslink alginate, the more shear thinning was observed. 1% w/v alginate was chosen since its viscosity was on the lower end of the human range (Figure 5.1, A) which could best accommodate the added viscosity of fillers - such as XG.

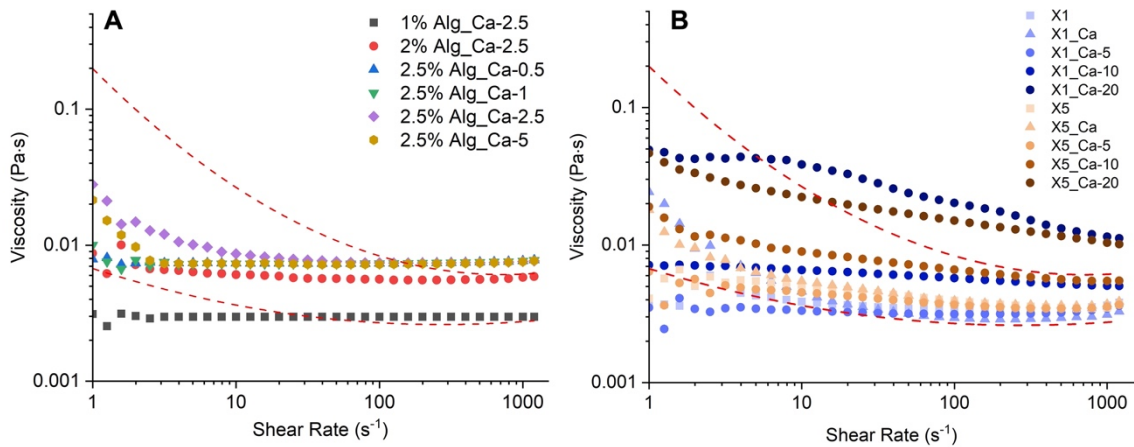


**Figure 5.1.** Viscosity profiles of (A) materials with various alginate concentrations (1, 2, 2.5% w/v) and  $\text{CaCl}_2$  concentrations (0.5, 1, 2.5, 5 mM) used to ionically crosslink alginate. (B) Viscosity profile of various 1% w/v alginate materials with two xanthan gum concentrations:  $1.0 \times 10^{-3}$  w/v % (purple) and  $5.0 \times 10^{-3}$  w/v % (orange). Square symbols represent the base material (alginate with XG), triangles represent the base material with 2.5 mM  $\text{CaCl}_2$ , and the circles represent the addition of microparticles to the ionic crosslinked materials at different v/v % concentrations (5, 10, 20%). All materials have 2% w/v Allura red. The dashed lines represent the range of reported human blood viscosity profile<sup>49</sup> fitted with a polynomial trend line.

XG was used as a co-polymer in the materials since it has shear-thinning properties<sup>221</sup>, good compatibility with alginate<sup>222-224</sup>, and provides stability<sup>225</sup>. Low concentrations of XG were necessary to design materials within the human

viscosity range since XG has excellent gelation properties<sup>225</sup> and high concentrations led to highly viscous materials. The higher assessed XG concentration ( $5.0 \times 10^{-3}\%$  w/v) had more shear thinning behaviour compared to the lower concentration, and when incorporated with low amounts of MPs showed typical properties of human blood (Figure 5.1, B). Therefore,  $5.0 \times 10^{-3}\%$  w/v XG was chosen as the optimal co-polymer concentration for the material base.

The optimal concentration of  $\text{CaCl}_2$  was chosen primarily based on the shear thinning behaviour (Figure 5.2). The shear-thinning behaviour of blood plays an important role in pattern formation at the crime scene since many impact events occur at high shear rates (e.g., impact velocities)<sup>16,21</sup>. While modelling blood spread can be done using effective viscosity<sup>226</sup>, the FBS materials should be able to mimic the entirety of the pseudoplastic behaviour since bloodstain pattern formation can occur across a range of shear rates<sup>49</sup>. As mentioned, materials made with higher concentrations of  $\text{Ca}^{2+}$  were observed to have more shear thinning, similar to other works<sup>227,228</sup>. 2 mM  $\text{CaCl}_2$  was chosen as the optimal crosslinking concentration since it had the most relevant shear thinning behaviour and displayed high shear viscosities in the middle of the human

range, especially when incorporated alongside MPs (Figure 5.2). The addition of the MPs appears to play a large role in altering the viscosity - even at a low concentration of 10% v/v - while maintaining the desirable non-Newtonian behaviour and exhibiting an important resemblance to the relationship between RBCs and viscosity in human blood<sup>17,28</sup>. The change in viscosity with small relative amounts of particles could be due to the size and morphology of the particles (discussed in Section 5.3.2) and/or their properties relating to deformability (Young's modulus). Other work has shown similar phenomena with 6  $\mu\text{m}$  stiff spherical particles, which have Young's modulus values of 2-6 GPa<sup>16</sup> ( $2\text{-}6 \times 10^6$  kPa). While we did not explicitly explore the deformability of our particles in this work, visualization of the drying of the FBS using microscopy suggests the MPs display deformability (Appendix II Figure A2.9). It has also been shown that calcium-alginate beads made from similar concentrations (although much larger in size) have Young's modulus values around 0.46 MPa<sup>229</sup> (460 kPa), suggesting deformability of our MPs, although they have slightly larger values than RBCs which typically display values between 1-30 kPa<sup>16,55</sup>. Exploring the deformability of our MPs is an important future avenue to fully understand the FBS behaviour in spreading dynamics<sup>16</sup>.

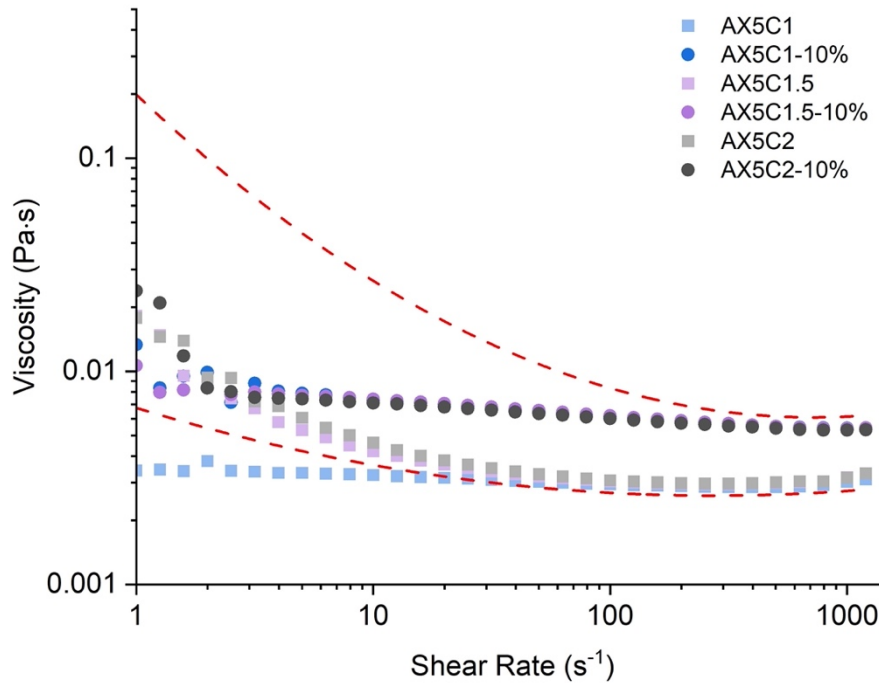


**Figure 5.2.** Viscosity profiles of materials made using 1% w/v alginate, 0.0005% w/v XG (AX5), 2% w/v Allura red with various  $\text{CaCl}_2$  concentrations ("C", 1, 1.5, 2 mM) and MP concentration (v/v %, 0, 10%). The dashed lines represent the range of reported human blood viscosity profile<sup>49</sup> fitted with a polynomial trend line.

The addition of fillers to the materials was necessary to achieve the most relevant fluid property profiles and visual characteristics. The MPs are essential to the synthetic blood material to imitate the cellular components of blood – such as the RBCs and WBCs, a concept discussed and validated in our previous work with DNA-crosslinked MPs<sup>218</sup>. Talc was added to increase the opacity of the materials for practical applications in forensic research and training since the combination of alginate/XG and red dye was relatively translucent (Appendix II Figure A2.10). Ferric citrate was desired due to its oxidative properties and

resemblance to the colour changes in blood relating to the aging process *ex vivo*<sup>230,231</sup>. In addition, Tween 20 was incorporated into the materials to lower the surface tension to the relevant human range without affecting the viscosity<sup>215,232</sup> and improve spreading on surfaces<sup>28</sup>.

Compared to the base material of alginate, XG, Allura red, and calcium chloride (AX5C2), the addition of a small amount of talc had little influence on the viscosity profile but did appear to lower the viscosity at high shear rates (Figure 5.3, A). The addition of ferric citrate, also at a low concentration, had an evident influence on the viscosity of the material - namely the decrease in the high shear viscosity and apparent loss in shear thinning behaviour, resembling a Newtonian fluid. When combined, the viscosity of the materials made with both talc and ferric citrate was very similar to those made with only ferric citrate, suggesting that ferric citrate has a greater effect on the material viscosity. Fe<sup>3+</sup> is capable of crosslinking with both alginate and xanthan gum<sup>233-235</sup>. It could be that the lower viscosity of the material when ferric citrate was included indicates a disruption or competitive binding/exchange in Ca<sup>2+</sup> for Fe<sup>3+</sup> ions. Materials made with just the base (AX5C2) and MPs up to 10% v/v all had relevant viscosity profiles to



human blood; however, the visual characteristics of blood were best achieved when MPs, talc, ferric citrate, and Tween 20 were all incorporated.

To include all desired fillers, the MP concentrations needed to be less than 10% v/v, since the combination of all components had too high of viscosities (Figure 5.3, A). Therefore, when analyzing slightly smaller concentrations of MPs added with the three desired fillers, a concentration of 9.5% v/v particles produced relevant behaviour of human blood (Figure 5.3, B). It is important to note that the inclusion of the three fillers (talc, Tween 20, and ferric citrate) was not only necessary to accomplish the visual features of blood (in addition to the Allura red), but their combination was necessary to achieve relevant pseudoplastic behaviour. When talc or ferric citrate was mixed with Tween 20, the materials had viscosities that were relatively high and exhibited abnormal shear thinning behaviour (Figure 5.3, A); however, when combined, the shear thinning is very similar to that of blood and the obtained high shear viscosities are also appropriate (Figure 5.3, B).

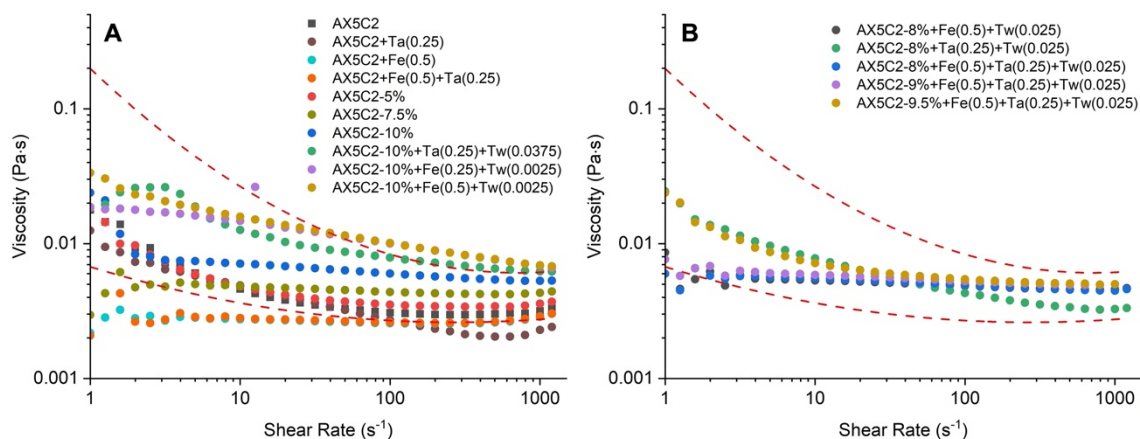


**Figure 5.3.** Viscosity profiles of materials made using 1% w/v alginate, 0.0005% w/v XG and 2 mM CaCl<sub>2</sub> (AX5C2) with various filler concentrations: talc ("Ta", 0, 0.25% w/v), ferric citrate ("Fe", 0, 0.5% w/v), Tween 20 ("Tw", 0, 0.0025, 0.025, 0.0375 % v/v), and MP concentration (0, 5, 7.5, 10% v/v) (A). Profiles in (B) shows a narrow range of MPs (8-9.5%) with various filler combinations. All materials contain 2% w/v Allura red dye. The dashed lines represent the range of reported human blood viscosity profile<sup>49</sup> fitted with a polynomial trend line.

Finally, we assessed the limit of ferric citrate that could be added to the materials. Since ferric citrate can imitate the oxidation process of blood once deposited, a higher concentration is ideal to observe the oxidative changes. Ferric citrate can also have interesting features related to wettability of the materials, where Fe<sup>3+</sup>-alginate interactions can lead to more hydrophobic material surfaces<sup>235</sup>, which can play a role in stain and pattern formation. Preliminary tests with ferric citrate above 1% w/v concentrations caused gelation, so concentrations at or below 1% were assessed. Interestingly, the higher concentration of ferric citrate added, the lower the viscosity of the materials, and ultimately the loss of shear thinning behaviour at 1% w/v ferric

citrate (Figure 5.4, A). This observation is like the behaviour previously observed (Figure 5.3) and suggests the disruption of the Ca-alginate interaction by  $\text{Fe}^{3+}$ . Although  $\text{Fe}^{3+}$ -alginate gels are known to have enhanced mechanical stability and stiffness<sup>235</sup>, we did not investigate oscillatory tests in our material optimization stage. While it could be argued that based on viscosity alone, 0.5% or 0.75% w/v ferric citrate is ideal, the evaluation of the drip stain features of droplet spread ( $D_s$ ) and the number of spines made from these materials supports the use of 0.5% w/v ferric citrate since it was most like the bovine blood (Figure 5.4, B, C).

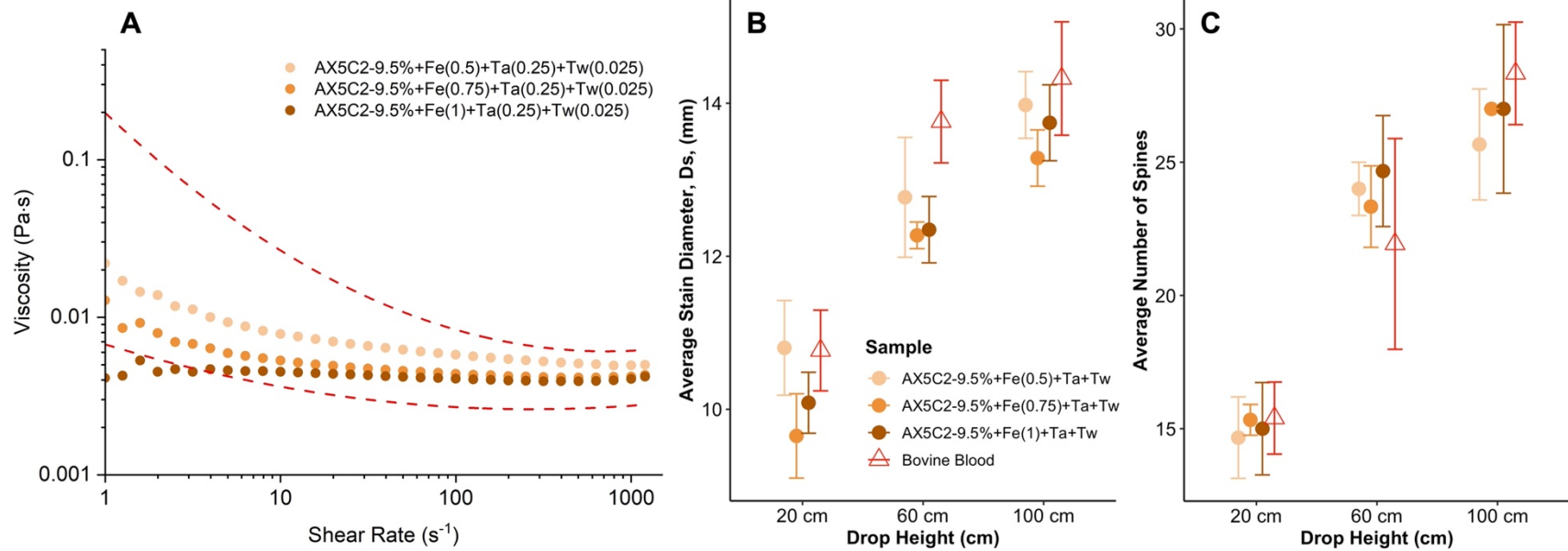


**Figure 5.4.** Influence of ferric citrate on material viscosity (A). The dashed lines represent the range of reported human blood viscosity profile<sup>49</sup> fitted with a polynomial trend line. The effect of ferric citrate on drip stain features of average stain diameter (B) and the average number of spines (C) compared to bovine blood ( $n=2$ ) is also shown.

### 5.3.2 Forensic Blood Simulant (FBS)

The FBS material has similar fluid properties to human blood at physiological temperature (37°C) and visually looks like fresh blood (Table 5.2). It should be noted that the density of the material is lower than human blood, but is comparable to other synthetic blood materials<sup>54,55</sup>. The colour of the FBS resembled fresh blood, but the potency of the Allura red dye led to difficulty in observing the low concentration of ferric citrate, where stains made with the FBS material did not undergo any colour changes. To overcome this colour difference, we incorporated a small amount of blue dye to emulate the colour of blood typically observed by BPA experts at the crime scene. The addition of the blue dye did not influence the viscosity profile of the FBS material, and both materials show reproducibility within the human range (Figure 5.5).

**Table 5.2.** Summarized property measurements of FBS material, FBS + blue dye (FBS + B), the bovine blood used (n=2) and the reported human ranges for each property summarized previously<sup>25</sup>. †The density was measured relative to MilliQ water.

Material	Surface Tension (mNm <sup>-1</sup> )	Effective Viscosity	Relative Density <sup>†</sup>
		(>100 s <sup>-1</sup> ) (mPa·s)	(kgm <sup>-3</sup> )
FBS	53.04 ± 1.01	6.03 ± 1.16	1025.80 ± 40.40
FBS + B (DNA)	52.66 ± 0.62	6.04 ± 0.35	1017.08 ± 9.75
Bovine Blood	58.17 ± 1.27	3.35 ± 0.13	1069.03 ± 8.06
Human blood	51-61	3.2-6.93	1052-1063

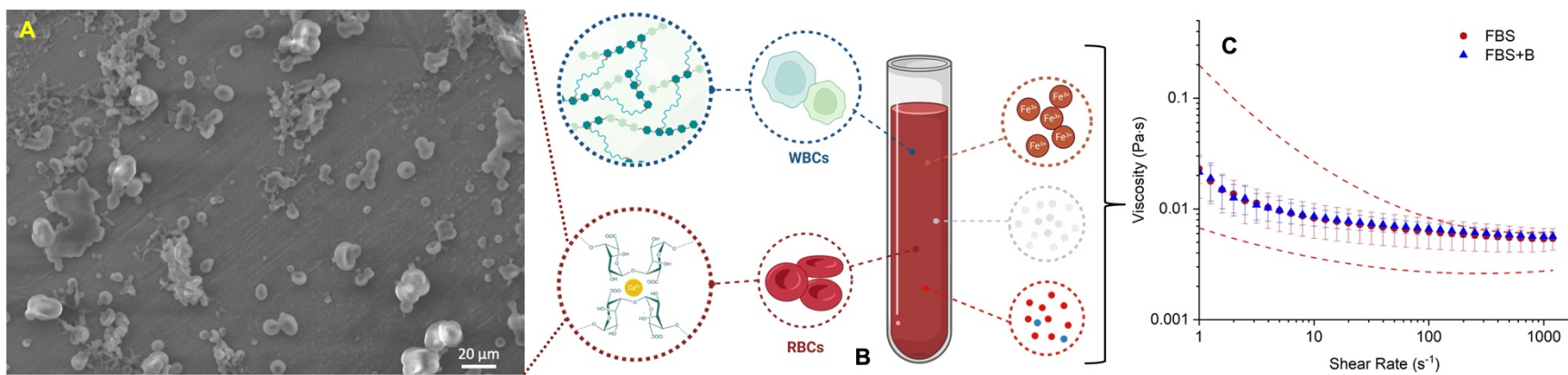


**Figure 5.5.** SEM image of concentrated MPs (A), the FBS components (B) and the average viscosity profiles (C) of FBS ( $n=7$ ) and FBS with 0.4% v/v blue dye (FBS+B,  $n=4$ ). The error bars represent the standard deviation of the replicates. The dashed lines represent the range of reported human blood viscosity profile<sup>49</sup> fitted with a polynomial trend line. Image in B was created with BioRender.com<sup>12</sup>.

<sup>12</sup> Copyright permission is in Appendix I.

The high water content of hydrogels is similar to blood plasma (~92% water)<sup>28</sup>, and provides other properties of blood plasma including viscoelasticity<sup>27</sup> since alginate and xanthan hydrogels are viscoelastic materials<sup>197,233</sup>. While not evaluated in this work, the soft electrosprayed MPs can drive the viscoelastic behaviour further, similar to RBCs which are known to play a crucial role in the spreading and splashing dynamics<sup>16</sup>. Ideally, MP concentration would be representative of the PCV% of human blood, which typically ranges from 40-50%<sup>18-25</sup>. Our cellular components only account for 9.5% v/v of the total material, largely due to the size of MPs used (~22  $\mu\text{m}$ ) compared to typical RBC size. Interestingly, the morphology of some of the MPs when visualized with SEM appears to have biconcave shapes and sizes similar to RBCs (Figure 5.5, A). Other work has generated similar morphologies of electrosprayed alginate MPs using the addition of alcohols in the collection bath and increasing the flow rate<sup>98</sup>. Enhancing the production of these MP morphologies shows promise for the FBS to achieve desirable PCV% values in the future. Regardless, since we could only achieve a low ratio of MPs in the FBS, the incorporation of other elements that drive the pseudoplastic behaviour such as alginate and xanthan gum was necessary. The spreading of blood is governed by the deformability of RBCs which aid in the resistance of friction between cells, where friction reduces

the spreading factor<sup>16,236</sup>. The soft gel characteristics of the MPs can allow for deformability and the ionically crosslinked alginate can also add overall deformability<sup>235</sup>, as discussed above. Importantly, the charged nature of the particles also aids in reducing friction between particles since similar surface charges would lead to repulsion and increased spreading factor. When assessed using microscopy, the MPs were shown to retain their shapes after shear was applied and the 'bloodstain' has formed (Appendix II Figure A2.11). While this was not directly assessed in this work, the use of high-speed video in the future to assess these spreading parameters would be valuable to understand the capabilities of the FBS in more complex crime scene scenarios, especially since both the microparticles and the FBS material displayed viscoelastic behaviour (Appendix II Figure A2.12).

Bovine blood was used in this validation to compare the FBS behaviour on our investigated target surface (67 lb coverstock) to control for the influence of surface variation on the resulting stain features. Relating to the applicability in BPA scenarios, both FBS and FBS+B have similar spreading ratios ( $D_s/D_0$ ) to bovine blood (Figure 5.6) and similar stain features (number of spines and scallops). The number of spines and scallops is an important and sometimes



overlooked feature in synthetic blood development, but plays a crucial role in modelling bloodstain mechanisms<sup>5,9,37,38</sup>. Importantly, the addition of the blue dye improved the stain appearance and more closely resembles day(s) old blood (Figure 5.7). It has been pointed out that comparing synthetic materials to blood may not be enough, and understanding how the material differs from Newtonian materials such as water, is also valuable<sup>39</sup>. The stain morphologies made with the FBS more closely resemble blood, where comparison of our drip stains shows a marked difference from water. Given that the FBS is water based, this emphasizes the role of the components that drive the non-Newtonian behaviour, such as the MPs, the alginate and xanthan.

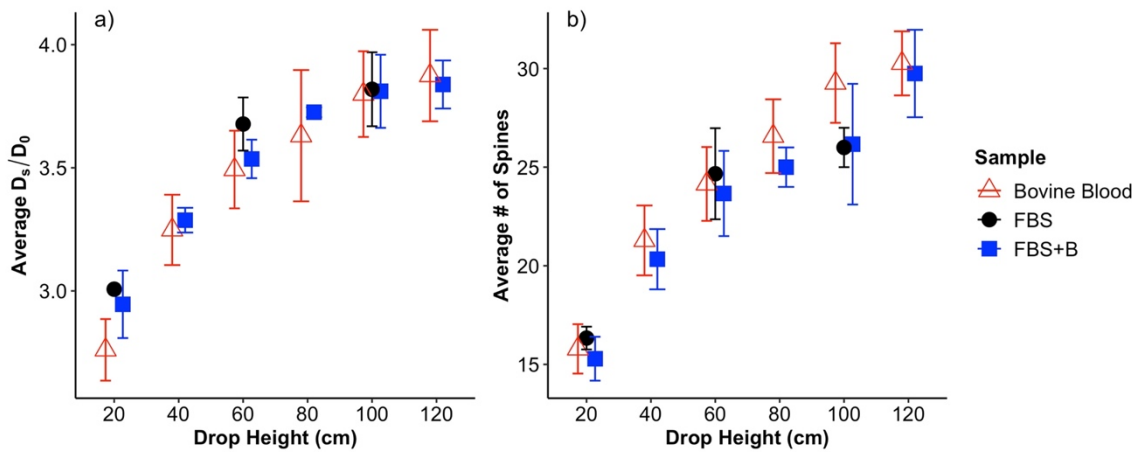


**Figure 5.6.** Overall comparison between FBS candidate (AX5C2 + Ferric citrate + Talc + Tween 20 + 9.5% particles), FBS + B (FBS material + 0.4% v/v blue dye) and bovine blood for 90° drip stains made on 67 lb coverstock. The comparison shows (a) the average spreading ratio ( $D_s/D_0$ ) and (b) the average number of spines.

### 5.3.3 BPA Scenarios

The ability of our FBS material to be used to make multiple bloodstain patterns enhances its use in training scenarios. Both FBS materials (with and without blue dye) can be used for practical BPA training scenarios to determine the impact angle ( $\alpha$ ) (Figure 5.7) and displayed general expected trends of drip stain simulation on a variety of target surfaces (Appendix II Figure A2.13). Another important pattern type is an impact pattern, which is a pattern made when an object strikes a liquid blood source<sup>237</sup>. Impact patterns made using the FBS+B show visually similar stain features to those made with whole blood (Figure 5.8). In addition, an important consideration for BPA training and research is the ability to process blood evidence to obtain DNA profiles. This concept is discussed in Section 5.3.5.

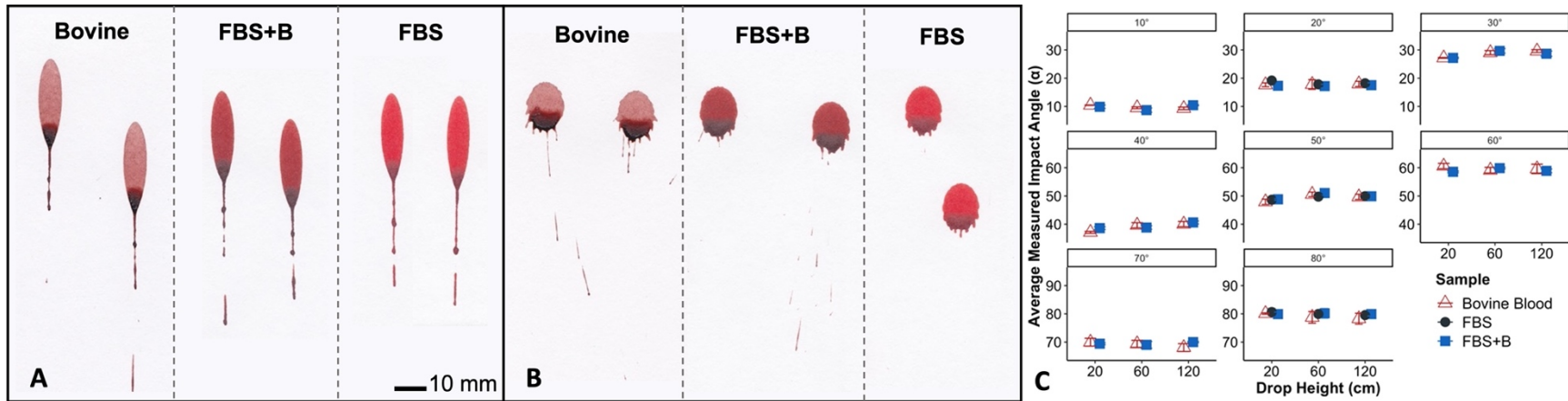


**Figure 5.7.** Comparison of FBS vs FBS + B drip stains with bovine blood (rep 1) from 10-90° impact angles. Comparisons show the stain features at A: 20°, 60 cm and B: 50°, 60 cm and C: the measured impact angle between the three materials.

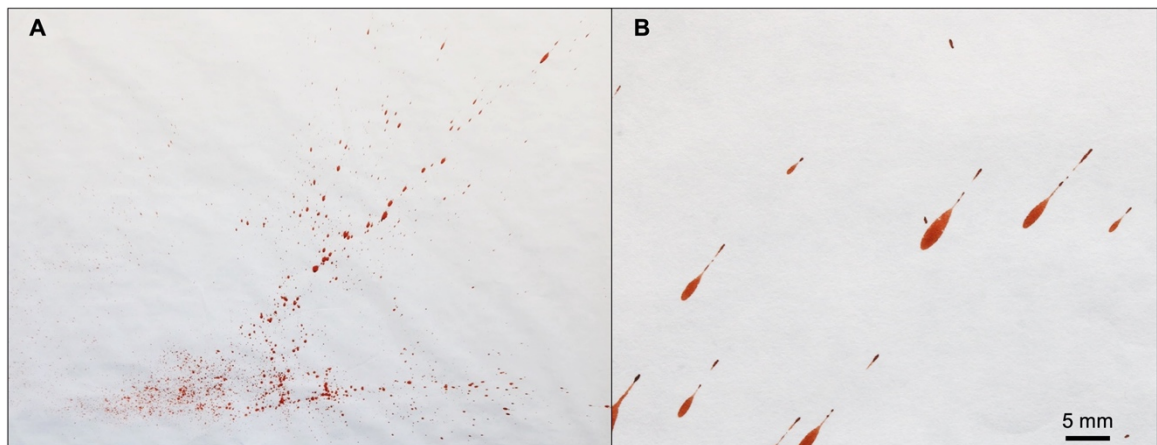


**Figure 5.8.** Impact pattern (A) made using FBS+B candidate and a close-up of upward moving stain morphology (B).

#### 5.3.4 FBS Stability

Understanding the shelf-life of the FBS materials has considerable application for BPA researchers and practitioners, where an improved shelf life over whole blood is desirable<sup>46</sup>. Designing a stable FBS was sought in our material development to provide accessible and reliable materials that have reasonable expiration. Fe<sup>3+</sup>-alginate hydrogels have been shown to have superior stability due to higher crosslinking density with GG and MG blocks on the alginate backbone<sup>235</sup> and xanthan gum has sufficient stabilizing properties<sup>225</sup>. We believe these components play a role in the stability of our FBS material over time (Figure 5.9). The stability of the properties of our material over the course of 12 weeks has a comparable shelf-life to other synthetic blood materials<sup>55</sup> and

can be stored at room temperature - enhancing its accessibility. The surface tension of the FBS did rise over the tested time interval but was shown to decrease again at 4 weeks (Table 5.3). This behaviour is likely caused by the potential degradation of Tween 20 in aqueous solutions<sup>238</sup>, especially since the base material (that does not contain Tween 20) showed little variation over the 4 weeks. Despite this, the other properties remained relatively constant. The average effective viscosity generally decreased over 10 weeks, with an apparent decrease in the extent of shear thinning behaviour of the FBS at 10 weeks. However, our assessment of the stain features at 12 weeks showed similar spreading ratios to fresh FBS. At 12 weeks of aging, the MPs remained intact which reasonably contributes to the FBS stability over time (Figure 5.9).

It is also important to note the similarities in the fluid properties between the FBS with and without DNA (Table 2, Figures 5 & 9). The inclusion of a complete DNA profile (and added DNA) may influence these properties - namely the viscosity - and will be explored further in the future. The included DNA in our material has been shown to have long-term stability when encapsulated in a hydrogel environment for up to 21 days<sup>197</sup>. After 4 weeks, the DNA in the FBS+B remained functional, where the material was able to be processed and generated the

expected allele size and morphology, showing the long-term stability of the genetic components as well.

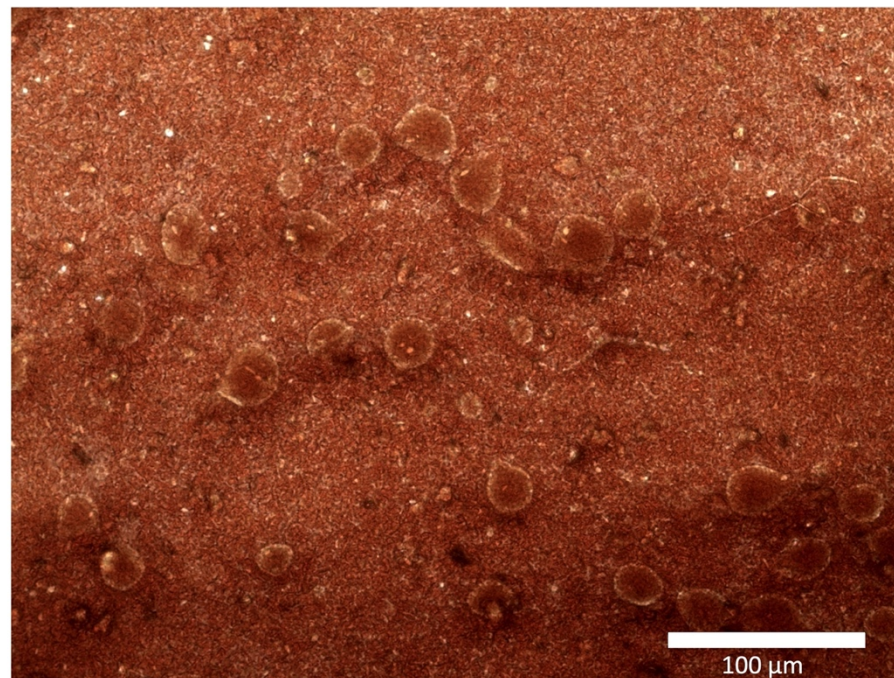
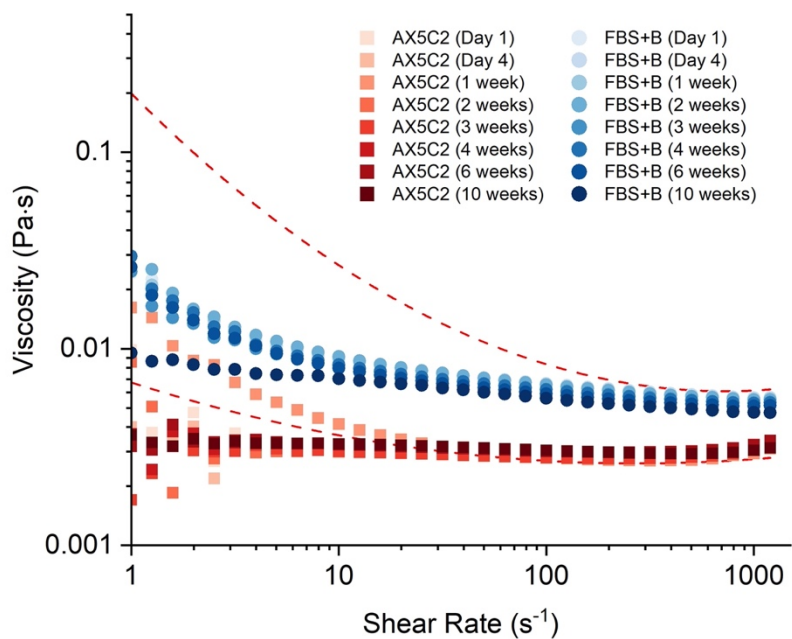


**Figure 5.9.** Viscosity profile of FBS base (AX5C2, includes red dye, talc and ferric citrate), and the FBS+B material over 10 weeks (left). The FBS + B material contains 0.5% v/v DNA-crosslinked MPs. The dashed lines represent the range of reported human blood viscosity profile<sup>49</sup> fitted with a polynomial trend line. The image on right is a microscopic image of MPs within the FBS after 12 weeks of storage.

**Table 5.3.** Summarized property measurements of DNA-FBS + blue dye (FBS + B) over 12 weeks.

Time (weeks)	Surface Tension (mN·m <sup>-1</sup> )	Effective Viscosity (mPa·s)	Density (kg/m <sup>3</sup> )	D <sub>s</sub> /D <sub>0</sub>
Day 1	52.72 ± 0.62	6.04 ± 0.35	1017.08 ± 9.75	20 cm: 2.85 ± 0.14 60 cm: 3.43 ± 0.09 100 cm: 3.82 ± 0.18
1	55.23 ± 0.55	5.93 ± 0.35	1014.29 ± 24.16	20 cm: 2.86 ± 0.08 60 cm: 3.56 ± 0.10 100 cm: 3.76 ± 0.08
2	58.15 ± 0.54	5.92 ± 0.36	1013.37 ± 5.06	20 cm: 2.98 ± 0.18 60 cm: 3.66 ± 0.07 100 cm: 3.84 ± 0.06
3	60.80 ± 0.40	5.66 ± 0.31	1012.04 ± 5.65	20 cm: 3.05 ± 0.02 60 cm: 3.61 ± 0.07 100 cm: 3.87 ± 0.10
4	57.65 ± 2.24	6.02 ± 0.35	1015.40 ± 15.09	20 cm: 3.02 ± 0.04 60 cm: 3.59 ± 0.09 100 cm: 3.89 ± 0.09
6	63.78 ± 0.33	5.40 ± 0.27	1017.71 ± 4.53	-
10	62.58 ± 0.69	5.08 ± 0.29	1023.98 ± 7.85	-
12	-	-	-	20 cm: 2.96 ± 0.04 60 cm: 3.59 ± 0.06 100 cm: 3.89 ± 0.11

### 5.3.5 Genetic capabilities

The FBS made with DNA-alginate crosslinked MPs (DNA-FBS) was able to be processed and interpreted similarly to human blood evidence - demonstrating the potential of these materials for forensic training scenarios (Figure 5.10). The use of a gel extraction kit provides an analogous procedure to DNA evidence processing and can effectively extract the crosslinked DNA from the FBS. This method does, however, have some visible differences from blood extraction.



The use of ethanol-based wash buffer caused some of the fillers to precipitate, where a red powder sat above the filter. A separate experiment assessing the extraction procedure with materials made with each filler individually showed that all fillers (talc, ferric citrate, Allura red) precipitated upon filtration and washing during DNA extraction; but since the Allura red dye is present in a higher concentration (2% w/v), the precipitate appears dominantly red. Upon the elution step with water, the dye is rehydrated, and the eluted DNA volume is red, which leads to PCR reactions that are also red in colour (Appendix II Figure A2.14). However, despite the apparent filter clogging and eluent colour, the DNA could still be extracted and amplified. The DNA amplification is best achieved using bovine serum albumin (BSA) in the PCR master mix, and dilution of the extracted DNA prior to PCR amplification (a 1:10 dilution was shown to be sufficient, Figure 5.10).

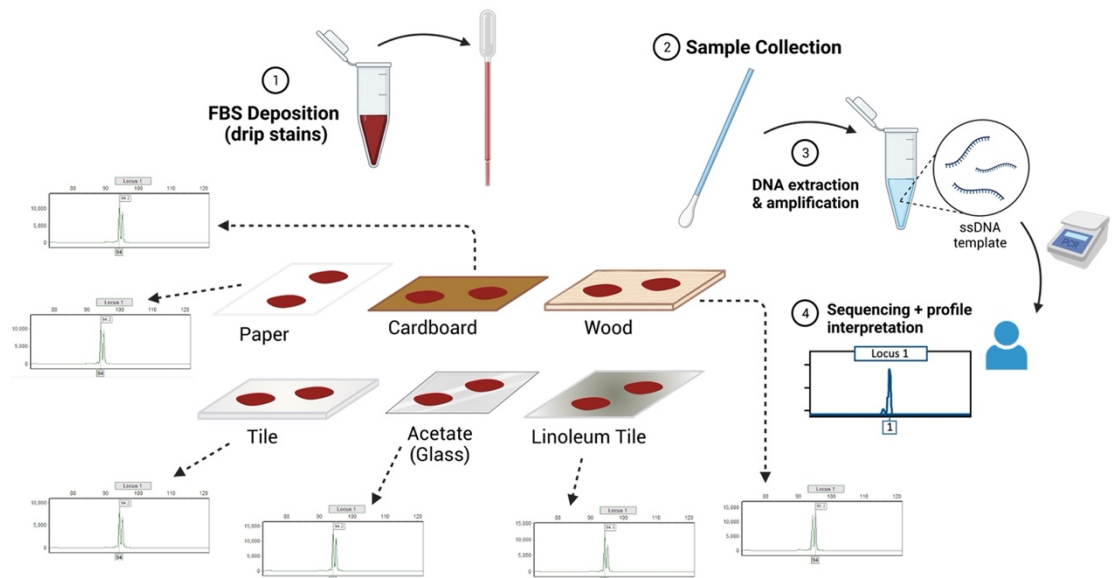


**Figure 5.10.** Process of DNA extraction from FBS material swabbed from various substrates. Each material was able to produce the included allele crosslinked in the MPs within the FBS. Image was created with BioRender.com.<sup>13</sup>

It is worth mentioning that the DNA-FBS explored here only assessed a single allele mimetic for the CSF1PO locus of the human genome. Our previous work has shown the potential of co-amplification of alleles within alginate hydrogels<sup>197</sup>, and suggests the potential for multiplexing to incorporate a relevant genetic profile for training needs in forensic science. We reason that the incorporation of an analogue “full DNA profile” is possible and depends on

---

<sup>13</sup> Copyright permission is in Appendix I.

the training needs of the forensic community. For example, these materials were designed for training in basic BPA pattern recognition and blood evidence processing, where it may be sufficient to only incorporate some loci for training purposes. Regardless, the DNA-FBS demonstrates functionality across a variety of substrates, further supporting the use of these materials in BPA scenarios with or without DNA.

#### **5.4 Conclusions**

This work investigated the design of multi-component FBS materials for use in forensic science research and training. We explored the complete design of these FBS materials and discuss the effect of each component. Our FBS materials are hydrogel-based that use alginate and xanthan gum co-polymers to promote pseudoplastic behaviour of blood. Importantly, we also incorporate MPs that were made using electrospray ionization to provide both DNA and non-DNA crosslinked MPs for added functionality. Our MPs can be reproducibly developed in the lab and their incorporation into the FBS material can deliver viscoelastic properties to enable accurate material behaviour and stain features. The MPs can also be made to contain relevant synthetic human DNA that can

integrate a full genetic profile (if desired), providing enhanced training options to other blood analogues (synthetic or mammalian). The FBS was shown to behave predictably and reproducibly in BPA scenarios of drip stains and impact patterns. Further, the material contains relevant fluid properties, especially relating to the viscosity and surface tension which play a major role in pattern formation. The FBS was also shown to have good stability, with a shelf life of over 4 weeks when stored in ambient conditions where the properties remain relevant. Future work should investigate the spreading dynamics of our material compared to human blood in more detail, further assessing its feasibility in other complex mechanisms related to BPA. The goal of this material is to provide safe, reliable, and long-term options for practitioners, researchers, and students to use viable blood alternatives in many areas relating to blood.

# Chapter 6

---

Conclusions, future work & considerations.

## **6.1 General Conclusion of Thesis**

The works outlined in this thesis have demonstrated the value of alginate-based hydrogels in soft material design, including FBS development. The alginate hydrogels were shown to provide favourable environments for ssDNA encapsulation and prolonged DNA stability (Chapter 2). In Chapter 2, the designed ssDNA was shown to be functional and suitable as mimetic human DNA for training purposes. The alginate hydrogels not only provided DNA functionality and stability, but the characterization of DNA binding in this system was also more conclusive and comprehensive (Chapter 4) compared to the other explored sol-gel systems discussed in Chapter 3.

The primary work described in Chapter 3 provides a valuable tool to the forensic community on the use of HRMS for the analysis of large biomacromolecules such as DNA. HRMS was shown to be a viable technique to accurately characterize ssDNA, and importantly confirmed that large DNA molecules remain intact when undergoing electrospray ionization. This knowledge was applied to

design a custom electrospray device that could produce microparticles representative of cellular components found in blood on a large scale.

The optimized conditions of the electrospray setup were described in Chapter 4. This chapter also demonstrated the binding between alginate and DNA using a variety of characterization techniques to investigate a hydrogel configuration (dual amine-terminated ssDNA covalently crosslinked to alginate) which has not been reported previously. Further, it was found that the DNA-alginate crosslinked materials could also be used to make MPs with the ESI and that the DNA remained functional throughout this process, supporting the use of these MPs as functional components in the FBS material.

Finally, the FBS was optimized to incorporate multiple functions of human blood such as the fluid properties and genetic capabilities. Various fillers (talc, ferric citrate, dye, Tween 20, and MPs) were modified in an alginate/xanthan gum polymer base ionically crosslinked with  $\text{CaCl}_2$  to obtain relevant viscosity, density, and surface tension of human blood (Chapter 5). The FBS material was found to be stable beyond the 4-weeks and visually looked similar to whole human blood when tested in impact patterns and drip stains on various surfaces.

Quantitatively, the drip stains made with the FBS showed similar spreading ratios, number of spines, and calculated  $\alpha$  angles when compared to stains made with bovine blood on the same surface. When DNA-crosslinked MPs were added to the FBS, stains made from this material were able to be swabbed and processed like blood evidence, demonstrating the value of the FBS in training scenarios.

## **6.2 General Commentary on FBS Performance**

The FBS material designed in this work has shown practical and demonstrative promise for use as training or research aid for BPA scenarios. Quantitatively, the material behaves like human blood at physiological temperature, providing clear relevance to scenarios that involve bloodshed at the crime scene. The use of alginate and xanthan gum as a polymer base satisfies a primary requirement of a blood simulant design relating to user safety<sup>46</sup>. Another benefit of using these polymers comes from their ability to be easily modified with crosslinkers to achieve specific function(s). The modification of alginate with the ssDNA crosslinkers in our FBS is an excellent example of alginate's potential in future

FBS development and enhancement. Through this modification, we were able to achieve genetic functionality within the FBS for added training benefits.

It should be noted that up to this point, the FBS has only been assessed using DNA-crosslinked materials that have used one strand size (or one 'allele'). The natural progression of the FBS development is the inclusion of a more complete reference genome, if desired, to assess its function in training. This reference genome could include the same number of CODIS loci used in casework or can use a number of loci that is sufficient for training scenarios. It was shown in Chapter 2 that DNA encapsulated in ionically crosslinked calcium-alginate hydrogels could be co-amplified with 2 'alleles'. It is reasoned that optimizing the multiplexing reaction and subsequent crosslinking ratios would be the only challenges in the design of a complete genetic reference since alginate has been shown to have no inhibition on DNA functionality. Collaboration with the forensic community on what exactly is required for training can help design tailored materials for this purpose. This has value in academic settings where students can be trained in biological evidence processing and interpretation of victim/suspect profiles and/or complex mixtures. The DNA-encapsulated materials discussed in Chapter 2 also provided added benefits; these relatively



clear materials can be used to create DNA-containing films on forensically relevant pieces of evidence and can be processed accordingly for training in evidence processing techniques.

The shelf-life of the FBS material was only investigated up to 12 weeks, but shows stability in the fluid properties within this time. This characteristic satisfies another requirement of designing viable FBSs, especially since it surpasses the shelf-life of most mammalian blood sources with consistent properties<sup>18,20,25,41</sup>. To truly test the applicability of the FBS in training scenarios, it should be integrated into training programs such as those in university courses or practitioner training programs. This will allow for collaboration on improvements and needs of the forensic community for future FBS materials.

### **6.3 Future Work in FBS Design**

The future of FBS development using the hydrogel system has many exciting avenues for continued development for applications in forensic science. Alginate hydrogels have been designed for a wide variety of applications in fields ranging from biomedical to the food industry, and its potential can be just

as dynamic in forensic science. From a training perspective, the FBS can be enhanced to include relevant properties necessary for accurate and reliable BPA training. The FBS can be modified with chemiluminescent dyes as fillers to provide enhanced training opportunities for sequencing the formation of bloodstain patterns as was previously demonstrated in the FBS materials designed by Stotesbury *et al.*<sup>46</sup>. Further, using a HRP enzyme that has structural similarities to hemoglobin has been shown to produce similar kinetics to reaction with luminol when integrated into a sol-gel matrix<sup>52</sup>. Theoretically, the same HRP enzyme can be encapsulated within the MPs for a similar reaction with luminol, especially given the smaller relative size of HRP compared to the MPs<sup>239</sup>. Research into the optimal concentrations of HRP, encapsulation rate, spray conditions, and the overall influence on the FBS fluid properties will need to be investigated. Integration of HRP into the MPs will provide chemically relevant RBC mimetics that could easily be integrated with the DNA-crosslinked MPs for an FBS with physical, biological, and chemical relevance in forensic scenarios. HRP has a high molecular weight<sup>239</sup> and the incorporation of this and other cellular components can also help achieve a more dense FBS material closer to the human blood range.

Further, the incorporation of other relevant biological and chemical components of blood can also be integrated into the FBS. This can include amino acids, and even the potential for clotting simulation. Alginate hydrogels are often used in drug release applications that can release the doped agents at a controlled rate<sup>62,98,240</sup>. It is reasoned that similar mechanisms can be used to release gelling agents or initiate crosslinking to simulate appropriate clotting rates of human blood *ex vivo*. These features typically require covalent modification of alginate, but could be effectively applied in a forensic setting. Other responsive functionalization could be easily integrated into the alginate backbone to have stimuli-responsive functions such as gelation, oxidation, degradation, etc. Mimicking blood degradation could be of value in time since deposition (TSD) where the determination of the age of a bloodstain is desired. It has been reported that inter-donor variability is a contributing issue in the accuracy of predictive models to estimate bloodstain age<sup>114,241,242</sup>, and designing materials that have standardized degradation could prove useful in building and testing TSD models.

## **6.4 Final Remarks**

The future of these materials is promising, and their limit is the innovation of their design. It is the hope that this work, in combination with the research already done on FBS materials, inspires collaboration between research and practice to strive towards standardized, functional and holistic FBS materials for research and training in forensic science. The aim(s) of the FBS designed here is to enhance accessibility for institutions that cannot currently access reliable blood sources. By designing materials that can be safely and reliably integrated into training and research programs, we can investigate and equip individuals with the tools to investigate the complex questions that are currently pressing in forensic science.

## References

- (1) Bevel, T.; Gardner, R. R. *Bloodstain Pattern Analysis: With an Introduction to Crime Scene Reconstruction*, 3rd ed.; CRC Press: Boca Raton, FL, 2008.
- (2) James, S. H.; Kish, P. Erwin.; Sutton, T. Paulette. *Principles of Bloodstain Pattern Analysis: Theory and Practice*; CRC Press: Boca Raton, FL, 2005.
- (3) National Academy of Science. *Strengthening Forensic Science in the United States: A Path Forward*; 2009. [https://doi.org/10.1016/0379-0738\(86\)90074-5](https://doi.org/10.1016/0379-0738(86)90074-5).
- (4) President's Committee of Advisors on Science and Technology. *Forensic Science in Criminal Courts: Ensuring Scientific Validity of Feature-Comparison Methods*; 2016.
- (5) Hulse-Smith, L.; Mehdizadeh, N. Z.; Chandra, S. Deducing Drop Size and Impact Velocity from Circular Bloodstains. *J Forensic Sci* **2005**, 50 (1), 54-63. <https://doi.org/10.1520/JFS2003224>.
- (6) Hulse-Smith, L.; Illes, M. A Blind Trial Evaluation of a Crime Scene Methodology for Deducing Impact Velocity and Droplet Size from Circular Bloodstains. *J Forensic Sci* **2007**, 52 (1), 65-69. <https://doi.org/10.1111/j.1556-4029.2006.00298.x>.

- (7) De Bruin, K. G.; Stoel, R. D.; Limborgh, J. C. M. Improving the Point of Origin Determination in Bloodstain Pattern Analysis. *J Forensic Sci* **2011**, *56* (6), 1476-1482. <https://doi.org/10.1111/j.1556-4029.2011.01841.x>.
- (8) Kabaliuk, N.; Jermy, M. C.; Williams, E.; Laber, T. L.; Taylor, M. C. Experimental Validation of a Numerical Model for Predicting the Trajectory of Blood Drops in Typical Crime Scene Conditions, Including Droplet Deformation and Breakup, with a Study of the Effect of Indoor Air Currents and Wind on Typical Spatter Drop Trajectories. *Forensic Sci Int* **2014**, *245*, 107-120. <https://doi.org/10.1016/j.forsciint.2014.10.020>.
- (9) Laan, N.; De Bruin, K. G.; Slenter, D.; Wilhelm, J.; Jermy, M.; Bonn, D. Bloodstain Pattern Analysis: Implementation of a Fluid Dynamic Model for Position Determination of Victims. *Sci Rep* **2015**, *5*, 1-8. <https://doi.org/10.1038/srep11461>.
- (10) Illes, M.; Boués, M. Investigation of a Model for Stain Selection in Bloodstain Pattern Analysis. *Can Soc Forensic Sci J* **2011**, *44* (1), 1-12. <https://doi.org/10.1080/00085030.2011.10768137>.
- (11) Taylor, M. C.; Laber, T. L.; Kish, P. E.; Owens, G.; Osborne, N. K. P. The Reliability of Pattern Classification in Bloodstain Pattern Analysis, Part 1:

- Bloodstain Patterns on Rigid Non-Absorbent Surfaces. *J Forensic Sci* **2016**, *61* (4), 922-927. <https://doi.org/10.1111/1556-4029.13091>.
- (12) Taylor, M. C.; Laber, T. L.; Kish, P. E.; Owens, G.; Osborne, N. K. P. The Reliability of Pattern Classification in Bloodstain Pattern Analysis–Part 2: Bloodstain Patterns on Fabric Surfaces. *J Forensic Sci* **2016**, *61* (6), 1461-1466. <https://doi.org/10.1111/1556-4029.13191>.
- (13) Hicklin, R. A.; Winer, K. R.; Kish, P. E.; Parks, C. L.; Chapman, W.; Dunagan, K.; Richetelli, N.; Epstein, E. G.; Ausdemore, M. A.; Busey, T. A. Accuracy and Reproducibility of Conclusions by Forensic Bloodstain Pattern Analysts. *Forensic Sci Int* **2021**, *325*, 110856. <https://doi.org/10.1016/j.forsciint.2021.110856>.
- (14) Ahmed, G.; Arjmandi Tash, O.; Cook, J.; Trybala, A.; Starov, V.; Tash, O. A.; Cook, J.; Trybala, A.; Starov, V. Biological Applications of Kinetics of Wetting and Spreading. *Adv Colloid Interface Sci* **2017**, *249*, 17-36. <https://doi.org/10.1016/j.cis.2017.08.004>.
- (15) Sadek, S. H.; Rubio, M.; Lima, R.; Vega, E. J. Blood Particulate Analogue Fluids: A Review. *Materials* **2021**, *14* (9), 16-21. <https://doi.org/10.3390/ma14092451>.

- (16) Yokoyama, Y.; Tanaka, A.; Tagawa, Y. Droplet Impact of Blood and Blood Simulants on a Solid Surface: Effect of the Deformability of Red Blood Cells and the Elasticity of Plasma. *Forensic Sci Int* **2021**, *331*, 111138. <https://doi.org/10.1016/j.forsciint.2021.111138>.
- (17) Baskurt, O. K.; Meiselman, H. J. Blood Rheology and Hemodynamics. *Semin Thromb Hemost* **2003**, *29* (5), 435-450. <https://doi.org/10.1055/s-2003-44551>.
- (18) Raymond, M. A.; Smith, E. R.; Liesegang, J. The Physical Properties of Blood - Forensic Considerations. *Sci Justice* **1996**, *36* (3), 153-160. [https://doi.org/10.1016/S1355-0306\(96\)72590-X](https://doi.org/10.1016/S1355-0306(96)72590-X).
- (19) Christman, D. A Study to Compare and Contrast Animal Blood to Human Blood Product. *I.A.B.P.A. News* **1996**, *12* (2), 10-25.
- (20) Larkin, B. A. J.; Banks, C. E. Exploring the Applicability of Equine Blood to Bloodstain Pattern Analysis. *Med Sci Law* **2016**, *56* (3), 190-199. <https://doi.org/10.1177/0025802414542456>.
- (21) Attinger, D.; Moore, C.; Donaldson, A.; Jafari, A.; Stone, H. A. Fluid Dynamics Topics in Bloodstain Pattern Analysis: Comparative Review and Research Opportunities. *Forensic Sci Int* **2013**, *231* (1-3), 375-396. <https://doi.org/10.1016/j.forsciint.2013.04.018>.



- (22) Wickhaml, L. L.; Bauersachs, R. M.; Wenby, R. B.; Sowemimo-Coker, S.; Meiselman, H. J.; Elsner, R. Red Cell Aggregation and Viscoelasticity of Blood from Seals, Swine and Man. *Biorheology* **1990**, *27*, 191-204.
- (23) Larkin, B. A. J.; Banks, C. E. Exploring the Effect of Specific Packed Cell Volume upon Bloodstain Pattern Analysis: Blood Drying and Dry Volume Estimation. *Can Soc Forensic Sci J* **2015**, *48* (4), 167-189. <https://doi.org/10.1080/00085030.2015.1083161>.
- (24) Palenske, N. M.; Saunders, D. K. Comparisons of Blood Viscosity between Amphibians and Mammals at 3°C and 38°C. *J Therm Biol* **2002**, *27* (6), 479-484. [https://doi.org/10.1016/S0306-4565\(02\)00020-7](https://doi.org/10.1016/S0306-4565(02)00020-7).
- (25) Orr, A.; Gualdieri, R.; Cossette, M. L.; Shafer, A. B. A.; Stotesbury, T. Whole Bovine Blood Use in Forensic Research: Sample Preparation and Storage Considerations. *Science and Justice* **2021**, *61* (3), 214-220. <https://doi.org/10.1016/j.scijus.2021.02.004>.
- (26) Thiriet, M. Biology and Mechanics of Blood Flows. Part I: Biology. In *Biology and Mechanics of Blood Flows*; Springer: New York, NY, 2008.
- (27) Brust, M.; Schaefer, C.; Doerr, R.; Pan, L.; Garcia, M.; Arratia, P. E.; Wagner, C. Rheology of Human Blood Plasma: Viscoelastic versus Newtonian

- Behavior. *Phys Rev Lett* **2013**, *110* (7), 6–10.  
<https://doi.org/10.1103/PhysRevLett.110.078305>.
- (28) Smith, F. R.; Brutin, D. Wetting and Spreading of Human Blood: Recent Advances and Applications. *Curr Opin Colloid Interface Sci* **2018**, *36*, 78–83. <https://doi.org/10.1016/j.cocis.2018.01.013>.
- (29) Rodrigues, T.; Mota, R.; Gales, L.; Campo-Deaño, L. Understanding the Complex Rheology of Human Blood Plasma. *J Rheol (N Y N Y)* **2022**, *66* (4), 761–774. <https://doi.org/10.1122/8.0000442>.
- (30) Windberger, U.; Bartholovitsch, A.; Plasenzotti, R.; Korak, K. J.; Heinze, G. Whole Blood Viscosity, Plasma Viscosity and Erythrocyte Aggregation in Nine Mammalian Species: Reference Values and Comparison of Data. *Exp Physiol* **2003**, *88* (3), 431–440. <https://doi.org/10.1113/eph8802496>.
- (31) Rosina, J.; Kvašňák, E.; Šuta, D.; Kolářová, H.; Málek, J.; Krajčí, L. Temperature Dependence of Blood Surface Tension. *Physiol Res* **2007**, *56* (Suppl. 1), S93–S98.
- (32) Hrnčíř, E.; Rosina, J. Surface Tension of Blood. *Physiol Res* **1997**, *46*, 319–321.
- (33) Mehri, R.; Mavriplis, C.; Fenech, M. Red Blood Cell Aggregates and Their Effect on Non-Newtonian Blood Viscosity at Low Hematocrit in a Two-Fluid

- Low Shear Rate Microfluidic System. *PLoS One* **2018**, 13 (7), 1-26.  
<https://doi.org/10.1371/journal.pone.0199911>.
- (34) Carneiro, J.; Lima, R.; Campos, J. B. L. M.; Miranda, J. M. A Microparticle Blood Analogue Suspension Matching Blood Rheology. *Soft Matter* **2021**, 17 (14), 3963-3974. <https://doi.org/10.1039/d1sm00106j>.
- (35) Brutin, D.; Sobac, B.; Loquet, B.; Sampol, J. Pattern Formation in Drying Drops of Blood. *J Fluid Mech* **2011**, 667, 85-95.  
<https://doi.org/10.1017/S0022112010005070>.
- (36) Yarin, A. L. Drop Impact Dynamics: Splashing, Spreading, Receding, Bouncing... *Annu Rev Fluid Mech* **2006**, 38 (1), 159-192.  
<https://doi.org/10.1146/annurev.fluid.38.050304.092144>.
- (37) Stotesbury, T.; Taylor, M. C.; Jermy, M. C. Passive Drip Stain Formation Dynamics of Blood onto Hard Surfaces and Comparison with Simple Fluids for Blood Substitute Development and Assessment. *J Forensic Sci* **2017**, 62 (1), 74-82. <https://doi.org/10.1111/1556-4029.13217>.
- (38) Adam, C. D. Fundamental Studies of Bloodstain Formation and Characteristics. *Forensic Sci Int* **2012**, 219 (1-3), 76-87.  
<https://doi.org/10.1016/j.forsciint.2011.12.002>.

- (39) Stotesbury, T.; Illes, M.; Wilson, P.; Vreugdenhil, A. A Commentary on Synthetic Blood Substitute Research and Development. *J Bloodstain Pattern Analysis* **2015**, *31* (2), 3-6.
- (40) de Castro, T. C.; Taylor, M. C.; Carr, D. J.; Athens, J.; Kieser, J. A. Storage Life of Whole Porcine Blood Used for Bloodstain Pattern Analysis. *Can Soc Forensic Sci J* **2016**, *49* (1), 26-37.  
<https://doi.org/10.1080/00085030.2015.1108770>.
- (41) Sparer, A.; Serp, B.; Schwarz, L.; Windberger, U. Storability of Porcine Blood in Forensics: How Far Should We Go? *Forensic Sci Int* **2020**, *311*, 110268. <https://doi.org/10.1016/j.forsciint.2020.110268>.
- (42) Kaibara, M.; Shinozaki, T.; Kita, R.; Iwata, H.; Ujiie, H.; Sasaki, K.; Li, J. Y.; Sawasaki, T.; Ogawa, H. Analysis of Coagulation of Blood in Different Species with Special Reference to Procoagulant Activity of Red Blood Cell. *J Japanese Soc Biorheol* **2006**, *20* (1), 35-43.
- (43) Horner, J. S.; Wagner, N. J.; Beris, A. N. A Comparative Study of Blood Rheology across Species. *Soft Matter* **2021**, *17* (18), 4766-4774.  
<https://doi.org/10.1039/d1sm00258a>.

- (44) Amin, T. M.; Sirs, J. A. The Blood Rheology of Man and Various Animal Species. *Quarterly Journal of Experimental Physiology* **1985**, *70* (1), 37-49. <https://doi.org/10.1113/expphysiol.1985.sp002895>.
- (45) Adili, N.; Melizi, M.; Belabbas, H. Species Determination Using the Red Blood Cells Morphometry in Domestic Animals. *Vet World* **2016**, *9* (9), 960-963. <https://doi.org/10.14202/vetworld.2016.960-963>.
- (46) Stotesbury, T.; Bruce, C.; Illes, M.; Hanley-Dafoe, R. Design Considerations for the Implementation of Artificial Fluids as Blood Substitutes for Educational and Training Use in the Forensic Sciences. *Forensic Sci Pol Manag* **2016**, *7* (3-4), 81-86. <https://doi.org/10.1080/19409044.2016.1218574>.
- (47) Millington, J. LTSN Physical Sciences Development Project : Final Report Development of a Synthetic Blood Substitute for Use in Forensic Science Teaching Research Framework Market Research : Commercially Available Blood Substitutes Theatrical Bloods. **2002**, 1-20.
- (48) Li, J.; Li, X.; Michielsen, S. Alternative Method for Determining the Original Drop Volume of Bloodstains on Knit Fabrics. *Forensic Sci Int* **2016**, *263*, 194-203. <https://doi.org/10.1016/j.forsciint.2016.04.018>.

- (49) Stotesbury, T.; Illes, M.; Wilson, P.; Vreugdenhil, A. J. The Application of Silicon Sol-Gel Technology to Forensic Blood Substitute Development: Mimicking Aspects of Whole Human Blood Rheology. *Forensic Sci Int* **2017**, *270*, 12-19. <https://doi.org/10.1016/j.forsciint.2017.03.020>.
- (50) Stotesbury, T.; Illes, M.; Wilson, P.; Vreugdenhil, A. J. The Application of Silicon Sol-Gel Technology to Forensic Blood Substitute Development: Investigation of the Spreading Dynamics onto a Paper Surface. *Forensic Sci Int* **2017**, *275*, 308-313. <https://doi.org/10.1016/j.forsciint.2017.03.020>.
- (51) Polacco, S.; Illes, M.; Stotesbury, T. The Use of a Forensic Blood Substitute for Impact Pattern Area of Origin Estimation via Three Trajectory Analysis Programs. *Can Soc Forensic Sci J* **2018**, *51* (2), 58-66. <https://doi.org/10.1080/00085030.2018.1463274>.
- (52) Polacco, S.; Wilson, P.; Illes, M.; Vreugdenhil, A. J.; Stotesbury, T. Luminol Reagent Control Materials in Bloodstain Pattern Analysis: A Silicon Sol-Gel Polymer Alternative. *Forensic Chem* **2019**, *12*, 91-98. <https://doi.org/10.1016/j.forc.2019.01.002>.
- (53) Li, J. Synthesis of Artificial Blood Substitute for Forensic Purposes [PhD Thesis], North Carolina State University, 2018.

- (54) Lee, S. Y.; Seo, Y. II; Moon, B. S.; Kim, J. P.; Goh, J. M.; Park, N. K.; Shin, S. H. Study on Development of Forensic Blood Substitute: Focusing on Bloodstain Pattern Analysis. *Forensic Sci Int* **2020**, *316*, 110461. <https://doi.org/10.1016/j.forsciint.2020.110461>.
- (55) Rubio, A.; López, M.; Rodrigues, T.; Campo-Deaño, L.; Vega, E. J. A Particulate Blood Analogue Based on Artificial Viscoelastic Blood Plasma and RBC-like Microparticles at a Concentration Matching the Human Haematocrit. *Soft Matter* **2022**, *18*, 7510-7523. <https://doi.org/10.1039/d2sm00947a>.
- (56) Lee, K. Y.; Mooney, D. J. Alginate: Properties and Biomedical Applications. *Progress in Polymer Science (Oxford)* **2012**, *37* (1), 106-126. <https://doi.org/10.1016/j.progpolymsci.2011.06.003>.
- (57) Ching, S. H.; Bansal, N.; Bhandari, B. Alginate Gel Particles—A Review of Production Techniques and Physical Properties. *Crit Rev Food Sci Nutr* **2017**, *57* (6), 1133-1152. <https://doi.org/10.1080/10408398.2014.965773>.
- (58) Draget, K. I.; Taylor, C. Chemical, Physical and Biological Properties of Alginates and Their Biomedical Implications. *Food Hydrocoll* **2011**, *25* (2), 251-256. <https://doi.org/10.1016/j.foodhyd.2009.10.007>.

- (59) Agüero, L.; Alpdagtas, S.; İlhan, E.; Zaldivar-Silva, D.; Gunduz, O. Functional Role of Crosslinking in Alginate Scaffold for Drug Delivery and Tissue Engineering: A Review. *Eur Polym J* **2021**, *160*, 110807. <https://doi.org/10.1016/j.eurpolymj.2021.110807>.
- (60) Álvarez-Castillo, E.; Aguilar, J. M.; Bengoechea, C.; López-Castejón, M. L.; Guerrero, A. Rheology and Water Absorption Properties of Alginate - Soy Protein Composites. *Polymers (Basel)* **2021**, *13* (1807), 1-15. <https://doi.org/10.3390/polym13111807>.
- (61) Neves, M. I.; Moroni, L.; Barrias, C. C. Modulating Alginate Hydrogels for Improved Biological Performance as Cellular 3D Microenvironments. *Front Bioeng Biotechnol* **2020**, *8* (665), 1-16. <https://doi.org/10.3389/fbioe.2020.00665>.
- (62) Augst, A. D.; Kong, H. J.; Mooney, D. J. Alginate Hydrogels as Biomaterials. *Macromol Biosci* **2006**, *6* (8), 623-633. <https://doi.org/10.1002/mabi.200600069>.
- (63) Gurikov, P.; Smirnova, I. Non-Conventional Methods for Gelation of Alginate. *Gels* **2018**, *4*, 1-14. <https://doi.org/10.3390/gels4010014>.



- (64) Rinaudo, M. Biomaterials Based on a Natural Polysaccharide: Alginate. *TIP Revista Especializada en Ciencias Químico-Biológicas* **2014**, 17 (1), 92-96.  
[https://doi.org/10.1016/S1405-888X\(14\)70322-5](https://doi.org/10.1016/S1405-888X(14)70322-5).
- (65) Davis, T. A.; Llanes, F.; Volesky, B.; Mucci, A. Metal Selectivity of *Sargassum* Spp. and Their Alginates in Relation to Their  $\alpha$ -L-Guluronic Acid Content and Conformation. *Environ Sci Technol* **2003**, 37 (2), 261-267.  
<https://doi.org/10.1021/es025781d>.
- (66) Christensen, B. E.; Indergaard, M.; Smidsrød, O. Polysaccharide Research in Trondheim. *Carbohydr Polym* **1990**, 13 (3), 239-255.  
[https://doi.org/10.1016/0144-8617\(90\)90057-Y](https://doi.org/10.1016/0144-8617(90)90057-Y).
- (67) Tavakoli, J.; Tang, Y. Hydrogel Based Sensors for Biomedical Applications: An Updated Review. *Polymers (Basel)* **2017**, 9 (8), 1-25.  
<https://doi.org/10.3390/polym9080364>.
- (68) Mantha, S.; Pillai, S.; Khayambashi, P.; Upadhyay, A.; Zhang, Y.; Tao, O.; Pham, H. M.; Tran, S. D. Smart Hydrogels in Tissue Engineering and Regenerative Medicine. *Materials* **2019**, 12 (3323), 1-22.  
<https://doi.org/10.3390/ma12203323>.
- (69) Bae, J.; Park, J.; Kim, S.; Cho, H.; Kim, H. J.; Park, S.; Shin, D. S. Tailored Hydrogels for Biosensor Applications. *Journal of Industrial and*

*Engineering Chemistry* **2020**, 89, 1-12.

<https://doi.org/10.1016/j.jiec.2020.05.001>.

- (70) Sharifi, S.; Blanquer, S. B. G.; Van Kooten, T. G.; Grijpma, D. W. Biodegradable Nanocomposite Hydrogel Structures with Enhanced Mechanical Properties Prepared by Photo-Crosslinking Solutions of Poly(Trimethylene Carbonate)-Poly(Ethylene Glycol)-Poly(Trimethylene Carbonate) Macromonomers and Nanoclay Particles. *Acta Biomater* **2012**, 8 (12), 4233-4243. <https://doi.org/10.1016/j.actbio.2012.09.014>.
- (71) Weerasundara, L.; Gabriele, B.; Figoli, A.; Ok, Y. S.; Bundschuh, J. Hydrogels: Novel Materials for Contaminant Removal in Water—A Review. *Crit Rev Environ Sci Technol* **2021**, 51 (17), 1970-2014. <https://doi.org/10.1080/10643389.2020.1776055>.
- (72) Maitra, J.; Shukla, V. K. Cross-Linking in Hydrogels - A Review. *Am J Polym Sci* **2014**, 4 (2), 25-31. <https://doi.org/10.5923/j.ajps.20140402.01>.
- (73) Devolder, R.; Kong, H. J. Hydrogels for in Vivo-like Three-Dimensional Cellular Studies. *WIREs Syst Biol Med* **2012**, 4, 351-365. <https://doi.org/10.1002/wsbm.1174>.

- (74) Schoenmakers, D. C.; Rowan, A. E.; Kouwer, P. H. J. Crosslinking of Fibrous Hydrogels. *Nat Commun* **2018**, *9* (1), 1–8. <https://doi.org/10.1038/s41467-018-04508-x>.
- (75) Nelson, C.; Tuladhar, S.; Launen, L.; Habib, A. 3D Bio-Printability of Hybrid Pre-Crosslinked Hydrogels. *Int J Mol Sci* **2021**, *22* (13481), 1–23. <https://doi.org/10.3390/ijms222413481>.
- (76) Liu, Y.; Zhang, Y.; An, Z.; Zhao, H.; Zhang, L.; Cao, Y.; Mansoorianfar, M.; Liu, X.; Pei, R. Slide-Ring Structure-Based Double-Network Hydrogel with Enhanced Stretchability and Toughness for 3D-Bio-Printing and Its Potential Application as Artificial Small-Diameter Blood Vessels. *ACS Appl Bio Mater* **2021**, *4* (12), 8597–8606. <https://doi.org/10.1021/acsabm.1c01052>.
- (77) Mallakpour, S.; Azadi, E.; Hussain, C. M. State-of-the-Art of 3D Printing Technology of Alginate-Based Hydrogels—An Emerging Technique for Industrial Applications. *Adv Colloid Interface Sci* **2021**, *293*, 102436. <https://doi.org/10.1016/j.cis.2021.102436>.
- (78) Li, X.; Sun, Q.; Li, Q.; Kawazoe, N.; Chen, G. Functional Hydrogels with Tunable Structures and Properties for Tissue Engineering Applications. *Front Chem* **2018**, *6*, 1–20. <https://doi.org/10.3389/fchem.2018.00499>.

- (79) Wang, K.; Hao, Y.; Wang, Y.; Chen, J.; Mao, L.; Deng, Y.; Chen, J.; Yuan, S.; Zhang, T.; Ren, J.; Liao, W. Functional Hydrogels and Their Application in Drug Delivery, Biosensors, and Tissue Engineering. *Int J Polym Sci* **2019**, *2019*, 1-15. <https://doi.org/10.1155/2019/3160732>.
- (80) Nam, S.; Stowers, R.; Lou, J.; Xia, Y.; Chaudhuri, O. Varying PEG Density to Control Stress Relaxation in Alginate-PEG Hydrogels for 3D Cell Culture Studies. *Biomaterials* **2019**, *200*, 15-24. <https://doi.org/10.1016/j.biomaterials.2019.02.004>.
- (81) Shapiro, J. M.; Oyen, M. L. Viscoelastic Analysis of Single-Component and Composite PEG and Alginate Hydrogels. *Acta Mechanica Sinica* **2014**, *30* (1), 7-14. <https://doi.org/10.1007/s10409-014-0025-x>.
- (82) Hernández-González, A. C.; Téllez-Jurado, L.; Rodríguez-Lorenzo, L. M. Alginate Hydrogels for Bone Tissue Engineering, from Injectables to Bioprinting: A Review. *Carbohydr Polym* **2020**, *229*, 115514. <https://doi.org/10.1016/j.carbpol.2019.115514>.
- (83) Radhakrishnan, J.; Subramanian, A.; Krishnan, U. M.; Sethuraman, S. Injectable and 3D Bioprinted Polysaccharide Hydrogels: From Cartilage to Osteochondral Tissue Engineering. *Biomacromolecules* **2017**, *18* (1), 1-26. <https://doi.org/10.1021/acs.biomac.6b01619>.

- (84) Hafeez, S.; Ooi, H. W.; Morgan, F. L. C.; Mota, C.; Dettin, M.; van Blitterswijk, C.; Moroni, L.; Baker, M. B. Viscoelastic Oxidized Alginates with Reversible Imine Type Crosslinks: Self-Healing, Injectable, and Bioprintable Hydrogels. *Gels* **2018**, 4 (4), 1-19. <https://doi.org/10.3390/gels4040085>.
- (85) Lee, K. Y.; Kong, H. J.; Larson, R. G.; Mooney, D. J. Hydrogel Formation via Cell Crosslinking. *Advanced Materials* **2003**, 15 (21), 1828-1832. <https://doi.org/10.1002/adma.200305406>.
- (86) Liberski, A.; Latif, N.; Raynaud, C.; Bollensdorff, C.; Yacoub, M. Alginate for Cardiac Regeneration: From Seaweed to Clinical Trials. *Glob Cardiol Sci Pract* **2016**, 2016 (1), e201604. <https://doi.org/10.21542/gcsp.2016.4>.
- (87) Wang, L.; Zhang, Q.; Wang, X.; Liu, J.; Yang, J. The Preparation and Forming Mechanism of the Red Blood Cell-Shaped Microspheres via Electrospraying. *J Appl Polym Sci* **2011**, 122, 2552-2556. <https://doi.org/10.1002/app.34374>.
- (88) Morais, A. Í. S.; Vieira, E. G.; Afewerki, S.; Sousa, R. B.; Honorio, L. M. C.; Cambrussi, A. N. C. O.; Santos, J. A.; Bezerra, R. D. S.; Furtini, J. A. O.; Silva-Filho, E. C.; Webster, T. J.; Lobo, A. O. Fabrication of Polymeric

- Microparticles by Electrospray: The Impact of Experimental Parameters. *J Funct Biomater* **2020**, 11 (4), 1-26. <https://doi.org/10.3390/jfb11010004>.
- (89) Wong, J. Y.; Bronzino, J. D. *Biomaterials*; Taylor & Francis: Boca Raton, FL, 2007.
- (90) Ahmed, E. M. Hydrogel: Preparation, Characterization, and Applications: A Review. *J Adv Res* **2015**, 6 (2), 105-121. <https://doi.org/10.1016/j.jare.2013.07.006>.
- (91) Chai, Q.; Jiao, Y.; Yu, X. Hydrogels for Biomedical Applications: Their Characteristics and the Mechanisms behind Them. *Gels* **2017**, 3 (6), 1-15. <https://doi.org/10.3390/gels3010006>.
- (92) Drury, J. L.; Mooney, D. J. Hydrogels for Tissue Engineering: Scaffold Design Variables and Applications. *Biomaterials* **2003**, 24 (24), 4337-4351. [https://doi.org/10.1016/S0142-9612\(03\)00340-5](https://doi.org/10.1016/S0142-9612(03)00340-5).
- (93) Hunt, J. A.; Chen, R.; Van Veen, T.; Bryan, N. Hydrogels for Tissue Engineering and Regenerative Medicine. *J Mater Chem B* **2014**, 2 (33), 5319-5338. <https://doi.org/10.1039/c4tb00775a>.
- (94) Sun, J.; Tan, H. Alginate-Based Biomaterials for Regenerative Medicine Applications. *Materials* **2013**, 6 (4), 1285-1309. <https://doi.org/10.3390/ma6041285>.

- (95) Priya, S. G.; Jungvid, H.; Kumar, A. Skin Tissue Engineering for Tissue Repair and Regeneration. *Tissue Engineering Part B* **2008**, *14* (1), 105-118. <https://doi.org/10.1089/teb/2007.0318>.
- (96) Alves Cardoso, D.; Van Den Beucken, J. J. J. P.; Both, L. L. H.; Bender, J.; Jansen, J. A.; Leeuwenburgh, S. C. G. Gelation and Biocompatibility of Injectable Alginate-Calcium Phosphate Gels for Bone Regeneration. *J Biomed Mater Res A* **2014**, *102* (3), 808-817. <https://doi.org/10.1002/jbm.a.34754>.
- (97) Kuo, C. K.; Ma, P. X. Ionically Crosslinked Alginate Hydrogels as Scaffolds for Tissue Engineering: Part 1. Structure, Gelation Rate and Mechanical Properties. *Biomaterials* **2001**, *22* (6), 511-521. [https://doi.org/10.1016/S0142-9612\(00\)00201-5](https://doi.org/10.1016/S0142-9612(00)00201-5).
- (98) Abasalizadeh, F.; Moghaddam, S. V.; Alizadeh, E.; Akbari, E.; Kashani, E.; Fazljou, S. M. B.; Torbati, M.; Akbarzadeh, A.; Akbarzadeh, A. Alginate-Based Hydrogels as Drug Delivery Vehicles in Cancer Treatment and Their Applications in Wound Dressing and 3D Bioprinting. *J Biol Eng* **2020**, *14* (1), 1-22. <https://doi.org/10.1186/s13036-020-0227-7>.

- (99) McKenzie, M.; Betts, D.; Suh, A.; Bui, K.; Kim, L. D.; Cho, H. Hydrogel-Based Drug Delivery Systems for Poorly Water-Soluble Drugs. *Molecules* **2015**, *20* (11), 20397–20408. <https://doi.org/10.3390/molecules201119705>.
- (100) Gombotz, W. R.; Wee, S. F. Protein Release from Alginate Matrices. *Adv Drug Deliv Rev* **1998**, *31* (3), 267–285. [https://doi.org/10.1016/S0169-409X\(97\)00124-5](https://doi.org/10.1016/S0169-409X(97)00124-5).
- (101) Koetting, M. C.; Peters, J. T.; Steichen, S. D.; Peppas, N. A. Stimulus-Responsive Hydrogels: Theory, Modern Advances, and Applications. *Mat Sci Eng R* **2015**, *93*, 1–49. <https://doi.org/10.1016/j.mser.2015.04.001>.
- (102) Klouda, L.; Mikos, A. G. Thermoresponsive Hydrogels in Biomedical Applications. *Eur J Pharm Biopharm* **2008**, *68* (1), 34–45. <https://doi.org/10.1016/j.ejpb.2007.02.025>.
- (103) Klouda, L. Thermoresponsive Hydrogels in Biomedical Applications A Seven-Year Update. *Eur J Pharm Biopharm* **2015**, *97*, 338–349. <https://doi.org/10.1016/j.ejpb.2015.05.017>.
- (104) Li, L.; Wang, Y.; Pan, L.; Shi, Y.; Cheng, W.; Shi, Y.; Yu, G. A Nanostructured Conductive Hydrogels-Based Biosensor Platform for Human Metabolite Detection. *Nano Lett* **2015**, *15* (2), 1146–1151. <https://doi.org/10.1021/nl504217p>.



- (105) Khajouei, S.; Ravan, H.; Ebrahimi, A. DNA Hydrogel-Empowered Biosensing. *Adv Colloid Interface Sci* **2019**, *275*, 102060. <https://doi.org/10.1016/j.cis.2019.102060>.
- (106) Herrmann, A.; Haag, R.; Schedler, U. Hydrogels and Their Role in Biosensing Applications. *Adv Healthc Mater* **2021**, *10* (11), 1-25. <https://doi.org/10.1002/adhm.202100062>.
- (107) Rowley, J. A.; Mooney, D. J. Alginate Type and RGD Density Control Myoblast Phenotype. *J Biomed Mater Res* **2002**, *60* (2), 217-223. <https://doi.org/10.1002/jbm.1287>.
- (108) Fonseca, K. B.; Bidarra, S. J.; Oliveira, M. J.; Granja, P. L.; Barrias, C. C. Molecularly Designed Alginate Hydrogels Susceptible to Local Proteolysis as Three-Dimensional Cellular Microenvironments. *Acta Biomater* **2011**, *7* (4), 1674-1682. <https://doi.org/10.1016/j.actbio.2010.12.029>.
- (109) Van Helmond, W.; O'Brien, V.; De Jong, R.; Van Esch, J.; Oldenhof, S.; De Puit, M. Collection of Amino Acids and DNA from Fingerprints Using Hydrogels. *Analyst* **2018**, *143* (4), 900-905. <https://doi.org/10.1039/c7an01692a>.

- (110) Fenton, L. A.; Horsfall, I.; Carr, D. J. Skin and Skin Simulants. *Australian Journal of Forensic Sciences* **2020**, 52 (1), 96-106.  
<https://doi.org/10.1080/00450618.2018.1450896>.
- (111) Tang, J. D.; Mura, C.; Lampe, K. J. Stimuli-Responsive, Pentapeptide, Nanofiber Hydrogel for Tissue Engineering. *J Am Chem Soc* **2019**, 141 (12), 4886-4899. <https://doi.org/10.1021/jacs.8b13363>.
- (112) Tozzo, P.; Scrivano, S.; Sanavio, M.; Caenazzo, L. The Role of DNA Degradation in the Estimation of Post-Mortem Interval: A Systematic Review of the Current Literature. *Int J Mol Sci* **2020**, 21 (10).  
<https://doi.org/10.3390/ijms21103540>.
- (113) Donaldson, A. E.; Lamont, I. L. Biochemistry Changes That Occur after Death: Potential Markers for Determining Post-Mortem Interval. *PLoS One* **2013**, 8 (11), 1-10. <https://doi.org/10.1371/journal.pone.0082011>.
- (114) Zadora, G.; Menzyk, A. In the Pursuit of the Holy Grail of Forensic Science - Spectroscopic Studies on the Estimation of Time since Deposition of Bloodstains. *TrAC - Trends Anal Chem* **2018**, 105, 137-165.  
<https://doi.org/10.1016/j.trac.2018.04.009>.
- (115) Bremmer, R. H.; De Bruin, K. G.; Van Gemert, M. J. C.; Van Leeuwen, T. G.; Aalders, M. C. G. Forensic Quest for Age Determination of Bloodstains.

*Forensic Sci Int* **2012**, 216 (1-3), 1-11.

<https://doi.org/10.1016/j.forsciint.2011.07.027>.

(116) Carr, D. J.; Wainwright, A. Variability of Simulants Used in Recreating Stab

Events. *Forensic Sci Int* **2011**, 210 (1-3), 42-46.

<https://doi.org/10.1016/j.forsciint.2011.01.032>.

(117) Jussila, J.; Leppäniemi, A.; Paronen, M.; Kulomäki, E. Ballistic Skin

Simulant. *Forensic Sci Int* **2005**, 150 (1), 63-71.

<https://doi.org/10.1016/j.forsciint.2004.06.039>.

(118) Zadnik, S.; Van Bronswijk, W.; Frick, A. A.; Fritz, P.; Lewis, S. W. Fingermark

Simulants and Their Inherent Problems: A Comparison with Latent Fingermark Deposits. *Journal of Forensic Ident* **2013**, 63 (5), 593-608.

(119) Steiner, R.; Roux, C.; Moret, S. Controlling Fingermark Variability for

Research Purposes: A Review. *WIREs Forensic Sci* **2019**, 1, e1338.

<https://doi.org/10.1002/wfs2.1338>.

(120) Humphrey, C.; Kumaratilake, J. Ballistics and Anatomical Modelling - A

Review. *Leg Med* **2016**, 23, 21-29.

<https://doi.org/10.1016/j.legalmed.2016.09.002>.

- (121) Hammond, H. A.; Jin, L.; Zhong, Y.; Thomas Caskey, C.; Chakraborty, R. Evaluation of 13 Short Tandem Repeat Loci for Use in Personal Identification Applications. *Am J Hum Genet* **1994**, 55 (1), 175-189.
- (122) National Institute of Standards and Technology. *STRBase (SRD-130) - CSF1PO*. [https://strbase.nist.gov/str\\_CSF1PO.htm](https://strbase.nist.gov/str_CSF1PO.htm) (accessed 2022-09-10).
- (123) Applied Biosystems. DNA Fragment Analysis by Capillary Electrophoresis. ThermoFisher Scientific 2014, pp 1-220.
- (124) Quong, D.; Neufeld, R. J. Electrophoretic Extraction and Analysis of DNA from Chitosan or Poly-L- Lysine-Coated Alginate Beads. *Applied Biochemistry and Biotechnology - Part A Enzyme Engineering and Biotechnology* **1999**, 81 (1), 67-77. <https://doi.org/10.1385/ABAB:81:1:67>.
- (125) Yin, Z. C.; Wang, Y. L.; Wang, K. A PH-Responsive Composite Hydrogel Beads Based on Agar and Alginate for Oral Drug Delivery. *J Drug Deliv Sci Technol* **2018**, 43, 12-18. <https://doi.org/10.1016/j.jddst.2017.09.009>.
- (126) New England BioLabs. *What is the composition of each buffer provided with the Monarch DNA Gel Extraction Kit? | NEB.*

<https://international.neb.com/faqs/2015/12/03/what-is-the-composition-of-each-buffer-provided-with-the-monarch-dna-gel-extraction-kit>.

- (127) Boom, R.; Sol, C. J. A.; Salimans, M. M. M.; Jansen, C. L.; Wertheim-Van Dillen, P. M. E.; Van Der Noordaa, J. Rapid and Simple Method for Purification of Nucleic Acids. *J Clin Microbiol* **1990**, 28 (3), 495-503. <https://doi.org/10.1128/jcm.28.3.495-503.1990>.
- (128) Ali, N.; Rampazzo, R. D. C. P.; Costa, A. Di. T.; Krieger, M. A. Current Nucleic Acid Extraction Methods and Their Implications to Point-of-Care Diagnostics. *Biomed Res Int* **2017**, 2017, 9306564. <https://doi.org/10.1155/2017/9306564>.
- (129) Chomczynski, P.; Sacchi, N. The Single-Step Method of RNA Isolation by Acid Guanidinium Thiocyanate-Phenol-Chloroform Extraction: Twenty-Something Years On. *Nat Protoc* **2006**, 1 (2), 581-585. <https://doi.org/10.1038/nprot.2006.83>.
- (130) Machado, A. H. E.; Lundberg, D.; Ribeiro, A. J.; Veiga, F. J.; Miguel, M. G.; Lindman, B.; Olsson, U. Encapsulation of DNA in Macroscopic and Nanosized Calcium Alginate Gel Particles. *Langmuir* **2013**, 29 (51), 15926-15935. <https://doi.org/10.1021/la4032927>.

- (131) Putney, S. D.; Benkovic, S. J.; Schimmel, P. R. A DNA Fragment with an  $\alpha$ -Phosphorothioate Nucleotide at One End Is Asymmetrically Blocked from Digestion by Exonuclease III and Can Be Replicated in Vivo. *Proc Natl Acad Sci USA* **1981**, 78 (12), 7350-7354.  
<https://doi.org/10.1073/pnas.78.12.7350>.
- (132) Clafré, S. A.; Rinaldi, M.; Gasparini, P.; Seripa, D.; Bisceglia, L.; Zelante, L.; Farace, M. G.; Fazio, V. M. Stability and Functional Effectiveness of Phosphorothioate Modified Duplex DNA and Synthetic "Mini-Genes." *Nucleic Acids Res* **1995**, 23 (20), 4134-4142.  
<https://doi.org/10.1093/nar/23.20.4134>.
- (133) The Centre of Forensic Sciences - Public Safety Division. *Handbook of Forensic Evidence for the Investigator*; Centre of Forensic Science, 2018.
- (134) Hedman, J.; Akel, Y.; Jansson, L.; Hedell, R.; Wallmark, N.; Forsberg, C.; Ansell, R. Enhanced Forensic DNA Recovery with Appropriate Swabs and Optimized Swabbing Technique. *Forensic Sci Int Genet* **2021**, 53, 102491.  
<https://doi.org/10.1016/j.fsigen.2021.102491>.
- (135) Levental, I.; Georges, P. C.; Janmey, P. A. Soft Biological Materials and Their Impact on Cell Function. *Soft Matter* **2007**, 3 (3), 299-306.  
<https://doi.org/10.1039/b610522j>.

- (136) Gross, J. H. *Mass Spectrometry*, 2nd ed.; Springer, Berlin, Heidelberg: Berlin, 2011.
- (137) Stock, N. L. Introducing Graduate Students to High-Resolution Mass Spectrometry (HRMS) Using a Hands-On Approach. *J Chem Educ* **2017**, *94* (12), 1978-1982. <https://doi.org/10.1021/acs.jchemed.7b00569>.
- (138) Riccardi Sirtori, F.; Altomare, A.; Carini, M.; Aldini, G.; Regazzoni, L. MS Methods to Study Macromolecule-Ligand Interaction: Applications in Drug Discovery. *Methods* **2018**, *144*, 152-174. <https://doi.org/10.1016/j.ymeth.2018.06.005>.
- (139) Murray, K. K.; Boyd, R. K.; Eberlin, M. N.; Langley, G. J.; Li, L.; Naito, Y. Definitions of Terms Relating to Mass Spectrometry (IUPAC Recommendations 2013). *Pure Appl Chem* **2013**, *85* (7), 1515-1609. <https://doi.org/10.1351/PAC-REC-06-04-06>.
- (140) Hofstadler, S. A.; Sannes-Lowery, K. A.; Hannis, J. C. Analysis of Nucleic Acids by Fticr MS. *Mass Spectrom Rev* **2005**, *24* (2), 265-285. <https://doi.org/10.1002/mas.20016>.
- (141) Muddiman, D. C.; Smith, R. D. Sequencing and Characterization of Larger Oligonucleotides by Electrospray Ionization Fourier Transform Ion

Cyclotron Resonance Mass Spectrometry. *Rev Anal Chem* **1998**, 17, 1.

<https://doi.org/10.1515/REVAC.1998.17.1.1>.

(142) Polo, L. M.; Limbach, P. A. Analysis of Oligonucleotides by Electrospray

Ionization Mass Spectrometry. *Curr Protoc Nucleic Acid Chem* **2001**, 10.2,

10.2.1-10.2.20. <https://doi.org/10.1002/0471142700.nc1002s00>.

(143) Null, A. P.; Hannis, J. C.; Muddiman, D. C. Preparation of Single-Stranded

PCR Products for Electrospray Ionization Mass Spectrometry Using the

DNA Repair Enzyme Lambda Exonuclease. *Analyst* **2000**, 125 (4), 619-

625. <https://doi.org/10.1039/a908022h>.

(144) Sannes-Lowery, K. A.; Drader, J. J.; Griffey, R. H.; Hofstadler, S. A. Fourier

Transform Ion Cyclotron Resonance Mass Spectrometry as a High

Throughput Affinity Screen to Identify RNA Binding Ligands. *Science*

(1979) **2000**, 19 (8), 481-491.

(145) Wunschel, D. S.; Fox, K. F.; Fox, A.; Bruce, J. E.; Muddiman, D. C.; Smith,

R. D. Analysis of Double-Stranded Polymerase Chain Reaction Products

from the Bacillus Cereus Group by Electrospray Ionization Fourier

Transform Ion Cyclotron Resonance Mass Spectrometry. *Rapid*

*Communications in Mass Spectrometry* **1996**, 10 (1), 29-35.



[https://doi.org/10.1002/\(SICI\)1097-0231\(19960115\)10:1<29::AID-RCM430>3.0.CO;2-#](https://doi.org/10.1002/(SICI)1097-0231(19960115)10:1<29::AID-RCM430>3.0.CO;2-#).

(146) Banerjee, S.; Mazumdar, S. Electrospray Ionization Mass Spectrometry: A Technique to Access the Information beyond the Molecular Weight of the Analyte. *Int J Anal Chem* **2012**, 2012, 1-40.  
<https://doi.org/10.1155/2012/282574>.

(147) Hettich, R. L.; Stemmler, E. A. Investigation of Oligonucleotide Fragmentation with Matrix-Assisted Laser Desorption/Ionization Fourier-Transform Mass Spectrometry and Sustained off-Resonance Irradiation. *Rapid Comm Mass Spec* **1996**, 10 (3), 321-327.  
[https://doi.org/10.1002/\(SICI\)1097-0231\(199602\)10:3<321::AID-RCM480>3.0.CO;2-M](https://doi.org/10.1002/(SICI)1097-0231(199602)10:3<321::AID-RCM480>3.0.CO;2-M).

(148) Koomen, J. M.; Russell, W. K.; Tichy, S. E.; Russell, D. H. Accurate Mass Measurement of DNA Oligonucleotide Ions Using High-Resolution Time-of-Flight Mass Spectrometry. *J Mass Spec* **2002**, 37 (4), 357-371.  
<https://doi.org/10.1002/jms.312>.

(149) Hannis, J. C.; Muddiman, D. C. Accurate Characterization of the Tyrosine Hydroxylase Forensic Allele 9.3 through Development of Electrospray Ionization Fourier Transform Ion Cyclotron Resonance Mass Spectrometry.

*Rapid Comm Mass Spec* **1999**, 13 (10), 954-962.

[https://doi.org/10.1002/\(SICI\)1097-0231\(19990530\)13:10<954::AID-](https://doi.org/10.1002/(SICI)1097-0231(19990530)13:10<954::AID-RCM593>3.0.CO;2-R)

[RCM593>3.0.CO;2-R](https://doi.org/10.1002/(SICI)1097-0231(19990530)13:10<954::AID-RCM593>3.0.CO;2-R).

- (150) Sannes-Lowery, K. A.; Hofstadler, S. A. Sequence Confirmation of Modified Oligonucleotides Using IRMPD in the External Ion Reservoir of an Electrospray Ionization Fourier Transform Ion Cyclotron Mass Spectrometer. *Journal of the American Society for Mass Spec* **2003**, 14 (8), 825-833. [https://doi.org/10.1016/S1044-0305\(03\)00335-0](https://doi.org/10.1016/S1044-0305(03)00335-0).
- (151) Shah, S.; Friedman, S. H. An ESI-MS Method for Characterization of Native and Modified Oligonucleotides Used for RNA Interference and Other Biological Applications. *Nat Protoc* **2008**, 3 (3), 351-356. <https://doi.org/10.1038/nprot.2007.535>.
- (152) Potier, N.; van Dorsselaer, A.; Cordier, Y.; Roch, O.; Bischoff, R. Negative Electrospray Ionization Mass Spectrometry of Synthetic and Chemically Modified Oligonucleotides. *Nucleic Acids Res* **1994**, 22 (19), 3895-3903. <https://doi.org/10.1093/nar/22.19.3895>.
- (153) Benson, L. M.; Null, A. P.; Muddiman, D. C. Advantages of *Thermococcus kodakaraensis* (KOD) DNA Polymerase for PCR-Mass Spectrometry Based

- Analyses. *Journal of the American Society for Mass Spec* **2003**, 14 (6), 601-604. [https://doi.org/10.1016/S1044-0305\(03\)00148-X](https://doi.org/10.1016/S1044-0305(03)00148-X).
- (154) Jiang, Y.; Hofstadler, S. A. A Highly Efficient and Automated Method of Purifying and Desalting PCR Products for Analysis by Electrospray Ionization Mass Spectrometry. *Anal Biochem* **2003**, 316 (1), 50-57. [https://doi.org/10.1016/S0003-2697\(03\)00024-1](https://doi.org/10.1016/S0003-2697(03)00024-1).
- (155) Tretyakova, N.; Villalta, P. W.; Kotapati, S. Mass Spectrometry of Structurally Modified DNA. *Chem Rev* **2013**, 113 (4), 2395-2436. <https://doi.org/10.1021/cr300391r>.
- (156) Rozenski, J. *Mongo Oligo Mass Calculator*. <https://mods.rna.albany.edu/masspec/Mongo-Oligo>.
- (157) Mogollón, N. G. S.; Quiroz-Moreno, C. D.; Prata, P. S.; De Almeida, J. R.; Cevallos, A. S.; Torres-Guérrez, R.; Augusto, F. New Advances in Toxicological Forensic Analysis Using Mass Spectrometry Techniques. *J Anal Methods Chem* **2018**, 2018, 1-17. <https://doi.org/10.1155/2018/4142527>.
- (158) Yan, H.; Yu, Z.; Zhao, Y.; Xiang, P.; Pan, M. Development of a High-Throughput Screening Analysis for 288 Drugs and Poisons in Human Blood Using Orbitrap Technology with Gas Chromatography-High

- Resolution Accurate Mass Spectrometry. *J Chromatogr A* **2018**, 1587, 209-226. <https://doi.org/10.1016/j.chroma.2018.12.022>.
- (159) Ojanperä, I.; Kolmonen, M.; Pelander, A. Current Use of High-Resolution Mass Spectrometry in Drug Screening Relevant to Clinical and Forensic Toxicology and Doping Control. *Anal Bioanal Chem* **2012**, 403 (5), 1203-1220. <https://doi.org/10.1007/s00216-012-5726-z>.
- (160) Bianchi, F.; Gregori, A.; Braun, G.; Crescenzi, C.; Careri, M. Micro-Solid-Phase Extraction Coupled to Desorption Electrospray Ionization-High-Resolution Mass Spectrometry for the Analysis of Explosives in Soil. *Anal Bioanal Chem* **2015**, 407 (3), 931-938. <https://doi.org/10.1007/s00216-014-8208-7>.
- (161) Hang, T. C.; Guiseppi-Elie, A. Frequency Dependent and Surface Characterization of DNA Immobilization and Hybridization. *Biosens Bioelectron* **2004**, 19 (11), 1537-1548. <https://doi.org/10.1016/j.bios.2003.12.014>.
- (162) McGill, X. L. @. *MetaboAnalyst* 5.0. <https://genap.metaboanalyst.ca/MetaboAnalyst/home.xhtml>.

- (163) Xia, J.; Psychogios, N.; Young, N.; Wishart, D. S. MetaboAnalyst: A Web Server for Metabolomic Data Analysis and Interpretation. *Nucleic Acids Res* **2009**, *37* (Suppl 2), 652-660. <https://doi.org/10.1093/nar/gkp356>.
- (164) Gabrielli, L.; Connell, L.; Russo, L.; Jiménez-Barbero, J.; Nicotra, F.; Cipolla, L.; Jones, J. R. Exploring GPTMS Reactivity against Simple Nucleophiles: Chemistry beyond Hybrid Materials Fabrication. *RSC Adv* **2014**, *4* (4), 1841-1848. <https://doi.org/10.1039/c3ra44748k>.
- (165) Gabrielli, L.; Russo, L.; Poveda, A.; Jones, J. R.; Nicotra, F.; Jiménez-Barbero, J.; Cipolla, L. Epoxide Opening versus Silica Condensation during Sol-Gel Hybrid Biomaterial Synthesis. *Chem Euro J* **2013**, *19*, 7856-7864. <https://doi.org/10.1002/chem.201204326>.
- (166) Szekalska, M.; Puciłowska, A.; Szymańska, E.; Ciosek, P.; Winnicka, K. Alginate: Current Use and Future Perspectives in Pharmaceutical and Biomedical Applications. *Int J Polym Sci* **2016**, *2016*, 1-17. <https://doi.org/10.1155/2016/7697031>.
- (167) Parreidt, T. S.; Müller, K.; Schmid, M. Alginate-Based Edible Films and Coatings for Food Packaging Applications. *Foods* **2018**, *7* (10), 1-38. <https://doi.org/10.3390/foods7100170>.

- (168) Gattás-Asfura, K. M.; Stabler, C. L. Chemoselective Cross-Linking and Functionalization of Alginate via Staudinger Ligation. *Biomacromolecules* **2009**, *10* (11), 3122–3129. <https://doi.org/10.1021/bm900789a>.
- (169) Kim, E.; Kim, M. H.; Song, J. H.; Kang, C.; Park, W. H. Dual Crosslinked Alginate Hydrogels by Riboflavin as Photoinitiator. *Int J Biol Macromol* **2020**, *154*, 989–998. <https://doi.org/10.1016/j.ijbiomac.2020.03.134>.
- (170) Bonino, C. A.; Samorezov, J. E.; Jeon, O.; Alsberg, E.; Khan, S. A. Real-Time in Situ Rheology of Alginate Hydrogel Photocrosslinking. *Soft Matter* **2011**, *7* (24), 11510–11517. <https://doi.org/10.1039/c1sm06109g>.
- (171) Samorezov, J. E.; Morlock, C. M.; Alsberg, E. Dual Ionic and Photo-Crosslinked Alginate Hydrogels for Micropatterned Spatial Control of Material Properties and Cell Behavior. *Bioconjug Chem* **2015**, *26* (7), 1339–1347. <https://doi.org/10.1021/acs.bioconjchem.5b00117>.
- (172) Moody, C. T.; Palvai, S.; Brudno, Y. Click Cross-Linking Improves Retention and Targeting of Refillable Alginate Deposits. *Acta Biomater* **2020**, *112*, 112–121. <https://doi.org/10.1016/j.actbio.2020.05.033>.
- (173) Cammarata, C. R.; Hughes, M. E.; Ofner III, C. M. Carbodiimide Induced Cross-Linking, Ligand Addition, and Degradation in Gelatin. *Mol Pharm* **2015**, *12* (3), 783–793. <https://doi.org/10.1021/mp5006118>.

- (174) Basu, T.; Bhutani, U.; Majumdar, S. Cross-Linker-Free Sodium Alginate and Gelatin Hydrogels: A Multiscale Biomaterial Design Framework. *J Mater Chem B* **2022**, *10* (19), 3614–3623. <https://doi.org/10.1039/d2tb00028h>.
- (175) Zhao, L.; Li, L.; Yang, G.; Wei, B.; Ma, Y.; Qu, F. Aptamer Functionalized DNA Hydrogels: Design, Applications and Kinetics. *Biosens Bioelectron* **2021**, *194*, 113597. <https://doi.org/10.1016/j.bios.2021.113597>.
- (176) Gačanin, J.; Synatschke, C. V.; Weil, T. Biomedical Applications of DNA-Based Hydrogels. *Adv Funct Mater* **2020**, *30* (4), 1–25. <https://doi.org/10.1002/adfm.201906253>.
- (177) Murakami, Y.; Maeda, M. DNA-Responsive Hydrogels That Can Shrink or Swell. *Biomacromolecules* **2005**, *6* (6), 2927–2929. <https://doi.org/10.1021/bm0504330>.
- (178) Basu, S.; Pacelli, S.; Paul, A. Self-Healing DNA-Based Injectable Hydrogels with Reversible Covalent Linkages for Controlled Drug Delivery. *Acta Biomater* **2020**, *105*, 159–169. <https://doi.org/10.1016/j.actbio.2020.01.021>.
- (179) Abune, L.; Davis, B.; Wang, Y. Aptamer-Functionalized Hydrogels: An Emerging Class of Biomaterials for Protein Delivery, Cell Capture, Regenerative Medicine, and Molecular Biosensing. *WIREs Nanomedicine*

and *Nanobiotechnology* **2021**, 13 (6), 1-25.

<https://doi.org/10.1002/wnan.1731>.

- (180) Li, W.; Wang, J.; Ren, J.; Qu, X. Endogenous Signalling Control of Cell Adhesion by Using Aptamer Functionalized Biocompatible Hydrogel. *Chem Sci* **2015**, 6 (12), 6762-6768. <https://doi.org/10.1039/c5sc02565f>.
- (181) Bush, J.; Hu, C. H.; Veneziano, R. Mechanical Properties of DNA Hydrogels: Towards Highly Programmable Biomaterials. *Appl Sci* **2021**, 11 (4), 1-20. <https://doi.org/10.3390/app11041885>.
- (182) Li, C.; Chen, P.; Shao, Y.; Zhou, X.; Wu, Y.; Yang, Z.; Li, Z.; Weil, T.; Liu, D. A Writable Polypeptide-DNA Hydrogel with Rationally Designed Multi-Modification Sites. *Small* **2015**, 11 (9-10), 1138-1143. <https://doi.org/10.1002/smll.201401906>.
- (183) Wu, Y.; Li, C.; Boldt, F.; Wang, Y.; Kuan, S. L.; Tran, T. T.; Mikhalevich, V.; Förtsch, C.; Barth, H.; Yang, Z.; Liu, D.; Weil, T. Programmable Protein-DNA Hybrid Hydrogels for the Immobilization and Release of Functional Proteins. *Chemical Communications* **2014**, 50 (93), 14620-14622. <https://doi.org/10.1039/c4cc07144a>.



- (184) Lu, C. H.; Guo, W.; Hu, Y.; Qi, X. J.; Willner, I. Multitriggered Shape-Memory Acrylamide-DNA Hydrogels. *J Am Chem Soc* **2015**, *137* (50), 15723-15731. <https://doi.org/10.1021/jacs.5b06510>.
- (185) Wang, C.; Fadeev, M.; Zhang, J.; Vázquez-González, M.; Davidson-Rozenfeld, G.; Tian, H.; Willner, I. Shape-Memory and Self-Healing Functions of DNA-Based Carboxymethyl Cellulose Hydrogels Driven by Chemical or Light Triggers. *Chem Sci* **2018**, *9* (35), 7145-7152. <https://doi.org/10.1039/c8sc02411a>.
- (186) Zhao, H.; Jiang, G.; Weng, J.; Ma, Q.; Zhang, H.; Ito, Y.; Liu, M. A Signal-Accumulating DNAzyme-Crosslinked Hydrogel for Colorimetric Sensing of Hydrogen Peroxide. *J Mater Chem B* **2016**, *4* (27), 4648-4651. <https://doi.org/10.1039/c6tb00825a>.
- (187) Yang, H.; Liu, H.; Kang, H.; Tan, W. Engineering Target-Responsive Hydrogels Based on Aptamer-Target Interactions. *J Am Chem Soc* **2008**, *130* (20), 6320-6321. <https://doi.org/10.1021/ja801339w>.
- (188) Zhu, Z.; Wu, C.; Liu, H.; Zou, Y.; Zhang, X.; Kang, H.; Yang, C. J.; Tan, W. An Aptamer Cross-Linked Hydrogel as a Colorimetric Platform for Visual Detection. *Angewandte Chemie* **2010**, *122* (6), 1070-1074. <https://doi.org/10.1002/ange.200905570>.

- (189) Pandey, R.; Lu, Y.; Osman, E.; Saxena, S.; Zhang, Z.; Qian, S.; Pollinzi, A.; Smieja, M.; Li, Y.; Soleymani, L.; Hoare, T. DNAzyme-Immobilizing Microgel Magnetic Beads Enable Rapid, Specific, Culture-Free, and Wash-Free Electrochemical Quantification of Bacteria in Untreated Urine. *ACS Sens* **2022**, 7 (4), 985–994. <https://doi.org/10.1021/acssensors.1c02440>.
- (190) Li, J.; Zhang, Y.; Zhu, L.; Chen, K.; Li, X.; Xu, W. Smart Nucleic Acid Hydrogels with High Stimuli-Responsiveness in Biomedical Fields. *Int J Mol Sci* **2022**, 23 (3), 1068. <https://doi.org/10.3390/ijms23031068>.
- (191) Um, S. H.; Lee, J. B.; Park, N.; Kwon, S. Y.; Umbach, C. C.; Luo, D. Enzyme-Catalysed Assembly of DNA Hydrogel. *Nat Mater* **2006**, 5 (10), 797–801. <https://doi.org/10.1038/nmat1741>.
- (192) Turner, D. A.; Baldwin, E.; Russell, K.; Wells, L. A. DNA-Crosslinked Alginate and Layered Microspheres to Modulate the Release of Encapsulated FITC-Dextran. *European Journal of Pharmaceutics and Biopharmaceutics* **2021**, 158, 313–322. <https://doi.org/10.1016/j.ejpb.2020.11.016>.
- (193) Lin, Y.; Sun, Y.; Dai, Y.; Sun, W.; Zhu, X.; Liu, H.; Han, R.; Gao, D.; Luo, C.; Wang, X. A “Signal-on” Chemiluminescence Biosensor for Thrombin Detection Based on DNA Functionalized Magnetic Sodium Alginate

Hydrogel and Metalloporphyrinic Metal-Organic Framework Nanosheets.

*Talanta* **2020**, *207*, 120300.

<https://doi.org/10.1016/j.talanta.2019.120300>.

- (194) Shi, P.; Zhao, N.; Coyne, J.; Wang, Y. DNA-Templated Synthesis of Biomimetic Cell Wall for Nanoencapsulation and Protection of Mammalian Cells. *Nat Commun* **2019**, *10* (1), 1-11. <https://doi.org/10.1038/s41467-019-10231-y>.
- (195) Gooch, J.; Daniel, B.; Parkin, M.; Frascione, N. Developing Aptasensors for Forensic Analysis. *TrAC - Trends Anal Chem* **2017**, *94*, 150-160. <https://doi.org/10.1016/j.trac.2017.07.019>.
- (196) Hai, J.; Wang, H.; Sun, P.; Li, T.; Lu, S.; Zhao, Y.; Wang, B. Smart Responsive Luminescent Aptamer-Functionalized Covalent Organic Framework Hydrogel for High-Resolution Visualization and Security Protection of Latent Fingerprints. *ACS Appl Mater Interfaces* **2019**, *11* (47), 44664-44672. <https://doi.org/10.1021/acsami.9b18251>.
- (197) Orr, A.; Wilson, P.; Stotesbury, T. Calcium-Alginate Tissue Gels (CATG): Proof-of-Concept Biomaterial Development. *Forensic Sci Int* **2021**, *329*, 111055. <https://doi.org/10.1016/j.forsciint.2021.111055>.

- (198) Basu, S.; Alkiswani, A. R.; Pacelli, S.; Paul, A. Nucleic Acid-Based Dual Cross-Linked Hydrogels for in Situ Tissue Repair via Directional Stem Cell Migration. *ACS Appl Mater Interfaces* **2019**, *11* (38), 34621–34633. <https://doi.org/10.1021/acsami.9b10074>.
- (199) Zhou, J.; Rossi, J. Aptamers as Targeted Therapeutics: Current Potential and Challenges. *Nat Rev Drug Discov* **2017**, *16* (3), 181–202. <https://doi.org/10.1038/nrd.2016.199>.
- (200) Lin, D. C.; Yurke, B.; Langrana, N. A. Mechanical Properties of a Reversible, DNA-Crosslinked Polyacrylamide Hydrogel. *J Biomech Eng* **2004**, *126* (1), 104–110. <https://doi.org/10.1115/1.1645529>.
- (201) Pan, W.; Wen, H.; Niu, L.; Su, C.; Liu, C.; Zhao, J.; Mao, C.; Liang, D. Effects of Chain Flexibility on the Properties of DNA Hydrogels. *Soft Matter* **2016**, *12* (25), 5537–5541. <https://doi.org/10.1039/c6sm00283h>.
- (202) Jiang, H.; Pan, V.; Vivek, S.; Weeks, E. R.; Ke, Y. Programmable DNA Hydrogels Assembled from Multidomain DNA Strands. *ChemBioChem* **2016**, *17* (12), 1156–1162. <https://doi.org/10.1002/cbic.201500686>.
- (203) Ewoldt, R. H.; Johnston, M. T.; Caretta, L. M. *Experimental Challenges of Shear Rheology: How to Avoid Bad Data*; Springer, 2015. [https://doi.org/10.1007/978-1-4939-2065-5\\_6](https://doi.org/10.1007/978-1-4939-2065-5_6).

- (204) Goudoulas, T. B.; Pan, S.; Germann, N. Double-Stranded and Single-Stranded Well-Entangled DNA Solutions under LAOS: A Comprehensive Study. *Polymer (Guildf)* **2018**, *140*, 240-254. <https://doi.org/10.1016/j.polymer.2018.02.061>.
- (205) Gu, S.; Cheng, G.; Yang, T.; Ren, X.; Gao, G. Mechanical and Rheological Behavior of Hybrid Cross-Linked Polyacrylamide/Cationic Micelle Hydrogels. *Macromol Mater Eng* **2017**, *302*, 1-7. <https://doi.org/10.1002/mame.201700402>.
- (206) Yesilyurt, V.; Webber, M. J.; Appel, E. A.; Godwin, C.; Langer, R.; Anderson, D. G. Injectable Self-Healing Glucose-Responsive Hydrogels with PH-Regulated Mechanical Properties. *Adv Mat* **2016**, *28* (1), 86-91. <https://doi.org/10.1002/adma.201502902>.
- (207) Besiri, I. N.; Goudoulas, T. B.; Germann, N. Impact of CaCl<sub>2</sub> Concentration and in Situ Rheometric Setup Configuration on Fast Alginate-Ca<sup>2+</sup> Reaction. *Phys Fluids* **2022**, *34* (5), 053104. <https://doi.org/10.1063/5.0090679>.
- (208) Huang, S.; Wang, J.; Zhang, Y.; Yu, Z.; Qi, C. Quaternized Carboxymethyl Chitosan-Based Silver Nanoparticles Hybrid: Microwave-Assisted

- Synthesis, Characterization and Antibacterial Activity. *Nanomaterials* **2016**, 6 (6), 118. <https://doi.org/10.3390/nano6060118>.
- (209) Di Foggia, M.; Taddei, P.; Torreggiani, A.; Dettin, M.; Tinti, A. Self-Assembling Peptides for Biomedical Applications: IR and Raman Spectroscopies for the Study of Secondary Structure Article. *Proteomics Research Journal* **2011**, 2 (3), 231-272.
- (210) Saarai, A.; Kasparkova, V.; Sedlacek, T.; Saha, P. On the Development and Characterisation of Crosslinked Sodium Alginate/Gelatine Hydrogels. *J Mech Behav Biomed Mater* **2013**, 18, 152-166. <https://doi.org/10.1016/j.jmbbm.2012.11.010>.
- (211) Wickramathilaka, M. P.; Tao, B. Y. Characterization of Covalent Crosslinking Strategies for Synthesizing DNA-Based Bioconjugates. *J Biol Eng* **2019**, 13 (1), 8-17. <https://doi.org/10.1186/s13036-019-0191-2>.
- (212) Ayouch, I.; Barrak, I.; Kassab, Z.; El Achaby, M.; Barhoun, A.; Draoui, K. Impact of the Drying Process on the Efficiency of Alginate Beads for Cadmium Removal from Water: Kinetic, Isotherm and Thermodynamic Study. *Environ Technol Innov* **2020**, 20, 101157. <https://doi.org/10.1016/j.eti.2020.101157>.

- (213) Cesco, C. T.; Valente, A. J. M.; Paulino, A. T. Methylene Blue Release from Chitosan/Pectin and Chitosan/Dna Blend Hydrogels. *Pharmaceutics* **2021**, *13* (6), 1-18. <https://doi.org/10.3390/pharmaceutics13060842>.
- (214) Perez-Masia, R.; Lagaron, J. M.; Lopez-Rubio, A. Surfactant-Aided Electro spraying of Low Molecular Weight Carbohydrate Polymers from Aqueous Solutions. *Carbohydr Polym* **2014**, *101* (1), 249-255. <https://doi.org/10.1016/j.carbpol.2013.09.032>.
- (215) Alallam, B.; Altahhan, S.; Taher, M.; Mohd Nasir, M. H.; Doolaanea, A. A. Electro sprayed Alginate Nanoparticles as Crispr Plasmid Dna Delivery Carrier: Preparation, Optimization, and Characterization. *Pharmaceutics* **2020**, *13* (8), 1-29. <https://doi.org/10.3390/ph13080158>.
- (216) Ecker, P.; Sparer, A.; Lukitsch, B.; Elenkov, M.; Seltenhammer, M.; Crevenna, R.; Gföhler, M.; Harasek, M.; Windberger, U. Animal Blood in Translational Research: How to Adjust Animal Blood Viscosity to the Human Standard. *Physiol Rep* **2021**, *9* (10), 1-10. <https://doi.org/10.14814/phy2.14880>.
- (217) Arthur, R. M.; Cockerton, S. L.; de Bruin, K. G.; Taylor, M. C. A Novel, Element-Based Approach for the Objective Classification of Bloodstain

Patterns. *Forensic Sci Int* **2015**, 257, 220-228.

<https://doi.org/10.1016/j.forsciint.2015.08.028>.

(218) Orr, A.; Wilson, P.; Stotesbury, T. DNA-Crosslinked Alginate Hydrogels:

Characterization, Microparticle Development, and Applications in

Forensic Science. *ACS Appl Polym Mater* **2023**, 5 (1), 583-592.

<https://doi.org/10.1021/acsapm.2c01673>.

(219) Kim, S.; Ma, Y.; Agrawal, P.; Attinger, D. How Important Is It to Consider

Target Properties and Hematocrit in Bloodstain Pattern Analysis? *Forensic*

*Sci Int* **2016**, 266, 178-184.

<https://doi.org/10.1016/j.forsciint.2018.04.001>.

(220) Eckmann, D. M.; Bowers, S.; Stecker, M.; Cheung, A. T. Hematocrit,

Volume Expander, Temperature, and Shear Rate Effects on Blood

Viscosity. *Anesth Analg* **2000**, 91 (3), 539-545.

<https://doi.org/10.1213/00000539-200009000-00007>.

(221) Zhong, L.; Oostrom, M.; Truex, M. J.; Vermeul, V. R.; Szecsody, J. E.

Rheological Behavior of Xanthan Gum Solution Related to Shear Thinning

Fluid Delivery for Subsurface Remediation. *J Hazard Mater* **2013**, 244-

245, 160-170. <https://doi.org/10.1016/j.jhazmat.2012.11.028>.



- (222) Pagano, C.; Puglia, D.; Luzi, F.; Michele, A. Di; Scuota, S.; Primavilla, S.; Ceccarini, M. R.; Beccari, T.; Iborra, C. A. V.; Ramella, D.; Ricci, M.; Perioli, L. Development and Characterization of Xanthan Gum and Alginate Based Bioadhesive Film for Pycnogenol Topical Use in Wound Treatment. *Pharmaceutics* **2021**, *13* (3), 1-19. <https://doi.org/10.3390/pharmaceutics13030324>.
- (223) Jena, S. R.; Dalei, G.; Das, S.; Nayak, J.; Pradhan, M.; Samanta, L. Harnessing the Potential of Dialdehyde Alginate-Xanthan Gum Hydrogels as Niche Bioscaffolds for Tissue Engineering. *Int J Biol Macromol* **2022**, *207*, 493-506. <https://doi.org/10.1016/j.ijbiomac.2022.03.024>.
- (224) Naji-Tabasi, S.; Shahidi-Noghabi, M.; Dovom, A. M. Investigating the Fabrication and Functional Properties of New Composite Hydrogels Containing Gellan/ Alginate/ Xanthan Gum. *J Solgel Sci Technol* **2023**, *105*, 637-649. <https://doi.org/10.1007/s10971-022-06014-5>.
- (225) BeMiller, J. N. Xanthan. In *Carbohydrate Chemistry for Food Scientists*; Woodhead Publishing and AACC International Press, 2018; pp 261-269. <https://doi.org/10.1016/b978-0-12-812069-9.00011-x>.

- (226) Laan, N.; De Bruin, K. G.; Bartolo, D.; Josserand, C.; Bonn, D. Maximum Diameter of Impacting Liquid Droplets. *Phys Rev Appl* **2014**, 2 (4), 044018-1-7. <https://doi.org/10.1103/PhysRevApplied.2.044018>.
- (227) Jiang, J. K.; Mu, Y.; Yu, H. Q. Differences in the Colloid Properties of Sodium Alginate and Polysaccharides in Extracellular Polymeric Substances with Regard to Membrane Fouling. *J Colloid Interface Sci* **2019**, 535, 318-324. <https://doi.org/10.1016/j.jcis.2018.10.002>.
- (228) Hazur, J.; Detsch, R.; Karakaya, E.; Kaschta, J.; Teßmar, J.; Schneidereit, D.; Friedrich, O.; Schubert, D. W.; Boccaccini, A. R. Improving Alginate Printability for Biofabrication: Establishment of a Universal and Homogeneous Pre-Crosslinking Technique. *Biofabrication* **2020**, 12, 045004. <https://doi.org/10.1088/1758-5090/ab98e5>.
- (229) Voo, W. P.; Ooi, C. W.; Islam, A.; Tey, B. T.; Chan, E. S. Calcium Alginate Hydrogel Beads with High Stiffness and Extended Dissolution Behaviour. *Eur Polym J* **2016**, 75, 343-353. <https://doi.org/10.1016/j.eurpolymj.2015.12.029>.
- (230) Gracheva, M.; Homonnay, Z.; Singh, A.; Fodor, F.; Marosi, V. B.; Solti, Á.; Kovács, K. New Aspects of the Photodegradation of Iron(III) Citrate:

- Spectroscopic Studies and Plant-Related Factors. *Photochem Photobiol Sci* **2022**, 21 (6), 983-996. <https://doi.org/10.1007/s43630-022-00188-1>.
- (231) Francis, A. J.; Dodge, C. J. Influence of Complex Structure on the Biodegradation of Iron-Citrate Complexes. *Appl Environ Microbiol* **1993**, 59(1), 109-113.
- (232) Heinz, H.; Pramanik, C.; Heinz, O.; Ding, Y.; Mishra, R. K.; Marchon, D.; Flatt, R. J.; Estrela-lopis, I.; Llop, J.; Moya, S.; Ziolo, R. F. Surface Science Reports Nanoparticle Decoration with Surfactants : Molecular Interactions , Assembly , and Applications. *Surf Sci Rep* **2017**, 72 (1), 1-58. <https://doi.org/10.1016/j.surfrep.2017.02.001>.
- (233) Kang, M.; Oderinde, O.; Liu, S.; Huang, Q.; Ma, W.; Yao, F.; Fu, G. Characterization of Xanthan Gum-Based Hydrogel with Fe<sup>3+</sup> Ions Coordination and Its Reversible Sol-Gel Conversion. *Carbohydr Polym* **2019**, 203, 139-147. <https://doi.org/10.1016/j.carbpol.2018.09.044>.
- (234) Bashir, S.; Hina, M.; Iqbal, J.; Rajpar, A. H.; Mujtaba, M. A.; Alghamdi, N. A.; Wageh, S.; Ramesh, K.; Ramesh, S. Fundamental Concepts of Hydrogels: Synthesis, Properties, and Their Applications. *Polymers (Basel)* **2020**, 12 (11), 1-60. <https://doi.org/10.3390/polym12112702>.

- (235) Massana Roquero, D.; Othman, A.; Melman, A.; Katz, E. Iron(III)-Cross-Linked Alginate Hydrogels: A Critical Review. *Mater Adv* **2022**, 3 (4), 1849-1873. <https://doi.org/10.1039/d1ma00959a>.
- (236) Grishaev, V.; Iorio, C. S.; Dubois, F.; Amirfazli, A. Complex Drop Impact Morphology. *Langmuir* **2015**, 31 (36), 9833-9844. <https://doi.org/10.1021/acs.langmuir.5b02162>.
- (237) AAFS Standards Board. *Terms and Definitions in Bloodstain Pattern Analysis*; Washington, DC, 2017.
- (238) Li, Y.; Hewitt, D.; Lentz, Y. K.; Ji, J. A.; Zhang, T. Y.; Zhang, K. Characterization and Stability Study of Polysorbate 20 in Therapeutic Monoclonal Antibody Formulation by Multidimensional Ultrahigh-Performance Liquid Chromatography-Charged Aerosol Detection-Mass Spectrometry. *Anal Chem* **2014**, 86 (10), 5150-5157. <https://doi.org/10.1021/ac5009628>.
- (239) Renneke, H. G.; Venkatachalam, M. A. Chemical Modification of Horseradish Peroxidase. *J Histochem Cytochem* **1979**, 27 (10), 1352-1353.
- (240) Abourehab, M. A. S.; Rajendran, R. R.; Singh, A.; Pramanik, S.; Shrivastav, P.; Ansari, M. J.; Manne, R.; Amaral, L. S.; Deepak, A. Alginate as a

Promising Biopolymer in Drug Delivery and Wound Healing: A Review of the State-of-the-Art. *Int J Mol Sci* **2022**, 23 (16), 1-57. <https://doi.org/10.3390/ijms23169035>.

(241) Weber, A.; Wójtowicz, A.; Lednev, I. K. Post Deposition Aging of Bloodstains Probed by Steady-State Fluorescence Spectroscopy. *J Photochem Photobiol B* **2021**, 221. <https://doi.org/10.1016/j.jphotobiol.2021.112251>.

(242) Elliott, C. I.; Shafer, A. B. A.; Stotesbury, T. E. The Crux of Time: A Meta-Analysis of Ex Vivo Whole Blood Degradation. *Frontiers in Analytical Science* **2022**, 2, 1-13. <https://doi.org/10.3389/frans.2022.928573>.

(243) Orr, A.; Wilson, P.; Stotesbury, T. Alginate/Xanthan Gum Hydrogels as Forensic Blood Substitutes for Bloodstain Formation and Analysis. *Soft Matter* **2023**. <https://doi.org/10.1039/D3SM00341H>.

# Appendix I



49 Spadina Ave. Suite 200  
Toronto ON M5V 2J1 Canada  
www.biorender.com

## Confirmation of Publication and Licensing Rights

March 14th, 2023  
Science Suite Inc.

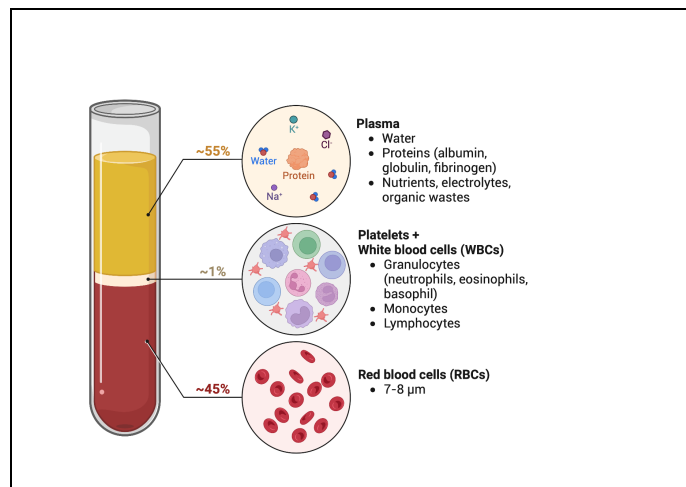
**Subscription:** Individual  
**Agreement number:** EH254GT935  
**Journal name:** PhD Thesis

To whom this may concern,

This document Teresa Sobue submitted that granted a license BioRender content, including icons, templates and attached completed graphic Alca de pu rcs U a r c t e n s t i o i B e i r o n d e s r e s BioRender content to be sublicensed for use in journal


All rights and ownership of BioRender content are reserved and should be accompanied by the following citation: "Created with BioRender"

BioRender content included in the completed graphic is for publication in a journal. For any commercial use of the graphic, please contact BioRender under an Industry BioRender Plan.



For any questions regarding this document, or other questions about publishing with BioRender refer to our [BioRender Publication Guide](#), or contact BioRender Support at [support@biorender.com](mailto:support@biorender.com).

Figure A1.1. Copyright permission obtained from BioRender for Figure 1.1 on page 3.



**Metal Selectivity of Sargassum spp. and Their Alginates in Relation to Their  $\alpha$ -L-Guluronic Acid Content and Conformation**

Author: Thomas A. Davis, Francisco Llanes, Bohumil Volesky, et al  
 Publication: Environmental Science & Technology  
 Publisher: American Chemical Society  
 Date: Jan 1, 2003

Copyright © 2003, American Chemical Society


**PERMISSION/LICENSE IS GRANTED FOR YOUR ORDER AT NO CHARGE**

This type of permission/license, instead of the standard Terms and Conditions, is sent to you because no fee is being charged for your order. Please note the following:

- Permission is granted for your request in both print and electronic formats, and translations.
- If figures and/or tables were requested, they may be adapted or used in part.
- Please print this page for your records and send a copy of it to your publisher/graduate school.
- Appropriate credit for the requested material should be given as follows: "Reprinted (adapted) with permission from (COMPLETE REFERENCE CITATION). Copyright (YEAR) American Chemical Society." Insert appropriate information in place of the capitalized words.
- One-time permission is granted only for the use specified in your RightsLink request. No additional uses are granted (such as derivative works or other editions). For any uses, please submit a new request.

If credit is given to another source for the material you requested from RightsLink, permission must be obtained from that source.

BACK
CLOSE WINDOW



**Polysaccharide research in Trondheim**

Author: Bjørn E. Christensen, Mentz Indergaard, Olav Smidsrød  
 Publication: Carbohydrate Polymers  
 Publisher: Elsevier  
 Date: 1990

Copyright © 1990 Published by Elsevier Ltd.

**Order Completed**

Thank you for your order.

This Agreement between Trent University – Amanda Orr ("You") and Elsevier ("Elsevier") consists of your license details and the terms and conditions provided by Elsevier and Copyright Clearance Center.


Your confirmation email will contain your order number for future reference.

License Number	5510770603945
License date	Mar 16, 2023

[Printable Details](#)

<p><b>Licensed Content</b></p> <table border="0" style="width: 100%;"> <tr> <td style="width: 30%;">Licensed Content Publisher</td> <td>Elsevier</td> </tr> <tr> <td>Licensed Content Publication</td> <td>Carbohydrate Polymers</td> </tr> <tr> <td>Licensed Content Title</td> <td>Polysaccharide research in Trondheim</td> </tr> <tr> <td>Licensed Content Author</td> <td>Bjørn E. Christensen, Mentz Indergaard, Olav Smidsrød</td> </tr> <tr> <td>Licensed Content Date</td> <td>Jan 1, 1990</td> </tr> <tr> <td>Licensed Content Volume</td> <td>13</td> </tr> <tr> <td>Licensed Content Issue</td> <td>3</td> </tr> <tr> <td>Licensed Content Pages</td> <td>17</td> </tr> </table> <p><b>About Your Work</b></p> <table border="0" style="width: 100%;"> <tr> <td style="width: 30%;">Title</td> <td>PhD Thesis</td> </tr> <tr> <td>Institution name</td> <td>Trent University</td> </tr> <tr> <td>Expected presentation date</td> <td>Apr 2023</td> </tr> </table> <p><b>Requestor Location</b></p> <table border="0" style="width: 100%;"> <tr> <td style="width: 30%;"></td> <td>Trent University 1600 West Bank Drive</td> </tr> <tr> <td>Requestor Location</td> <td>Peterborough, ON K9L 0G2 Canada Attn: Trent University</td> </tr> </table> <p><b>Price</b></p> <table border="0" style="width: 100%;"> <tr> <td style="width: 30%;">Total</td> <td>0.00 CAD</td> </tr> </table>	Licensed Content Publisher	Elsevier	Licensed Content Publication	Carbohydrate Polymers	Licensed Content Title	Polysaccharide research in Trondheim	Licensed Content Author	Bjørn E. Christensen, Mentz Indergaard, Olav Smidsrød	Licensed Content Date	Jan 1, 1990	Licensed Content Volume	13	Licensed Content Issue	3	Licensed Content Pages	17	Title	PhD Thesis	Institution name	Trent University	Expected presentation date	Apr 2023		Trent University 1600 West Bank Drive	Requestor Location	Peterborough, ON K9L 0G2 Canada Attn: Trent University	Total	0.00 CAD	<p><b>Order Details</b></p> <table border="0" style="width: 100%;"> <tr> <td style="width: 30%;">Type of Use</td> <td>reuse in a thesis/dissertation</td> </tr> <tr> <td>Portion</td> <td>figures/tables/illustrations</td> </tr> <tr> <td>Number of figures/tables/illustrations</td> <td>1</td> </tr> <tr> <td>Format</td> <td>both print and electronic</td> </tr> <tr> <td>Are you the author of this Elsevier article?</td> <td>No</td> </tr> <tr> <td>Will you be translating?</td> <td>No</td> </tr> </table> <p><b>Additional Data</b></p> <table border="0" style="width: 100%;"> <tr> <td style="width: 30%;">Portions</td> <td>Fig. 3.</td> </tr> </table> <p><b>Tax Details</b></p> <table border="0" style="width: 100%;"> <tr> <td style="width: 30%;">Publisher Tax ID</td> <td>GB 494 6272 12</td> </tr> </table>	Type of Use	reuse in a thesis/dissertation	Portion	figures/tables/illustrations	Number of figures/tables/illustrations	1	Format	both print and electronic	Are you the author of this Elsevier article?	No	Will you be translating?	No	Portions	Fig. 3.	Publisher Tax ID	GB 494 6272 12
Licensed Content Publisher	Elsevier																																												
Licensed Content Publication	Carbohydrate Polymers																																												
Licensed Content Title	Polysaccharide research in Trondheim																																												
Licensed Content Author	Bjørn E. Christensen, Mentz Indergaard, Olav Smidsrød																																												
Licensed Content Date	Jan 1, 1990																																												
Licensed Content Volume	13																																												
Licensed Content Issue	3																																												
Licensed Content Pages	17																																												
Title	PhD Thesis																																												
Institution name	Trent University																																												
Expected presentation date	Apr 2023																																												
	Trent University 1600 West Bank Drive																																												
Requestor Location	Peterborough, ON K9L 0G2 Canada Attn: Trent University																																												
Total	0.00 CAD																																												
Type of Use	reuse in a thesis/dissertation																																												
Portion	figures/tables/illustrations																																												
Number of figures/tables/illustrations	1																																												
Format	both print and electronic																																												
Are you the author of this Elsevier article?	No																																												
Will you be translating?	No																																												
Portions	Fig. 3.																																												
Publisher Tax ID	GB 494 6272 12																																												

**Figure A1.2.** Copyright permission obtained for Figure 1.2 on page 10. Copyrights are obtained from the American Chemical Society (top) and Carbohydrate Polymers (bottom) for the manuscripts where Figure 1.2 was adapted from.




**Calcium-Alginate Tissue Gels (CATG): Proof-of-concept biomaterial development**  
Author: Amanda Orr, Paul Wilson, Theresa Stotesbury  
Publication: Forensic Science International  
Publisher: Elsevier  
Date: December 2021  
© 2021 Elsevier B.V. All rights reserved.

**Journal Author Rights**

Please note that, as the author of this Elsevier article, you retain the right to include it in a thesis or dissertation, provided it is not published commercially. Permission is not required, but please ensure that you reference the journal as the original source. For more information on this and on your other retained rights, please visit: <https://www.elsevier.com/about/our-business/policies/copyright#Author-rights>

BACK CLOSE WINDOW

*Figure A1.3. Copyright permission obtained from Elsevier (Forensic Science International) for Chapter 2 publication.*



**The use of high-resolution mass spectrometry (HRMS) for the analysis of DNA and other macromolecules: A how-to guide for forensic chemistry**  
Author: Amanda Orr, Theresa Stotesbury, Paul Wilson, Naomi L. Stock  
Publication: Forensic Chemistry  
Publisher: Elsevier  
Date: June 2019  
© 2019 Published by Elsevier B.V.

**Journal Author Rights**

Please note that, as the author of this Elsevier article, you retain the right to include it in a thesis or dissertation, provided it is not published commercially. Permission is not required, but please ensure that you reference the journal as the original source. For more information on this and on your other retained rights, please visit: <https://www.elsevier.com/about/our-business/policies/copyright#Author-rights>

BACK CLOSE WINDOW

*Figure A1.4. Copyright permission obtained from Elsevier (Forensic Chemistry) for Chapter 3 publication.*



## Confirmation of Publication and Licensing Rights

March 27th, 2023  
Science Suite Inc.

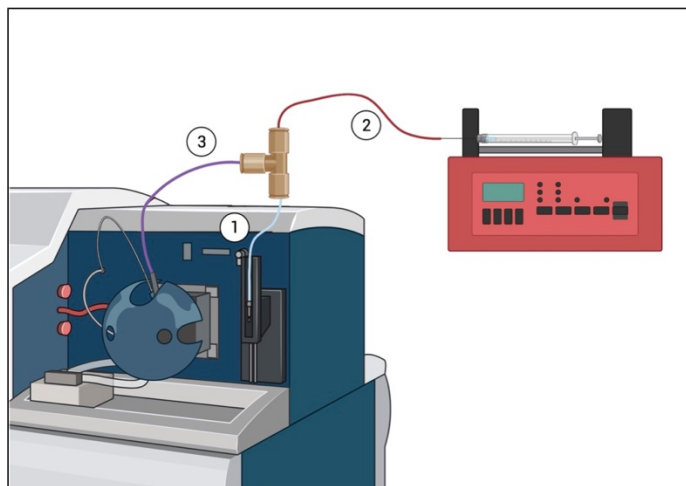
**Subscription:** Individual  
**Agreement number:** JB256BSDWE  
**Journal name:** PhD Thesis

To whom this may concern,

This document is to confirm that Theresa Stotesbury has been granted a license to use the BioRender content, including icons, templates and other original artwork, appearing in the attached completed graphic pursuant to BioRender's [Academic License Terms](#). This license permits BioRender content to be sublicensed for use in journal publications.

All rights and ownership of BioRender content are reserved by BioRender. All completed graphics must be accompanied by the following citation: "Created with BioRender.com".

BioRender content included in the completed graphic is not licensed for any commercial uses beyond publication in a journal. For any commercial use of this figure, users may, if allowed, recreate it in BioRender under an Industry BioRender Plan.



For any questions regarding this document, or other questions about publishing with BioRender refer to our [BioRender Publication Guide](#), or contact BioRender Support at [support@biorender.com](mailto:support@biorender.com).

Figure A1.5. Copyright permission obtained from BioRender for Figure 3.8 on page 88.

**DNA-Crosslinked Alginate Hydrogels: Characterization, Microparticle Development, and Applications in Forensic Science**

**Author:** Amanda Orr, Paul Wilson, Theresa Stotesbury  
**Publication:** ACS Applied Polymer Materials  
**Publisher:** American Chemical Society  
**Date:** Jan 1, 2023

*Copyright © 2023, American Chemical Society*

**PERMISSION/LICENSE IS GRANTED FOR YOUR ORDER AT NO CHARGE**

This type of permission/license, instead of the standard Terms and Conditions, is sent to you because no fee is being charged for your order. Please note the following:

- Permission is granted for your request in both print and electronic formats, and translations.
- If figures and/or tables were requested, they may be adapted or used in part.
- Please print this page for your records and send a copy of it to your publisher/graduate school.
- Appropriate credit for the requested material should be given as follows: "Reprinted (adapted) with permission from {COMPLETE REFERENCE CITATION}. Copyright {YEAR} American Chemical Society." Insert appropriate information in place of the capitalized words.
- One-time permission is granted only for the use specified in your RightsLink request. No additional uses are granted (such as derivative works or other editions). For any uses, please submit a new request.

If credit is given to another source for the material you requested from RightsLink, permission must be obtained from that source.

[BACK](#) [CLOSE WINDOW](#)

*Figure A1.6. Copyright permission obtained from the American Chemical Society (ACS Applied Polymer Materials) for Chapter 4 publication.*

## Confirmation of Publication and Licensing Rights

September 21st, 2022  
Science Suite Inc.

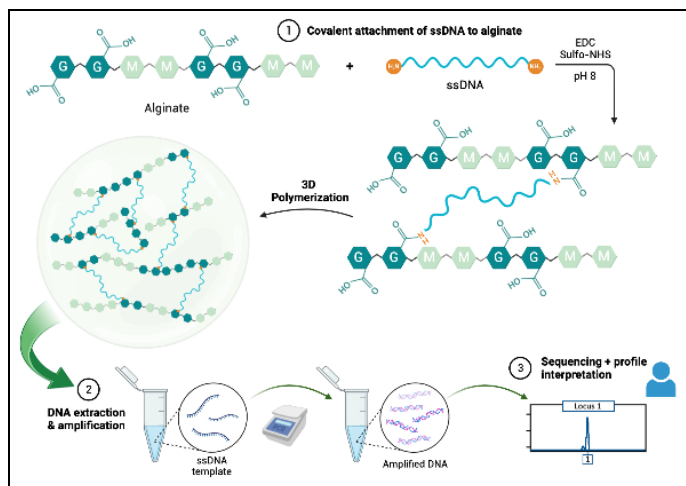
**Subscription:** Individual  
**Agreement number:** UW24FJSX9D  
**Journal name:** ACS Applied Polymer Materials

To whom this may concern,

This document is a BioRender content that granted a license to Science Suite Inc. for the use of BioRender content, including icons, templates and attached completed graphics. The BioRender content is licensed to Science Suite Inc. for the use of BioRender content to be sublicensed for use in journal publications.

All rights and ownership of BioRender content are reserved and should be accompanied by the following citation: "Created with BioRender."

BioRender content included in the completed graphic is published in a journal. For any commercial use of the BioRender under an Industry BioRender Plan.



For any questions regarding this document, or other questions about publishing with BioRender refer to our [BioRender Publication Guide](#), or contact BioRender Support at [support@biorender.com](mailto:support@biorender.com).

**Figure A1.7.** Copyright permission obtained from BioRender for Chapter 4 Graphical Abstract on page 100.

## Confirmation of Publication and Licensing Rights

September 21st, 2022  
 Science Suite Inc.

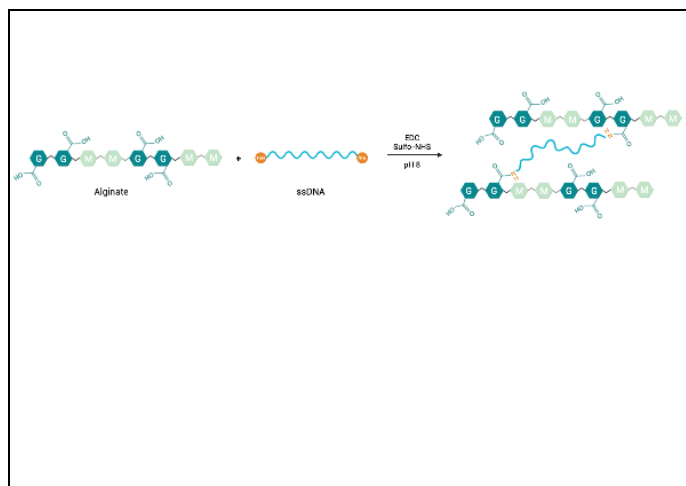
**Subscription:** Individual  
**Agreement number:** DP24FJR20S  
**Journal name:** ACS Applied Polymer Materials

To whom this may concern,

This document is a ~~subscription~~ <sup>license</sup> that granted a license to use BioRender content, including icons, templates and attached completed graphic ~~academic results~~ <sup>academic results</sup> in the BioRender content to be sublicensed for use in journal

All rights and ownership of BioRender content are reserved and should be accompanied by the following citation: "Created with BioRender"

BioRender content included in the completed graphic is not to be published in a journal. For any commercial use of the BioRender under an Industry BioRender Plan.



For any questions regarding this document, or other questions about publishing with BioRender refer to our [BioRender Publication Guide](#), or contact BioRender Support at [support@biorender.com](mailto:support@biorender.com).

Figure A1.8. Copyright permission obtained from BioRender for Scheme 1 on page 109.

## Confirmation of Publication and Licensing Rights

March 24th, 2023  
Science Suite Inc.

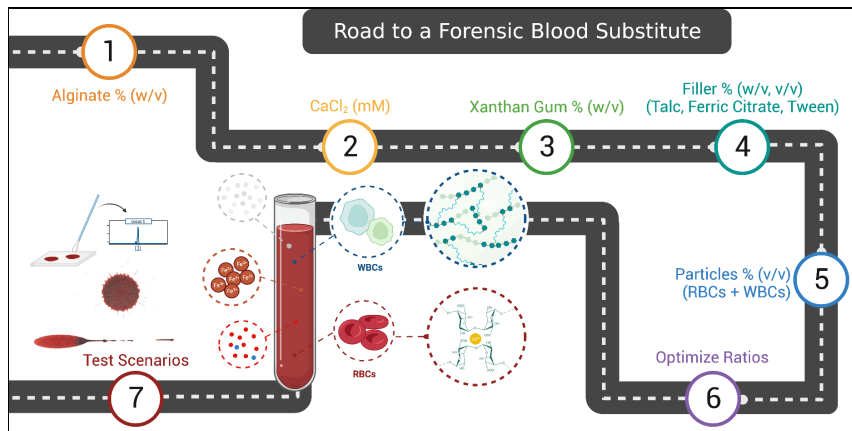
**Subscription:** Individual  
**Agreement number:** MG255UY1R4  
**Journal name:** Soft Matter

To whom this may concern,

This document is a BioRender subscription that granted a license to use BioRender content, including icons, templates and graphics. The attached completed graphic is a demonstration of the BioRender content to be sublicensed for use in journal articles.

All rights and ownership of BioRender content are reserved and should be accompanied by the following citation: "Created with BioRender."

BioRender content included in the completed graphic is published in a journal. For any commercial use of the BioRender under an Industry BioRender Plan.



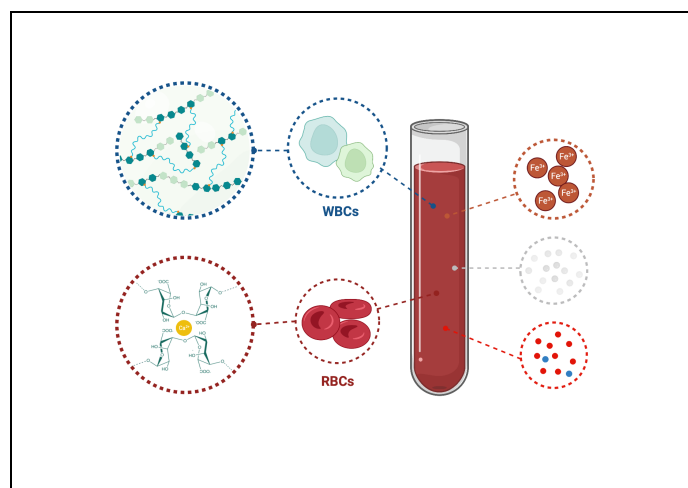
For any questions regarding this document, or other questions about publishing with BioRender refer to our [BioRender Publication Guide](#), or contact BioRender Support at [support@biorender.com](mailto:support@biorender.com).

Figure A1.9. Copyright permission obtained from BioRender for Chapter 5 Graphical Abstract on page 135.

## Confirmation of Publication and Licensing Rights

March 24th, 2023  
Science Suite Inc.

**Subscription:** Individual  
**Agreement number:** RB255UXXIU  
**Journal name:** Soft Matter



For any questions regarding this document, or other questions about publishing with BioRender refer to our [BioRender Publication Guide](#), or contact BioRender Support at [support@biorender.com](mailto:support@biorender.com).

**Figure A1.10.** Copyright permission obtained from BioRender for graphic in Figure 5.5 on page 161.

## Confirmation of Publication and Licensing Rights

March 24th, 2023  
Science Suite Inc.

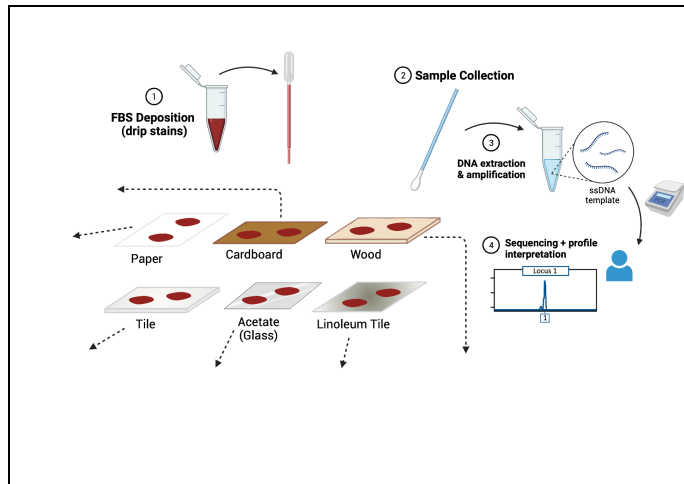
**Subscription:** Individual  
**Agreement number:** TQ255UXU3T  
**Journal name:** Soft Matter

To whom this may concern,

This document Theresa Schaefer submitted that granted a license BioRender content, including icons, templates and attached completed graphic Academic Article in the BioRender's BioRender content to be sublicensed for use in journal

All rights and ownership of BioRender content are reserved be accompanied by the following citation: "Created with

BioRender content included in the completed graphic is publication in a journal. For any commercial use of the BioRender under an Industry BioRender Plan.



For any questions regarding this document, or other questions about publishing with BioRender refer to our [BioRender Publication Guide](#), or contact BioRender Support at [support@biorender.com](mailto:support@biorender.com).

Figure A1.11. Copyright permission obtained from BioRender for graphic in Figure 5.10 on page 170.

## Appendix II

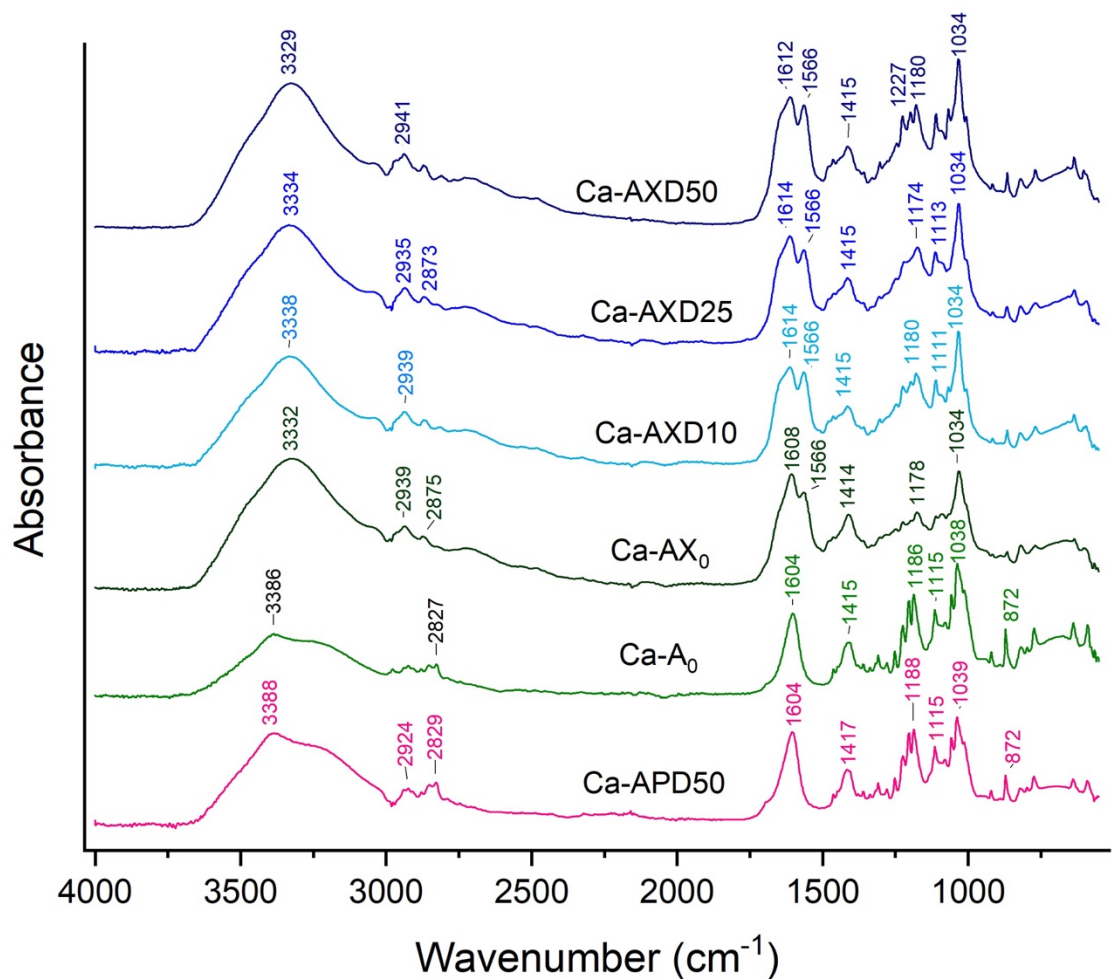


**Figure A2.1.** FTIR spectra for six different ionic and dual crosslinked alginate materials. Materials AX<sub>0</sub>, AXD10, AXD25, and AXD50 were covalently crosslinked using EDC/Sulfo-NHS and calcium (+Ca<sup>2+</sup>, dual crosslinked); and samples A<sub>0</sub> and APD50 were mixed with calcium, but without the addition of EDC/NHS (+Ca<sup>2+</sup>, ionic crosslinked).



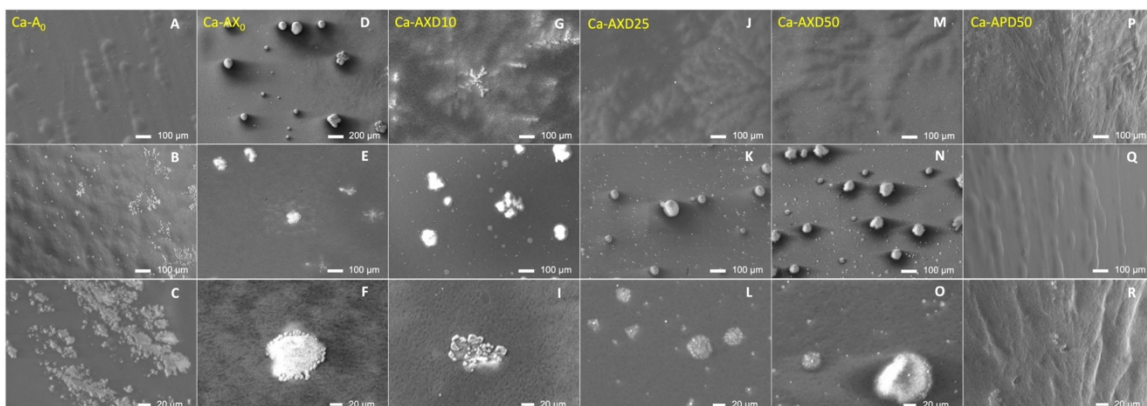


**Figure A2.2.** SEM images of ionically crosslinked and dual crosslinked materials with  $\text{Ca}^{2+}$ . Samples from left to right are:  $\text{Ca-A}_0$  (A-C),  $\text{Ca-AX}_0$  (D-F),  $\text{Ca-AXD10}$  (G-I),  $\text{Ca-AXD25}$  (J-L),  $\text{Ca-AXD50}$  (M-O), and  $\text{Ca-APD50}$  (P-R). The first two rows represent magnification at approximately 1000 x except for D, which shows larger particles at 500 x, and the bottom row is 4000 x.

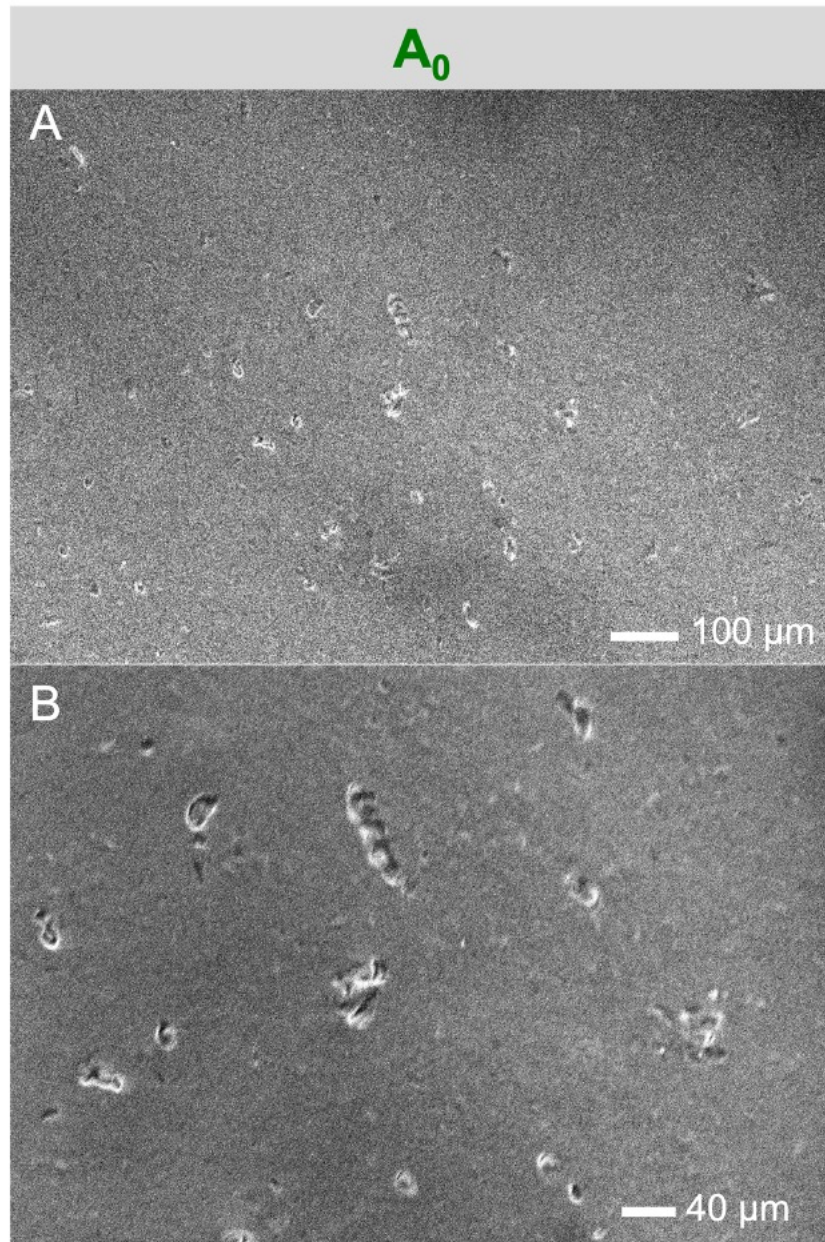


**Figure A2.3.** High resolution SEM images of sample A<sub>0</sub> (1% w/v alginate) taken at 1000 x (A) and 2000 x (B) magnification.

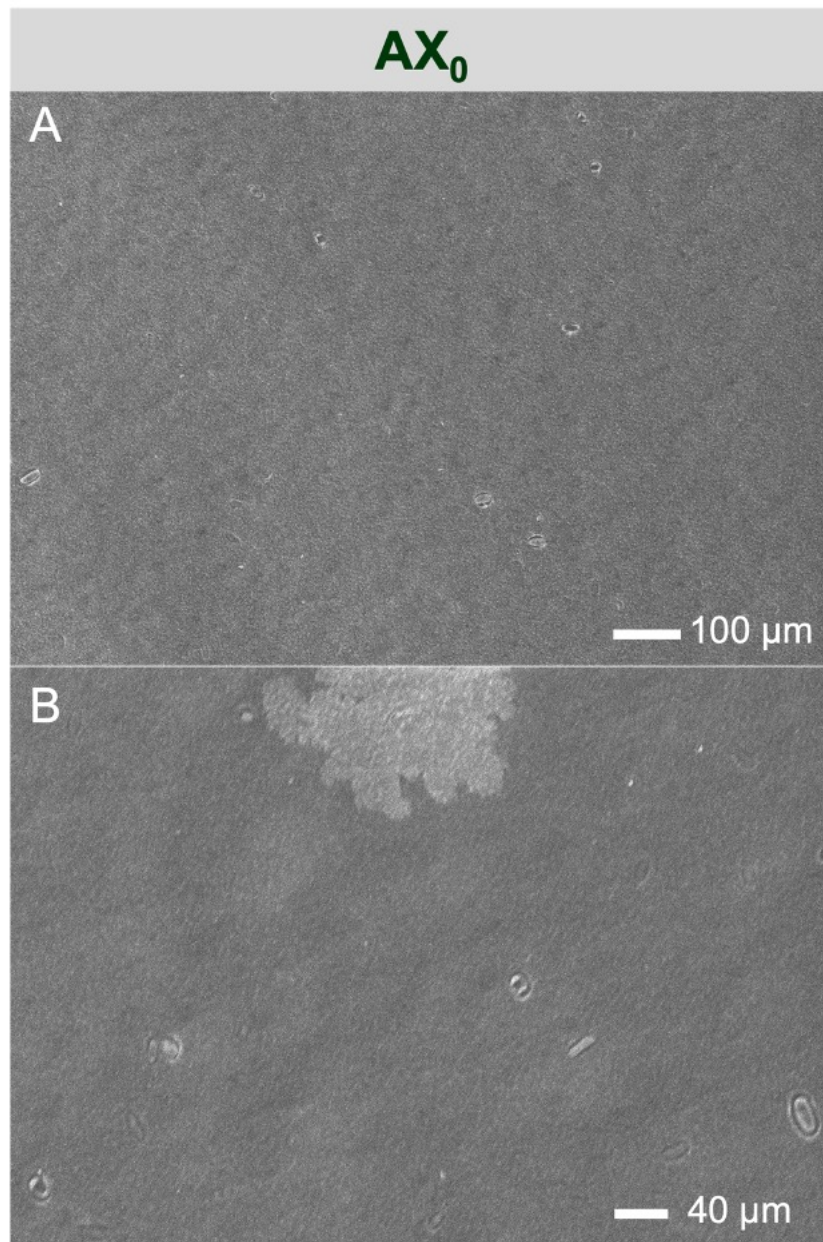


**Figure A2.4.** High resolution SEM images of sample AX<sub>0</sub> (1% w/v alginate crosslinking control) taken at 1000 x (A) and 2000 x (B) magnification.

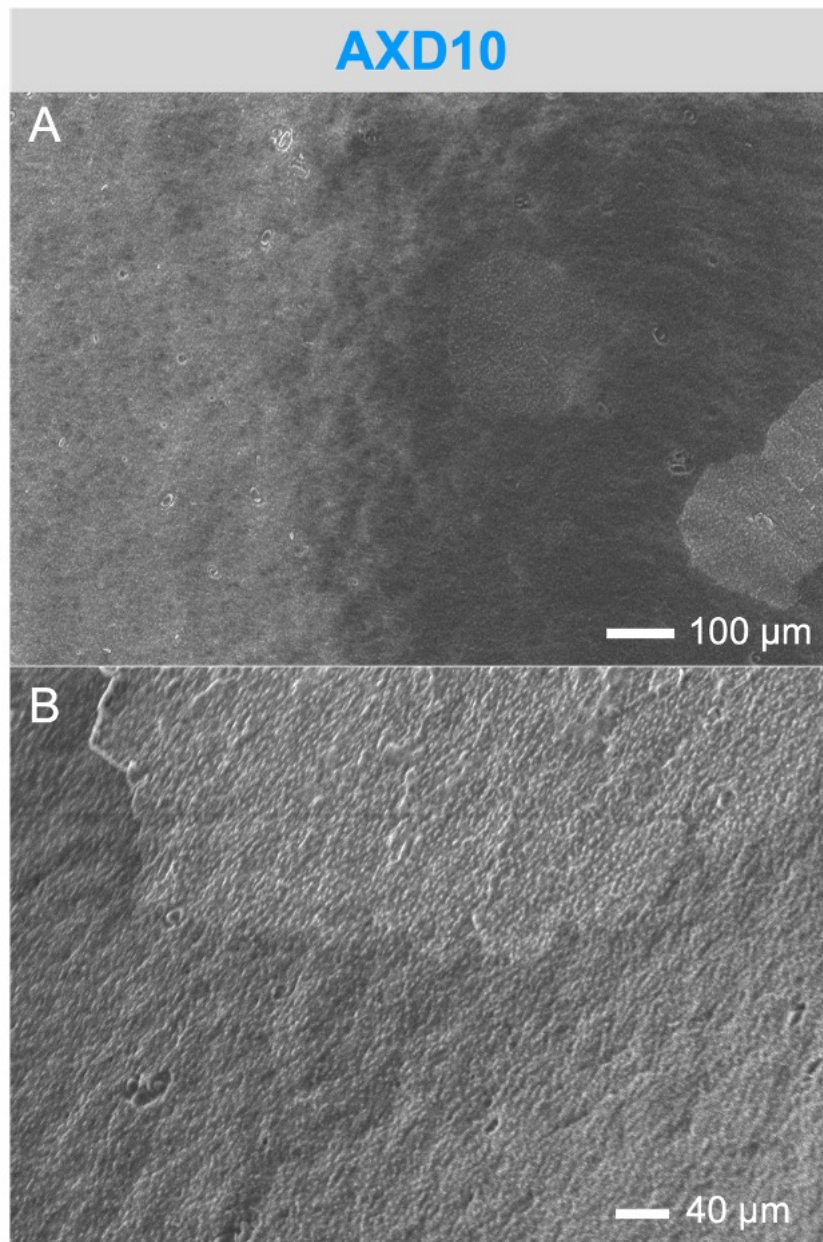


**Figure A2.5.** High resolution SEM images of sample AXD10 (1% w/v alginate covalently crosslinked with 10 nmol of N-DNA-N) taken at 1000 x (A) and 2000 x (B) magnification.

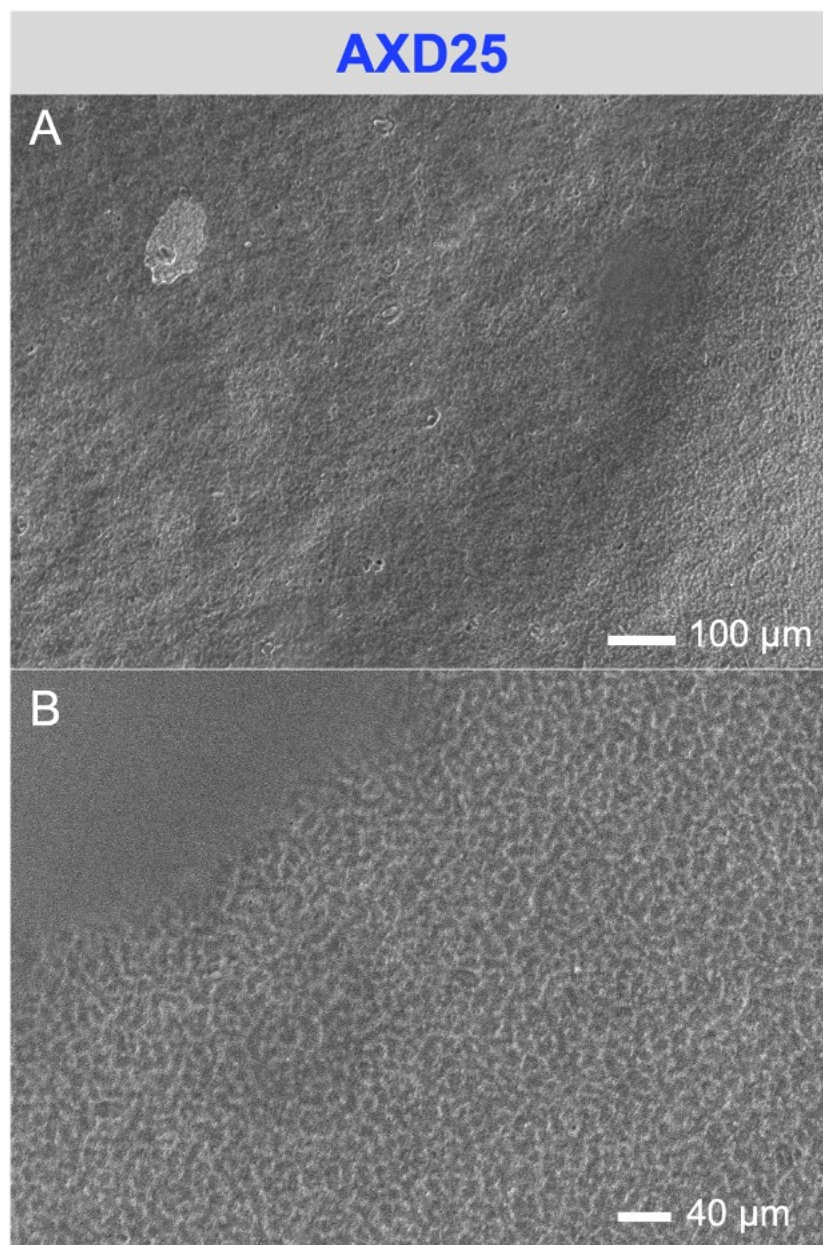


**Figure A2.6.** High resolution SEM images of sample AXD25 (1% w/v alginate covalently crosslinked with 25 nmol of N-DNA-N) taken at 1000 x (A) and 2000 x (B) magnification.

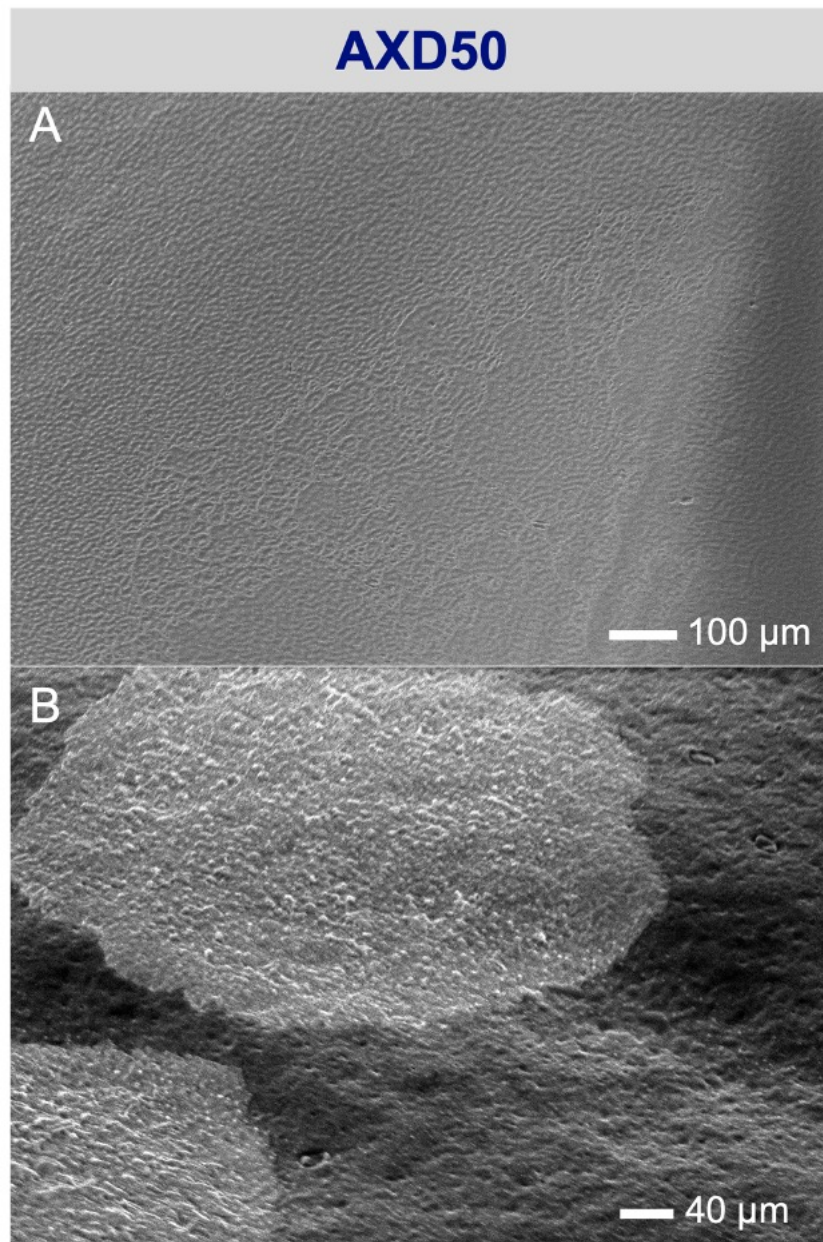


**Figure A2.7.** High resolution SEM images of sample AXD50 (1% w/v alginate covalently crosslinked with 50 nmol of N-DNA-N) taken at 1000 x (A) and 2000 x (B) magnification.

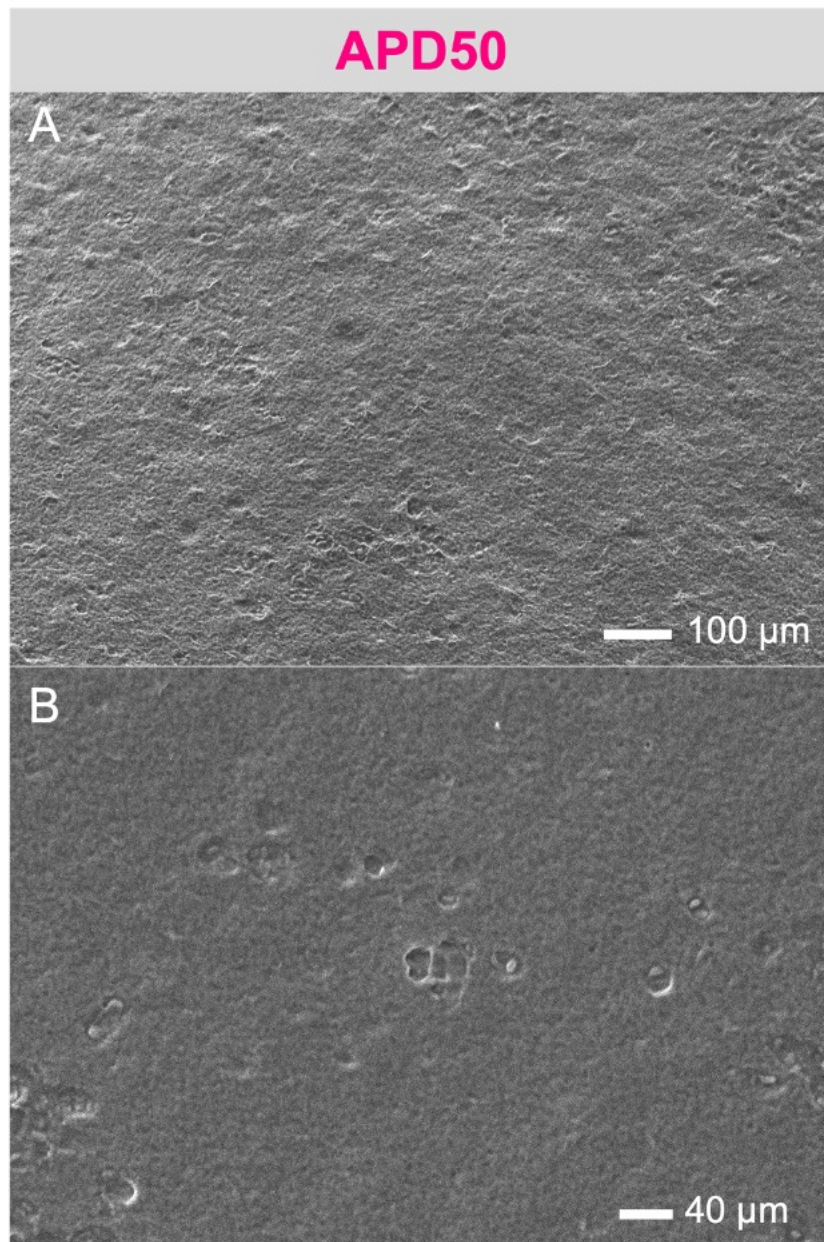


**Figure A2.8.** High resolution SEM images of sample APD50 (1% w/v alginate mixed with 50 nmol of N-DNA-N) taken at 1000 x (A) and 2000 x (B) magnification.

**Table A2.1.** The composition of each FBS candidate material assessed in this work. Components include alginate, CaCl<sub>2</sub> (Ca), xanthan gum (XG), electrosprayed microparticles (MPs), ferric citrate (FeCit), magnesium silicate (talc) and Tween 20 (Tween 20).

Sample	Alginate (w/v%)	Ca <sup>2+</sup> (mM)	XG (w/v%) ×10 <sup>-3</sup>	MPs (v/v%)	FeCit (w/v%) ×10 <sup>-3</sup>	Talc (w/v%) ×10 <sup>-1</sup>	Tween 20 (v/v%)
AX5C1	1%	1	5.0				
AX5C1-10%	1%	1	5.0	10			
AX5C1.5	1%	1.5	5.0				
AX5C1.5-5%	1%	1.5	5.0	5			
AX5C1.5-10%	1%	1.5	5.0	10			
AX5C1.5-10% + Ta + Tw	1%	1.5	5.0	10		2.5	3.75 ×10 <sup>-2</sup>
AX5C1.5-10% + Fe+ Tw	1%	1.5	5.0	10	5.0		2.5 ×10 <sup>-3</sup>
X1_Ca-5%	1%	2	1.0	5			
X1_Ca-10%	1%	2	1.0	10			
X1_Ca-15%	1%	2	1.0	15			
X1_Ca-20%	1%	2	1.0	20			
AX5C2	1%	2	5.0				
X5_Ca-5%	1%	2	5.0	5			
AX5C2-5%	1%	2	5.0	5			
AX5C2-7.5%	1%	2	5.0	7.5			
AX5C2-8% + Ta + Tw	1%	2	5.0	8		2.5	2.5 ×10 <sup>-2</sup>
AX5C2-8% + Fe + Tw	1%	2	5.0	8	5.0		2.5 ×10 <sup>-2</sup>
AX5C2-8% + Fe + Ta + Tw	1%	2	5.0	8	5.0	2.5	2.5 ×10 <sup>-2</sup>
AX5C2-9% + Fe + Ta + Tw	1%	2	5.0	9	5.0	2.5	2.5 ×10 <sup>-2</sup>
AX5C2-9.5% + Fe + Ta + Tw	1%	2	5.0	9.5	5.0	2.5	2.5 ×10 <sup>-2</sup>
AX5C2-9.5% + Fe + Ta + Tw	1%	2	5.0	9.5	7.5	2.5	2.5 ×10 <sup>-2</sup>
AX5C2-9.5% + Fe + Ta + Tw	1%	2	5.0	9.5	10.0	2.5	2.5 ×10 <sup>-2</sup>
X5_Ca-10%	1%	2	5.0	10			
AX5C2-10%	1%	2	5.0	10			
AX5C2-10% + Ta + Tw	1%	2	5.0	10		2.5	3.75 ×10 <sup>-2</sup>
AX5C2-10% + Fe + Tw	1%	2	5.0	10	2.5		
AX5C2-10% + Fe + Tw	1%	2	5.0	10	5.0		2.5 ×10 <sup>-3</sup>
X5_Ca-15%	1%	2	5.0	15			
X5_Ca-20%	1%	2	5.0	20			
X5_Ca	1%	2.5	5.0				



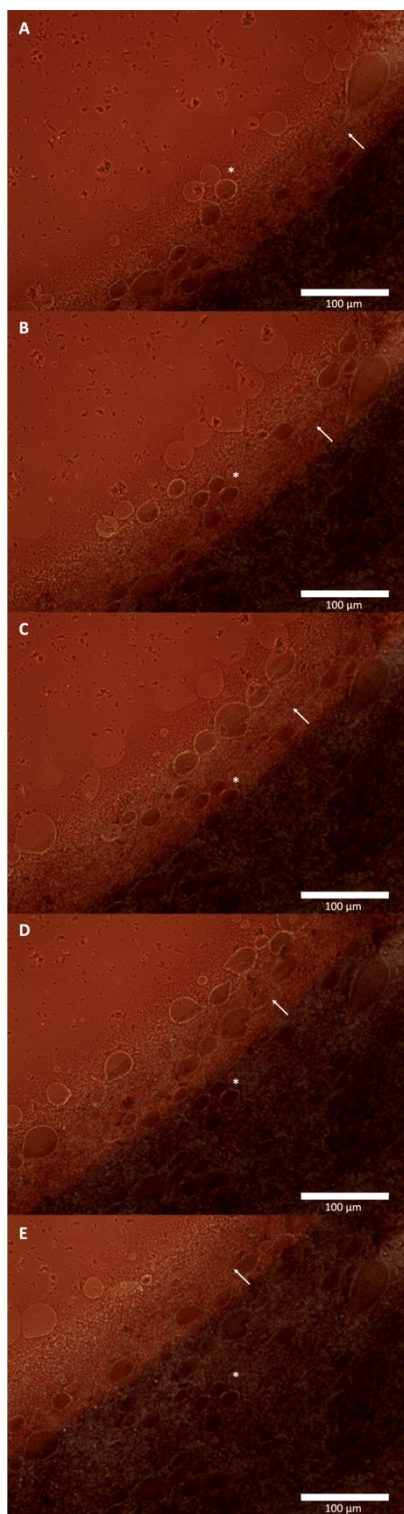


**Figure A2.9.** Time-lapse of FBS droplet drying. Images A-E represent ~30 s time intervals between images. \* Denotes the same cluster of MPs and the arrow indicates drying front.

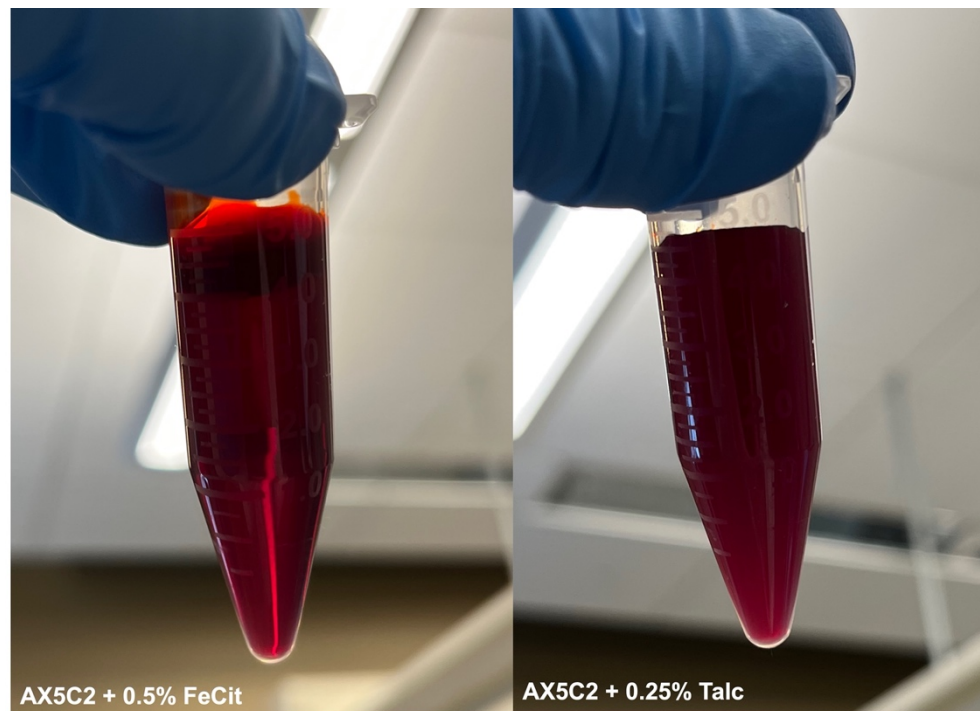


**Figure A2.10.** Appearance of FBS base material (1% w/v alginate,  $5.0 \times 10^{-2}$  w/v % XG, 2 mM  $\text{CaCl}_2$ , "AX5C2") with ferric citrate (left) or talc (right).

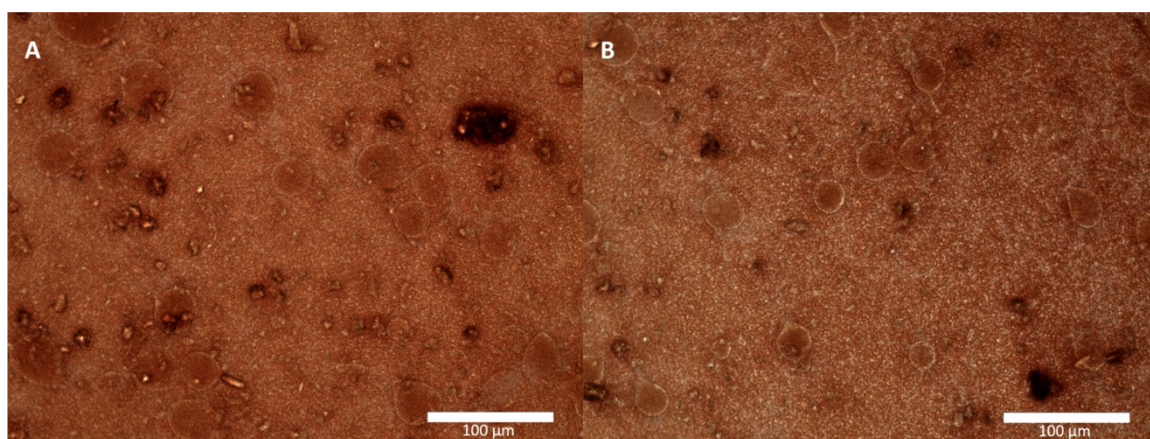


**Figure A2.11.** Microscope images of MPs within the FBS material before (A) and after (B) applied shear rates of  $1\text{-}1200 \text{ s}^{-1}$ .

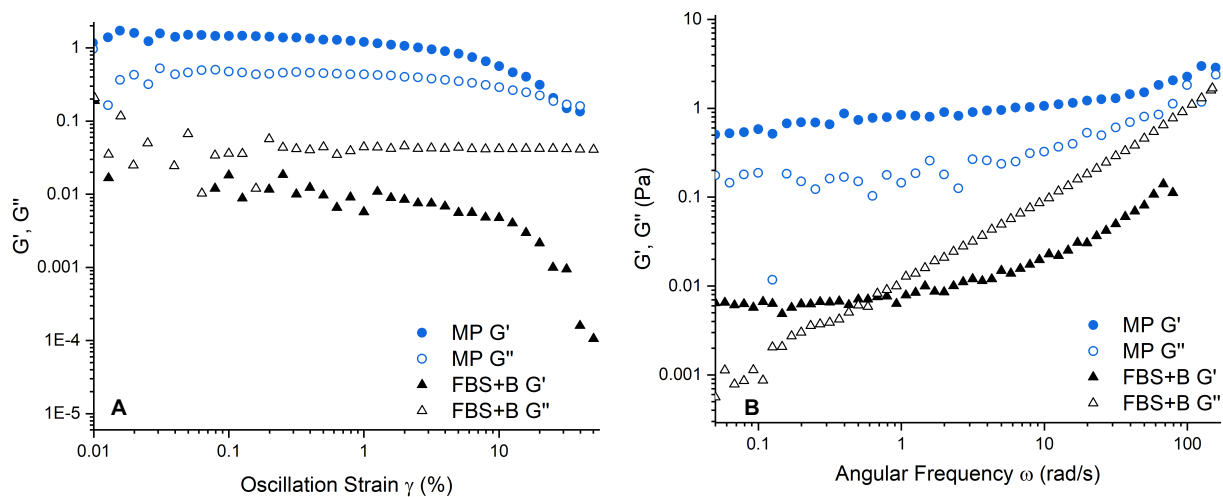


**Figure A2.12.** Amplitude sweep (A) and frequency sweep (B) of a concentrated MP solution (blue) and FBS + B (black). Filled-in symbols represent the storage modulus ( $G'$ ) and non-filled symbols represent the loss modulus ( $G''$ ).

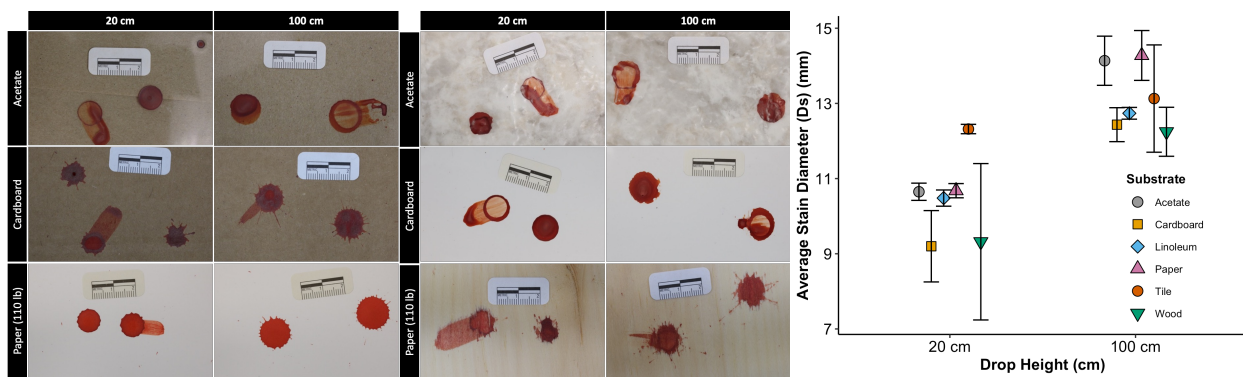


**Figure A2.13.** Drip stains dropped from 20 and 100 cm on six substrates: acetate paper, cardboard, paper, linoleum tile, tile, and wood (left). And the corresponding average stain diameter ( $D_s$ ,  $n=4$ ) (right).

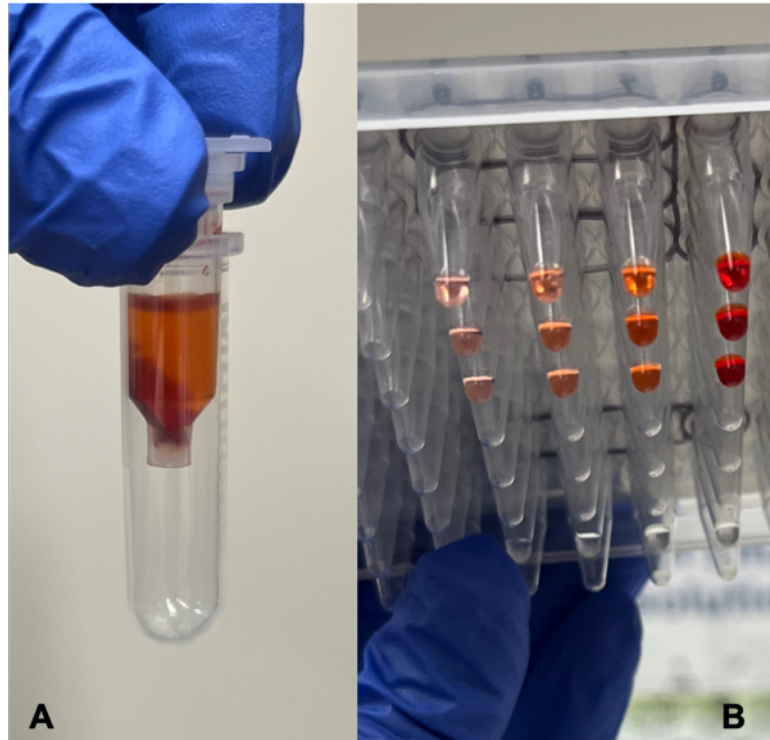


**Figure A2.14.** Image of filtration tube during extraction procedure where the red dye precipitates inside the filter (A) and the resulting PCR plate with various dilutions of extracted material from FBS (B). From left to right, the extracted DNA was added as 1:40 dilution, 1:20 dilution, 1:10 dilution, and stock.